



**HAL**  
open science

# Shear thickening in dense suspensions: revealing the frictional transition

Cécile Clavaud

► **To cite this version:**

Cécile Clavaud. Shear thickening in dense suspensions: revealing the frictional transition. Soft Condensed Matter [cond-mat.soft]. Aix Marseille Université, 2018. English. NNT: . tel-01970535

**HAL Id: tel-01970535**

**<https://theses.hal.science/tel-01970535>**

Submitted on 23 Mar 2020

**HAL** is a multi-disciplinary open access archive for the deposit and dissemination of scientific research documents, whether they are published or not. The documents may come from teaching and research institutions in France or abroad, or from public or private research centers.

L'archive ouverte pluridisciplinaire **HAL**, est destinée au dépôt et à la diffusion de documents scientifiques de niveau recherche, publiés ou non, émanant des établissements d'enseignement et de recherche français ou étrangers, des laboratoires publics ou privés.

# AIX-MARSEILLE UNIVERSITÉ

## École Doctorale 353 : Sciences pour l'Ingénieur : Mécanique, Physique, Micro et Nanoélectronique

Institut Universitaire des Systèmes Thermiques Industriels/UMR CNRS 7343

Thèse présentée en vue d'obtenir le grade universitaire de docteur

Discipline: Mécanique et Physique des Fluides

**Cécile CLAUD**

**Rhéoépaississement des suspensions denses : mise en évidence  
de la transition frictionnelle**

Shear thickening in dense suspensions: revealing the frictional transition

Soutenue le 10/07/2018 devant le jury composé de:

Élisabeth LEMAIRE	INPHYNI	Rapporteuse
Matthieu WYART	EPFL	Rapporteur
Élisabeth CHARLAIX	Université Grenoble-Alpes	Examinatrice
Romain MARI	LiPhy	Examineur
Laurence TALINI	Sorbonne Universités	Examinatrice
Yoël FORTERRE	IUSTI	Directeur de thèse
Bloen METZGER	IUSTI	Co-Directeur de thèse

Numéro national de thèse/suffixe local: 2018AIXM0260/019ED353



---

## Remerciements

---

The prayers of most religions generally praise and thank the gods involved, either out of general piety or in the hope that he or she will take the hint and start acting responsibly.

---

Terry Pratchett, *Faust Eric*.

En premier lieu, je voudrais remercier mes directeurs de thèse, Bloen et Yoël, de m'avoir donné l'opportunité de travailler sur un sujet passionnant et de m'avoir accompagnée durant ces trois années. Merci pour votre patience, pour la confiance que vous m'avez accordée, et pour tout ce que vous m'avez appris lors de ces trois ans d'expériences qui ne fonctionnent pas toujours comme on le voudrait, mais qui donnent toujours lieu à des discussions scientifiquement très enrichissantes.

Merci à Élisabeth Lemaire et Matthieu Wyart d'avoir pris le temps de rapporter mon manuscrit. Merci également à Élisabeth Charlaix, Romain Mari, et Laurence Talini d'avoir accepté de compléter mon jury de thèse.

Merci aux membres du laboratoire et de l'équipe GEP, notamment Laurence, Blanche, et Pascale, pour la bonne ambiance qui règne à l'IUSTI. Merci aux doctorant·e·s et post-doctorant·e·s avec qui j'ai partagé moult repas, cafés, vidéos du midi, et discussions à propos de tout et de rien : Matthieu, Saif, Yixian, Antoine, Joris, Loren, Sergio, Coraline, Aloïs, Hugo, Régis, et Émilie (qui nous espionne tous secrètement pour l'IRPHE). Merci à Ariane, Dominique, Delphine, Romain et Pascal, de m'avoir aidée à ne pas me noyer dans les eaux troubles de l'administration. Merci également aux membres de l'atelier : Sady, Paul et Frédéric, pour leur disponibilité.

Merci à ma maman "sans qui" (je cite approximativement) "je ne serais pas qui je suis", et à mon papa (qui lui ne s'est pas auto-remercié), de me soutenir littéralement depuis le tout début. Merci à Alice, que j'aime quand même même si une de ses premières actions a été de me donner un coup de poing dans l'œil. Merci à Corinne, Olivier et Martin de m'avoir accueillie comme iels l'ont fait.

Enfin, merci à toutes celles et ceux que je n'ai pas encore remercié, ami·e·s de plus ou moins longue date. Claire (trèèèè longue date) avec qui j'ai chanté, bavardé (et joué) à l'orchestre, et partagé des cours de solfège pas toujours très



studieux. Hélène, pour les beaux yeux de qui j'ai déménagé de deux étages à la ME. Diane, ma binôme préférée. Mariam, avec qui j'ai partagé une expérience de la vie en collocation pas si courte, mais intense. La 356, you know who you are. Comme quoi, voler des peluches héroïquement et les échanger contre des rançons de cacahuètes, ça mène à tout. La diaspora mathématique lyonnaise : Sylvain, François, François, et également François, sans oublier bien sûr François, Adriane, Blanche, Benoît, Romain, Matthias, Corentin, Agathe, les petit·e·s jeunes Hugo et Ariane, et les seul·e·s autres non matheuxses du groupe : Cyrielle, Cécile et Fred. Merci pour toutes ces après-midi jeux passés en votre compagnie, souvent à la colloc Garibaldi, accompagnés de brique au chocolat et de super caramel au beurre salé, pour les soirées au Ninkasi ou au Biéristan, les randos, l'escalade, bref, merci pour ces moments.

Et finalement, merci à Thomas, qui me fais à manger et qui me laisse lui voler son peignoir.



# Contents

<b>Introduction en français</b>	<b>1</b>
<b>Introduction in English</b>	<b>3</b>
<b>1 State of the art</b>	<b>5</b>
1.1 What is shear thickening? . . . . .	5
1.1.1 Notions of rheology . . . . .	5
1.1.2 Shear-thickening suspensions . . . . .	7
1.1.3 Applications of shear thickening . . . . .	9
1.2 Physical origin of shear thickening . . . . .	11
1.2.1 Rheology of ideal non-Brownian dense suspensions . . . . .	11
1.2.2 A brief history of shear thickening: from contacts to hydrodynamics... to contacts . . . . .	18
1.3 The frictional transition model . . . . .	24
1.3.1 General principle . . . . .	24
1.3.2 Numerical simulations . . . . .	26
1.3.3 A heuristic model . . . . .	28
1.3.4 First experimental support . . . . .	30
1.4 General aim of this thesis . . . . .	34
<b>2 Revealing the frictional transition using rotating drum flows</b>	<b>37</b>
2.1 The avalanche angle: a macroscopic signature of microscopic friction . . . . .	38
2.1.1 Background . . . . .	38
2.1.2 Experiments with a classical frictional suspension . . . . .	44
2.1.3 Experiments with a shear-thickening suspension . . . . .	49
2.2 Compaction and dilatancy . . . . .	54
2.2.1 Background . . . . .	55
2.2.2 Experiments . . . . .	58
2.2.3 Discussion . . . . .	62
2.3 Unveiling the frictional transition using a model suspension . . . . .	65
2.3.1 Glass and silica surfaces in aqueous ionic solutions . . . . .	65
2.3.2 Experiments . . . . .	68
2.3.3 Relation to the macroscopic rheology . . . . .	73
2.4 Conclusion of the chapter . . . . .	75
<b>3 The Darcytron: a pressure-imposed rheometer for colloidal suspensions</b>	<b>79</b>
3.1 General concept . . . . .	80

3.2	Proof of concept with a classical suspension . . . . .	84
3.2.1	Experimental set-up and protocol . . . . .	84
3.2.2	Definition of the average parameters . . . . .	87
3.2.3	Preliminary experiments . . . . .	87
3.2.4	Systematic results . . . . .	92
3.2.5	Discussion . . . . .	95
3.3	First results with silica suspensions . . . . .	98
3.3.1	Experimental set-up and protocol . . . . .	98
3.3.2	First experiments: the frictional transition . . . . .	100
3.3.3	Unexpected oscillations . . . . .	101
3.4	Conclusion and discussion . . . . .	104
<b>4</b>	<b>Conclusion and future works</b>	<b>107</b>
4.1	Conclusion . . . . .	107
4.1.1	Rotating drum experiments . . . . .	108
4.1.2	Experiments with the Darcytron . . . . .	110
4.2	Future works . . . . .	111
4.2.1	The Capillarytron . . . . .	111
4.2.2	Hysteresis . . . . .	112
<b>A</b>	<b>Rhéologie d'un milieu granulaire répulsif 2D : une expérience modèle pour comprendre le rhéoépaississement</b>	<b>115</b>
<b>B</b>	<b>Revealing the frictional transition in shear-thickening suspensions</b>	<b>143</b>
<b>C</b>	<b>Suspensions rhéoépaississantes : principes et applications</b>	<b>145</b>
	<b>Bibliography</b>	<b>147</b>



La *rhéologie* est le domaine de la physique qui étudie la façon dont la matière s'écoule. La matière solide, la matière liquide, et quelque part entre les deux, les milieux granulaires comme le sable. Le sable est-il un solide, ou un liquide ? C'est déjà une question complexe. Mais dans de nombreuses situations, les grains sont en plus mélangés à un fluide ; on appelle cela une *suspension*, et c'est encore plus compliqué.

Certaines suspensions sont capables de s'écouler comme un liquide lorsqu'on les agite doucement, et de soudainement se comporter comme un solide si on les touille trop vite. Cette propriété est appelée le rhéoépaississement. L'exemple le plus emblématique de suspension rhéoépaississante est le mélange d'amidon de maïs et d'eau. Ce phénomène est une source intarissable d'amusement : si vous remplissez une piscine d'un mélange d'amidon de maïs et d'eau, par exemple, vous pouvez courir dessus ! Depuis les premières observations expérimentales dans les années 1930, le rhéoépaississement fascine les physiciens et intéresse les industriels. La plupart des premières études publiées sur le rhéoépaississement tenaient à le décrire comme un phénomène nuisible dont il fallait se débarrasser. En effet, beaucoup de fluides industriels sont rhéoépaississants, ce qui peut causer des dommages dans les pompes, mélangeurs et tuyaux utilisés pour les transporter. Ces dernières années, au contraire, de nouveaux matériaux exploitant l'existence d'un état liquide sous faible contrainte dans les suspensions rhéoépaississantes ont vu le jour. Cela a donné lieu par exemple au développement d'armures souples ou de bétons autoplaçants.

L'origine physique du rhéoépaississement est longtemps restée mystérieuse. Plusieurs mécanismes ont été proposés, mais aucun ne parvenait à faire consensus. Très récemment, en 2013–2014, un scénario cohérent décrivant l'origine microscopique du rhéoépaississement a émergé à partir de travaux numériques [1, 2] et théoriques [3] menées au Levich Institute et à l'Université de New York. Ces travaux décrivent le rhéoépaississement comme une transition frictionnelle, nécessitant de prendre en compte à la fois les interactions colloïdales et le frottement à l'échelle des contact entre grains.

Cette nouvelle vision du rhéoépaississement constitue un changement de para-

digme, car elle place la physique du contact à l'échelle microscopique au cœur de la rhéologie des suspensions, qu'on a longtemps crue dominée par les interactions hydrodynamiques. Ma thèse s'inscrit dans ce nouveau point de vue. Son objectif est de développer des outils expérimentaux originaux permettant de sonder les propriétés frictionnelle de suspensions colloïdales, et de faire le lien avec leur rhéologie. Pour cela, je me suis inspirée de configurations issues de la physique des milieux granulaires. Dans un premier temps, j'ai étudié les angles d'avalanche et les propriétés de compaction et de dilatance de suspensions newtoniennes et rhéoépaississantes, dans un écoulement de tambour tournant. Le résultat de ces travaux (publiés dans [4]) a fourni une première preuve expérimentale directe du scénario de transition frictionnelle. Dans un second temps, j'ai développé un nouveau type de rhéomètre à pression imposée, adapté à l'étude de suspensions colloïdales : le "Darcytron".

Le manuscrit est organisé comme suit. Le premier chapitre dresse un état de l'art de la rhéologie des suspensions denses et du phénomène de rhéoépaississement au moment où ma thèse a commencé. Les deux chapitres suivants constituent le cœur du travail de thèse, et sont consacrés respectivement aux expériences en tambours tournants et aux expériences sur le Darcytron. Enfin le dernier chapitre résume le travail effectué et propose quelques perspectives. Les articles déjà publiés sur ce travail ( [4] publié dans le journal PNAS et [5] publié aux éditions Techniques de l'Ingénieur), ainsi que mon rapport de stage de M2 sur une expérience différente (milieu granulaire 2D répulsif) mais directement en lien avec le sujet de cette thèse, se trouvent en annexe.

---

## Introduction in English

---

With magic, you can turn a frog into a prince. With science, you can turn a frog into a Ph.D and you still have the frog you started with.

---

Terry Pratchett, Ian Stewart and Jack Cohen, *The Science of Discworld*.

*Rheology*. It is the study of how matter flows. Solid matter, liquid matter, and, at the frontier between them, granular matter like sand. Is sand a solid, or a liquid? That is a good question. And then, because it wasn't complicated enough, physicists put granular matter in a liquid, called this a *suspension*, and decided to study it.

Some suspensions can flow like a liquid when they are stirred gently, and suddenly behave like a solid if you stir them too fast. This property is called shear thickening. The most iconic example of such a suspension is the mix of cornstarch particles in water. Shear thickening can be the source of much fun: if you fill a swimming pool with cornstarch in water, you can actually run across it, for example. It has been fascinating physicists and interesting industries since it was first observed in the 1930's. Most of the initial studies about this phenomenon viewed it as a nuisance and aimed to suppress it. Indeed, many industrial fluids exhibit this rheological behaviour, which can cause important damage to pumps, mixers or pipes used to transport them. However, recent years have seen the development of new materials, which take advantage of the existence of a liquid-like regime at low stress in shear-thickening suspensions. This was used for example for the production of soft body armours, or for the formulation of self-compacting concretes.

The physical origin of shear thickening has long remained a mystery. Several explanations were put forward, but no consensus could be reached. Quite recently, in 2013–2014, a coherent scenario describing the microscopic origin of shear thickening emerged from numerical [1, 2] and theoretical [3] works conducted at the Levich Institute and at New York University. They described shear thickening as a frictional transition, which requires taking into account both colloidal interactions and solid friction at the grains' scale.

This new explanation of shear-thickening is the basis for a completely different vision of dense suspensions' rheology. Indeed, it gives microscopic contact physics



the central place, when for a long time it was believed that suspensions' rheology was dominated by hydrodynamic interactions. My PhD work took place in this context of a new viewpoint being adopted by the community. The objective of this thesis is to develop original experiments allowing to probe the frictional properties of colloidal suspensions, and to relate these properties to the suspension's rheology. To do this, I drew inspiration from granular media physics. First, I studied steady avalanches, compaction, and dilatancy effects, in a Newtonian and a shear-thickening suspension, using rotating drum flows. This study (published in [4]) provided a first experimental proof of the frictional transition scenario. In order to fully explore the transition, I then developed a new, pressure-imposed rheometer, suited to the study of colloidal suspensions: the 'Darcytron'.

This manuscript is organised as follows. The first chapter presents the state of the art on dense suspensions rheology and shear thickening at the beginning of my PhD. The two following chapters form the heart of my PhD work. They concern respectively the rotating drum experiments, and the Darcytron ones. Finally, the last chapter summarises our results, and proposes some ideas for future works. The appendices contain the two papers concerning this work already published ( [4] published in PNAS, and [5] published in *Techniques de l'Ingénieur* ), along with my Master's Degree dissertation on a different but related experiment (2D repulsive granular medium).

# CHAPTER 1

---

## State of the art

---

Everything starts somewhere, although some physicists disagree.

---

Terry Pratchett, *Hogfather*.

In this chapter, we present the state of the art on shear thickening in dense suspensions at the time when this thesis work began. We first define shear thickening and some of its applications, focusing more specifically on discontinuous shear thickening observed at high solid concentrations. We then discuss the physical origin of this phenomenon, giving a brief historical account of the different mechanisms proposed and a background on the rheology of dense suspensions. Finally, we present the frictional transition model proposed in 2013–2014 to explain shear thickening. The experimental validation of this model is the main objective of this work.

This chapter is based on an invited review we wrote for *Techniques de l'Ingénieur* (see [5] or Appendix C).

## 1.1 What is shear thickening?

### 1.1.1 Notions of rheology

When a fluid is stirred, it resists to the imposed movement in a way that depends on its nature. For instance, it is easier to make water flow than honey. The physical quantity that characterizes this resistance is the fluid's *viscosity*  $\eta$ . To define it, let us consider a simple shear flow, as represented on Figure 1.1. A fluid layer of thickness  $h$  is contained between two plates, one of which is moving at speed  $U$ , which causes a flow to develop in the fluid. In the steady state, the fluid's velocity is horizontal and depends linearly on the height with respect to the bottom plate, as shown by the blue arrows on Figure 1.1. We can then define the *shear rate*  $\dot{\gamma}$  as  $\dot{\gamma} = U/h$ . To maintain this flow, a *shear stress*  $\tau$  (force per unit area) has to be

applied tangentially by the moving plate on the fluid. The fluid's viscosity is then defined as  $\eta = \tau/\dot{\gamma}$  (see [6] for a general textbook in fluid mechanics). Since  $\tau = \eta\dot{\gamma}$ , the higher the fluid's viscosity, the more it will resist to an imposed flow. For instance, honey has a viscosity of  $10 \text{ Pa} \cdot \text{s}$ , whereas water's viscosity is  $0.001 \text{ Pa} \cdot \text{s}$ , which is one of the lowest viscosities among fluids.

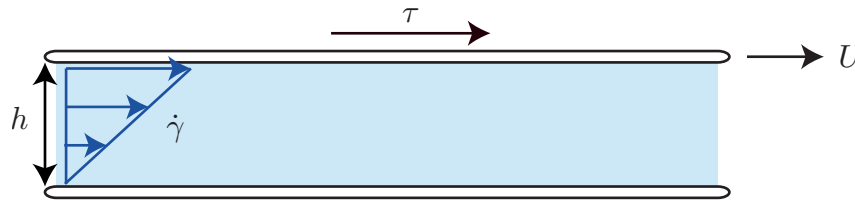


Figure 1.1 – Simple shear geometry: a fluid layer of thickness  $h$  is contained between two plates, one of which is moving with speed  $U$ .

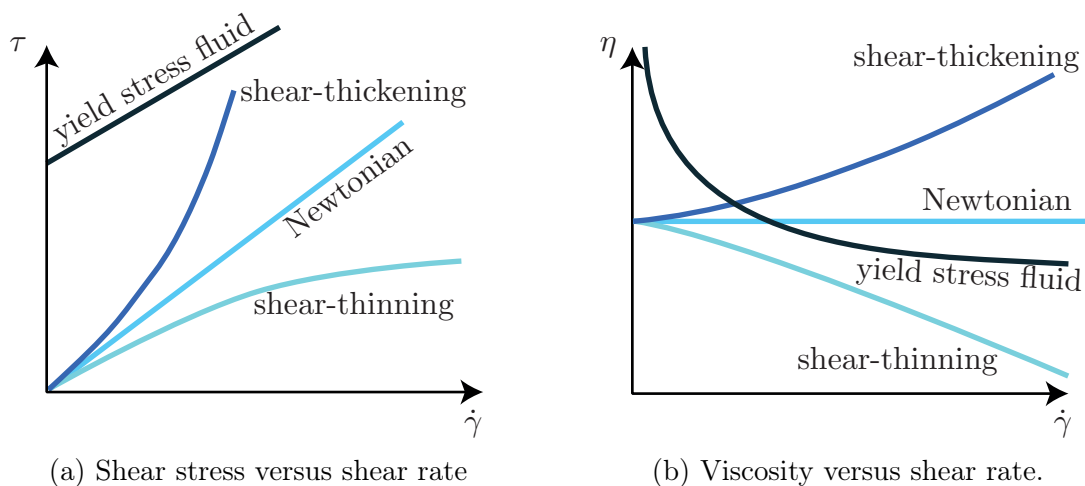
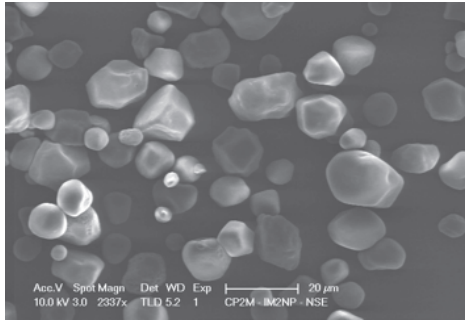


Figure 1.2 – Typical Newtonian and non Newtonian rheologies for different types of fluids.

For most fluids like gases and simple liquids, the viscosity doesn't depend on the shear rate  $\dot{\gamma}$  and the shear stress  $\tau$  is thus proportional to  $\dot{\gamma}$ . These fluids are called *Newtonian*. But many natural and industrial fluids like polymer solutions, gels, emulsions, or foams have a more complex behaviour. Their viscosity might decrease with the shear rate. Such fluids are called *shear-thinning* fluids. Conversely, their viscosity might increase with the shear rate: they are then called *shear-thickening* fluids. Some fluids have a diverging viscosity at vanishing shear-rate, which means they have a flow threshold, as is the case for example for mud or toothpaste. These are called *yield stress fluids*. Figure 1.2 summarizes these different rheological behaviours. The common feature of all these complex fluids is that they possess a microstructure at an intermediate scale between that of the fluid molecules and that of the flow. This microstructure is due for example to the presence of macromolecules, bubbles, particles, or droplets in the fluid. It is responsible for their non-Newtonian rheological behaviours (see for example [6, 7]).

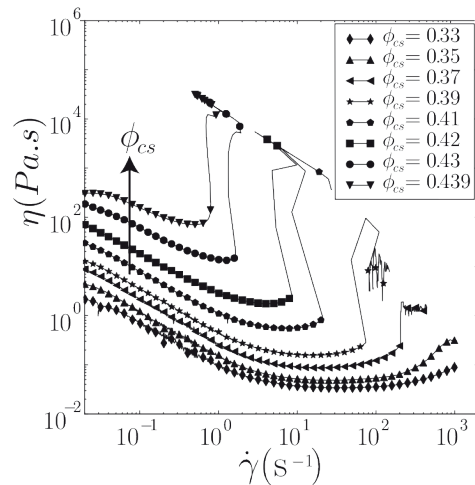
### 1.1.2 Shear-thickening suspensions

As mentioned in the previous section, shear thickening in complex fluids is an intriguing rheological behaviour in which the fluid's viscosity increases with the shear rate. In this thesis, we focus on the reversible shear thickening observed in some dense suspensions of particles. This phenomenon is arguably one of the most dramatic non-Newtonian behaviour in complex fluids (see [8,9] for a general review). The archetypal example of such suspensions is the mixture of cornstarch particles in water, see Figure 1.3. At low *packing fractions*  $\phi$ , the viscosity of this mixture is Newtonian, meaning that it does not depend on the imposed shear rate (not shown in Fig. 1.3). The packing fraction  $\phi = V_p/V_{\text{tot}}$  is defined as the ratio between the volume occupied by the particle  $V_p$  and the total volume of the suspension  $V_{\text{tot}}$ . For intermediate values of the packing fraction, a first regime is observed where the suspension's viscosity increases smoothly with the shear rate. This behaviour is known as *continuous shear thickening* (see [9]). When the packing fraction is high enough, the suspension's viscosity exhibits a transition at a critical shear rate  $\dot{\gamma}_c$ . This transition is characterized by a brutal increase of the viscosity, which can span several orders of magnitudes. This behaviour, known as *discontinuous shear thickening* (see [9]), is at the heart of this thesis. Finally, for higher packing fractions, the suspension's viscosity no longer reaches a defined value but seems to diverge at a critical shear rate. The medium then behaves like a solid. This last regime is sometimes called *shear jamming* (see [8, 10]).



— 20  $\mu\text{m}$

(a) Cornstarch grains: image taken with a Scanning Electron Microscope (SEM).

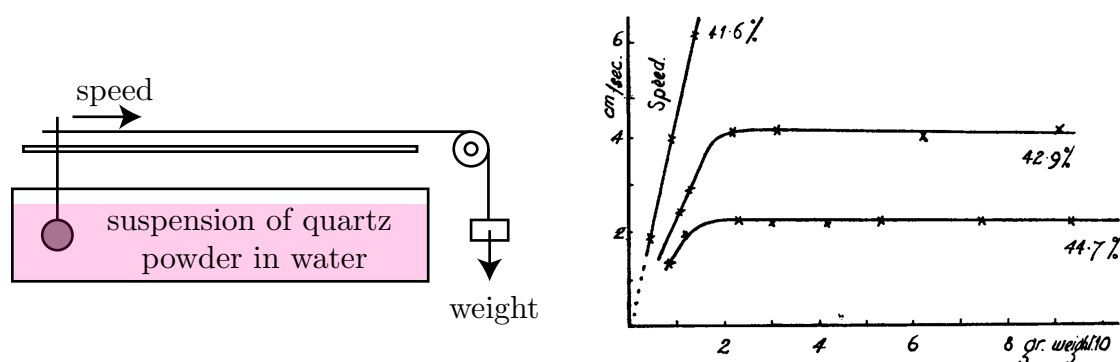


(b) Rheology of suspensions of cornstarch in a density-matched aqueous suspending fluid. From [11].

Figure 1.3 – Cornstarch suspensions: the archetypal example of shear thickening.

Historically, shear thickening in dense suspensions was first observed in coatings such as paints and inks. It presented industrial issues in their production. The first published studies were conducted with suspensions of vegetable origin, like corn, rice or potato starch, see for example [12] published by Williamson and Heckert in 1931. Freundlich and Röder studied suspensions of quartz or starch

grains in water in 1938 in [13]. Their results are presented in Figure 1.4. They moved a sphere in a suspension of quartz powder in water, and plotted its speed as a function of the pulling force applied on it. They observed that the behaviour of the suspension strongly depends on the packing fraction  $\phi$  of the suspension. As illustrated in Figure 1.4b, the measured suspension evolves from having a Newtonian behaviour at low packing fraction ( $\phi = 41.6\%$ , linear relation between the speed and the force) to having a shear-thickening one at higher packing fractions: above a critical pulling force applied on the sphere, its speed saturates. In their paper, Williamson and Heckert also showed that the nature of the suspending fluid was important: while suspensions of cornstarch in water are shear-thickening as stated above, the use of alcohol as the suspending fluid suppresses shear thickening (see [11–13]).



(a) Experimental set-up: a sphere moves through a suspension of quartz powder in water, pulled by a weight.

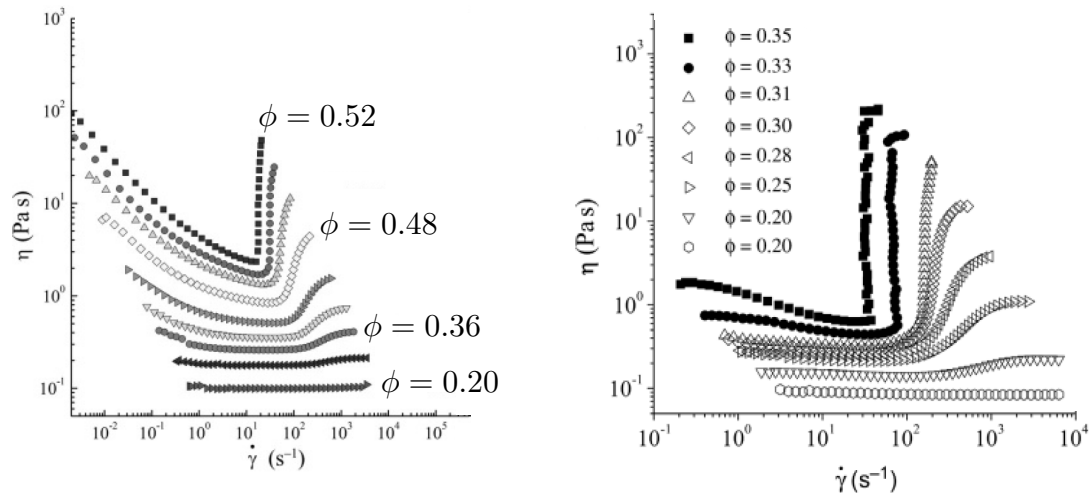
(b) Relation between the weight pulling the sphere (horizontal axis) and its speed (vertical axis). Note that the axes are inverted compared to the classical representation used in rheology. From [13].

Figure 1.4 – Pioneer experiments on shear-thickening suspensions conducted in 1938 by Freunlich and Röder in [13].

Since these first studies, shear thickening has been observed in numerous suspensions of particles from varied materials (silica, calcium carbonate, titanium oxide, etc.), as illustrated in Figure 1.5. Most data in the literature deal with Brownian particles (see for example [14]), that is, particles with a typical size inferior to a micron, subjected to thermal motion. But shear thickening can also be observed in suspensions of larger, non-Brownian particles (for instance in [8, 13, 15]). This led some researchers to think that perhaps all suspensions could exhibit shear thickening. Barnes for example wrote in his seminal review [16] published in 1989 that ‘given the right circumstances, all suspensions of solid particles will show the phenomenon’ (see also [17]). However, shear thickening doesn’t seem to be a common property of every dense suspension. From literature, the two well-identified common features of shear thickening suspensions are:

- the fact that the particles are relatively small, with a diameter  $d$  typically smaller than  $50\ \mu\text{m}$ ,

- the influence of the physical and chemical properties of the medium: presence of a surface treatment on the particles, nature of the suspending fluid, etc.



(a) Viscosity of 450 nm silica beads suspensions in a poly(ethylene glyco) and water mix, as a function of the shear rate, for different values of the packing fraction  $\phi$ .

(b) Viscosity of a calcium carbonate suspension as a function of the shear rate, for different values of the packing fraction  $\phi$ .

Figure 1.5 – Examples of shear-thickening suspensions. From [9].

### 1.1.3 Applications of shear thickening

Shear thickening in dense suspensions is not just an intriguing phenomenon. Many industrial fluids like ink, paint, fresh concrete, liquid chocolate, or ceramic pastes exhibit this rheological behaviour. Understanding its microscopic origin therefore has applications in industrial sectors ranging from glass manufacturing and civil engineering to the food industry.

In many situations, shear thickening is a behaviour that industries wish to avoid. A brutal increase in the viscosity of a transported fluid can damage pumps, mixers, and pipes. The first studies about shear thickening were conducted to solve a problem in the paper industry. While coating paper sheets with suspension films at high speed, the suspension's viscosity would sometimes increase so sharply that it tore the paper, damaging the whole production line in the process (see [18]).

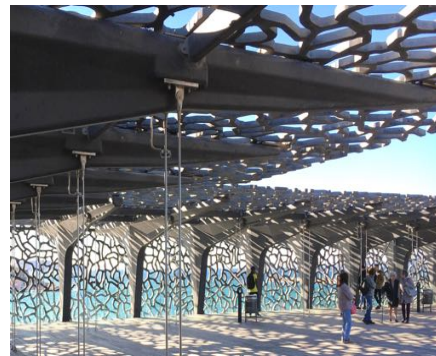
However, shear-thickening fluids are also characterized by a low viscosity state at low shear rates, which can be of use when working with dense suspensions. This is the case with casting processes using metallic or ceramic powders. The powder is usually dispersed in a liquid to make it easier to work with. The particles undergo surface treatment so that the suspension's viscosity becomes low even at high packing fractions. Another example comes from the chocolate industry. Chocolate is a suspension of ground cocoa beans and sugar in a continuous fat

phase made primarily of cocoa butter. The addition of lecithin allows for a very liquid chocolate paste even when using less fat (and therefore working at high packing fractions, see [19]).

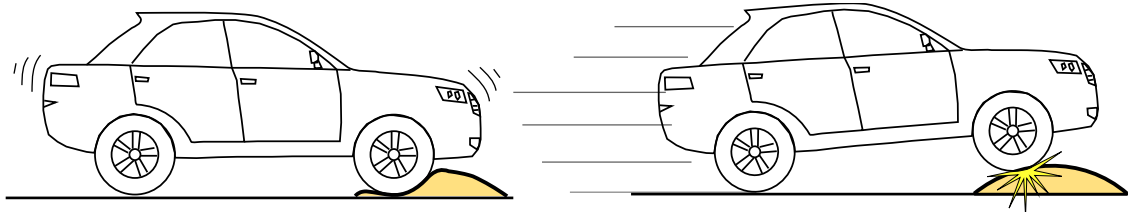
One of the most important applications of shear thickening is found in the concrete industry. In order to obtain a robust dry concrete, it is necessary to use fresh concrete with a high packing fraction. However, this hinders the flowability of the suspension. Maintaining a good flowability even with a high packing fraction has been an active research area since the sixties. Around this time, American highway manufacturers found by chance that adding a small amount of polymers to fresh concrete allowed them to obtain a material with better characteristics than normal concrete (see [20]). Since then, the use of these polymers, called superplasticisers, has allowed for a new generation of concrete (see Figure 1.6). Industrial research is now focused on understanding the mechanisms by which these polymers reduce the viscosity of fresh concrete suspensions, in order to optimize their formulation.



(a) Sketch illustrating the high flowability of modern concrete.



(b) Picture of the light structures of the Mucem museum in Marseille, enabled by modern concrete.



(c) Intelligent speed bump: it solidifies when the car's speed exceeds the speed limit.

Figure 1.6 – Applications of shear thickening in the concrete industry (Fig. 1.6a and 1.6b) and to road safety (Fig. 1.6c).

Recently, shear thickening has inspired the conception of new suspensions, to be used in soft body armours, sports equipments, or supple medical prosthetics. Shear-thickening suspensions can indeed absorb a lot of energy when impacted, while staying liquid the rest of the time (see [21]). Therefore, these soft equipments wouldn't hinder motion, while still protecting the body in the case of a bullet impact, a fall, or a sudden and sharp movement. Most of the recently patented techniques for the manufacturing of soft body armours involve the ingress of a shear-thickening fluid into a fibrous medium. For example, it is possible to ingress

Kevlar<sup>®</sup> with a suspension of silica micro particles in polyethylene glycol. This material can absorb three times as much energy as a standard Kevlar<sup>®</sup> vest (see [22]). There are several brands nowadays, for example Armourgel<sup>®</sup>, D3O<sup>®</sup>, or ARTi-LAGE, that sell clothes and joints protections using this kind of technique. The SFT Technologies firm sells medical fabrics protecting the skin from needlestick injuries. Finally, Badennova recently manufactured intelligent speed bumps, consisting in a supple sleeve filled with a shear-thickening suspension. The shear thickening transition is tuned to the speed limit, so that drivers who abide by it do not damage their car. For a car moving above the speed limit, the speed bump behaves as a solid one. This is illustrated in Figure 1.6c.

## 1.2 Physical origin of shear thickening

### 1.2.1 Rheology of ideal non-Brownian dense suspensions

As we have seen in the previous section, discontinuous shear thickening is observed for suspensions of solid particles immersed in a liquid when particles are small but not necessarily Brownian. Inertial effects and thermal motion thus do not seem essential for explaining this phenomenon. The shape of the particle is also not a key ingredient, as shear thickening has been observed both for spherical and irregular particles (see Figure 1.5 for example). It is therefore interesting to look into the expected rheology of an ideal or *classical* suspension made of non-Brownian hard spheres immersed in a viscous Newtonian fluid. The rheology of such non-Brownian suspensions has been the subject of many research since the seminal work of Einstein [23] in 1905 on the viscosity of dilute suspensions, and is still an active field of research (see [24] for a recent review). In this section, we show that for a classical suspension, the form of the rheology is strongly constrained by dimensional analysis.

#### Volume-imposed rheology and dimensional analysis

Let us consider a classical suspension of monodisperse hard spheres of diameter  $d$  in a Newtonian fluid of viscosity  $\eta_f$ , with packing fraction  $\phi$ . The suspension is placed between two plates and undergoes a viscous simple shear flow with shear rate  $\dot{\gamma}$ , see Figure 1.7. We consider size effects to be negligible, that is  $d \ll h$ , where  $h$  is the distance between the plates.

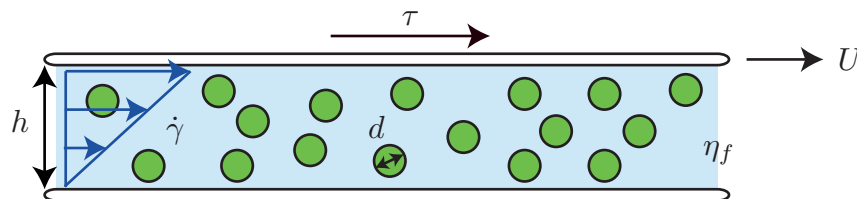


Figure 1.7 – Classical suspension undergoing a simple shear flow in an imposed volume geometry.



In this setting, we thus have four control parameters which are  $d$ ,  $\eta_f$ ,  $\phi$ , and  $\dot{\gamma}$ , depending on three dimensions: length, mass and time. Dimensional analysis then tells us that the system is controlled by one dimensionless parameter, which is here the packing fraction  $\phi$  (see [25] for a good textbook reference on dimensional analysis). Since  $\eta_f \dot{\gamma}$  is dimensionally the only stress scale in the system, we can express the shear rate  $\tau$  needed to shear the suspension as:

$$\tau = \eta_f \dot{\gamma} \cdot \eta_s(\phi), \quad (1.1)$$

where  $\eta_s$  is a function of the packing fraction  $\phi$  called the *dimensionless shear viscosity*. The suspension's viscosity  $\eta = \tau / \dot{\gamma}$  (see 1.1.1) is then:

$$\eta = \eta_f \eta_s(\phi). \quad (1.2)$$

Dimensional analysis thus imposes that the viscosity of an ideal suspension depends on the suspending fluid's viscosity and on the suspension's packing fraction, but not on the shear rate. Therefore, the rheology of such a suspension is necessarily Newtonian. The typical dependence of the dimensionless shear viscosity  $\eta_s$  with the packing fraction  $\phi$  is given in Figure 1.8. At very low packing fractions (typically  $\phi < 0.05$ ), one recovers the *dilute* regime predicted by Einstein:  $\eta_s = 1 + 2.5\phi$ . This increase in viscosity is purely hydrodynamic. It comes from the additional dissipation induced by the presence of a non-deforming particle in the extensional part of the shear flow (see [7]). For larger packing fractions, in the *semi-dilute* regime (typically up to  $\phi = 0.15$ ), the hydrodynamic interactions between particles come into play and the viscosity grows as  $\phi^2$ . Finally, for even larger packing fractions, contacts and steric constraints between particles become predominant. As a result, the viscosity rapidly increases, and diverges at the *critical packing fraction*  $\phi_c$  (see [7, 24]). Above this critical packing fraction, there can be no continuous flow in the suspension, which behaves like a solid.

The divergence of viscosity close to the critical packing fraction can be described by a power law:

$$\eta_s \propto (\phi_c - \phi)^{-\alpha} \text{ as } \phi \rightarrow \phi_c, \quad (1.3)$$

with  $\alpha \simeq 2$  (Maron–Pierce model in Fig. 1.9, see [24]), but other empirical functions have been proposed (see Fig. 1.9 and [24]). Importantly, the critical packing fraction  $\phi_c$  at which the suspension's viscosity diverges is not a universal value. In particular, it depends on the frictional interactions between particles via the *microscopic friction coefficient*  $\mu_p$ . For frictionless spheres ( $\mu_p = 0$ ),  $\phi_c^{\mu_p=0} \simeq 64\%$  is close to the *random close packing* that is obtained by repeated taping or vibrations (see [2]). However, for frictional particles ( $\mu_p \neq 0$ ), the critical packing fraction is smaller, typically within the range of 55% to 60% depending on  $\mu_p$ . We will see that this dependence of the critical packing fraction on the frictional properties of the particle is essential for the understanding of the shear thickening transition. Figure 1.9 gathers many experimental and numerical data on the dimensionless shear viscosity of non-Brownian suspensions conducted over the last years, for different particles and microscopic friction coefficient. All data collapse pretty well on a single curve when the packing fraction is normalised by the critical packing fraction  $\phi_c$  (see [24] and references therein).

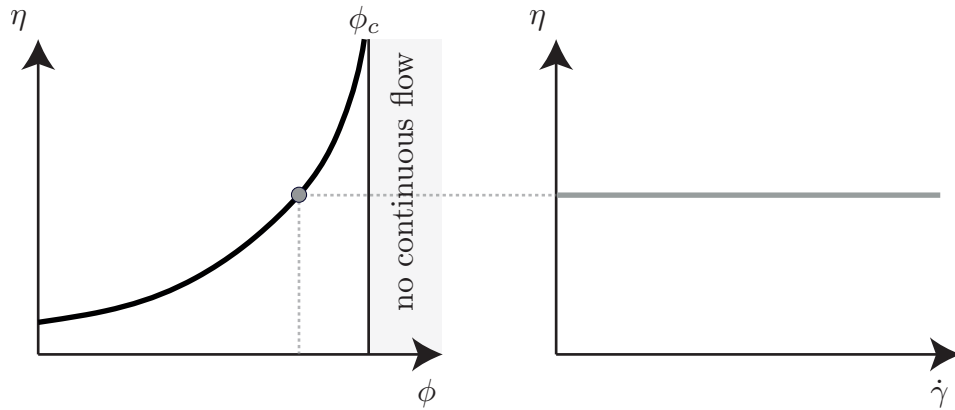


Figure 1.8 – Viscosity of a classical suspension as a function of the imposed packing fraction (left) or the imposed the shear rate (right).

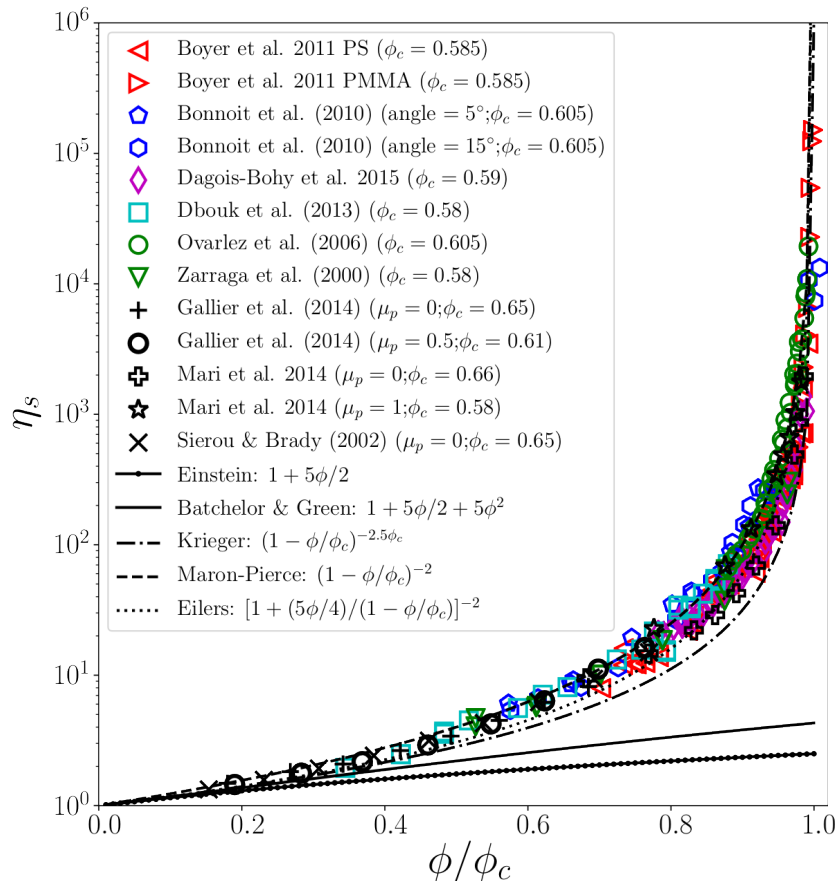


Figure 1.9 – Dimensionless shear viscosity as a function of the packing fraction for classical suspensions. From [24].

### Pressure-imposed rheology

Most experiments and numerical simulations studying dense suspensions used rheometric configurations close to the simple shear flow sketched in Figure 1.7: a

shear cell where the packing fraction is controlled and the total volume of the suspension is fixed. However, the proliferation of contacts leading to the divergence of the viscosity when  $\phi \rightarrow \phi_c$  makes it difficult to investigate the behaviour of a suspension close to its critical packing fraction  $\phi_c$ . As a result, a completely different approach, inspired by the rheology of dry granular flows (see [26]), has been carried out more recently. The idea is to conduct rheological experiments in which the pressure on the particles is controlled, while the volume of the suspension is free to adjust.

Let us consider the same suspension as before, now sheared between a plate and a mobile grid (see Figure 1.10). The suspending fluid is free to move through the grid, but not the particles. In this geometry, we can impose the *granular pressure*  $P$  on the grains by applying a force on the mobile grid.

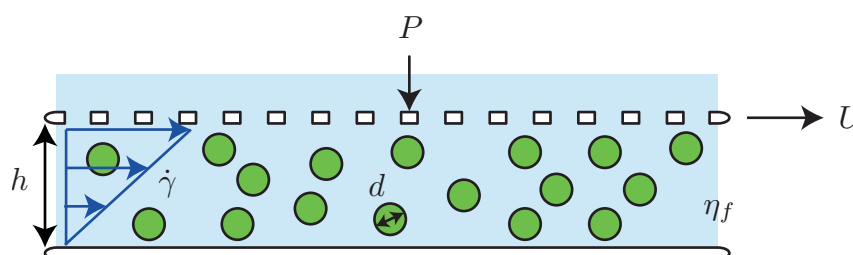


Figure 1.10 – Classical suspension undergoing a simple shear flow in a pressure-imposed geometry.

The volume, and therefore the packing fraction  $\phi$ , is no longer imposed as the fluid can pass back and forth through the grid. Following [27] (see also [24, 28]), we define the *viscous number*  $J$  by:

$$J = \frac{\eta_f \dot{\gamma}}{P}. \quad (1.4)$$

In this setting,  $J$  is the only dimensionless parameter controlling the system (by the same dimensional analysis arguments as before, see [25]). Dimensional analysis then implies that the shear stress  $\tau$  is proportional to the granular pressure  $P$ , and that the packing fraction  $\phi$  is a function of  $J$ :

$$\begin{cases} \tau = \mu(J)P, \\ \phi = \phi(J). \end{cases} \quad (1.5)$$

The function  $\mu$  is called the suspension's *macroscopic friction coefficient*, by analogy with the friction laws of Coulomb. The shapes of  $\mu$  and  $\phi$  as functions of  $J$  were first determined using a pressure-imposed set-up developed at IUSTI, sketched in Figure 1.11 (see [28]). They were further reproduced in discrete numerical simulations (see [24] and references therein). They are given in Figure 1.12. The important thing to note is that both functions remain finite in the quasi-static regime, that is, when  $J \rightarrow 0$ . We have  $\phi \rightarrow \phi_c$  as  $J \rightarrow 0$ , where  $\phi_c$  is the critical packing fraction defined earlier, and  $\mu$  converges to a given value  $\mu_c$  called the *critical or quasi-static macroscopic friction coefficient* of the suspension. As for

the critical packing fraction,  $\mu_c$  depends on the microscopic friction coefficient  $\mu_p$  between the particles. It varies from  $\mu_c \simeq 0.1$  for frictionless particles to  $\mu_c = 0.3$  to 0.4 for frictional particles (see Figure 1.13). Therefore, the macroscopic friction coefficient of the suspension gives access to the microscopic friction coefficient between the particles. We will use this important property in this thesis.

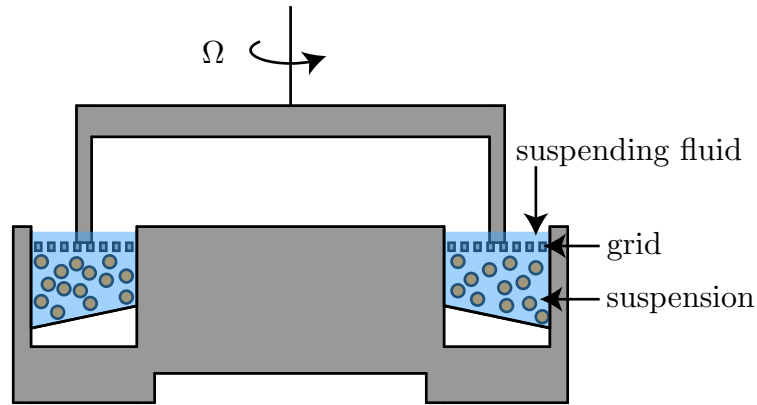


Figure 1.11 – Experimental set-up used in [28] to measure the rheology of a dense suspension in a pressure-imposed geometry.

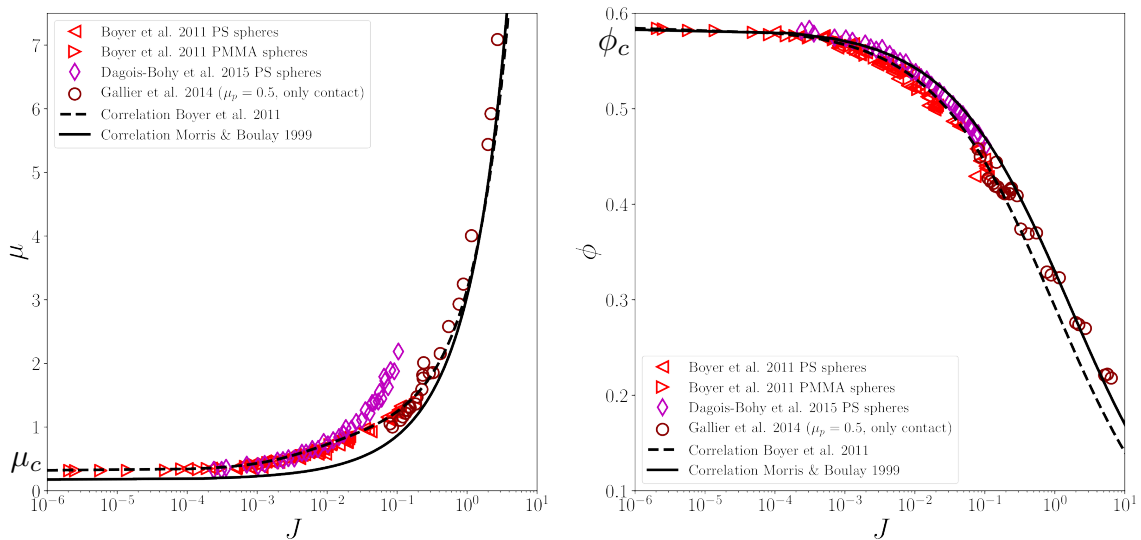
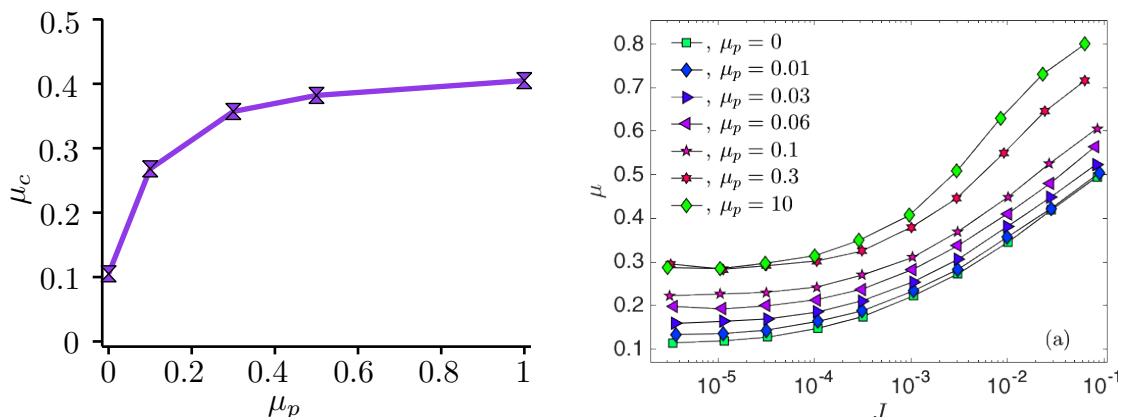


Figure 1.12 – Rheology of a classical suspension in a pressure-imposed. From [24].

### Link between the volume-imposed and pressure-imposed approaches

At first glance, the frictional expression of the rheology in the pressure-imposed configuration (Equation (1.5)) seems very different from the Newtonian rheology predicted for the same suspension in a volume-imposed configuration (Equation (1.1)). However, there is no physical reason for the suspension to behave differently in an imposed volume or in an imposed pressure configuration. We should



(a) Theoretical model for a granular medium of soft, frictional, noncohesive spheres. Model constants from [29].

(b) Simulations of a 2D suspension of hard spheres. From [30].

Figure 1.13 – Relation between the quasi-static macroscopic friction coefficient  $\mu_c$  and the microscopic friction coefficient  $\mu_p$  between the grains. Numerical simulations with different conditions. See [29] and [30].

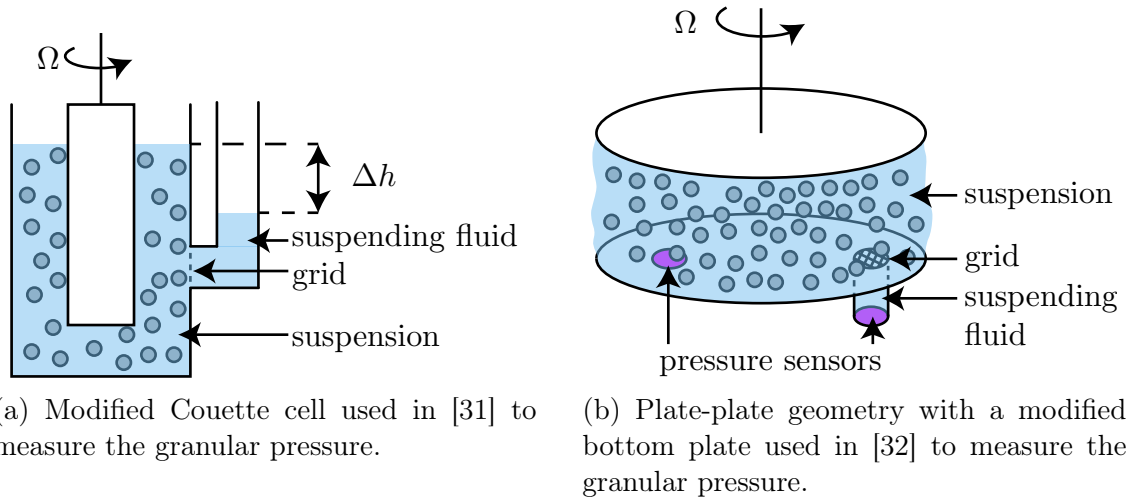
therefore be able to relate Equation (1.1) to (1.5). Indeed, using  $J = \eta_f \dot{\gamma} / P$  and the fact that  $J \mapsto \phi(J)$  is a bijection, we can write:

$$\begin{cases} \tau = \frac{\mu(J(\phi))}{J(\phi)} \eta_f \dot{\gamma}, \\ P = \frac{1}{J(\phi)} \eta_f \dot{\gamma}, \end{cases} \quad (1.6)$$

where  $\phi \mapsto J(\phi)$  is the inverse function of  $J \mapsto \phi(J)$ . We recover the linear relation between  $\tau$  and  $\dot{\gamma}$  obtained at constant volume, with a dimensionless shear viscosity given by  $\eta_s(\phi) = \mu(J(\phi)) / J(\phi)$ . Therefore, through the measure of  $\mu(J)$  and  $\phi(J)$ , one can compute  $\eta_s(\phi)$ . The advantage of this approach is that it allows for the indirect measure of  $\eta_s$  close to its divergence, since both  $\mu$  and  $\phi$  have a finite limit as  $\phi \rightarrow \phi_c$ . Using a pressure-imposed configuration is thus a very appropriate method to study the scaling laws of the rheological behaviour of the suspension close to its critical packing fraction.

Equation (1.6) gives the expression of the granular pressure in an imposed volume configuration. Physically, this pressure comes from the solid contact forces exerted by the sheared particles onto the plates of the cell. Note that since the suspension is incompressible, these forces which tend to push the plates outwards are compensated by a pressure coming from the fluid phase, which tends to pull the plates in (see [24] for a complete explanation). Measuring the granular pressure of a suspension in a volume-imposed configuration is difficult, since it is not easy to separate the fluid's contribution from the particle's contribution to the total stress. Still, few attempts exist in the literature. In 2009, Deboeuf et al. conducted experiments inspired by osmotic pressure measurements in [31]. The idea is to use a Couette-like cell with a grid connecting a tube to the fixed outer cylinder,

as illustrated in Figure 1.14a. The suspension is confined between the two cylinders and the grid prevents the particles from going into the tube. At rest, the fluid in the tube and the fluid in the cell reach the same height. When the suspension is sheared (by rotating the inner cylinder), a granular pressure develops in the system, and as explained above it creates a negative pressure in the fluid phase contained in the cell. Another experiment was developed in 2013 by Dbouk et al. [32]. The authors used a plate-plate geometry with a modified bottom plate, as illustrated in Figure 1.14b. On one side of the plate, they put pressure sensors which directly measure the total normal force  $P_{\text{tot}}$  applied on the plate by the suspension. On the other side, they put pressure sensors behind grids which only let the fluid pass through, so that they measure the pressure  $P_f$  in the fluid. The granular pressure  $P$  is simply  $P = P_{\text{tot}} - P_f$ .



(a) Modified Couette cell used in [31] to measure the granular pressure.

(b) Plate-plate geometry with a modified bottom plate used in [32] to measure the granular pressure.

Figure 1.14 – Measuring the granular pressure in an imposed volume configuration. See [31, 32].

The main message of this section is that whatever the approach used (volume-imposed or pressure-imposed rheometry), dimensional analysis imposes that suspensions of frictional non-Brownian hard spheres have a Newtonian rheology. At constant volume, the viscosity of such suspensions should be independent of the shear rate for all packing fractions, whatever the precise mechanism leading to the increase of viscosity close to the critical packing fraction is. How can we then explain that some suspensions exhibit shear thickening? In the following section, we present a brief historical account of the mechanisms that have been proposed to explain shear thickening, from its very first description in the 1930's to the beginning of the 2010's (see [9] for a more complete review)

## 1.2.2 A brief history of shear thickening: from contacts to hydrodynamics... to contacts

### First descriptions: a granular point of view, already

The first proposed interpretations of shear thickening considered the contribution of contacts between particles to be crucial. Freundlich and Röder identified the shear-thickening behaviour they measured as *dilatancy*, a concept first introduced by Reynolds in 1885 in [33]. Dilatancy is the tendency for compact granular media to transiently dilate when they are slowly sheared from rest. We define this concept more precisely in Chapter 2, but for now what is important to note is that it is an effect which relies on the existence of frictional contacts. Freundlich and Röder proposed an explanation of shear thickening based on a change in the microstructure of the suspension, as illustrated in Figure 1.15. In the Newtonian regime (part *a* on the curve), they postulate that the grains are uniformly distributed, as sketched on the left of Figure 1.15. Upon reaching a certain value of the shear rate, they expect that the particles will no longer be able to maintain this microstructure but rather will start ‘pil[ing] up in front of the moving sphere’ (recall that their experimental set-up is a sphere moving through a shear-thickening suspension, see Figure 1.4a in Section 1.1.2). They predict that this leads to the formation of the microstructure sketched on the right of Figure 1.15, which they say ‘always causes a suspension of this kind to behave like a solid system’ as long as the packing fraction is high enough. Williamson and Heckert also believed that shear thickening is caused by the presence of contacts between the grains in the suspension, though they distinguish shear thickening, which they call inverted plasticity, from Reynold’s dilatancy (see [12]). Although this description remains very qualitative, it is interesting to note that the early attempts to explain shear thickening already put forward the role of contacts and the link with granular media.

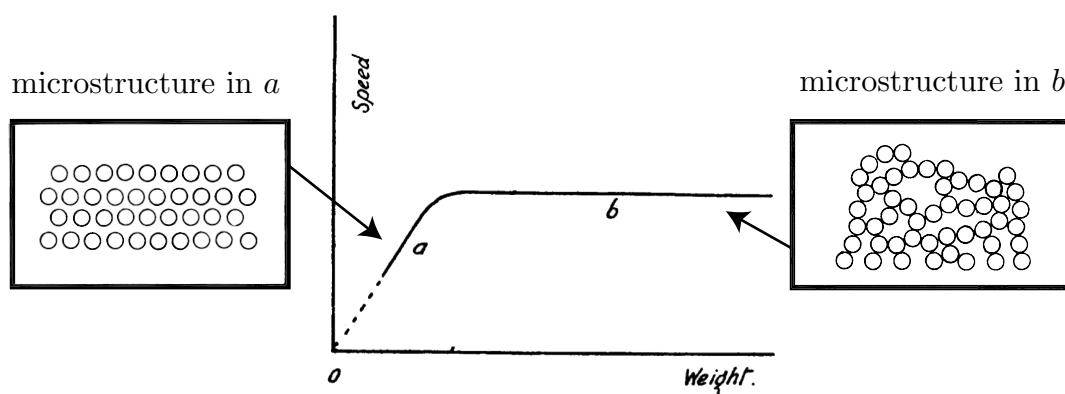


Figure 1.15 – An explanation of shear thickening put forward by Freundlich and Röder in [13]: a change in the microstructure of the suspension causes the grains to form frictional contacts, which jams the system. From [13].

### The importance of being colloidal

As stated in Section 1.1.2, most data on shear thickening deals with Brownian suspensions. In these systems, the particles have a typical size between 1 nm and 1  $\mu\text{m}$ , and are therefore strongly sensitive to van der Waals attraction (see [34]). To balance out this attraction and avoid aggregation, they often undergo surface treatment aiming to stabilise the suspension, by creating a repulsive barrier around them. Some researchers from the colloidal suspensions community put forward shear-induced aggregation as an explanation for shear thickening (see [35] for example). The idea is that above a certain shear rate, the hydrodynamic forces overcome the repulsive barrier and the particles are free to form aggregates. In 1972, Lee and Reder developed a model based on this idea (see [36]). It allowed them to derive an expression of the critical shear rate above which a suspension shear thickens, as a function of the particles' size, the intensity of the repulsive barrier, the packing fraction, and the suspending fluid's viscosity. They experimentally confirmed that '[t]he critical shear rate decreases with increasing particle size, medium viscosity, and concentration, and increases with increasing colloidal stability' [9, 36], as predicted by their model. We will see that this critical shear rate balancing hydrodynamic and short range repulsive forces is a key ingredient of the modern explanation of shear thickening, although the mechanism is very different from shear-induced aggregation.

### Hydrodynamics take over

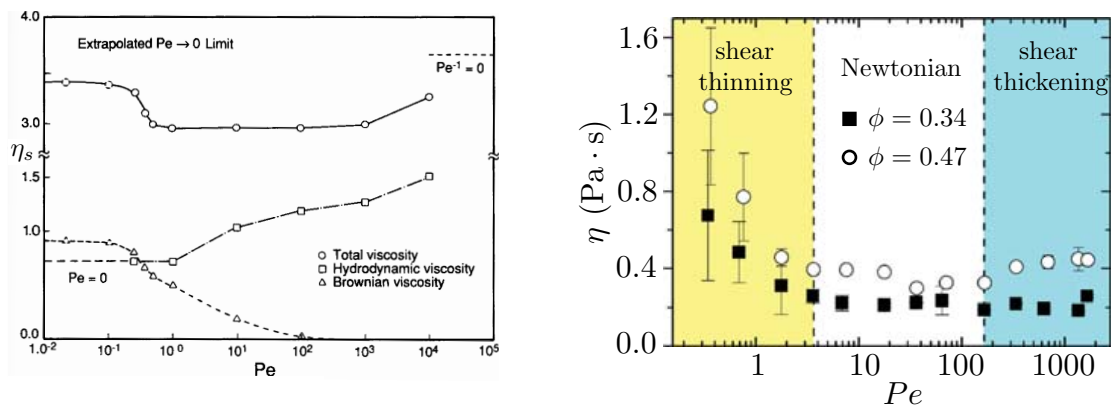
At the end of the eighties, Brady and Bossis developed a numerical simulation method for Brownian suspensions, which they called Stokesian Dynamics (see [37–39]). It describes a suspension as a collection of hard spheres immersed in a Newtonian fluid and subjected to hydrodynamic forces (viscous drag, lubrication) as well as thermal motion, but with no contact forces between the particles (either hard repulsion or friction). The justification was that, since lubrication forces diverge at contact, they should prevent solid contact. Therefore, hydrodynamics alone should be enough to describe the rheology. In this setting, the only dimensionless control parameter besides the packing fraction  $\phi$  is the Péclet number:

$$Pe = \frac{3\pi\eta_f d^3 \dot{\gamma}}{4k_B T},$$

which compares the relative importance of shear and hydrodynamic forces to thermal motion ( $k_B$  is the Boltzmann constant, and  $T$  is the temperature of the system). Figure 1.16a shows that for a given  $\phi$ , the shear viscosity in the numerical simulations depends on the Péclet number. We observe a first Newtonian plateau at low  $Pe$ , followed by a shear-thinning regime around  $Pe = 1$ . There is a second Newtonian plateau resulting from the competition between thermal motion and hydrodynamics. Finally, we observe a small shear thickening above  $Pe = 10^3$ . This increase in viscosity at high Péclet numbers was attributed by the authors to the creation of dense clusters of particles, which they called hydroclusters. The idea is that these clusters increase the suspension's viscosity due to the divergence of the lubrication forces. These hydroclusters have been observed experimentally by

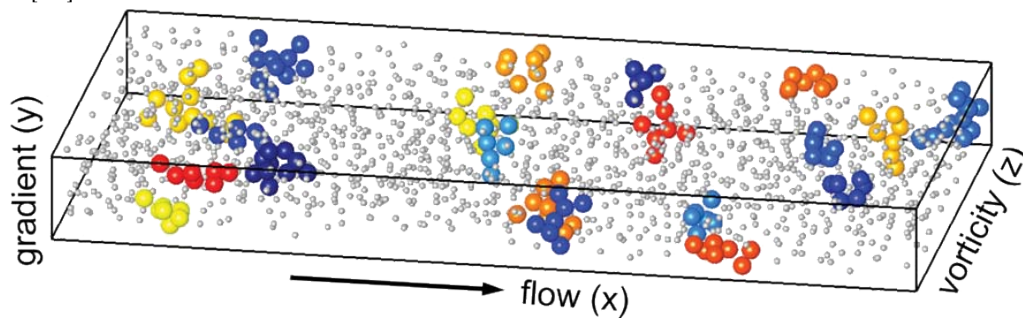


Cheng et al. (see [40] and Figure 1.16c). They also observe a mild shear thickening for large enough packing fractions (see Figure 1.16b).



(a) Relative viscosity of a simulated monolayer of immersed Brownian hard spheres, as a function of the Péclet number. From [39].

(b) Viscosity of a suspension of Brownian silica spheres in a Newtonian liquid, as a function of the Péclet number. From [40].



(c) Experimental observation of hydroclustering at high shear rate in a suspension of Brownian silica spheres in a Newtonian liquid. From [40].

Figure 1.16 – Mild shear thickening behaviour and hydroclusters at high Péclet numbers in Brownian suspensions.

Therefore, a purely hydrodynamic description of suspensions only predicts a weak continuous shear thickening with a viscosity increase by a factor 2 or 3. However, we have seen that, experimentally, it is possible to observe increases over one or two decades (see for instance the examples presented in Section 1.1.2). In addition, the interpretation of this mild shear thickening as stemming from the formation of hydroclusters in the suspension only holds for suspensions of Brownian particles. While it seems that hydroclusters do form at high shear rates in such suspensions (see [40]), this interpretation cannot be generalised to non-Brownian suspensions like cornstarch.

### Inertial transition

During the 2000's, together with the rise of studies on the rheology of dry granular flows, the importance of contacts in dense suspension was increasingly recognised.

In this context, a different explanation of shear thickening has been proposed, describing it as a transition between a viscous and an inertial flow regime [41, 42]. The idea is that at high packing fraction and shear rate, collisions between particles become important. The suspension's behaviour is thus closer to that of a dry granular material, an idea already put forward by Bagnold in the 1950's (see [43]). Let us consider a non-Brownian suspension of monodisperse hard spheres in a volume-imposed simple shear configuration. We assume that the momentum transfer occurs only through collisions between particles. In this case, the fluid's viscosity is no longer a relevant control parameter (see [24]), but we need to take into account the particles' density  $\rho_p$ , and their diameter  $d$ . By dimensional analysis, we obtain a Bagnold's scaling (see [43]) for the shear stress  $\tau$ :

$$\tau = \rho_p d^2 \eta_I(\phi) \dot{\gamma}^2, \quad (1.7)$$

where  $\eta_I$  is a dimensionless function of the packing fraction  $\phi$ , which diverges when  $\phi \rightarrow \phi_c$  (see [24]). At fixed packing fraction, the suspension's viscosity  $\eta = \tau/\dot{\gamma}$  thus depends linearly on the shear rate:

$$\eta = \rho_p d^2 \eta_I(\phi) \dot{\gamma}.$$

This analysis shows that an inertial suspension shear thickens. Following [44], we can assume that the crossover from a Newtonian behaviour at low shear rates (viscous flow) to a shear-thickening behaviour at high shear rates (inertial flow) occurs when the viscous stress (Eq. (1.1)) is equal to the inertial stress (Eq. (1.7)):

$$\eta_s(\phi) \dot{\gamma} = \rho_p d^2 \eta_I(\phi) \dot{\gamma}^2.$$

This yields a critical shear stress  $\dot{\gamma}_c$  given by:

$$\dot{\gamma}_c = \frac{\eta_f}{\rho_p d^2} \frac{\eta_s(\phi)}{\eta_I(\phi)}. \quad (1.8)$$

Some studies suggest that both functions  $\eta_s$  and  $\eta_I$  have the same divergence, meaning that as  $\phi \rightarrow \phi_c$  we can write  $\dot{\gamma}_c \propto \eta_f/(\rho_p d^2)$  (see [45] for example). In this case, the viscous to inertial transition doesn't depend on the suspension's packing fraction. For cornstarch particles in water ( $d = 10 \mu\text{m}$ ,  $\rho_p = 1500 \text{ kg} \cdot \text{m}^{-3}$ ), this criterion predicts a critical shear rate of  $\dot{\gamma}_c \sim 10^4 \text{ s}^{-1}$ . This is orders of magnitude larger than the critical shear rate  $\dot{\gamma}_c = 2 \text{ s}^{-1}$  reported by Fall et al. in [46], thus ruling out inertia as a mechanism for shear thickening. However, other theoretical studies (see [47]) suggest that the divergence of  $\eta_s$  is slower than that of  $\eta_I$ , meaning that  $\dot{\gamma}_c \rightarrow 0$  as  $\phi \rightarrow \phi_c$ . This would suggest that at high enough packing fraction, a suspension would always become inertial. Using  $40 \mu\text{m}$  polystyrene beads in water, Fall et al. indeed reported a decrease of  $\dot{\gamma}_c$  to 0 as  $\phi \rightarrow \phi_c$  (see Figure 1.17). However, their system is so far the only one for which the dimensionless shear viscosity in the Newtonian regime diverges like  $\eta_s \propto (\phi_c - \phi)^{-1}$  as  $\phi \rightarrow \phi_c$ . The question of whether the critical shear rate depends on the packing fraction or not is thus not yet resolved (see [24]). This makes it difficult to completely rule out any inertial effect in dense suspensions. However, let us stress that an inertial flow regime only induces a linear increase of the suspension's viscosity with the shear rate. This is a priori not sufficient to explain the strong shear thickening observed in suspensions of cornstarch in water for example.

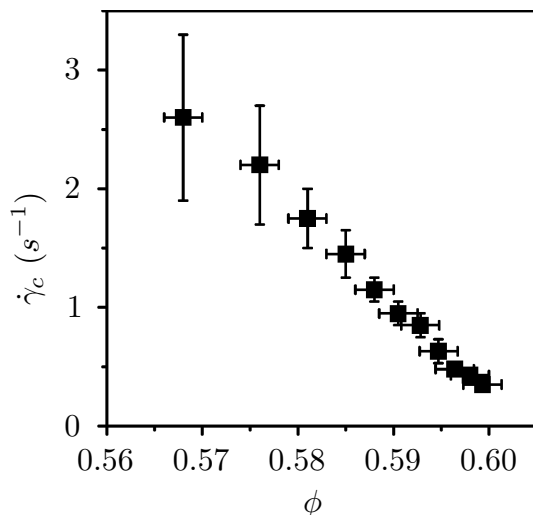
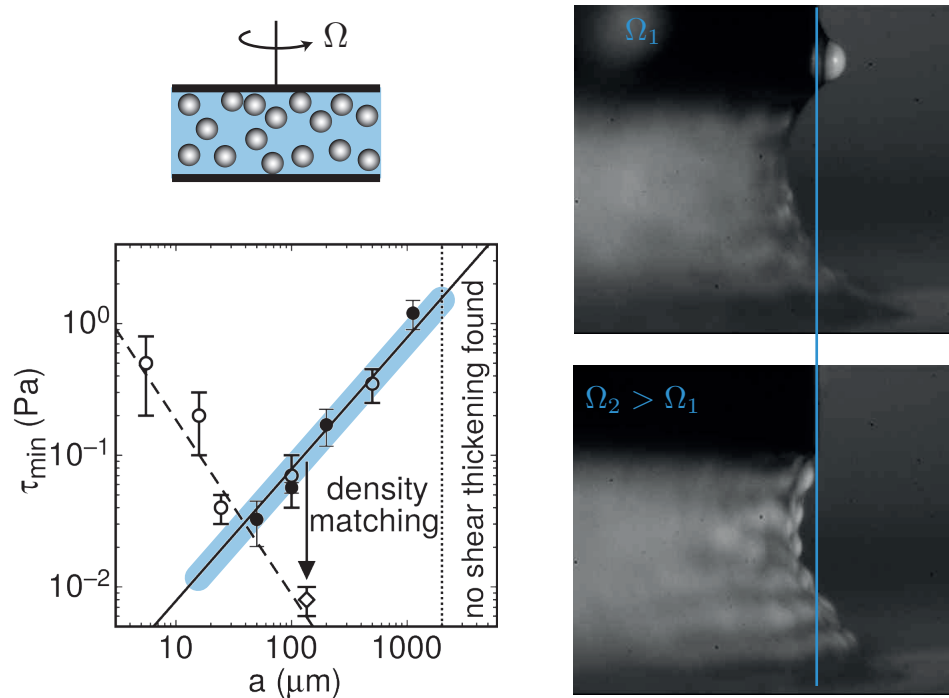


Figure 1.17 – Evolution of the critical shear rate at which the transition from the viscous to the inertial regime occurs with the packing fraction of the suspension. From [41].

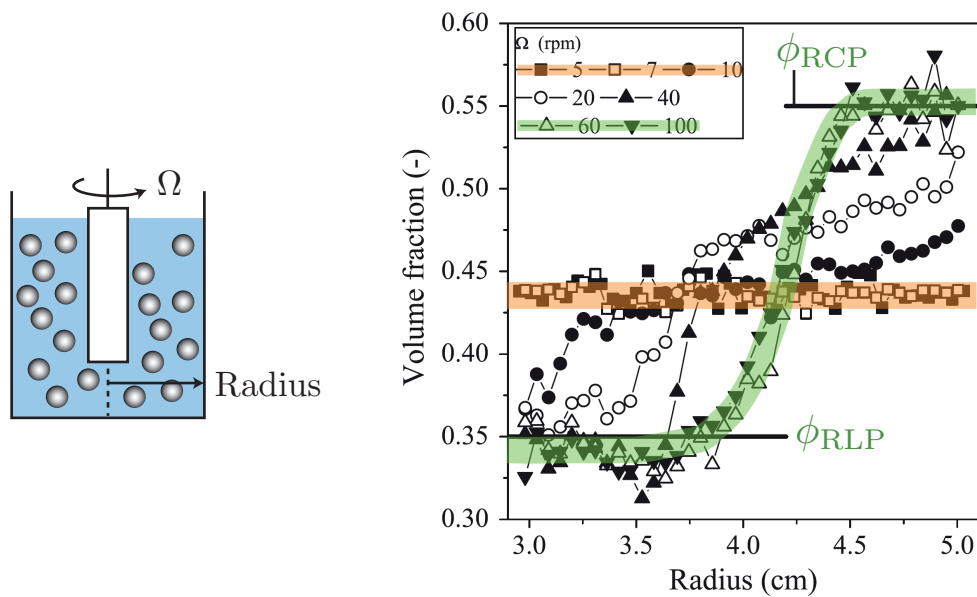
### Does shear thickening exist?

At the same period, some authors also questioned the actual existence of shear thickening as an intrinsic rheological behaviour (see [8, 10, 15]). For instance, Brown and Jaeger performed experiments in a plate-plate geometry over a wide range of particles size from  $5\ \mu\text{m}$  to  $1\ \text{mm}$  in non density-matched liquids (see [8]). Surprisingly, they report an apparent shear thickening behaviour even for very large particles. The onset stress  $\tau_{\text{min}}$  at which shear thickening appears first decreases and then increases with particle size, as shown in Figure 1.18a (left). In their interpretation, shear thickening appears at high packing fractions because the dilation induced by shear is frustrated by a confining stress, coming either from the surface tension at the liquid-air interface or from a solid boundary. For shear thickening to be observed, they argue that this ‘confining stress must significantly exceed all stresses that prevent shear between grains and dilation, such as interparticle interactions or gravity’. The increase of dilation induced by an increase of shear rate is clearly visible in Figure 1.18a (right). However, we have seen in Section 1.2.1 that dilatancy under flow is observed for all suspensions of hard spheres, even though their rheology is Newtonian by dimensional analysis. Indeed, this is simply the granular pressure term at constant volume, or the decrease of  $\phi$  with  $J$  at constant pressure. Therefore, dilatancy alone cannot explain discontinuous shear thickening. The fact that Brown and Jaeger observed discontinuous shear thickening for large particles likely comes from experimental artefacts, in their case resuspension effects due to the use of non density-matched suspension.

More recently, Fall et al. proposed that shear thickening is in fact a macroscopic result of a local viscous to inertial transition enhancing particles migration in the system (see [10]). The authors used a large gap Couette cell filled with a



(a) Apparent shear thickening and dilation under shear observed by Brown and Jaeger in [8].



(b) Experimental observation of migration in a suspension of cornstarch in water. Adapted from [10].

Figure 1.18 – Migration, sedimentation, and confinement effects, are three experimental artefacts that can cause apparent shear thickening.

suspension of cornstarch in water, sketched in Figure 1.18b (left). For low values of the rotating speed  $\Omega$ , the particles are homogeneously distributed in the cell (data point highlighted in orange). At higher rotating speeds, the particles mi-

grate to the outer cylinder of the cell due to stress inhomogeneities (data points highlighted in green). Surprisingly, when the authors plot the local relation between the shear stress, shear rate and packing fraction in the flowing region, they always found a Newtonian or shear-thinning behaviour, although the macroscopic response (torque versus rotation) is shear-thickening.

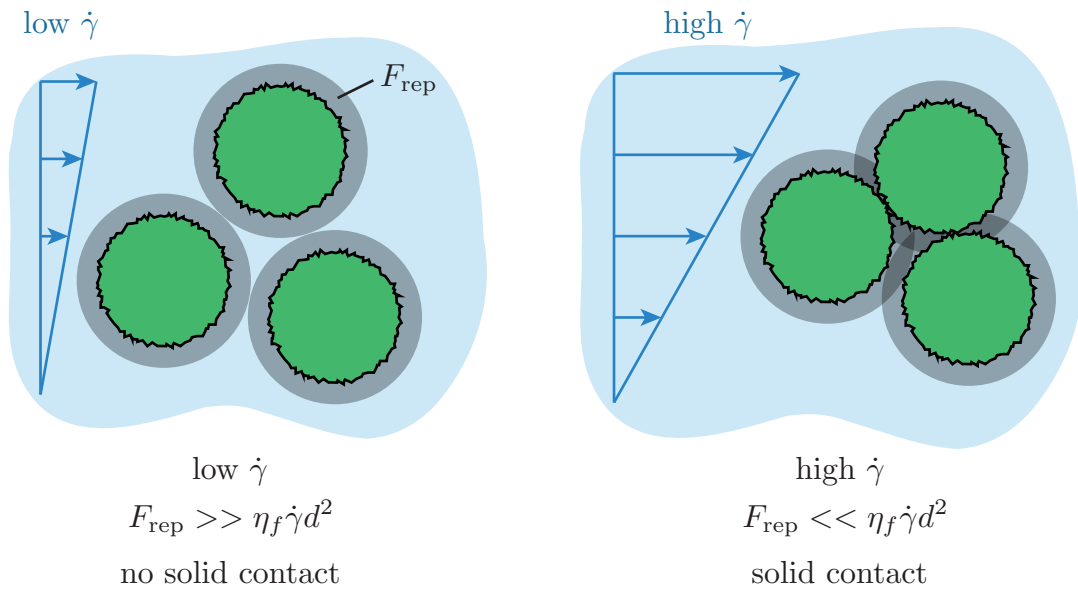
Following their observations, the authors conclude that shear thickening is not an intrinsic rheology of the suspension, but comes from inhomogeneities in the rheometer. However, in our opinion this does not explain the fact that only certain dense suspensions shear thicken regardless of the measuring geometry.

## 1.3 The frictional transition model

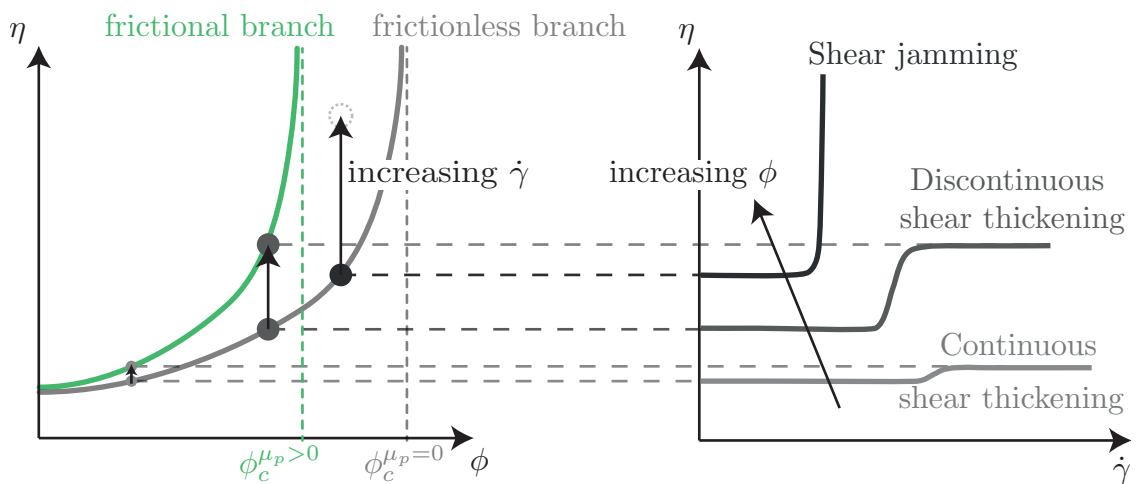
The previous overview shows that, until the beginning of 2010's, no clear explanation for the physical origin of shear thickening had emerged. The hydroclusters scenario based purely on hydrodynamics seemed valid to capture continuous shear thickening for Brownian systems, but failed to describe discontinuous shear thickening. For non-Brownian particles, the situation was even more obscure. A growing number of studies showed that contact and frictional interactions play a major role in the rheology of dense suspensions and in the shear thickening phenomenon [15, 28, 41, 42, 48], but we have seen that dimensional analysis imposes that an ideal non-Brownian suspension must be Newtonian, whatever the nature (lubricated or frictional) of the contact. The situation changed in 2013–2014, with a serie of numerical [1, 2] and theoretical [3] works describing shear thickening as a *frictional transition*. This transition requires to take into account both the frictional interactions between particles at contact, and the existence of a short-range repulsive force between particles. In the following, we detail this model, which is at the origin of my PhD work.

### 1.3.1 General principle

Let us consider, as before, a suspension of non-Brownian frictional hard spheres of diameter  $d$  in a Newtonian fluid of viscosity  $\eta_f$ , with packing fraction  $\phi$ , undergoing a viscous flow with shear rate  $\dot{\gamma}$ . We now add a new ingredient: the existence of a short-range repulsive force  $F_{\text{rep}}$  between the grains (see Figure 1.19a). In practice, this force could come from the existence of a surface charge on the particles, or from polymer brushes grafted on them (see [49] for example). In this setting, the competition between the repulsive force and the hydrodynamic forces controls the nature of the contact, as illustrated in Figure 1.19a. When the shear rate is low, the hydrodynamic forces are small and the repulsive force is the dominant force scale in the system. In this case, the particles cannot come into contact, and the suspension behaves *as if* it was a suspension of frictionless spheres, that is particles whose microscopic friction coefficient is  $\mu_p = 0$ . Conversely, at high shear rates the repulsive force is overcome by the hydrodynamic forces. The grains then come into contact, and the suspension behaves as a classical suspension of frictional particles, with a microscopic friction coefficient  $\mu_p \neq 0$ .



(a) Change in the nature of the contacts between repulsive grains, depending on the shear rate, which controls the relative importance of the hydrodynamic forces and the repulsive force.



(b) Shear thickening as a result of a frictional transition in the suspension. The suspension can evolve on either the frictionless (light grey) or the frictional (green) rheological curve (viscosity as a function of the packing fraction, on the right) depending on the nature of the contacts between the particles. At a given packing fraction, increasing the shear rate changes the frictional behaviour of the suspension and makes it go from one curve to the other.

Figure 1.19 – The general principle of the frictional transition model.

This transition between a frictionless state at low shear rates and a frictional state at high shear rates has a dramatic consequence of the rheology. Indeed, we have seen that the viscosity of a non-Brownian suspension diverges at a critical packing fraction  $\phi_c$  that *depends on the value of the microscopic friction coefficient*  $\mu_p$  (see Fig. 1.9). Therefore, frictional non-Brownian suspensions with a repulsive

force have two possible rheological branches, as illustrated in Figure 1.19b. If the shear rate  $\dot{\gamma}$  is small enough, the suspension's viscosity is given by the frictionless branch:  $\eta = \eta^{\mu_p=0}$ , which diverges at  $\phi_c^{\mu_p=0} = 64\%$ . Conversely, if  $\dot{\gamma}$  is large enough, the suspension's viscosity is given by the frictional branch:  $\eta = \eta^{\mu_p>0} > \eta^{\mu_p=0}$ , which diverges at  $\phi_c^{\mu_p>0} < \phi_c^{\mu_p=0}$ . Within this simple framework, it is possible to qualitatively explain the different regimes observed in shear-thickening suspensions. When  $\phi < \phi_c^{\mu_p>0}$ , the transition between the two asymptotic rheologies is continuous for low  $\phi$ , and discontinuous for high  $\phi$ . For  $\phi_c^{\mu_p>0} < \phi < \phi_c^{\mu_p=0}$ , only the frictionless state can flow continuously, and there is no frictional state accessible at large shear rates. The medium thus shear jams.

The existence of a repulsive force between the particles implies that there now exists an additional dimensionless parameters besides the packing fraction  $\phi$ , given by:

$$\dot{\Gamma} = \frac{\eta_f \dot{\gamma} d^2}{F_{\text{rep}}}. \quad (1.9)$$

Contrarily to the ideal suspension case seen before (see Eq. (1.2)), the suspension's viscosity now depends on the shear rate as well as the packing fraction, through:

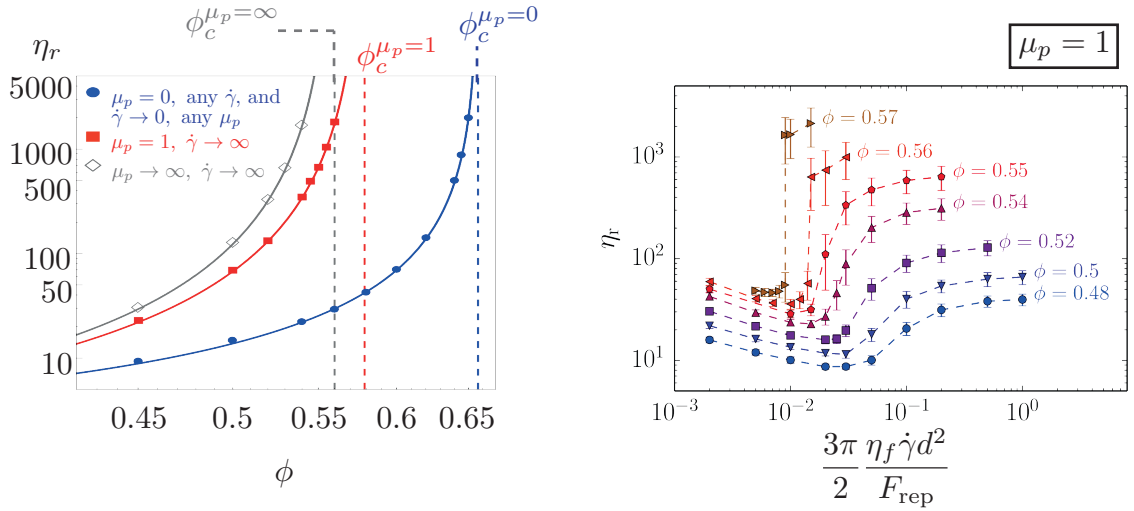
$$\eta = \eta_f \eta_s(\phi, \dot{\Gamma}). \quad (1.10)$$

The *dimensionless shear rate*  $\dot{\Gamma}$  represents the ratio of the hydrodynamic forces  $\eta_f \dot{\gamma} d^2$  to the repulsive force  $F_{\text{rep}}$ . It controls the transition between the frictionless and the frictional states (Fig. 1.19a).

### 1.3.2 Numerical simulations

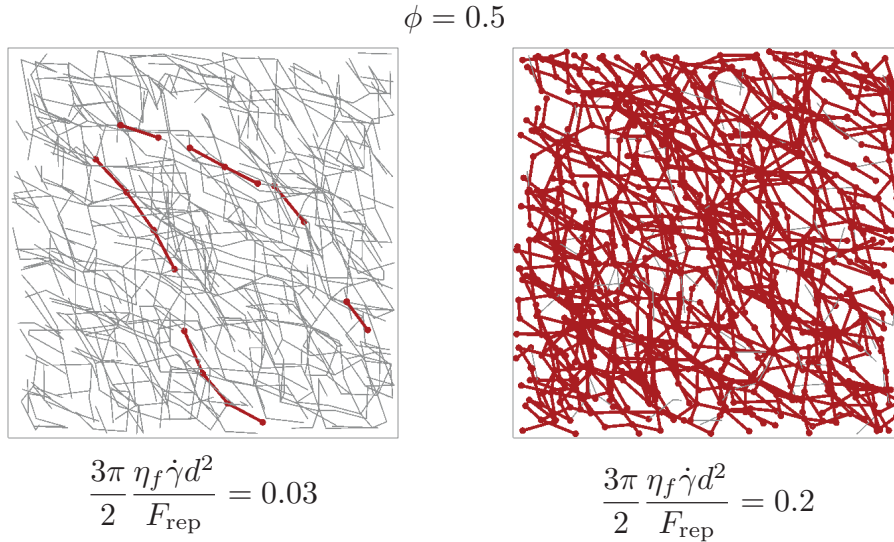
The ideas behind the frictional transition model emerged from numerical simulations done by Seto, Mari, Morris, and Denn [1,2]. Their approach is fundamentally different from that of Stokesian Dynamics [38]. Indeed, in [1,2] the authors introduced solid contacts between the particles in their simulations, thus highlighting the importance of friction in the rheological behaviour of dense suspensions. The different forces acting on the particles in the simulations are the following.

- The drag force, which scales like the relative velocity between the particle and the unperturbed shear flow.
- The lubrication forces between two particles, whose amplitude scales as the relative velocity between them and as the inverse of their separation distance.
- A granular-like contact force, which describes the contact between two particles as a frictional one, following a Coulomb law. It is characterized by a microscopic friction coefficient  $\mu_p$ . This force also prevents the interpenetration of particles.
- A short-range repulsive force  $F_{\text{rep}}$ , in the form of an electrostatic double-layer force or in the form of a threshold force.



(a) Relative viscosity of the suspension as a function of the packing fraction, for different values of the microscopic friction coefficient  $\mu_p$  and the shear rate  $\dot{\gamma}$ .

(b) Relative viscosity of the suspension as a function of the rescaled shear rate, for different values of the packing fraction, with  $\mu_p = 1$ .



(c) Evolution of the number of frictional contacts (red bars) with increasing shear rate.

Figure 1.20 – Simulations of a suspension of repulsive non-Brownian hard spheres in a Newtonian fluid. Figures adapted from [2].

Figures 1.20a and 1.20b give the principal results of the numerical simulations. First, we observe that the suspension's rheology does exhibit two different viscosity curves depending on the shear-rate (Fig. 1.20a). At very low shear rates, the viscosity curve follows that of a frictionless suspension, whatever the value of  $\mu_p$ . At high shear rates, the viscosity curve diverges at a critical packing fraction  $\phi_c^{\mu_p > 0} < \phi_c^{\mu_p = 0}$ . The simulations also reproduce the main phenomenology of shear-thickening suspensions (Fig. 1.20b). At low packing fractions, the simulated suspension exhibits continuous shear thickening, then with increasing packing frac-



tions it undergoes discontinuous shear thickening. As expected, the discontinuous transition is characterized by a strong increase of the number of frictional contacts, which percolate across the system (see Figure 1.20c).

In the simulations, the discontinuous shear thickening transition occurs at a critical shear stress  $\tau_c$  or a critical shear rate  $\dot{\gamma}_c$  that are linked to the repulsive force  $F_{\text{rep}}$  by:

$$\begin{cases} \tau_c = \beta \frac{F_{\text{rep}}}{d^2}, \\ \dot{\gamma}_c = \beta \frac{F_{\text{rep}}}{\eta^{\mu_p=0}(\phi) d^2}, \end{cases} \quad (1.11)$$

where  $\beta \simeq 0.04$ . These relations state that the critical shear stress for the apparition of shear thickening scales as the inverse of the particles' diameter squared. This explains why shear thickening can only be observed with small enough particles (see Section 1.1.2). For larger particles, the repulsive force, if it exists, would be overcome by any other force and the suspension would only exist in its frictional state.

Finally, these simulations were also conducted on Brownian suspensions, see [50]. The results show that thermal motion plays the same role as a repulsive force, by preventing the formation of frictional contacts under shear when the shear rate is small. Therefore, thermal motion together with friction induces a shear-thickening behaviour in the suspension. The expression of the critical shear stress can be generalised to repulsive Brownian suspensions by:

$$\tau_c \simeq \beta \frac{F_{\text{rep}}}{d^2} + 40 \frac{k_B T}{d^3}, \quad (1.12)$$

where  $k_B$  is the Boltzmann constant and  $T$  is the system's temperature. Usually, the Brownian part of the critical shear stress overcomes the repulsive part when  $d < 0.1 \mu\text{m}$ .

### 1.3.3 A heuristic model

Soon after the numerical simulations of Seto et al., Wyart and Cates proposed in 2014 a heuristic model that formalizes the frictional transition scenario [3]. The authors consider a non-Brownian suspension in which interparticle friction is activated only when the granular pressure  $P$  overcome a repulsive pressure  $P_{\text{rep}} = F_{\text{rep}}/d^2$ . The idea is to describe the crossover between the two rheological branches (frictionless and frictional) accessible to the suspension as a function of a *dimensionless pressure*  $\Pi = P/P_{\text{rep}}$ . Both viscosity branches diverge at a critical packing fraction which is  $\phi_c^{\mu_p=0}$  when all the contacts are frictionless, and  $\phi_c^{\mu_p>0}$  when all the contacts are frictional. For intermediate cases, the authors propose that the critical packing fraction at which the suspension's viscosity diverges can be written as a linear interpolation between the two limiting critical packing fractions:

$$\phi_c(f) = f \phi_c^{\mu_p>0} + (1 - f) \phi_c^{\mu_p=0}, \quad (1.13)$$

where  $f$  is the fraction of frictional contacts between two particles. They assumed that  $f$  is an increasing function of the dimensionless pressure  $\Pi$ , going from 0

when  $\Pi \ll 1$  (the suspension behaves as if it was frictionless) to 1 when  $\Pi \gg 1$  (the suspensions recovers its frictional behaviour). In their paper, the authors chose the following expression:

$$f(\Pi) = 1 - \exp(-\Pi), \quad (1.14)$$

which is compatible with numerical simulations (see Figure 1.21 and [2]). Finally, they close the model by writing the granular pressure  $P$  as:

$$P = c \cdot \eta_f \dot{\gamma} \cdot (\phi_c(f) - \phi)^{-2}, \quad (1.15)$$

where  $c$  is a constant. Equation (1.15) simply expresses the divergence of the granular pressure close to the critical packing fraction (see Equation (1.6)).

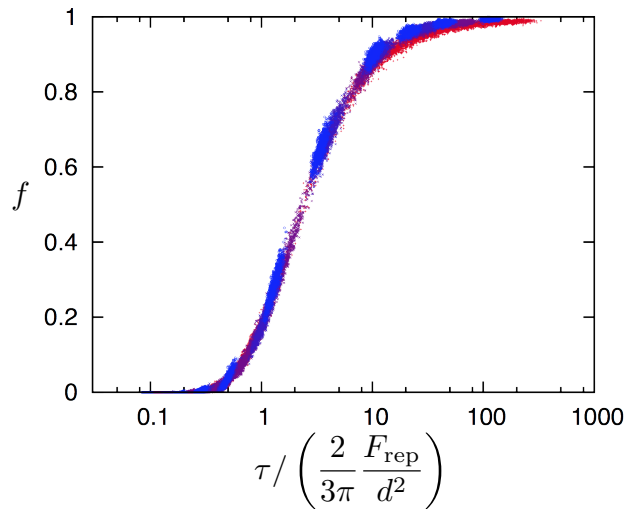


Figure 1.21 – Fraction of frictional contacts as a function of the shear stress rescaled by the repulsive stress, for different values of the packing fraction. From [2].

The rheological curves predicted by the model (using Equations (1.13), (1.14), and (1.15)) are shown in Figure 1.22, which gives the dimensionless pressure  $\Pi$  as function of the shear rate for different packing fractions. Note that similar plots would be obtained if the more usual shear stress  $\tau$  was used instead of  $\Pi$ . The model recovers the main feature of shear-thickening suspensions. For low values of the packing fraction, the dimensionless pressure exhibits two Newtonian plateaus connected by a portion of curve of higher slope. In this range of packing fraction, the suspension thus undergoes continuous shear thickening. At a packing fraction  $\phi_{DST} = 55.4\%$ , the slope connecting the two Newtonian plateaus becomes infinite (grey vertical line and dashed black curve). This marks the onset of discontinuous shear thickening. In a range of packing fractions above  $\phi_{DST}$ , the rheological curves are S-shaped. There are two values of  $\dot{\gamma}$ , called  $\dot{\gamma}^-$  and  $\dot{\gamma}^+$ , for which the tangent to the curve is vertical. The system can then flow either with a high viscosity (corresponding to values of  $\Pi$  in the upper Newtonian plateau) or with a low viscosity (corresponding to values of  $\Pi$  in the lower Newtonian plateau), and the chosen viscosity depends on its history (the green portion is forbidden). This S-shape thus induces an hysteretic loop in the rheology (highlighted in yellow)

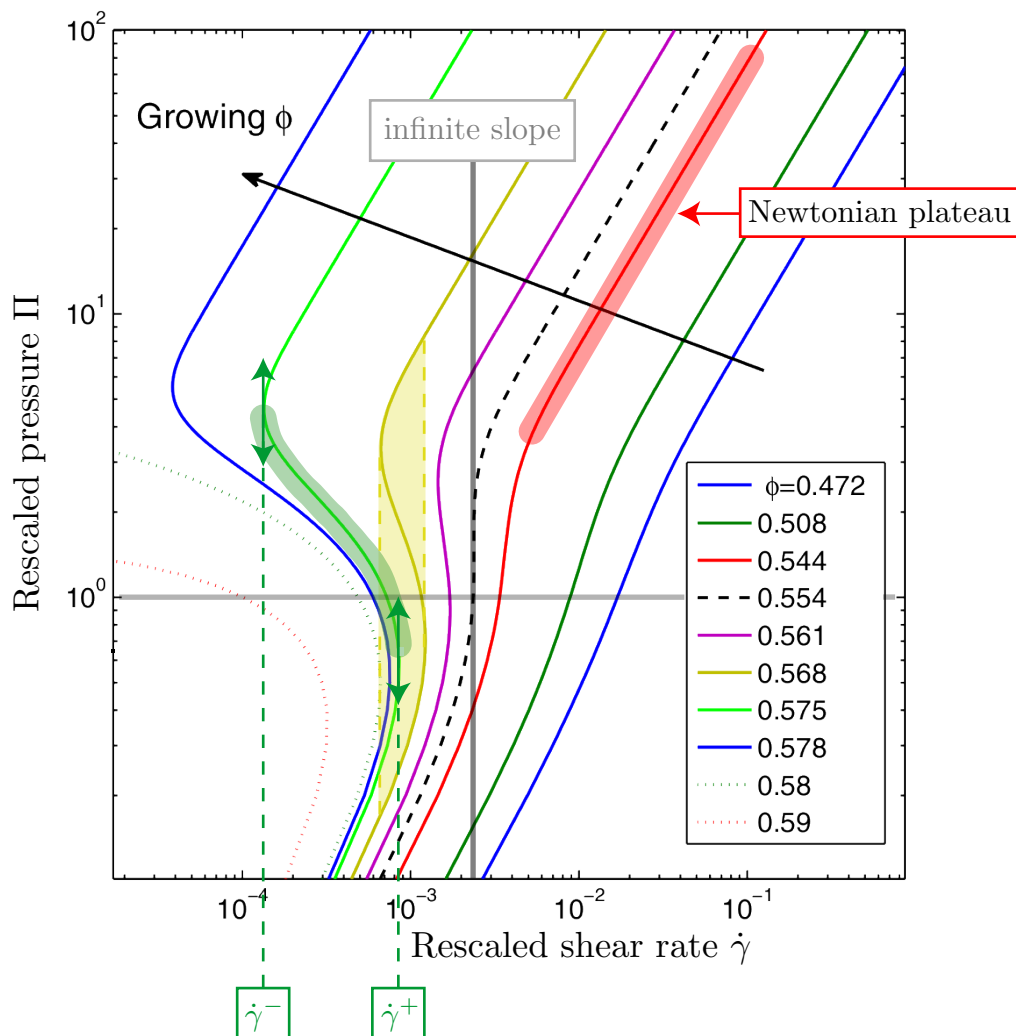


Figure 1.22 – Evolution of the dimensionless pressure with the shear rate, for different packing fractions. Adapted from [3].

and gives rise to a discontinuous shear thickening rheology for high enough packing fractions. Finally, above a second critical packing fraction given by  $\phi_c^{\mu_p > 0}$ , there is no longer a second Newtonian plateau: the system shear jams if the shear rate is too high. This is illustrated by the phase diagram shown in Figure 1.23, which summarises the model's predictions.

### 1.3.4 First experimental support

The frictional transition mechanism proposed by Seto et al. in 2013 and Wyart and Cates in 2014 thus provides a first consistent framework explaining the discontinuous shear thickening observed in dense suspensions. At the beginning of my PhD, some studies had started to investigate this model experimentally.

The first experiments were conducted by Guy et al., who studied suspensions of poly(methyl methacrylate) (PMMA) particles subjected to steric repulsion through

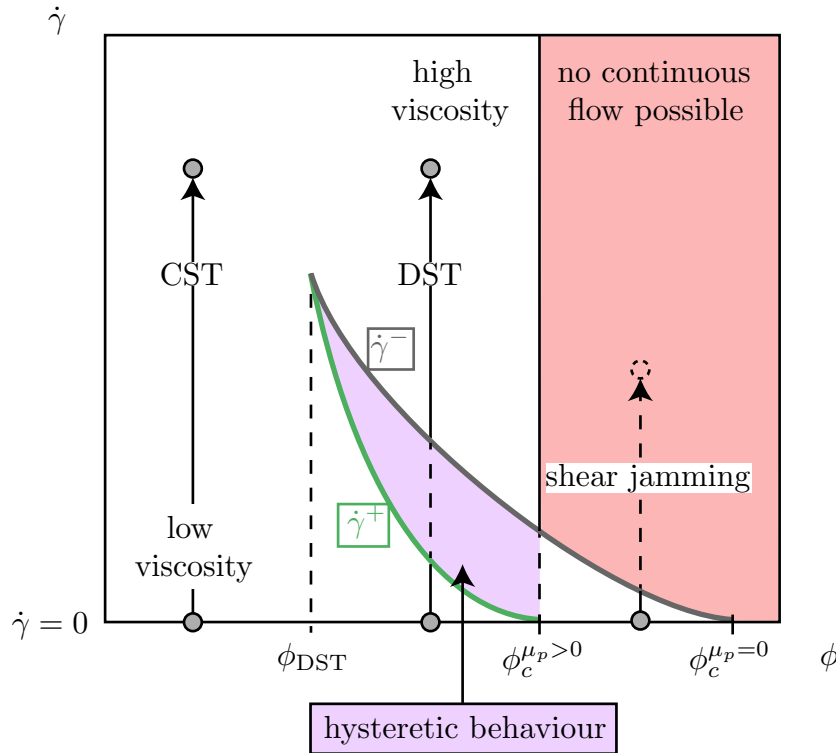
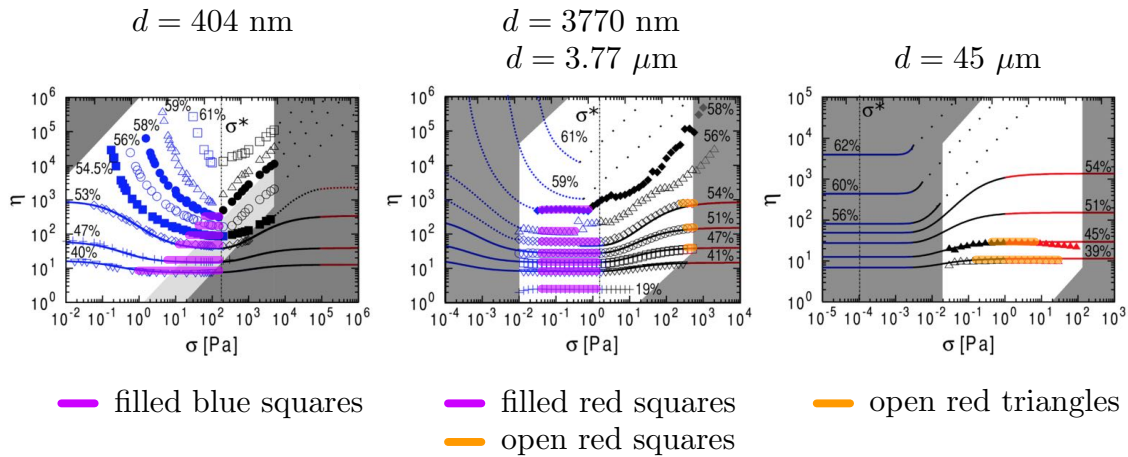


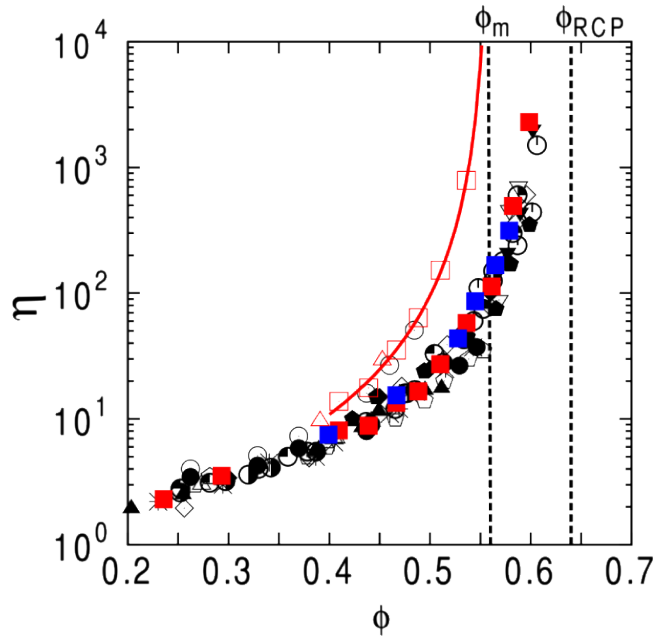
Figure 1.23 – Theoretical phase diagram in the  $(\dot{\gamma}, \phi)$  plane. Adapted from [3] and [2]. CST stands for continuous shear thickening, and DST for discontinuous shear thickening.

the presence of polymeric ‘hairs’ grafted on their surfaces [51]. They measured the viscosity of the suspension as a function of the shear stress in a cone-plate geometry, for different packing fractions  $\phi$  and particles’ diameter  $d$ . The symbols in Figure 1.24a correspond to these measurements. They then fitted their data to the model of Wyart and Cates (solid lines in Fig. 1.24a), and extracted a low viscosity and a high viscosity plateau from data highlighted in purple and orange in Fig. 1.24a. Figure 1.24b shows that the low and high viscosity data measured with this method indeed fall onto two different rheological curves, as predicted by the frictional transition model. Moreover, the authors found that the critical stress at which the discontinuous shear thickening occurs varies as  $\tau_c \propto d^{-2}$ , as predicted by Equation (1.11) for a constant repulsive force. We note however that the data presented in Fig. 1.24a does not constitute a clear validation of the model. First, the two plateaus used to build the viscosity curves appear only for certain particle’s size, and sometimes consist of only very few data points. Second, for high packing fractions ( $\phi \geq 56\%$ ), the flow is unsteady and data actually correspond to temporal averages. Finally, to collapse the viscosities in Fig. 1.24b, the values of the packing fraction for the  $d = 45 \mu\text{m}$  data had to be shifted *ad hoc*.

A second kind of experiments, based on shear reversal, have been performed by Lin et al. in [52]. The principle is to apply a constant shear rate in one direction and then change suddenly the direction of the flow (and thus the sign of the shear rate). They conducted these experiments with shear-thickening suspensions



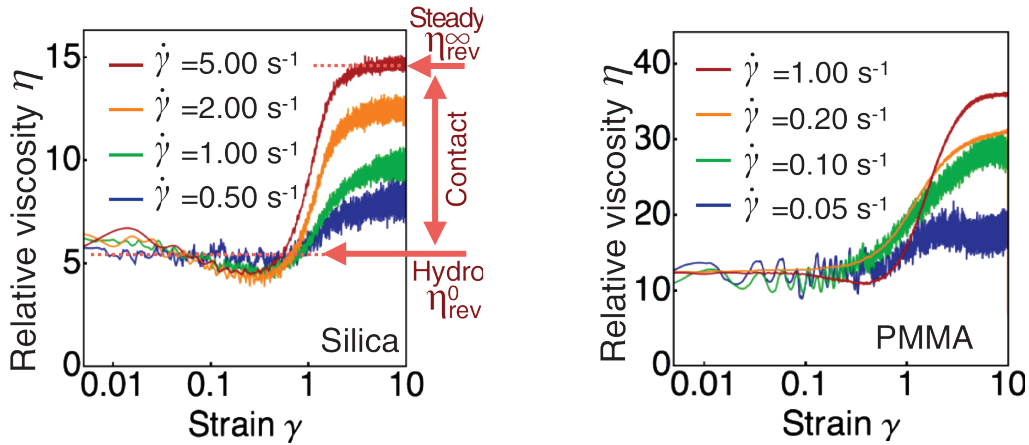
(a) Rheological measurements for grafted PMMA particles, with three different particles diameters  $d$ . The highlighted plateaus give the corresponding data points in Fig. 1.24b. Adapted from [51].



(b) Evolution of the relative viscosity with the packing fraction. Data extracted from Fig. 1.24a (grafted PMMA particles with three different particles diameters  $d$ ) and from literature (see [51] and references therein). From [51].

Figure 1.24 – Experimental results from [51].

containing either stabilised silica particles (Fig. 1.25a) of diameter  $d = 2 \mu\text{m}$  or stabilised PMMA particles (Fig. 1.25b) of diameter  $d = 1.4 \mu\text{m}$ . As we can see in Figure 1.25, the viscosity first drops to a lower plateau upon reversing the shear direction, and then increases after a transient strain to a higher plateau whose value depends on the imposed shear rate. Following [54], the authors interpreted these results by saying that the lower plateau corresponds to the sole contribution of hydrodynamic forces whereas the second plateau also takes into account the contribution of frictional contacts. Their results thus show that the amount of



(a) Relative viscosity as a function of time after shear reversal, suspension of silica particles.

(b) Relative viscosity as a function of time after shear reversal, suspension of PMMA particles.

Figure 1.25 – Influence of the fraction of frictional contacts on the relative viscosity of shear-thickening suspensions. From [52].

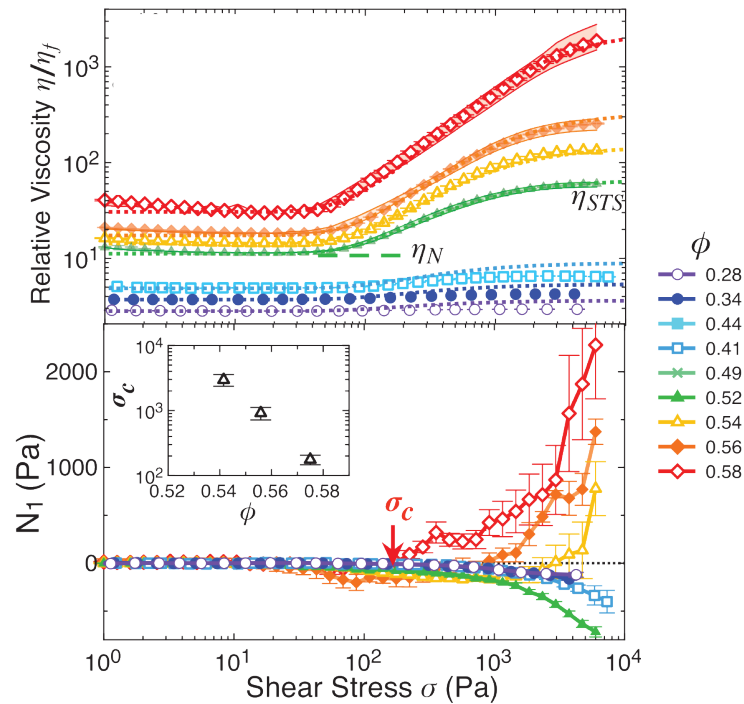


Figure 1.26 – Relative viscosity and first normal difference as functions of the shear stress for different packing fractions, in a suspension of silica beads. From [53].

frictional contacts in the system increases with the shear rate, which is consistent with the frictional transition model.

A last experiment, conducted by Royer et al. in [53], investigated the first normal stress difference  $N_1$  of shear-thickening suspensions of silica beads with

diameter  $d = 1.54 \mu\text{m}$ . The authors state that its sign is a way to determine the dominant force scale in the system: if  $N_1 < 0$ , hydrodynamic forces control the behaviour of the suspension, while if  $N_1 > 0$  frictional contact forces dominate in the system. They show that for high enough values of the packing fraction  $\phi$ , the first normal stress difference is indeed positive above a certain onset stress  $\sigma_c$ , as illustrated in Figure 1.26. This onset stress also decreases with increasing  $\phi$  (Fig. 1.26). It should however be noted that the relation between  $N_1$  and the presence of contact is still debated in dense non-Brownian suspensions (see [24]), making this experiment difficult to interpret.

These three studies all present interesting results consistent with the frictional transition model, but neither directly measure the frictional properties of shear-thickening suspensions, which is the key quantity of the mechanism. Therefore, though they tend to confirm that shear thickening does stem from frictional contacts developing in the suspension, they do not constitute a direct validation of the frictional transition model.

## 1.4 General aim of this thesis

This overview shows that our understanding of shear thickening was at a turning point when this PhD started in 2015. Long recognized as an important property of dense suspensions, shear thickening received with the frictional transition model a first consistent description [1–3]. In contrast with previous explanations of shear thickening, like the hydrocluster scenario based purely on hydrodynamics, this approach puts microscopic contact physics at the core of dense suspensions' rheology. The frictional transition model proposes that shear thickening is driven by the activation of friction above an onset stress, needed to overcome repulsive forces between particles. Once introduced in numerical simulations or formalized with a heuristic model, this mechanism enables the recovery of the main features of shear thickening in non-Brownian suspensions, including continuous shear thickening, discontinuous shear thickening, and shear-jamming.

However, testing this scenario is experimentally challenging. We have seen that standard rheological techniques, performed under fixed packing fraction, provide information only about the suspension's shear rate, shear stress, and viscosity. Therefore, they cannot give access to the suspension's friction coefficient  $\mu$ , which is the key quantity one needs to access to test the model. A promising way to obtain this information is to adopt a granular point of view and perform experiments at fixed granular pressure  $P$ . As we have seen, such an approach has been used with success recently to investigate the rheology of dense suspensions close to their critical packing fraction [24, 28]. However, experimental devices used so far were developed to study suspensions made of macroscopic particles and cannot be used to study shear thickening suspensions, whose particles are too small.

The aim of this thesis is precisely to develop new pressure-imposed approaches for shear-thickening suspensions, in order to understand the physical origin of this phenomenon. In the first part of this manuscript (Chapter 2), we use a classical configuration of dry granular media, rotating drum flows, in order to access the

macroscopic frictional properties of suspensions. This study enables us to provide a first direct support of the frictional transition scenario (paper published in [4]). However, we will see that rotating drum flows cannot be used to change the applied granular pressure and thus fully explore the transition. In the second part (Chapter 3), we thus propose a new rheological set-up, called the *Darcytron*, which provides a way to perform pressure-imposed experiments on colloidal suspensions. We first validate the concept behind this device on classical, non shear-thickening suspensions, before describing the first results obtained with shear-thickening suspensions. Finally, Chapter 4 presents our conclusions, with some prospects and current work in progress.





---

### Revealing the frictional transition using rotating drum flows

---

“Why don’t we just mix up absolutely everything and see what happens?”  
“It’s got to be worth a try”

---

Dialogue between the Dean and Archchancellor Ridcully.  
In *Hogfather*, by Terry Pratchett.

In this chapter, we use a configuration inspired by granular flows, rotating drum flows, to provide the first evidence of the frictional transition in shear-thickening suspensions. Our idea is to investigate flow properties that are macroscopic signatures of the microscopic friction between particles: the avalanche angles, compaction and dilatancy effects. We first compare the quasi-static steady avalanche angle, compaction, and dilatancy effects, in a standard Newtonian suspension (large glass beads in a viscous liquid) and in a typical shear thickening suspension (starch particles in water) flowing under gravity. This comparison reveals that particles in shear-thickening suspensions are frictionless under low confining pressure, as predicted by the frictional transition model. Then, to bridge microscopic contact physics to the macroscopic rheology, we use a model suspension (silica beads in aqueous ionic solutions) where the short-range repulsive force can be tuned. We find that when the repulsive force is the dominant force scale, the suspension has a frictionless state under low stress and a shear-thickening macroscopic rheology. By contrast, when the repulsive force is no longer dominant, the frictionless state disappears and so does the macroscopic shear-thickening rheology.

The results presented in this chapter led to the publication: Clavaud et al., Proc. Nat. Acad. Sci. USA, vol 114, 5147–5152 (2017) (see [4] or Appendix B).

## 2.1 The avalanche angle: a macroscopic signature of microscopic friction

### 2.1.1 Background

#### The avalanche angle

Our daily experience tells us that sand piles form cones with a well-defined angle  $\theta_c$ , as illustrated in Figure 2.1. Below the pile angle, the medium is stable and behaves like a solid. Above it, it flows like a liquid and an avalanche develops. This is a classical property of granular matter, whether dry or fully immersed in a liquid; think of sub-aqueous dunes for example (see [55] for a general textbook on granular matter). This well-defined avalanche angle comes from the fact that the onset of the flow in a granular material is given by a friction criterion. Let us consider the mechanical equilibrium under gravity of a granular layer of thickness  $h$  at the free surface of the pile (highlighted in green in Fig. 2.1). We can write the shear stress  $\tau$  and the normal stress  $P$  that it is subjected to as:

$$\begin{cases} \tau = \phi \Delta \rho g h \sin(\theta), \\ P = \phi \Delta \rho g h \cos(\theta), \end{cases} \quad (2.1)$$

where  $\phi$  is the packing fraction of the pile,  $\Delta \rho = \rho_p - \rho_f$  is the density difference between the particles and the surrounding fluid, and  $g$  is the gravity. We have seen in Chapter 1 that the flow onset occurs when the ratio of the tangential to normal stress is equal to the quasi-static macroscopic friction coefficient of the granular material:  $\tau/P = \mu_c$ . This yields:

$$\mu_c = \tan(\theta_c). \quad (2.2)$$

Therefore, the avalanche angle  $\theta_c$  is a direct measurement of the quasi-static macroscopic friction coefficient  $\mu_c$  of the granular medium.

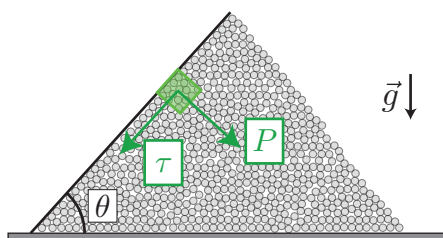
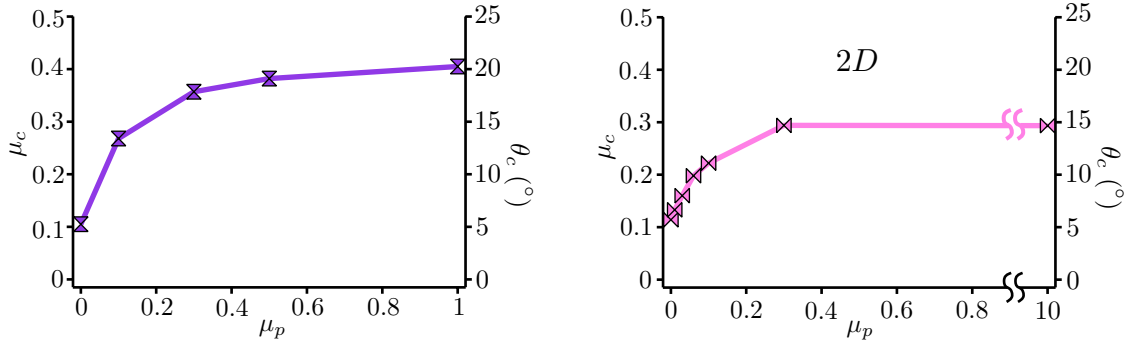


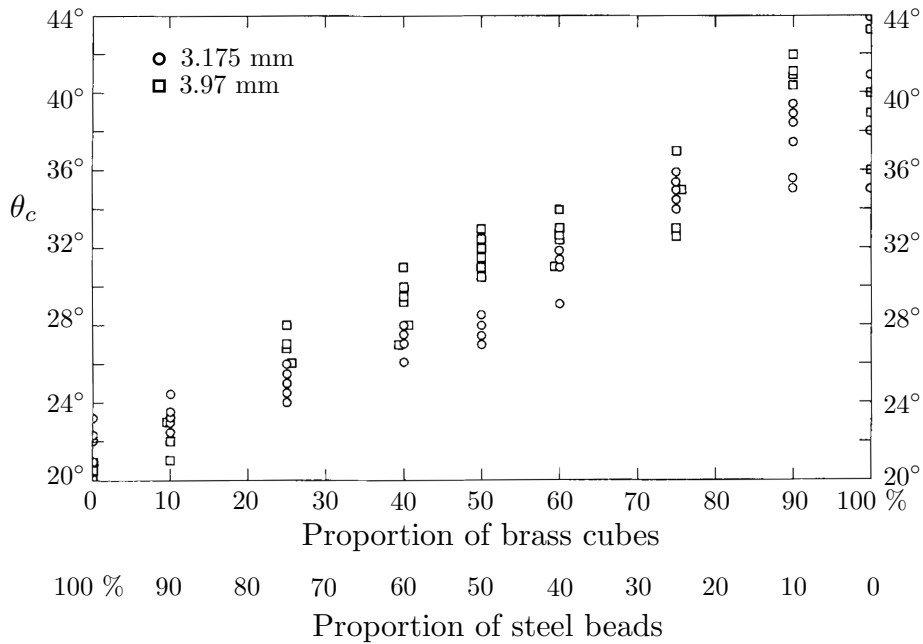
Figure 2.1 – Sketch of a dry granular medium forming a pile with a well-defined angle  $\theta$ .

This macroscopic friction coefficient has two very different physical origins. First, we have seen in Chapter 1 that  $\mu_c$  depends on the microscopic friction coefficient  $\mu_p$  between the particles. We recall in Figures 2.2a and 2.2b the relation



(a) Relation between  $\mu_c$ ,  $\theta_c = \arctan(\mu_c)$ , and  $\mu_p$ , in 3D discrete simulations of soft inertial spheres. From [29].

(b) Relation between  $\mu_c$ ,  $\theta_c = \arctan(\mu_c)$ , and  $\mu_p$ , in 2D discrete simulations of hard disks suspended in a viscous liquid. From [30].



(c) Avalanche angle  $\theta_c$  for a mixture of spheres and cubes. From [56].

Figure 2.2 – Influence of the microscopic friction coefficient  $\mu_p$  and the particle shape on the macroscopic friction  $\mu_c$ .

between  $\mu_c$ , the avalanche angle  $\theta_c$ , and  $\mu_p$ , obtained for spherical particles in discrete numerical simulations in [29, 30]. For frictional grains ( $0.1 < \mu_p < 1$ ), the macroscopic friction coefficient  $\mu_c \simeq 0.4$  has only a weak dependence on  $\mu_p$  and yields a typical avalanche angle  $\theta_c \simeq 25^\circ$ . By contrast, when the microscopic friction  $\mu_p$  becomes very small ( $\mu_p < 0.1$ ), the macroscopic friction  $\mu_c$  and the avalanche angle  $\theta_c$  sharply drop. Note that for frictionless spheres ( $\mu_p = 0$ ), numerical simulations predict a very small yet non-zero value for the macroscopic friction:  $\mu_c \simeq 0.1$ , and for the avalanche angle:  $\theta_c = 5.76^\circ$  (see [57]). The second origin of the macroscopic friction and avalanche angle is the geometry of the particles. This explains why piles of irregular particles like sand particles or a

mixture of spherical and cubic particles (see Fig. 2.2c) have an avalanche angle higher than those made of purely spherical particles. This geometrical contribution also explains the non-zero avalanche angle of piles made of frictionless spheres ( $\theta_c = 5.76^\circ$ , see [57]).

### Rotating drum flows

The previous discussion shows that the avalanche angle gives direct access to the frictional properties of the granular medium. Several methods can be used to measure this angle, as illustrated in Figure 2.3.

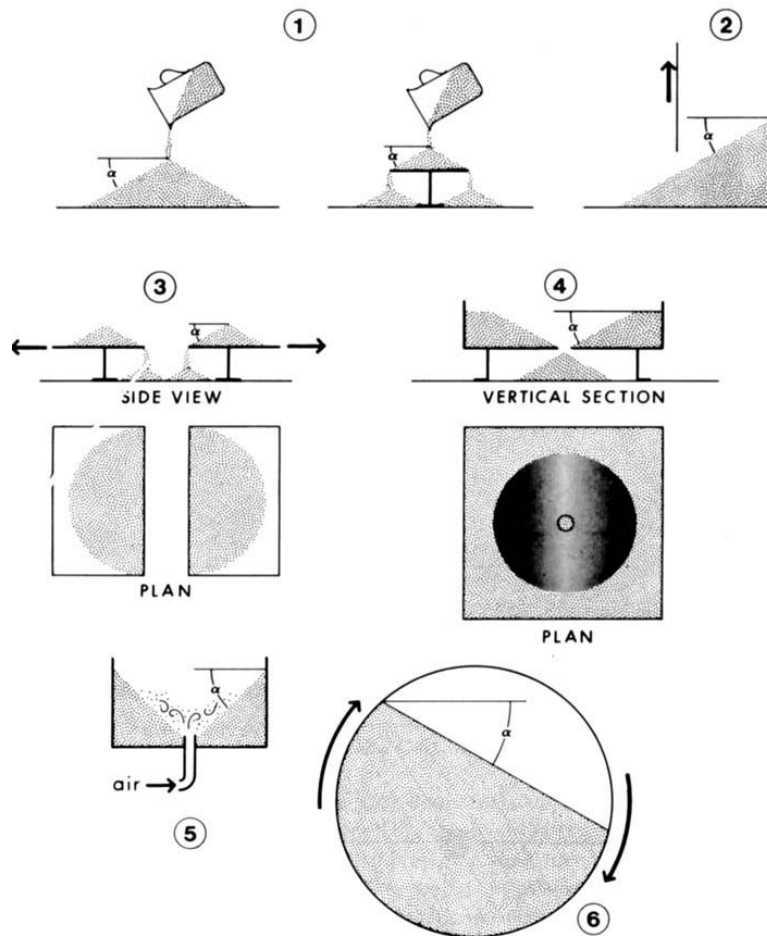
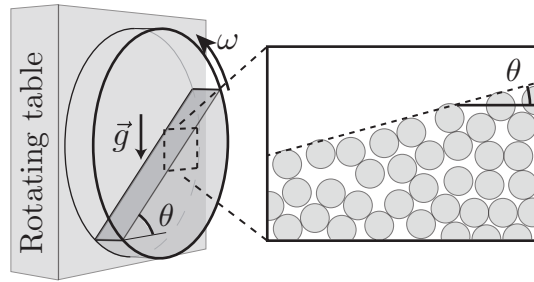


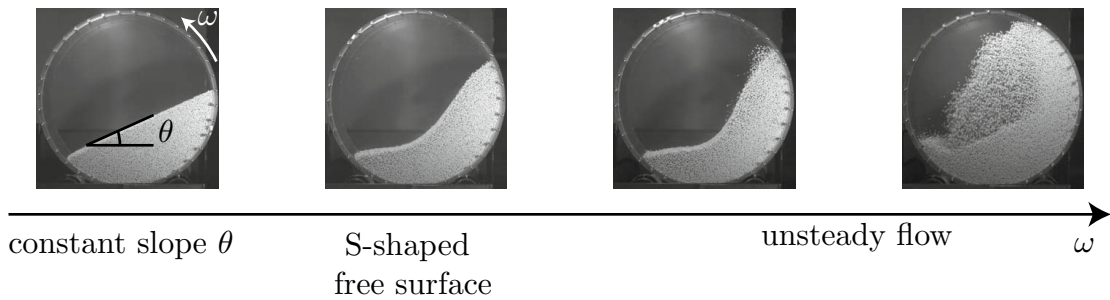
Figure 2.3 – Different methods for measuring the pile angle (here denoted by  $\alpha$ ), from the historical paper of Carrigy [56].

One of the simplest way is to use a half-filled cylinder rotating along its axis (see Figure 2.4a). Depending on the rotation speed  $\omega$  of the cylinder, different flow regimes are observed (see Figure 2.4b). For fast rotations, the grains are fluidised and the flow is unsteady. When the rotation speed decreases, the system reaches a steady state characterised by a steady avalanche flow at the surface of the pile, on top of a region experiencing a rigid rotation with the drum. The free surface of the flow adopts either a S-shape (high  $\omega$ ) or a constant slope  $\theta$  (low  $\omega$ ) depending

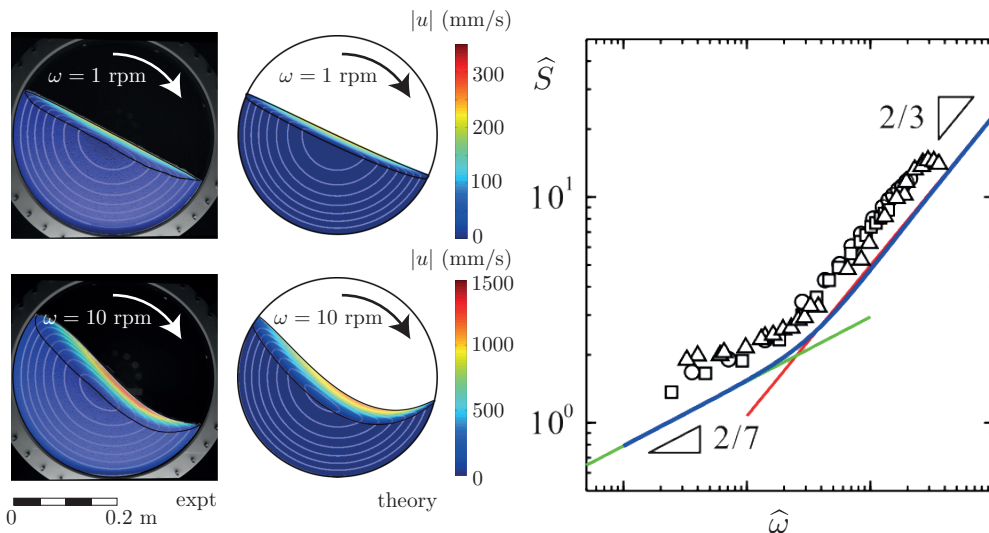
on the rotation speed (Fig. 2.4b and Fig. 2.4c, left). In the steady regime, mass and momentum conservation together with a constitutive law for the granular rheology allow one to predict the full flow field. Using this approach, Hung et al. obtained non-trivial scaling laws for the evolution of the avalanche angle  $\theta$  with the rotation speed  $\omega$  (Fig. 2.4c, right). The avalanche angle decreases with a rescaled rotation speed that depends on both the granular medium properties and the drum geometry (see [58]).



(a) Rotating drum flow: sketch and notations.



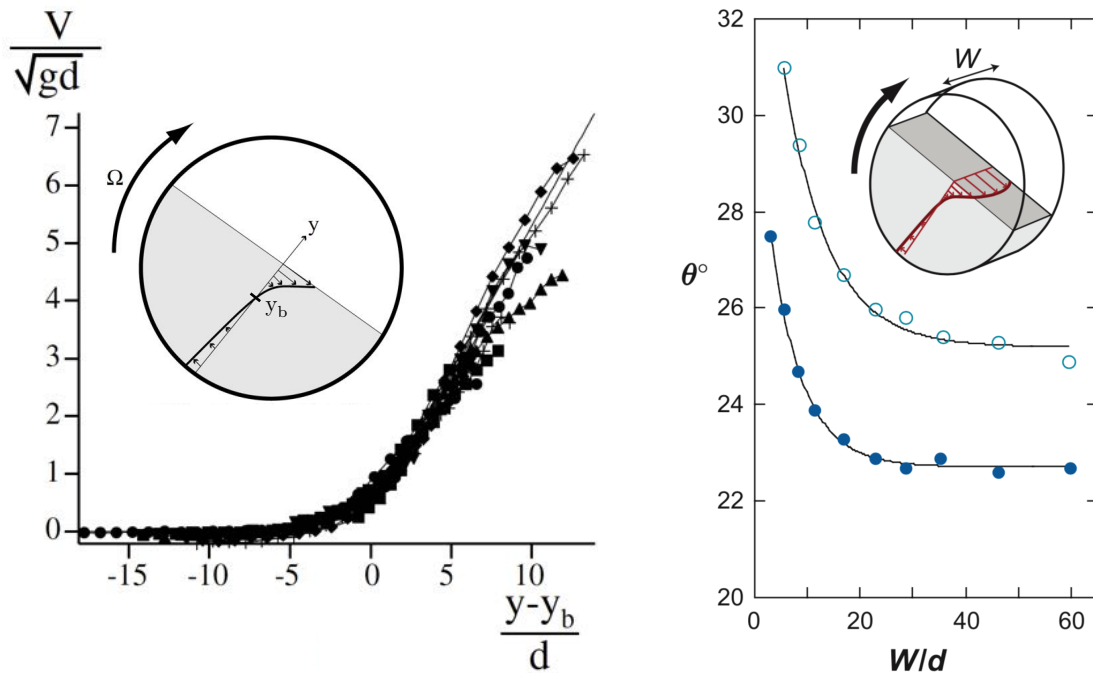
(b) Evolution of the air-grains interface with the rotating speed  $\omega$ . Pictures from [59].



(c) Evolution of the excess slope  $\hat{S}$  (defined as the avalanche angle minus the quasi-static avalanche angle) as function of the rescaled rotation speed  $\hat{\omega}$ . From [58].

Figure 2.4 – Rotating drum configuration.

Finally, for very low rotation speeds  $\omega$ , the flow properties no longer depend on the rotation speed (see [60]). The velocity profile is localised close to the free surface and the flow depth  $h$  is approximately  $h \sim 10d$  (where  $d$  is the particles' diameter), independently of the rotation speed (see Fig. 2.5a). In this quasi-static regime, the steady avalanche angle  $\theta$  also reaches a constant angle, that is independent of the drum's geometry for large enough drums (Fig. 2.5b, filled circles). The quasi-static avalanche angle can thus be identified with the angle  $\theta_c$  discussed above defined by  $\theta_c = \arctan(\mu_c)$ . Note that the quasi-static avalanche angle usually differs from the angle needed to start the flow from a pile at rest (called the starting angle, see the open circles in Figure 2.5b). This hysteretic behaviour is typical of granular materials (see [55]).



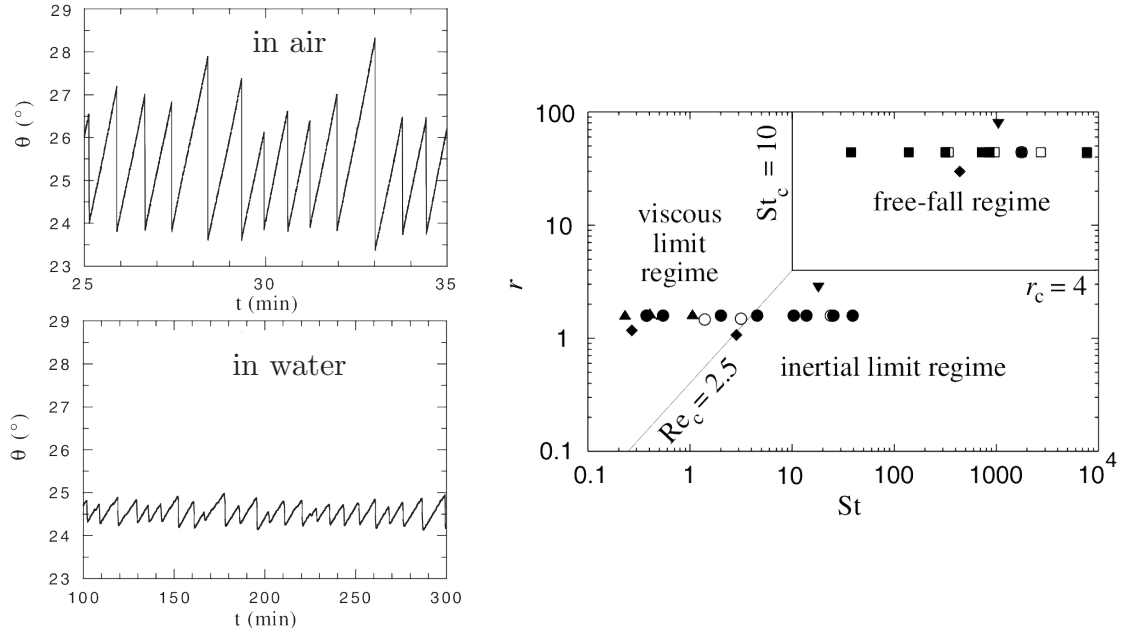
(a) Velocity profile in the quasi-static regime, for several rotation speeds. Adapted from [60].

(b) Quasi-static avalanche angle as function of the drum's width. Adapted from [55].

Figure 2.5 – Quasi-static regime.

Most experiments in rotating drums have been performed on dry granular flows. However, experiments with submarine granular media, using non-buoyant suspensions, also exist. Figure 2.6a compares the time evolution of the avalanche angle in the quasi-static regime for macroscopic glass beads in air (top) or immersed in water (bottom). Although the temporal fluctuations differ, the main observation is that the mean avalanche angle is the same (approximately  $25^\circ$ ), whether grains are flowing in air or under water. This confirms that in the quasi-static regime, the macroscopic friction  $\mu_c$  is set by the contact interactions between particles and not by hydrodynamic interactions (see Chapter 1).

In the sequel, we will study rotating drum suspension flows for which inertia is negligible, and the flow is quasi-static. By estimating the time that one particle



(a) Avalanche angle as function of time in the quasi-static regime, for glass beads ( $d = 230 \pm 30 \mu\text{m}$ ) in air (top) or in water (bottom). From [61].

(b) Transition between the viscous, free-fall, and inertial regimes in the  $(St, r)$  plane, proposed by Courrech du Pont et al. in [61].

Figure 2.6 – Dry versus submarine rotating drum flows.

takes to fall over one diameter  $d$  under gravity, Courrech du Pont et al. proposed in [61] that the transition between the viscous and the inertial regime is controlled by two dimensionless quantities, the Stokes number  $St$  and the square root of the density ratio  $r$  (see Figure 2.6b), given by:

$$St = \frac{\sqrt{\rho_p \Delta \rho g \sin(\theta) d^3}}{18\sqrt{2}\eta_f}, \quad (2.3)$$

$$r = \sqrt{\frac{\rho_p}{\rho_f}}. \quad (2.4)$$

The Stokes number  $St$  is the ratio of the inertial falling time to the viscous falling time. The viscous regime occurs when  $St \ll 1$ . In this case, the quasi-static regime is defined by  $J \ll 1$ , where the viscous number  $J = \eta_f \dot{\gamma} / P$  (see Chapter 1). In a rotating drum, we have  $\dot{\gamma} \sim \omega(D/h)^2$ , where  $D$  is the drum's diameter, and the pressure is imposed by gravity:  $P \sim \Delta \rho g h$ , with  $h \simeq 10d$ . The quasi-static limit is then defined by:

$$J_{\text{drum}} = \frac{\eta_f \omega D^2}{\Delta \rho g (10d)^3} \ll 1. \quad (2.5)$$



## Summary

This overview shows that the rotating drum configuration provides a unique way to probe the frictional properties of dense suspensions, and thus investigate the frictional transition model proposed for shear thickening.

For low rotation speeds, the avalanche angle  $\theta_c$  is a direct measure of the quasi-static macroscopic friction coefficient  $\mu_c = \tan \theta_c$  of the suspension. This coefficient is itself in bijection with the microscopic friction coefficient  $\mu_p$  between the particles. As discussed in Chapter 1, the fact that we can access the frictional properties of the suspension in the quasi-static regime is a characteristic feature of pressure-imposed configurations like gravity driven flows.

Additionally, in the rotating drum configuration the slope of the avalanche is set by the flowing layer of grains that is located near the free surface of the pile. In the quasi-static regime, the thickness of the layer  $h$  is of the order of a few particle diameters ( $h \simeq 10d$ ). This means that the measure of the avalanche angle gives access to the frictional state of the grains under very low confining pressure:  $P \simeq 10\phi\Delta\rho gd$ . The rotating drum configuration is thus very well suited to probe the existence of a frictionless state at low confining pressure in shear-thickening suspensions.

In the sequel, we first study the avalanche properties of a classical frictional suspension as a benchmark, before conducting experiments with shear-thickening suspensions.

## 2.1.2 Experiments with a classical frictional suspension

### Particles and fluid

We use large glass beads of diameter  $d = 487 \pm 72 \mu\text{m}$  and density  $\rho_p = 2500 \text{ kg} \cdot \text{m}^{-3}$  (see Fig. 2.7a). The particles are immersed in a mixture of Ucon<sup>TM</sup> oil in water, prepared as follows: 157.7 g of pure water is mixed with 67.5 g of 75 H 9000 Ucon<sup>TM</sup> oil in a clean, stirred beaker, at approximately 50 °C to accelerate mixing. Hereafter, pure water means water demineralised by filtration through micropores and subjected to ultra violet light in order to kill any remaining organism (done by an Elga Purelab<sup>®</sup> flex machine). The beaker is then put under a vacuum pump to eliminate any gas bubble. The viscosity of the mixture, measured in a Couette geometry (Anton–Paar Rheolab QC), is  $\eta_f = 57 \text{ mPa} \cdot \text{s}$  and its density is  $\rho_f = 1005 \text{ kg} \cdot \text{m}^{-3}$ . With these values, one obtains a Stokes number  $St \simeq 4 \times 10^{-3}$  and  $r = 1.6$  (with  $\theta = 25^\circ$ , see Equation (2.3)). Therefore, the suspension in the rotating drum is well into the viscous regime (see Fig. 2.6b).

The rheological behaviour of such granular suspensions of macroscopic frictional particles is well-studied and is expected to be Newtonian when the packing fraction is fixed (see Chapter 1). We have checked this using a density-matched fluid made of a mixture of 30 wt% water, 13 wt% glycerol, and 57 wt% sodium polytungstate to avoid sedimentation. The neutrally buoyant suspension (with a packing fraction  $\phi = 50\%$ ) is then sheared in a large gap plane–plane configuration with rough plates (Fig. 2.7b). The viscosity is obtained from increasing and decreasing ramps of shear rate after a preshear. No migration effects were no-

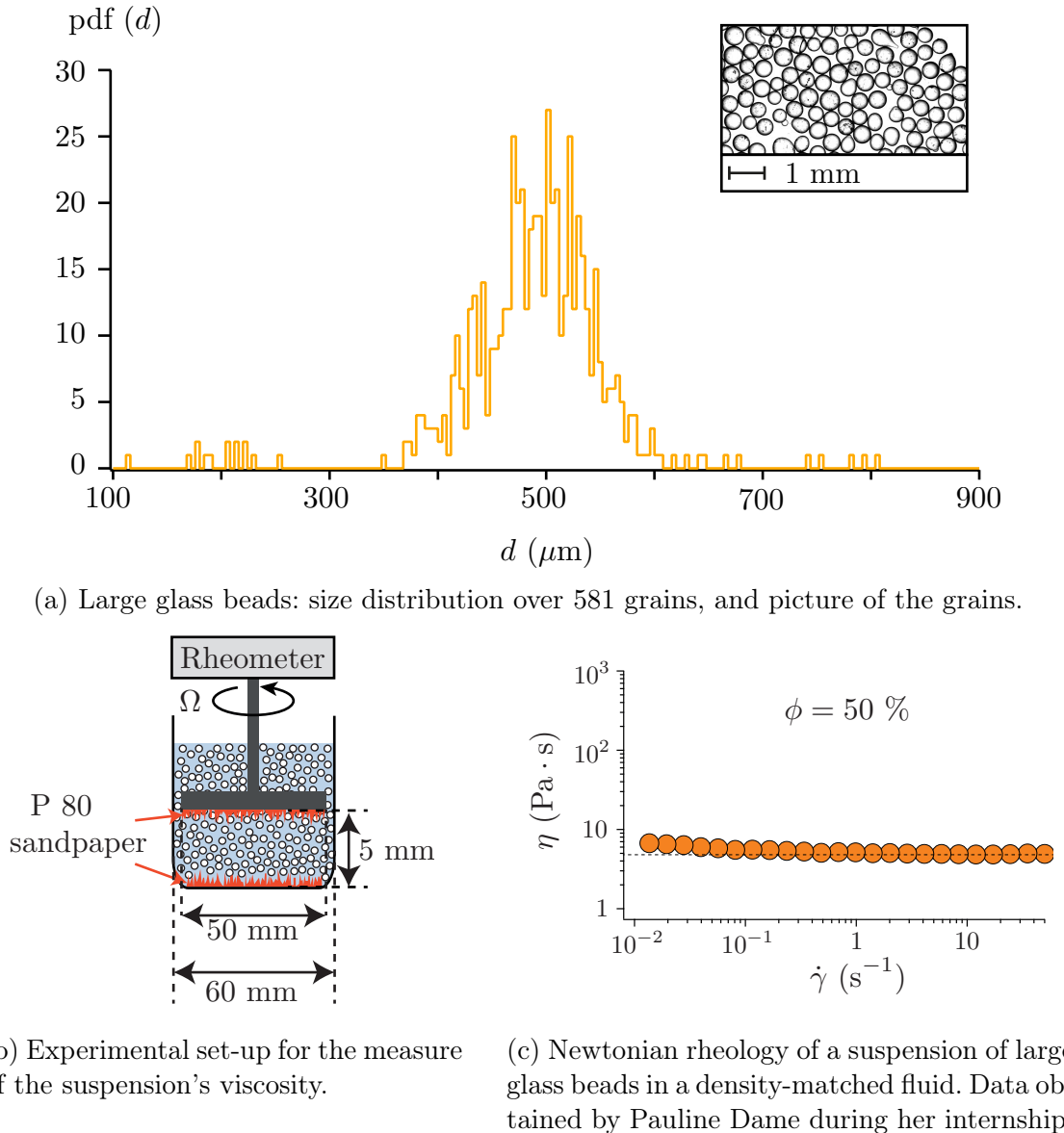
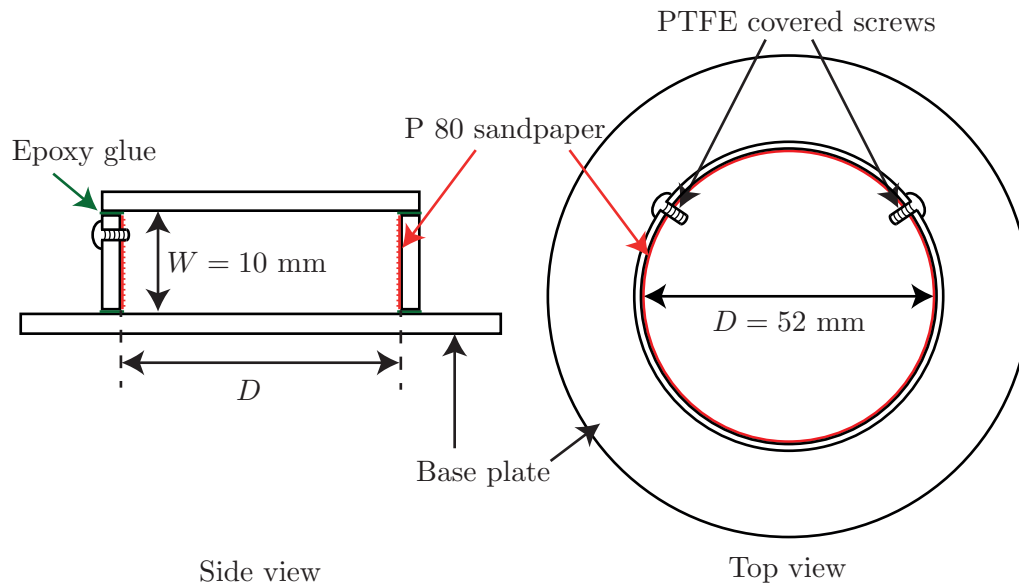


Figure 2.7 – Characterisation of the classical frictional suspension made of large glass beads.

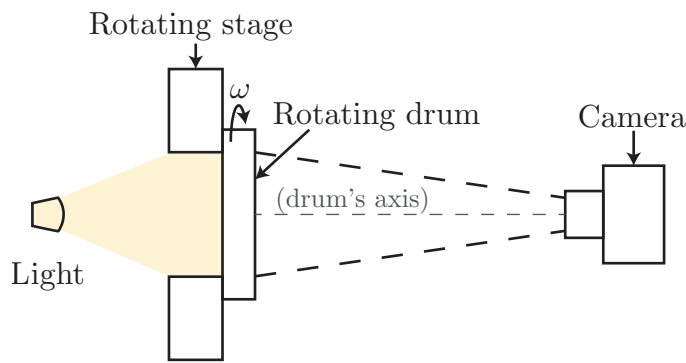
ticeable. Over the range of shear rates investigated, the rheological behaviour is Newtonian as anticipated (Fig. 2.7c).

### Experimental set-up and data analysis

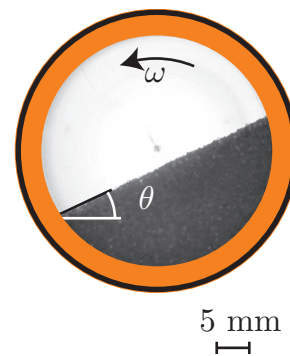
We made our own rotating drum by cutting PMMA plates with a laser cutter and assembling the obtained pieces together, as illustrated in Figure 2.8a. The drum's diameter is  $D = 52$  mm and its depth is  $W = 10$  mm. These dimensions, which give  $W/D < 1$  and  $W/d = 20$ , were set to ensure that only one avalanche develops in the depth of the drum, and that we are not subjected to wall effects (see [61–63]). It is made of a circular base plate on which we glued a concentric PMMA ring with



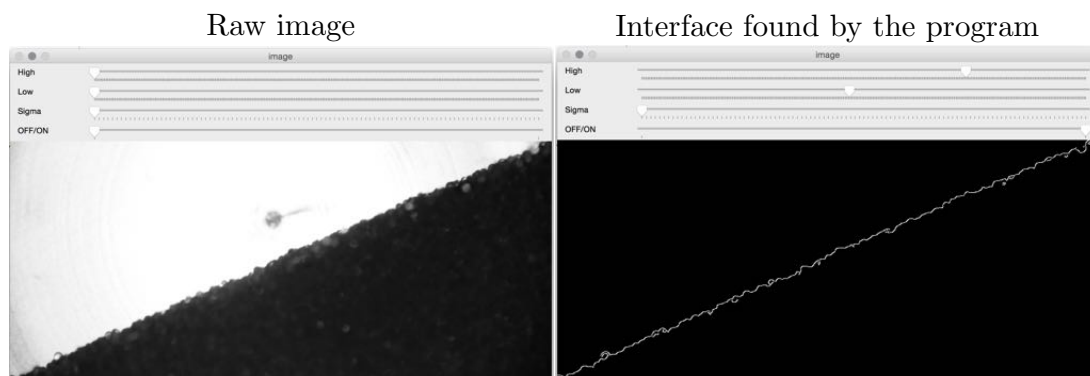
(a) Side and top view sketches of the rotating drum used for the large glass beads suspensions.



(b) Side-view sketch of the experimental set-up used to measure the pile angle of the large glass beads suspensions during their steady avalanches.



(c) Photograph of the face of the drum taken by the camera.



(d) Data processing: defining the edge detection parameters.

Figure 2.8 – Experimental set-up and data analysis used for the steady avalanche experiments.

an epoxy adhesive. To avoid wall slip, the inner wall is coarsened by gluing P80 sandpaper on it with superglue. The ring is pierced with two filling holes that can be sealed with polytetrafluoroethylene (PTFE) covered screws.

Any glassware, plastic sample bottle or plastic or stainless steel utensil used at any point in preparing the experiments was cleaned with isopropyl alcohol and then rinsed with pure water prior to being used. Some plastic utensils couldn't be cleaned with isopropyl alcohol and were very thoroughly cleaned with pure water. Special care was taken to clean the particles and the drum.

- The particles were immersed in pure water in a clean beaker and cleaned as follows. They were subjected to ultra sounds for 15 min, then the supernatant fluid was thrown away and replaced by pure water. This was repeated until the supernatant fluid was clear, then 3 times more. They were then taken with a clean stainless steel spoon and put into the sample bottle containing the Ucon™ oil and water mix, taking care not to add too much water during the transfer. Some water was necessarily added, so we measured the fluid's density and viscosity after the experiments.
- The rotating drum was rinsed with pure water, then filled with pure water and subjected to ultra sounds for 15 min. It was then emptied and this procedure was repeated. Then it was emptied, rinsed again with pure water, and left to dry. It was finally filled with the suspension of large glass beads in the Ucon™ and water mix with a clean plastic pipette, and sealed with the PTFE covered screws. At the end of this procedure, the sediment formed by the particles filled half the drum, the rest being filled by the suspending fluid.

Once filled, the drum was fixed to a PI M-06.PD rotating stage which has a minimum rotation speed of  $10^{-3} \text{ }^\circ \cdot \text{s}^{-1}$  and a maximum rotating speed of  $90 \text{ }^\circ \cdot \text{s}^{-1}$ . We controlled it with a PI Mercury C-863 DC motor controller. We took photographs of the system along the axis of the drum, as shown in Figure 2.8b. The rotating stage is hollowed in the middle, which allowed us to illuminate the drum from behind. The pictures thus show the front face of the drum, as shown in Figure 2.8c, with the sediment in black and the fluid in white. For each experiment, the framerate depends on  $\omega$ , but we tried to take at least one picture every  $1^\circ$ .

Pictures were processed as follows to extract the pile slope angle  $\theta$  as a function of time. For each photograph, we used edge detection based on the luminosity gradient to find the points belonging to the interface between the sediment and the fluid above it (see Figure 2.8d). These points were then fitted with a line, whose slope gives the pile angle  $\theta$  for the corresponding photograph. By looping on all photographs and using the value of the frame rate, we obtained the time evolution of  $\theta$ . This image analysis was done using custom made Python scripts written by Antoine Bérut.

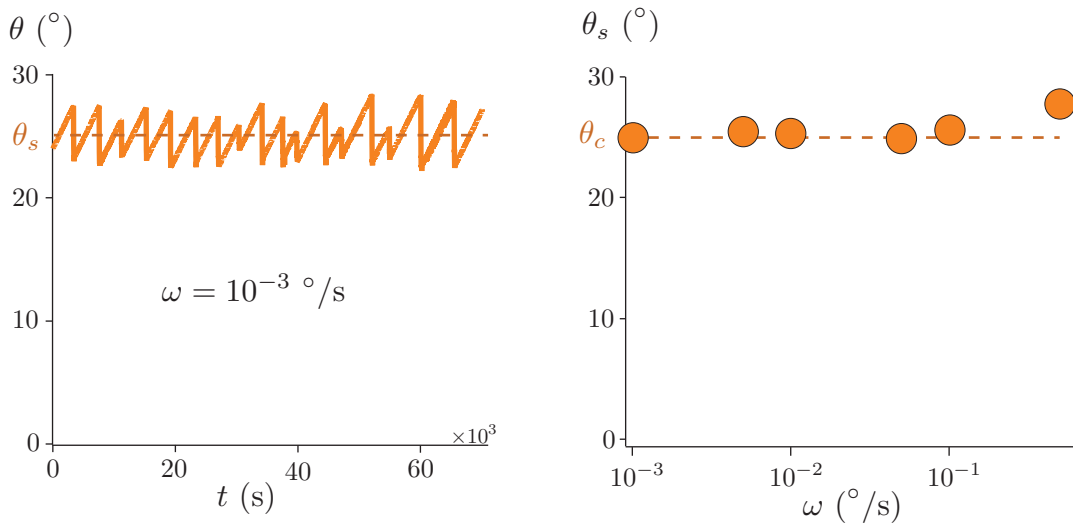
## Results

To measure the steady avalanche angle, we use the following protocol.

1. The drum is rotated at  $90 \text{ }^\circ \cdot \text{s}^{-1}$  for  $3600^\circ$  to resuspend the grains.

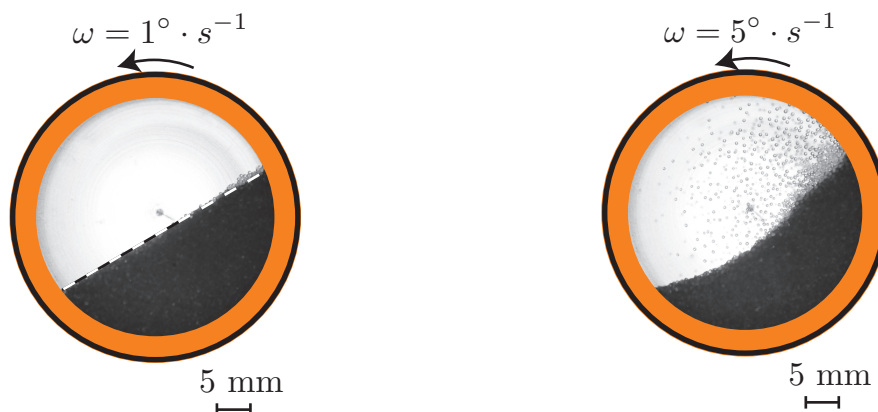
2. The grains are left to settle during one minute.
3. The rotating speed of the drum is set to the target rotating speed  $\omega$  and we take pictures of the drum.

Note that for very low rotation speed and long-time experiments, the measurements can be very sensitive to external vibration. In a first set of experiments, the vibrations induced by the mechanical shutter of the camera resulted in a slow creep of the avalanche angle. We thus disconnected the camera from the optical table where the experimental set-up was lying.



(a) Time evolution of the slope angle for a rotating speed of  $\omega = 10^{-3} \text{ }^\circ \cdot \text{s}^{-1}$ .

(b) Evolution of the steady avalanche angle with the rotating speed.



(c) At  $\omega = 1 \text{ }^\circ \cdot \text{s}^{-1}$ , some particles at the top of the avalanche never really settle.

(d) At  $\omega = 5 \text{ }^\circ \cdot \text{s}^{-1}$ , a non negligible fraction of the grains are resuspended.

Figure 2.9 – Steady avalanches for a frictional suspension of large glass beads ( $d = 487 \pm 72 \text{ } \mu\text{m}$ ) in a non-buoyant viscous fluid (Ucon<sup>TM</sup> and water,  $\eta_f = 57 \text{ mPa} \cdot \text{s}$ ).

Figure 2.9a is an example of the steady state time evolution of  $\theta$  for a low rotating speed ( $\omega = 10^{-3} \text{ }^\circ \cdot \text{s}^{-1}$ ). The slope angle  $\theta$  oscillates around a mean

steady avalanche angle  $\theta_s$  whose value is independent of the rotating speed in the range  $10^{-3} \text{ }^\circ \cdot \text{s}^{-1} \leq \omega \leq 10^{-1} \text{ }^\circ \cdot \text{s}^{-1}$  (see Figure 2.9b). The system is thus in its quasi-static regime. This is compatible with the estimation of the viscous number  $10^{-6} < J_{\text{drum}} < 10^{-4}$  for these rotation speeds, drum's geometry and suspension's properties (Equation (2.5)). With  $\theta_c = 25.3 \pm 0.3^\circ$ , the quasi-static macroscopic friction coefficient of the suspension is  $\mu_c = \tan(\theta_c) = 0.47$ , a typical value for a frictional system. As expected,  $\theta_s$  increases with  $\omega$  when the system is no longer in its quasi-static regime. Above  $\omega = 1 \text{ }^\circ \cdot \text{s}^{-1}$ , some particles never really settle, as we can see in Figure 2.9c. The interface between the sediment and the fluid above is no longer well-defined, and as a result neither is  $\theta_s$ . Then above  $\omega = 5 \text{ }^\circ \cdot \text{s}^{-1}$ , the system is nearly completely resuspended, as shown in Figure 2.9d.

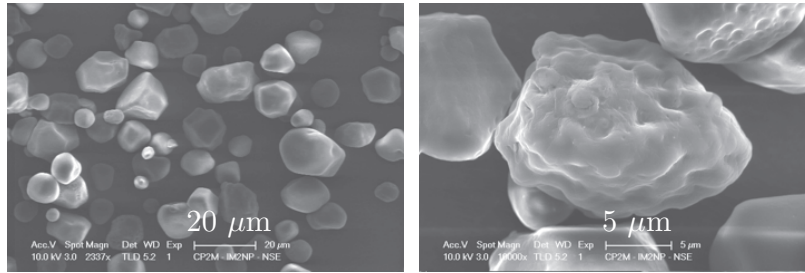
In conclusion, using a rotating drum, we recover a classical frictional behaviour for our suspension of large glass beads in a viscous fluid. This is consistent with previous works (see [61] for example). In the sequel, we use the same technique in order to investigate the frictional behaviour of shear-thickening suspensions.

### 2.1.3 Experiments with a shear-thickening suspension

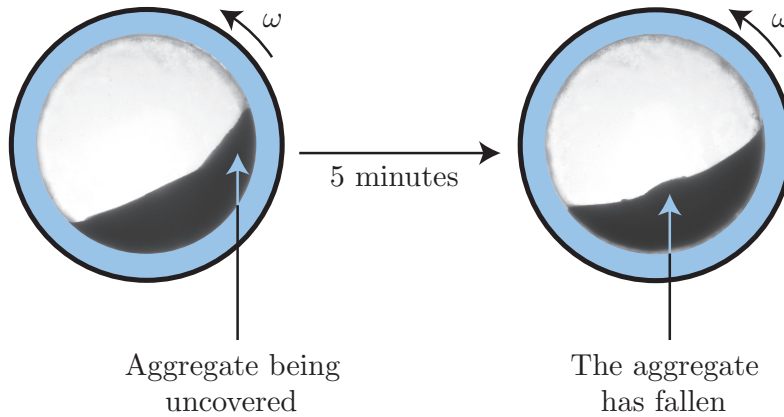
#### Preliminary experiments using cornstarch

We have seen in Chapter 1 that the typical examples of shear-thickening suspensions are suspensions of cornstarch in water, which exhibit discontinuous shear thickening for packing fractions above  $\phi \simeq 40\%$  (see [11]). We thus used such suspensions for our first experiments.

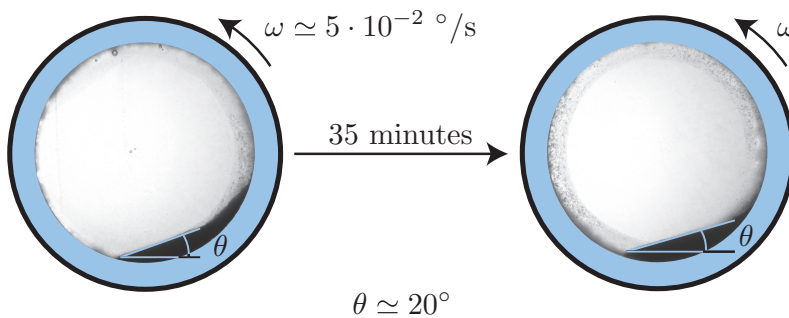
We used cornstarch from the brand Maïzena<sup>®</sup>. Figure 2.10a shows pictures of the grains in Scanning Electron Microscopy (SEM). As we can see, they are poly-disperse, with an angular shape and a seemingly rough surface. Their diameter  $d$  is included between  $5 \text{ } \mu\text{m}$  and  $25 \text{ } \mu\text{m}$  (see [64]). We used filtered water as the suspending fluid. Since the density of starch particles is about  $\rho_p = 1500 \text{ kg} \cdot \text{m}^{-3}$ , the particles sediment and form a pile at the bottom of the drum. Figure 2.10b shows typical cornstarch avalanche flows for a low rotation speed. By contrast with the experiments with large glass beads, the free surface of the avalanche is neither steady nor uniform. Aggregates seem to form in the bulk of the sediment, which are then excavated and broken when they emerge at the free surface. There are several possible explanations for the formation of these aggregates. First, the system ages due to the hydrolysis of the particles and the presence of bacteria which feed of the starch. Another possible explanation is that they result from a granular pressure on the grains high enough to create multiple contacts between them, combined with a long static contact time in the bulk during the solid rotation. We tried to decrease the granular pressure by reducing the size of the sediment (see Figure 2.10c). For very small sediment's depth (approximately  $1.5 \text{ mm}$ ), the surface flow is smooth, giving a pile angle of about  $\theta_s \simeq 20^\circ$ . However, this value is difficult to interpret. First, the sediment's depth is of the same order of magnitude as the drum's width  $W$ . The flow is thus no longer localised at the free surface but extends down to the rough boundary of the drum (see [60]). Second, we have seen that the link between the microscopic friction  $\mu_p$  and macroscopic friction  $\mu_c$  is well documented for smooth spherical particles (see Section 2.1.1 and



(a) Cornstarch particles in SEM.



(b) Rotating drum filled with a suspension of cornstarch in water, showing the uncovering and later fall of an aggregate.



(c) Rotating drum with a very thin sediment of cornstarch immersed in water.

Figure 2.10 – Cornstarch particles: a famous shear-thickening suspension, not so easy to work with.

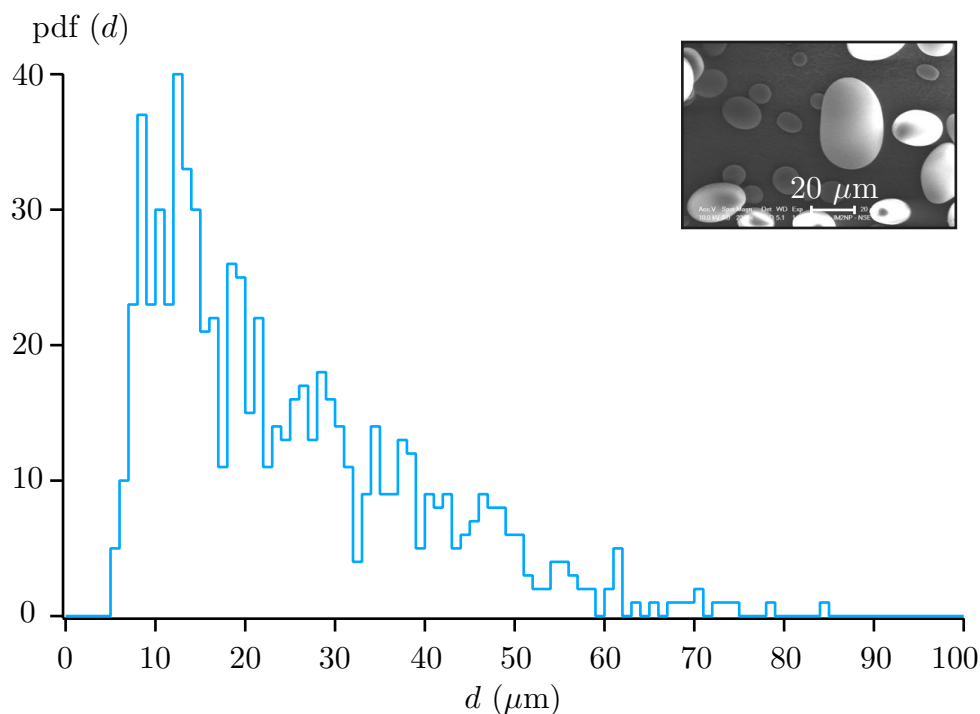
Fig. 2.2b). However, for highly irregular and polydisperse particles like cornstarch grains, this connection is less direct since the avalanche angle strongly increases with the degree of angularity (Fig. 2.2c).

### Potato starch: first evidence of a frictionless state

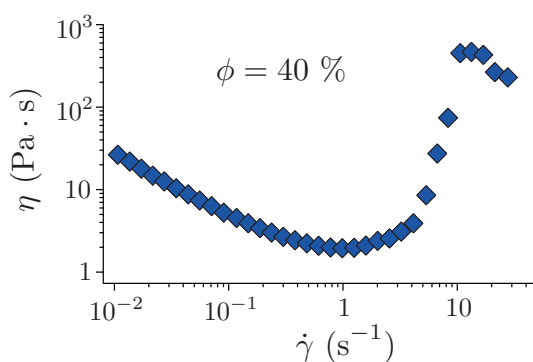
To avoid the difficulty associated with the irregular sharp-edge shape of cornstarch grains, we turned to similar but smoother grains: potato starch. We also designed a new drum in order to control the temperature of the system throughout the

experiments and avoid ageing.

Potato starch is composed of polydisperse ovoid grains of average major axis  $25 \pm 15 \mu\text{m}$  (see Figure 2.11a) and density  $\rho_p = 1500 \text{ kg} \cdot \text{m}^{-3}$ . We characterized the rheological behaviour of this system by suspending the particles with a density matched fluid composed of a mixture of 45 wt% water and 55 wt% cesium chloride. The same plane-plane geometry as in Figure 2.7b was used. As shown in Figure 2.11, the suspension exhibits a typical shear-thickening behaviour, with a strong increase of the viscosity above a critical shear rate.



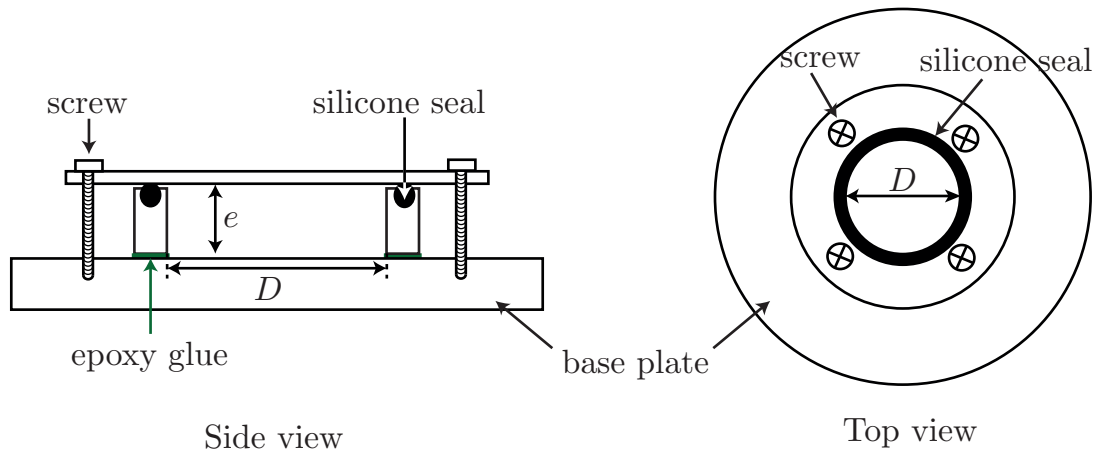
(a) Potato starch: size distribution over 736 grains, and picture obtained in SEM.



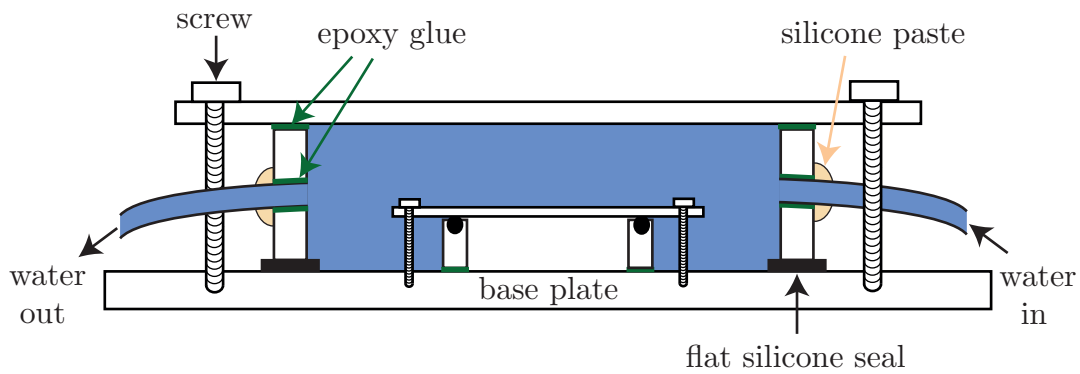
(b) Shear-thickening rheology of a suspension of potato starch in a density-matched fluid. The rheological set-up is the same as the one used in Figure 2.7b. Data obtained by Pauline Dame during her internship.

Figure 2.11 – Characterisation of the potato starch grains.

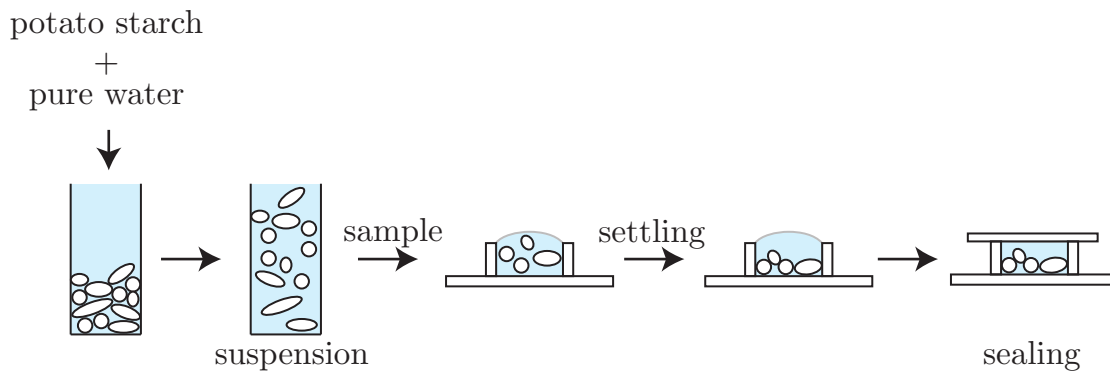




(a) Side and top view sketches of the rotating drum used for potato starch in water suspensions.



(b) Water circulation apparatus.



(c) Preparation and filling protocol of the drum for the potato starch suspensions.

Figure 2.12 – Experimental set-up and preparation protocol for the potato starch suspensions.

The drum is made of PMMA. It has a diameter  $D = 12\text{ mm}$  and a width  $W = 3\text{ mm}$  (see Figure 2.12a). These dimensions give  $W/D < 1$  and  $W/d = 120$ , ensuring the absence of wall effects. It is sealed by screwing its cover on a silicone joint. The inner surface is roughened using a P80 sandpaper to avoid wall slip. On top of the drum, a closed cell with a water circulation is built to keep

the system's temperature at 7°C during the experiments (see Figure 2.12b). The cell is connected to a Fisher Bioblock Scientific thermal bath with flexible tube, to accommodate the rotation of the drum during experiments.

Before any experiment, the drum was cleaned as follows. The base plate with the ring, the silicone seal and the cover plate were cleaned with tap water and soap, then thoroughly rinsed, first with tap water to remove any soap, then with pure water. They were then immersed in pure water in a clean beaker and subjected to ultra sound for 15 min. The water was then thrown away, replaced by pure water, and the drum was subjected to ultra sound again. The water was thrown away again, and replaced by pure water if the drum had to be stored before being filled. Before filling the drum, every part of it was dried with pressurised air and placed on a paper towel, with the silicone seal directly put inside its furrow.

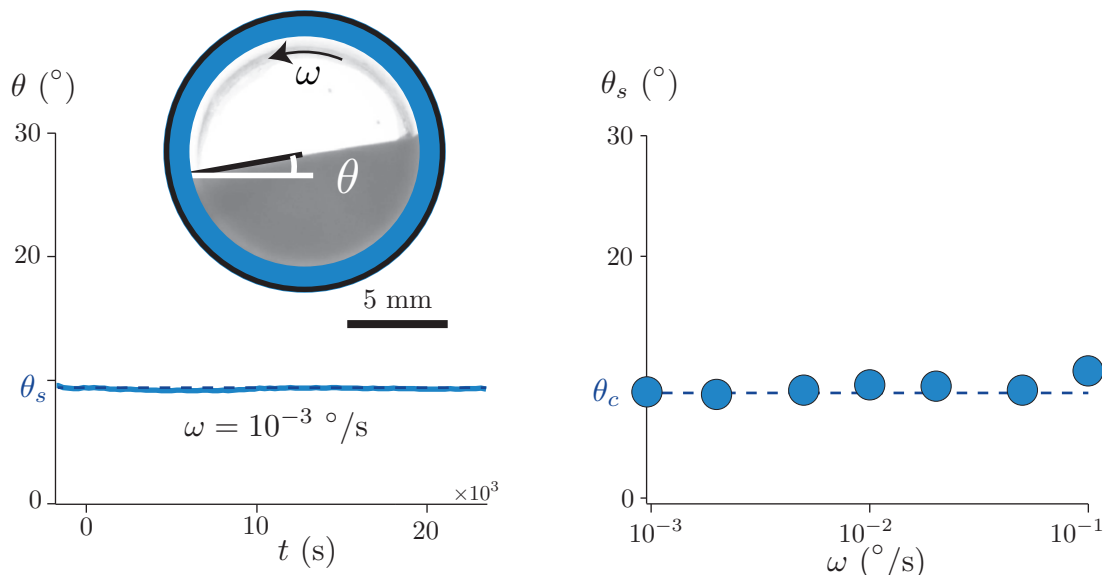
We made a new suspension every time we conducted a new experiment, so one suspension was never used for more than 2 days. With this precaution and the use of a 7°C thermal bath, we avoided ageing during our experiments. The way we made a new suspension is as follows (see Figure 2.12c). In a clean beaker, we put approximately 1 g of potato starch and approximately 4 g of pure water. Just before filling the drum, we suspended all the grains and collected the suspension with a clean pipette. This allowed us to obtain a sediment filling only half the drum, the rest of the drum being filled with pure water. We filled the drum with a pipette, taking care to form a dome with the fluid so there would not be any air bubble in the suspension once the drum was closed. We waited until the suspension was sedimented on the bottom of the drum. Then we applied the cover plate, keeping the side that was in contact with the paper towel outwards. Once applied, the cover plate was pressed down and screwed rapidly, to avoid the formation of air bubbles.

Once the drum was sealed, it was fixed to the same rotating stage as described in Section 2.1.2. Steady avalanches are obtained using the following protocol.

1. The drum is rotated by 180° back and forth to suspend the grains.
2. The grains are left to settle during one minute.
3. The rotating speed of the drum is set to the target rotating speed  $\omega$  and we take pictures of the drum. The total amplitude of the rotation is reduced to a maximum of 600° because of the presence of the tubes for the cold water circulation.

Figure 2.13a shows a picture of the rotating drum filled with the potato starch particles in water, in the steady avalanche regime, for a low rotation speed  $\omega = 10^{-3} \text{ }^\circ \cdot \text{s}^{-1}$ . The time evolution of the avalanche angle  $\theta$  is presented in the same figure. By contrast with cornstarch particles, the slope of the pile is very well defined. It shows no temporal fluctuation during the rotation of the drum. In the range of rotation speeds  $10^{-3} \text{ }^\circ \cdot \text{s}^{-1} \leq \omega \leq 10^{-1} \text{ }^\circ \cdot \text{s}^{-1}$ , the steady avalanche angle  $\theta_s$  is constant, suggesting that the flow is in the quasi-static regime (Figure 2.9b). The main result is that the quasi-static avalanche angle is  $\theta_c = 8.5 \pm 0.3^\circ$ . This is much smaller than any pile angles reported so far for a granular assembly.

From this value, we can compute the macroscopic friction coefficient of the suspension:  $\mu_c = \tan \theta_c = 0.15$ . This value is slightly larger than the expected value for frictionless spheres ( $\mu_c = 0.105$ ) (see [57] and Fig. 2.2). However, potato starch particles are not perfect spheres, which geometrically increases the macroscopic friction coefficient (see section 2.1.1). Therefore, our results indicate that the microscopic friction coefficient  $\mu_p$  between the potato starch particles nearly vanishes in the flow at the top of the pile.



(a) Time evolution of the slope angle for a rotating speed of  $\omega = 10^{-3} \text{ }^\circ/\text{s}$ .

(b) Evolution of the steady avalanche angle with the rotating speed.

Figure 2.13 – Steady avalanches in the quasi-static regime with suspensions of potato starch in pure water.

It is interesting to check that the hypotheses of a viscous and quasi-static regime are valid for our measurements, since inertia or dynamic effects strongly impact the flow of submarine granular media (see [55]). Here the Stokes number is  $St \simeq 6 \times 10^{-3}$  and  $r = 1.5$ , which means that inertia is indeed negligible (see the phase diagram in Fig. 2.6b). For the rotation speeds considered, the viscous number is also very small:  $3 \times 10^{-5} \leq J_{\text{drum}} \leq 3 \times 10^{-3}$ , confirming that we are in the quasi-static regime. Finally, we can estimate the granular pressure in the flowing layer using Equation (2.1). Assuming that the layer is about 10 particles high and that its packing fraction is 64%, we obtain  $P \sim 1 \text{ Pa}$ . The frictionless behaviour evidenced here therefore characterises the microscopic contact properties of the potato starch particles under very low granular pressure.

## 2.2 Compaction and dilatancy

The previous results, based on the measurement of the steady avalanche angle, strongly suggest that real shear-thickening suspensions have a frictionless behav-

ior at low confining stress. This is a first direct support of the frictional transition scenario presented in the introduction. To confirm our results, we conducted additional experiments using another macroscopic signature of microscopic friction: compaction and dilatancy effects. In this section, we first discuss these notions in granular media and their link with friction, before describing our experimental results.

### 2.2.1 Background

#### Compaction and Reynolds' dilatancy

A well-known property of frictional granular piles is that they can compact under gravity. This is done daily in the kitchen when cooking rice or baking cakes: you pour rice or flour into a measuring cup, and tap it on the side to compact the grains and measure the needed amount. By doing this, you give energy to the grains and as a result they increase their packing fraction. This tapping procedure have been extensively used in controlled experiments to study the compaction of granular media, as illustrated in Figure 2.14. The compaction depends on both the number of taps and their amplitude, but seems to saturate for large numbers of taps (highlighted in blue in Figure 2.14). The main result it that a pile of frictional grains subjected to gravity is stable for a range of packing fractions  $\phi_{\min} \leq \phi \leq \phi_{\max}$  (see [55]). The minimal packing fraction is the *random loose packing*  $\phi_{\text{RLP}}$ , whose value is about  $\phi_{\text{RLP}} = 55\%$  for frictional spheres (usually, such a low value can only be achieved after slow sedimentation in a very viscous liquid). The maximum packing fraction achievable by careful tapping is the *random close packing*  $\phi_{\text{RCP}} = 64\%$  (see [55]).

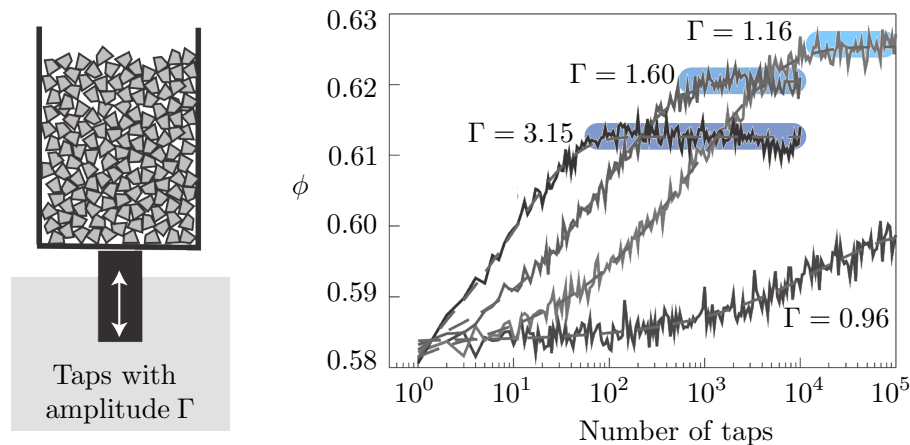
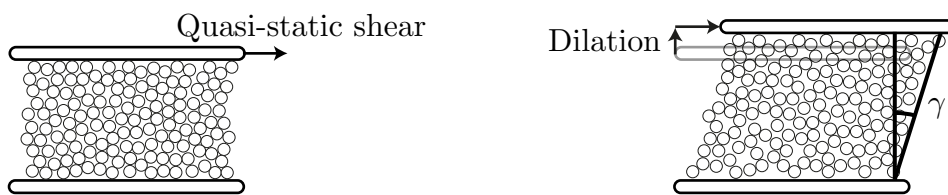


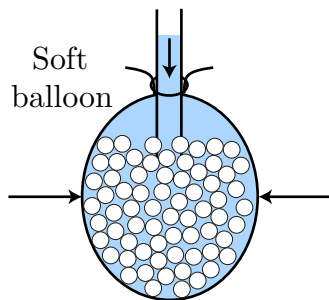
Figure 2.14 – Compaction of a dry granular medium. Adapted from [55] and [65].

The fact that granular piles have stable states for packing fractions both below and above the critical flowing packing fraction  $\phi_c$  has important consequences for their transient behaviour under deformation. When slowly sheared at fixed pressure, dense granular piles with initial packing fractions  $\phi > \phi_c$  cannot deform without dilating. Therefore, in addition to a deformation in the direction of the shear,

the medium also deforms transversally to this direction (see Figure 2.15a). This is the famous Reynolds *dilatancy* effect, first reported by O. Reynolds in 1885 [33] (see Figure 2.15b). It explains why compact wet sand dries out when you step on it (Fig. 2.15c). Reynolds dilatancy has been studied in controlled geometries like sheared boxes, for example by Wroth in [66], whose results are presented in Figure 2.15d. As we can see, if the sediment is initially dense the packing fraction decreases with the deformation  $\gamma$  until it reaches the critical packing fraction  $\phi_c$ . Conversely, if the sediment is initially loose, the packing fraction increases with  $\gamma$ , until it reaches  $\phi_c$ . We see that after a deformation of approximately 60%, the system has forgotten its initial state (loose or dense), and simply flows at its critical packing fraction  $\phi_c$ .



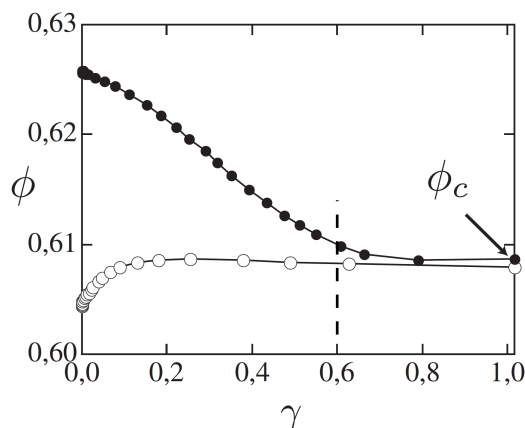
(a) Shearing densely packed grains leads to a transient dilation.



(b) Reynolds' dilatancy experiment. Adapted from [55].



(c) Sand drying around a foot, from [55].



(d) Transient dilatancy or compaction of a sheared granular medium. Data from [66] and figure from [55].

Figure 2.15 – Reynolds dilatancy.

Reynold's dilatancy can have dramatic consequences on the starting avalanche behaviour of a granular medium when the grains are immersed in a liquid. In this case, the transient dilation or compaction towards  $\phi_c$  must be accompanied by an inward or outward liquid flow, and thus a positive or negative pore pressure  $P_f$  between the grains. Since the granular rheology is frictional ( $\tau = \mu P$ ), the addition of the pore pressure to the total granular pressure  $P$  transiently modifies the strength of the medium. This coupling between dilatancy and pore pressure was clearly demonstrated by Pailha et al. in [67]. The authors investigated the transient avalanching behaviour of a granular layer immersed in a viscous fluid and suddenly tilted above the avalanche angle  $\theta_c$  (see Fig. 2.16a). They also controlled the initial packing fraction  $\phi_i$  of the sediment by tapping the box that contains the grains and fluid (see Fig. 2.16b). Figure 2.16c shows that for initially loose sediments ( $\phi_i < 58\%$ ), the transient avalanche accelerates immediately after the box is tilted, while for initially dense sediments ( $\phi_i > 58\%$ ) there is a delay  $t_{\text{trig}}$  before the avalanche starts to slowly accelerate. This difference in behaviour can be explained through Reynolds dilatancy and pore pressure. For initially dense sediments, the medium must dilate in order to flow. The liquid must then be sucked in, which induces a negative pore pressure that presses the grains against each other, thereby enhancing friction. The avalanche is strongly delayed. Conversely, for initially loose sediments, the medium must compact when it starts to flow. This compaction induces an expulsion of the fluid from the sediment, and thus a positive pore pressure, which fluidises the medium and explains the fast initial acceleration.

### Link between compaction, Reynolds dilatancy, and friction

The property of granular media to compact, and subsequently to dilate under shear, is strongly related to the existence of frictional solid contacts between the particles. It is the presence of solid friction between the grains that allows a granular pile to be mechanically stable over a wide range of packing fractions below the maximal packing fraction  $\phi_{RCP} = 64\%$ . We have seen in Chapter 1 that it is also the microscopic friction coefficient  $\mu_p$  that shifts the critical flowing packing fraction  $\phi_c$  to values smaller than  $64\%$ . By contrast, for frictionless hard spheres (that is, with  $\mu_p = 0$ ), the conditions of mechanical equilibrium and non-overlap between grains impose only one possible coordination number for the pile (that is, the average number of nearest neighbours is fixed, see [55]). This suggests that perfectly frictionless beads packs at equilibrium only have access to one packing fraction, and that this packing fraction is  $\phi_c^{\mu_p=0} \simeq \phi_{RCP} = 64\%$ . This conclusion is supported by the numerical simulations of Peyneau and Roux [57]. They showed that the packing fraction of isotropic or continuously sheared granular packings of frictionless hard spheres was always the same and close to  $64\%$ , at least for large systems. This seems to indicate that for frictionless beads, the only accessible configuration is the random close packing, as illustrated in Figure 2.17. In a granular suspension made of frictionless grains, there should therefore be no possible compaction under gravity, and as a consequence no Reynolds dilatancy effect. Studying compaction and dilatancy effects in a suspension is thus a very

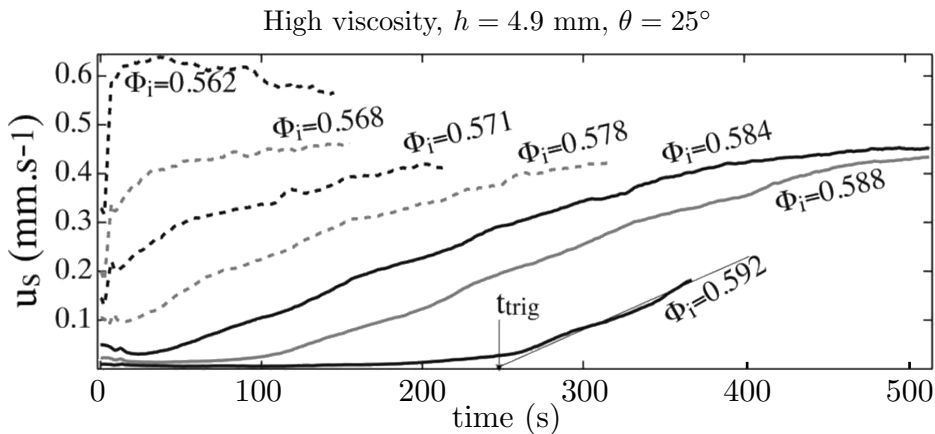
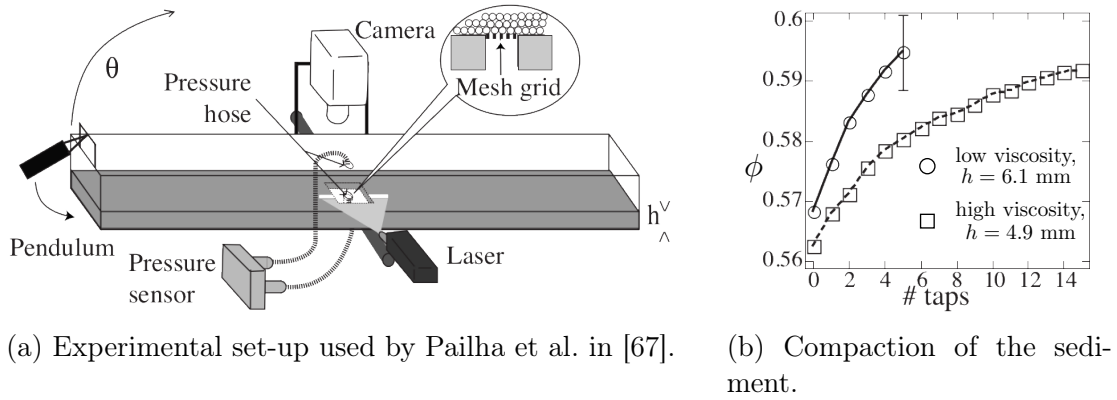


Figure 2.16 – Effect of dilatancy and pore pressure feedback on the transient avalanche behaviour of granular suspensions. Figures from [67].

good way to probe its frictional behaviour.

## 2.2.2 Experiments

As in the previous section, we have compared the compaction and dilatancy properties of the classical frictional suspension of large glass beads in a viscous fluid and the shear-thickening suspension of potato starch in water. To this end, we use the same rotating drum set-up as before and establish a protocol inspired by the study of Pailha et al. in [67]. We first compact the sediment and then tilt it to an angle far above the critical avalanche angle  $\theta_c$  to study the behaviour of the starting avalanche. The experimental protocol is described in Figure 2.18b, and below.

1. The grains are first suspended by continuously rotating the drum at  $90^\circ \cdot \text{s}^{-1}$ .
2. They are then left to settle on the bottom of the drum for  $\simeq 1$  min. At the end, the free surface of the sediment is horizontal. We then take a photograph of the drum's front face.

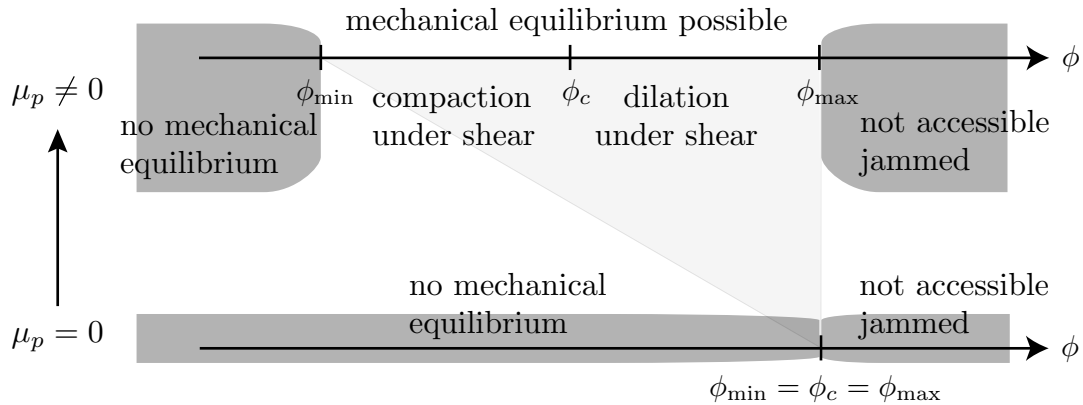
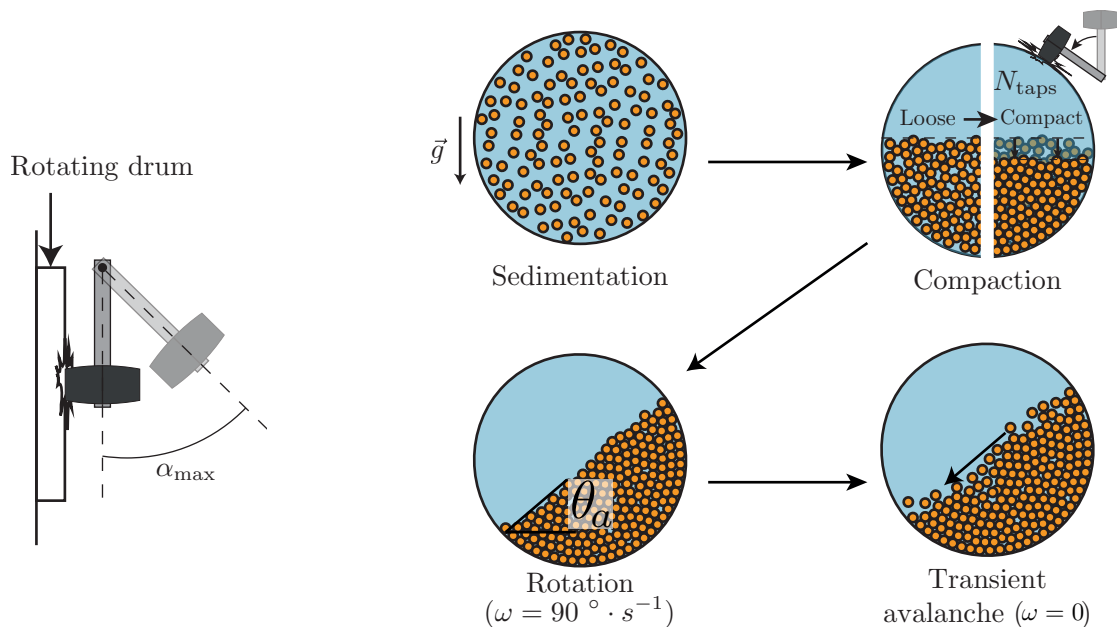


Figure 2.17 – Range of packing fractions for which mechanical equilibrium under gravity is possible for a granular pile, as a function of the microscopic solid friction coefficient  $\mu_p$ .



(a) Experimental set-up.

(b) Experimental protocol.

Figure 2.18 – Experimental set-up and protocol used to study compaction and dilatancy effects in our suspensions.

3. We compact the sediment by tapping  $N_{\text{taps}}$  times on the drum with a rubber mallet, as illustrated in Figure 2.18a. This is done in three steps:
  - (a) tap 10 times on the front face of the drum with the mallet (20 times for the potato starch),
  - (b) let the system relax for 30 s,
  - (c) take a photograph of the drum's front face.



These three steps are repeated as many times as necessary to reach the desired value of  $N_{\text{taps}}$ .

4. The drum is then rapidly rotated (at  $90^\circ \cdot \text{s}^{-1}$ ) at a fixed angle  $\theta_a$   $10^\circ$  above the avalanche angle.
5. An avalanche then develops and its flowing dynamics is recorded by filming the drum at 24 images per second.

Note that for the experiments with potato starch in water suspensions, we did not use the water circulation. These experiments are quite fast, so ageing is not a problem.

To compute the initial packing fraction of the sediment as a function of the number of taps, all of the photographs were processed at the same time. First, image correlation is used to correct for any drift between the different photographs. Then, a circle centered on the drum is drawn on the first image, and any part not contained into the circle is erased. A luminosity threshold is used to separate the interior of the drum into the part containing only the suspending fluid, of no interest here, and the part containing the sediment. The latter gives us the sediment's area  $A(N_{\text{taps}})$  after  $N_{\text{taps}}$  taps. The corresponding sediment's packing fraction  $\phi(N_{\text{taps}})$  is then computed using the following formula:

$$\phi(N_{\text{taps}}) = \phi(0) \frac{A(0)}{A(N_{\text{taps}})}, \quad (2.6)$$

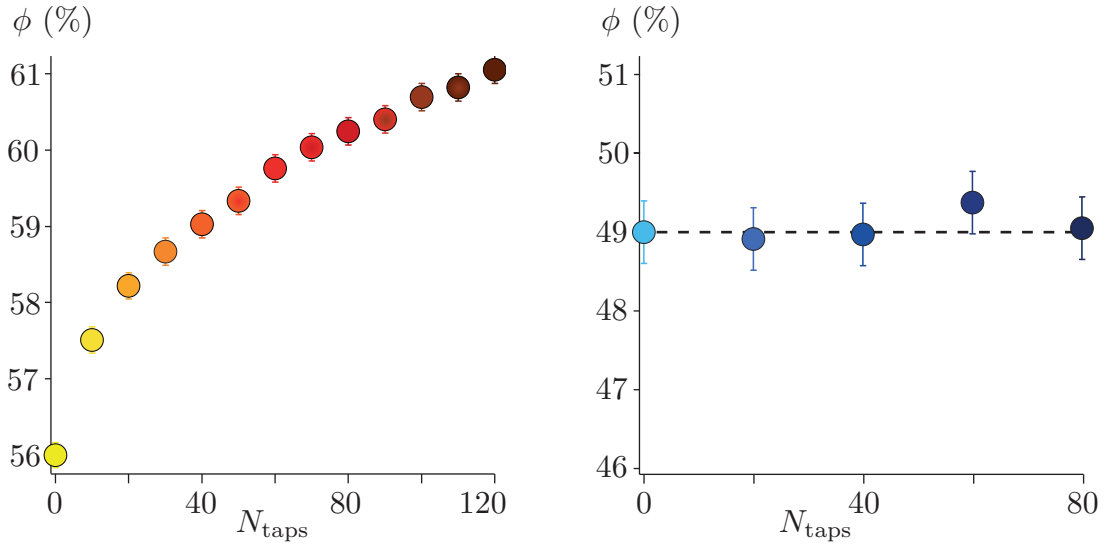
where  $A(0)$  is the area of the sediment measured just after sedimentation (no tap) and  $\phi(0)$  is its packing fraction.

For the large glass beads, we obtained  $\phi(0)$  in-situ by directly measuring the mass of the particles inside the drum and by computing the volume of the sediment from:  $V_{\text{sed}} = WA(0)$ . For the potato starch suspension, since the drum is too small this technique was not precise enough. We therefore measured  $\phi(0)$  independently in a larger container (measurement conducted by Pauline Dame during her internship).

The time evolution of the pile angle during the transient avalanches was obtained with the same Python program as for the steady avalanches.

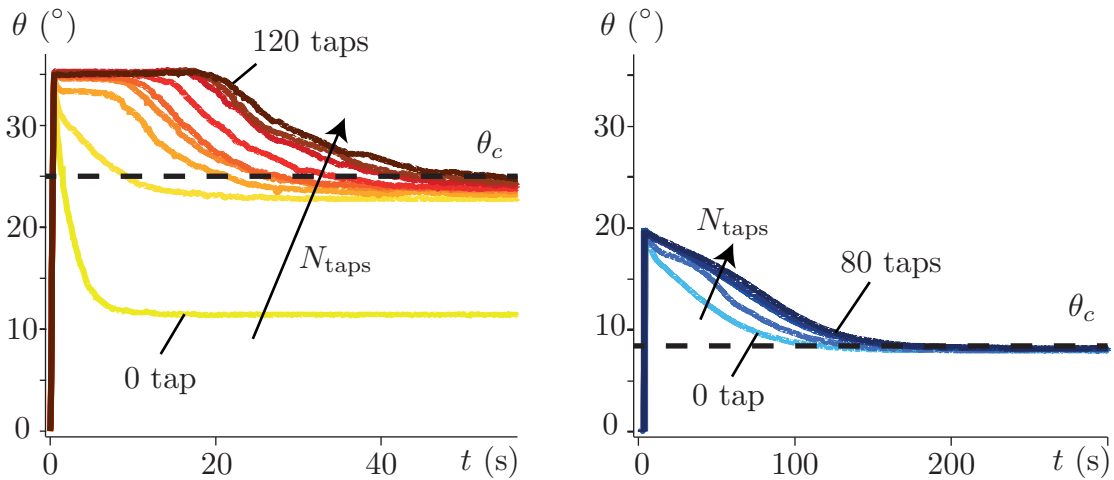
Figure 2.19 (top) compares the compaction behaviour of the large glass beads suspension (Fig. 2.19a) and the potato starch suspension (Fig. 2.19b). The large glass beads exhibit the typical behaviour of a pile of frictional particles. The packing fraction of the glass beads sediment, which right after sedimentation starts from a loose state ( $\phi(0) = 56.0 \pm 0.3\%$ ), progressively increases with the number of taps to eventually reach a dense state ( $\phi(120) = 61.0 \pm 0.3\%$ ). Conversely, it was not possible to compact the sediment of potato starch in pure water no matter how many taps we gave on the drum. There is thus only one possible state of compaction for these grains, which is a signature of a frictionless behaviour as explained in Section 2.2.1. For the suspension of potato starch in pure water, we measured  $\phi(0) = 49.0 \pm 0.8\%$ . This value may seem small, as the expected value for the critical packing fraction of a suspension of frictionless monodisperse

spheres is  $\phi_c = 64\%$ . However, as already pointed out, the potato starch particles are neither monodisperse nor spherical. Additionally, they have a tendency to swell in water (see [68] for example), so the packing fraction measured from the dry particles' density can be quite different from the real one.



(a) Classical suspension of large frictional glass beads in a viscous fluid.

(b) Shear-thickening suspension of potato starch in pure water.



(c) Classical suspension of large frictional glass beads in a viscous fluid.

(d) Shear-thickening suspension of potato starch in pure water.

Figure 2.19 – Compaction (top) and transient avalanches (bottom) of a classical suspension of frictional beads (Fig. 2.19a and 2.19c, glass beads of diameter  $d = 487 \pm 72 \mu\text{m}$  in a Ucon<sup>TM</sup> oil and water mix of viscosity  $\eta_f = 57 \text{ mPa} \cdot \text{s}$ ) and of a shear-thickening suspension (Fig. 2.19b and 2.19d, potato starch grains of average size  $d = 25 \pm 15 \mu\text{m}$  in pure water).

Figure 2.19 (bottom) shows that the transient avalanches behaviour is also very different for the large beads and shear-thickening suspensions. For the large

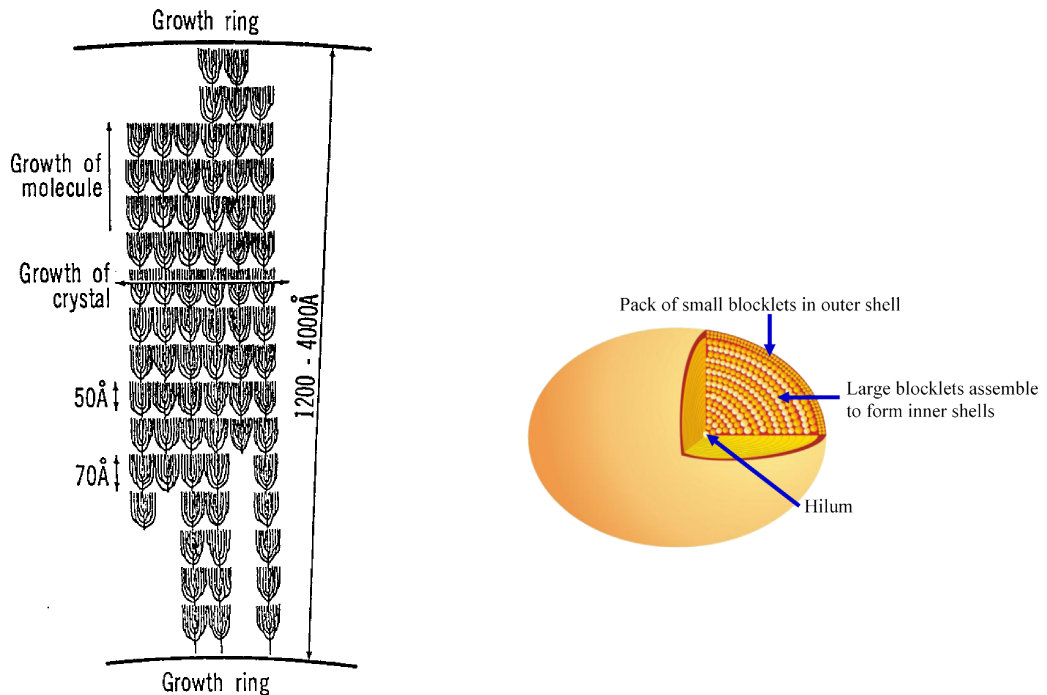
glass beads, the transient behaviour strongly depends on the initial preparation (see Fig. 2.19c). For an initially loose packing (0 tap), the avalanche rapidly flows until its angle relaxes to an angle much lower than  $\theta_c$  (the quasi-static steady avalanche angle measured earlier). Conversely, for an initially compact sediment (120 taps), one observes a long delay during which the avalanche stays still. It then slowly flows, relaxing to  $\theta_c$ . Such a change in the avalanche dynamics with the packing of the initial sediment is a clear signature of Reynolds dilatancy effects and pore pressure coupling, as explained in Section 2.2.1. For  $\phi < \phi_c$ , the medium compacts when the avalanche starts, which induces an expulsion of the fluid and a positive pore pressure that fluidises the flow. Conversely, for  $\phi > \phi_c$ , the medium must dilate in order to flow, which induces a suction of the fluid and a negative pore pressure that strongly delays the avalanche. We found that the transition between the fluidised and delayed behaviours occurs for a packing fraction  $\phi_c \simeq 58\%$ , which is consistent with previous work on similar particles (see Figure 2.16b and [67]).

The transient avalanches of the potato starch suspension strongly contrast with these results (see Fig. 2.19d). Since there is only one packing fraction accessible to the system, we observe no dilatancy effects: all the avalanches relax without delay towards the quasi-static steady avalanche angle  $\theta_c = 8.5^\circ$ , whatever the initial preparation. We still observe a slight difference in the dynamics depending on the preparation, which we attribute to small rearrangements in the microstructure of the sediment, possibly related to the ovoid shape of the particles. However, these experiments again show that, under low confining pressure, potato starch particles behave as if they were frictionless.

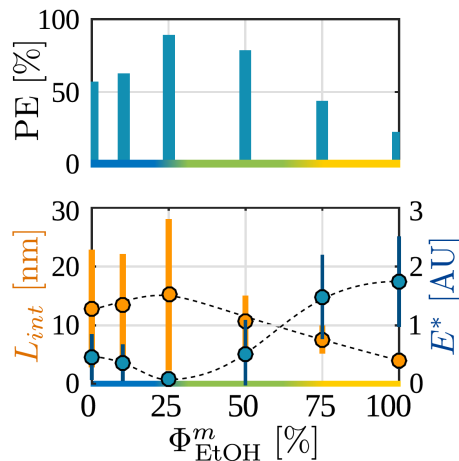
### 2.2.3 Discussion

In the previous experiments, we studied three macroscopic properties of dense suspensions: steady avalanche angles, compaction behaviour, and dilatancy effects, which give access to the microscopic solid friction between particles at very low confining pressure (the weight of a few grains). By comparing a classical frictional suspension of macroscopic particles and a typical shear-thickening suspension of starch, we found three macroscopic signatures of a frictionless behavior in the shear-thickening suspension: a very low quasi-static steady avalanche angle, the absence of compaction, and no dilatancy effect. These results are consistent with the frictional transition model, which proposes that shear-thickening suspensions behave as frictionless suspensions at low granular pressure. We have seen in Chapter 1 that the frictional transition model attributes the existence of this frictionless state to the presence of a repulsive force between the grains. This suggests the existence of a short-range repulsive force or a microscopic pressure-dependent friction between the starch particles.

The nature of interaction forces between starch particles, and even the precise structure of starch grains, are actually still poorly understood. Potato starch grains seem to be formed by the growth of polymers, amylose and amylopectine, in concentric growth rings around a central point called the hilum, see [69, 70] and Figures 2.20a and 2.20b. In [69], Lineback proposes a “hairy billiard ball” model,



(a) Polymers growing in concentric growth rings and forming a starch grain. From [69]. (b) Internal structure of a potato starch grain. From [70].



(c) Fraction of pulling events and interaction length between two cornstarch grains, as a function of the ethanol to water ratio. From [71].

Figure 2.20 – Structure of a starch grain, and interaction forces between starch surfaces.

saying that the growing polymers form a brush-like structure at the surface of a grain. In [72], Park et al. observe cornstarch particles in Atomic Force Microscopy (AFM) and say that their surface is decorated by 2 to 5 nm high fibers. The presence of polymer brushes at the grains' surfaces could induce a steric repulsion between the particles. However, there doesn't seem to be a consensus as to the exact structure of starch grains.

Interactions between starch particles seem strongly dependent on the suspending fluid, as shown by Oyarte Gálvez et al. in [71]. The authors studied the effect of changing the suspending fluid from water to mixes of ethanol and water. They showed that the rheology of suspensions of cornstarch in water and ethanol mixes goes from shear-thickening in pure water to non shear-thickening in pure ethanol. They relate this to AFM measurements in which they measure the interaction force between a cornstarch grain glued to a steel surface and another cornstarch grain attached to the AFM cantilever. By recording the force exerted on the cantilever both while approaching and retracting it from the cornstarch grain glued on a steel surface, they are able to compute an interaction length  $L_{\text{int}}$  between two starch particles. They also observe sharp peaks in the retracting force curve, which they claim are the signature of polymers at the surface of the grains, disentangling from one another. As we can see in Figure 2.20c, the frequency of these sharp peaks, denoted by PE (for ‘pulling events’), depends on the nature of the suspending fluid, and is higher in water than in ethanol. The authors interpret this as the fact that there are polymers at the surface of the grains, and that these are completely insoluble in ethanol. The interaction length between two grains is also shown to be fluid-dependent, and larger in water than in ethanol. This suggests that there are indeed polymers at the surface of starch grains. In water, they appear to be at least mildly soluble. They would therefore be unfolded, hence a larger interaction length, and a possible steric repulsion explaining shear thickening. In ethanol, they seem to be insoluble. They would thus be coiled, hence a shorter interaction length, and no more steric repulsion, which would explain the absence of a shear-thickening behaviour.

We tried to modify the interactions between potato starch grains, and possibly their frictional behaviour, by studying a suspension of potato starch in a mix of ethanol and water. For approximately 50 wt% of ethanol in the suspending fluid, the suspension seems to no longer shear thicken, which is consistent with [71]. However, as we can see in Figure 2.21, the avalanches in a rotating drum exhibit strong signs of adhesion with this system (see [73, 74]). It was thus not possible to further investigate the frictional behaviour of these suspensions.

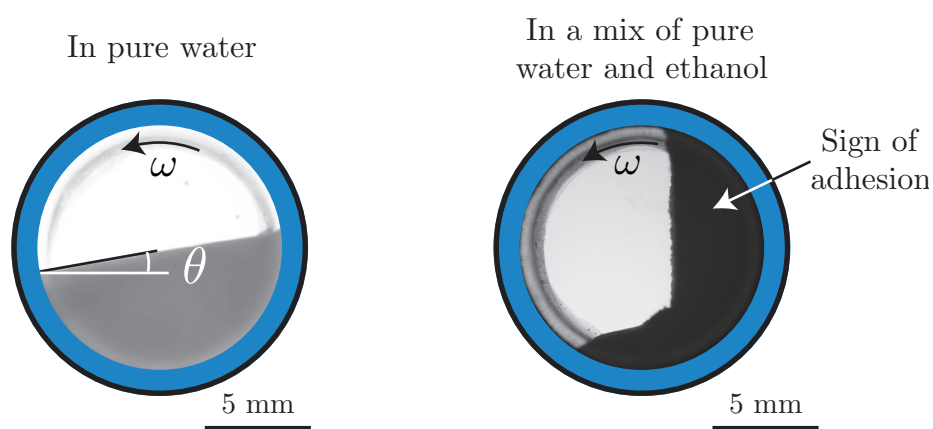


Figure 2.21 – Comparison of the behaviour of a potato starch suspension in pure water and in a water and ethanol mix, in a steadily rotating drum.

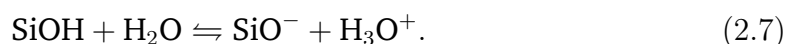
In conclusion, though the proposed model of a ‘hairy billiard ball’ fits the observed phenomenology of starch particles, there doesn’t seem to be a clear consensus on their exact structure. In particular, we don’t have enough information concerning the existence of a short-range repulsive force between potato starch particles. Additionally, assuming that it does have a steric origin, trying to control this force leads to experimental difficulties. Potato starch is thus not the ideal system to fully investigate the frictional transition model. For this reason, we chose to conduct additional experiments with a model suspension where interaction forces can be controlled.

## 2.3 Unveiling the frictional transition using a model suspension

### 2.3.1 Glass and silica surfaces in aqueous ionic solutions

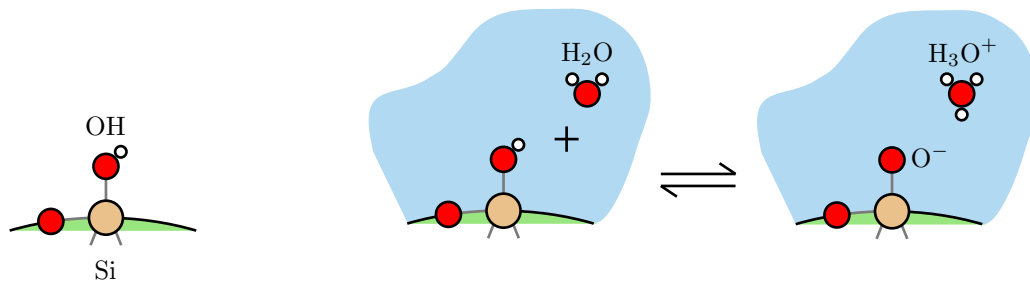
Our objective was to find a non-Brownian suspension with easily controllable short-range repulsive forces between the particles. Moreover, since our experiments are based on gravity-driven flows (avalanches), the density of the particles must be significantly larger than the density of the liquid to form a well-defined pile at the bottom of the drum. For these reasons, we chose to work with suspensions of microbeads of glass or silica particles in aqueous ionic solutions.

At the surface of glass or pure silica, one finds silanol groups, that is, SiOH groups, as illustrated in Figure 2.22a (see [75]). When in contact with water, these silanol groups are hydroxylated into silicic acid groups by the following chemical reaction:

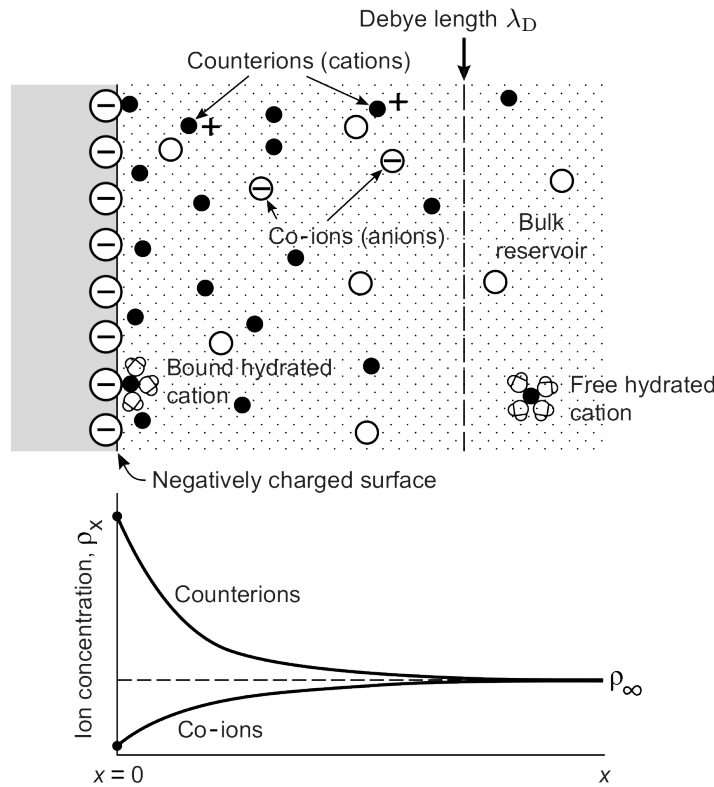


This leads to the presence of a negative surface charge on glass or silica surfaces immersed in aqueous solutions. In response to this negative surface charge, the *counter-ions* (of opposite charge) present in the solution are attracted by the surface. Some are transiently bound to the surface, while the others form a diffusive atmosphere close to it, in thermal equilibrium. Away from the surface, some *co-ions* (of the same charge as the surface charge) are found in the counter-ions atmosphere. Then, at a certain distance  $\lambda_D$  from the surface, the concentrations of both co- and counter-ions relax back to their bulk concentration. The distance  $\lambda_D$  is called the *Debye length*. This spatial organisation of ions close to a charged surface, which results from both electrostatic interactions and thermal motion, is called the electrostatic double layer and is illustrated in Figure 2.22b (see [34] for a general textbook on surface and interface interactions). It is responsible for the presence of a repulsive force between the particles.

The interactions between silica surfaces in aqueous solutions have been studied experimentally using a Surface Force Apparatus or Atomic Force Microscopy, for example by Vigil et al. in 1994 in [75] (see Figure 2.23a), or more recently by Valmaco et al. in [76] in 2016 (see Figure 2.23b). In pure water or at low ionic concentrations, the interaction force is repulsive as expected, and decreases



(a) Simplified surface chemistry of glass or silica in the presence of water. Inspired by [75]. Left: a silanol group at the surface of glass or pure silica. Right: hydroxylation of a silanol group into a silicic acid group.



(b) Double layer in an electrolyte near a surface with a negative surface charge, with the associated evolution of the co- and counter-ions concentrations. From [34].

Figure 2.22 – Charge repartition near a silica surface in an aqueous ionic solution.

roughly exponentially far away from the surface, as:

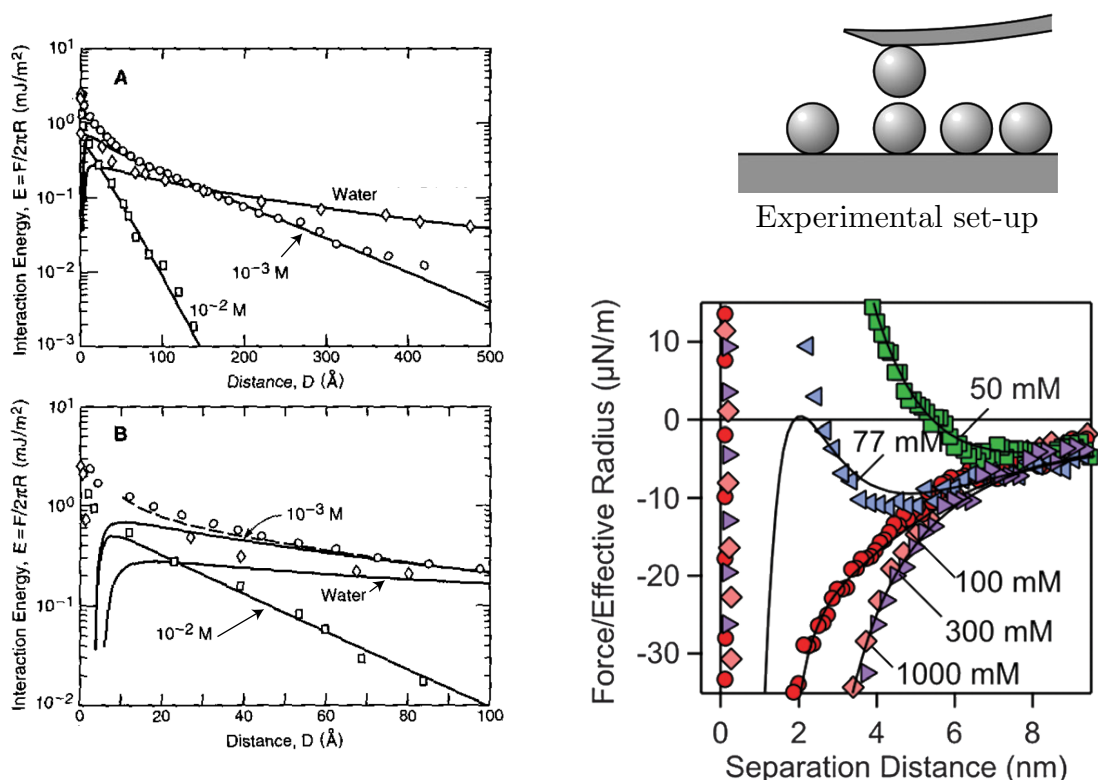
$$F_{\text{rep}}(z) = F_0 \exp\left(-\frac{z}{\lambda_D}\right), \quad (2.8)$$

where  $z$  is the separation between the two surfaces, and  $F_0$  is the intensity of the force at vanishing separation. For an ionic solution of monovalent ions (like NaCl

in water) at ambient temperature, the Debye length is given by:

$$\lambda_D = \frac{0.304}{\sqrt{[\text{NaCl}]}} \text{ nm}, \quad (2.9)$$

with  $[\text{NaCl}]$  expressed in  $\text{mol} \cdot \text{L}^{-1}$  (see [34]). Typically,  $\lambda_D$  varies from about  $1 \mu\text{m}$  in pure water to about  $1 \text{ nm}$  in  $[\text{NaCl}] = 10^{-1} \text{ mol} \cdot \text{L}^{-1}$  solutions. Glass or silica beads in ionic solutions are thus a good model system to control the repulsive force and study the frictional transition. Note that the chemical equilibrium of Equation (2.7) is sensitive to the pH of the medium (see [77]), which affects the surface charge of the particles and the value of the force  $F_0$  at contact. Therefore, the repulsive force could also be controlled by the pH of the solution.



(a) Force between a silica plate and a silica bead in water and various ionic solutions of different concentrations. From [75].

(b) Interparticle force between two silica beads in aqueous KCl solutions of different concentrations. From [76].

Figure 2.23 – Interaction force between silica surfaces in aqueous ionic solutions. The fits (solid lines) are the prediction of the DLVO theory (for DeJarguin, Landau, Verwey, and Overbeek) that combines the electrostatic repulsion from the double-layer and the attractive van der Waals interactions (see [34]). The DLVO theory works well except very close to the surface ( $50 \text{ \AA}$ ), where more complex physical and chemical ingredients are at play.



### 2.3.2 Experiments

We first conducted preliminary experiments using highly polydisperse microscopic glass beads available in the lab, with diameter  $d$  such that  $1 \mu\text{m} \leq d \leq 45 \mu\text{m}$ . We used the same drum as for the potato starch experiments, without the cooling device. Figure 2.24 presents the results we obtained when investigating the steady avalanche behaviour of these microscopic glass beads in various suspending fluids: filtered water, water with added cooking salt, and a pH = 10 and a pH = 7 buffer solutions. Interestingly, we observe that this system can behave as a suspension of either frictional or a frictionless particles depending on the suspending liquid. However, the avalanches often showed signs of adhesion with this system, probably due to the high polydispersity of the suspension. Furthermore, it was not possible to independently control the pH and the ionic concentration, since the buffer solutions contain ions. Finally, the glass beads of our sample were often non-spherical and their chemical composition is not well known. For these reasons, we turned to a more controlled system made of pure silica microbeads.

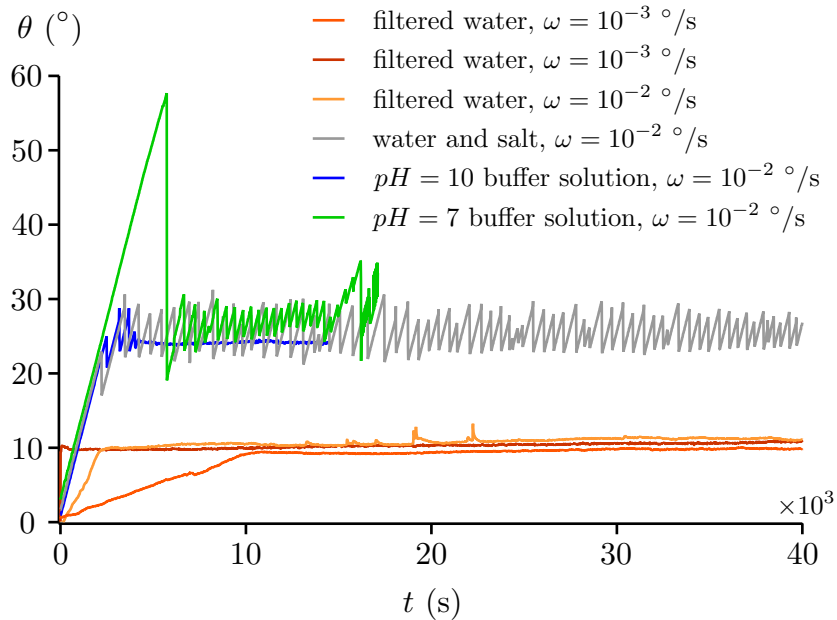


Figure 2.24 – Preliminary experiments with polydisperse microscopic glass beads in different suspending fluids.

We used commercial non porous silica particles from Microparticles GmbH with diameter  $d = 23.56 \pm 1.06 \mu\text{m}$  and density  $\rho_p = 1.85 \text{ g} \cdot \text{cm}^{-3}$ . They are sold in plastic bottles containing 5 wt% of particles in pure water. As we can see in Figure 2.25, the particles are fairly spherical and monodisperse. For the suspending fluid, we used either pure water or aqueous ionic solutions, prepared either by dissolving Sigma-Aldrich<sup>®</sup> NaCl powder into pure water using a volumetric flask, or by diluting such a solution. For these suspensions, the gravitational Péclet number  $Pe_g = \phi \Delta \rho g d / k_B T$  is  $Pe_g \sim 10^5$ , so Brownian motion is negligible. The Stokes number is  $St \simeq 6 \times 10^{-3}$  to  $1 \times 10^{-2}$  (using  $\theta_c = 6^\circ$  to  $25^\circ$ ), meaning that the suspension is in the viscous flowing regime. With this system, we conducted the same

rotating drum experiments as described previously (Sections 2.1 and 2.2) to systematically investigate the steady avalanches, compaction, and dilatancy effects of the suspension. These experiments were conducted with Pauline Dame (student at Centrale Marseille), during her internship in the lab.

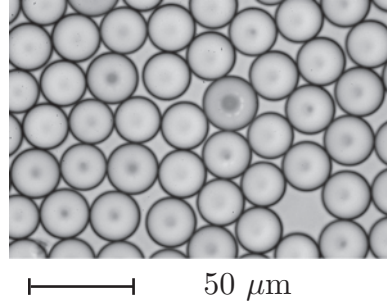


Figure 2.25 – Picture of the silica beads taken with an optical microscope.

We first compare two extreme cases: one with silica beads immersed in pure water, and the other with the beads immersed in a solution of water and NaCl with a large concentration of salt ( $[\text{NaCl}] = 10^{-1} \text{ mol} \cdot \text{L}^{-1}$ ) to fully screen the Debye layer. As illustrated in Figure 2.26 (green data), in the presence of a large concentration of salt which screens the repulsive force, the suspension behaves as frictional. The quasi-static steady avalanche angle is large:  $\theta_c = 27.5 \pm 0.5^\circ$ . The packing fraction of the sediment evolves from a loose packing right after sedimentation to a dense packing after 60 taps. Finally, the dynamics of the transient avalanche strongly depend on the initial packing, showing features related to the dilatancy effects discussed earlier. Conversely, the silica beads in pure water behave as frictionless particles (Figure 2.26, black data). The quasi-static steady avalanche angle is  $\theta_c = 6.0 \pm 0.3^\circ$ . This value is remarkably close to the quasi-static macroscopic friction angle obtained numerically for ideal frictionless spheres:  $\theta = 5.76 \pm 0.22^\circ$  (see [57], and recall Section 2.1.1). Additionally, no compaction of the sediment and no discernible effect of the initial packing on the transient avalanches are observed. These results clearly demonstrate that the presence of a short-range repulsive force can lead under low stress to a frictionless behaviour of the particles.

Note that with these suspensions, we only measured the relative evolution  $\Delta\phi$  of the packing fraction ( $\Delta\phi = \phi(N_{\text{taps}}) - \phi(0)$ ), and not its absolute value. We have indeed noticed that  $\phi(0)$  depends on the system size. This size effect can be explained by the finite range of the repulsive force between the grains. A silica particle in an aqueous solution may be thought of as a hard core of diameter  $d$  surrounded by a soft shell of thickness  $\lambda_D$ . Therefore, the effective volume of the particles varies between  $(4\pi/24)(d + 2\lambda_D)^3$  and  $(4\pi/24)d^3$ , depending on the confining pressure acting on the particles. Assuming  $\lambda_D \ll d$ , this yields an apparent packing fraction which lies between  $\phi_{\text{max}} \cdot (1 + \frac{2\lambda_D}{d})^{-3} \simeq \phi_{\text{max}} \cdot (1 - 6\frac{\lambda_D}{d})$  and  $\phi_{\text{max}}$ , where  $\phi_{\text{max}}$  is the packing fraction at contact. If we take  $\phi_{\text{max}} = 0.64$  (frictionless case),  $\lambda_D \simeq 1 \mu\text{m}$  (pure water) and  $d \simeq 24 \mu\text{m}$ , this gives a variation of packing fraction between 48 % and 64 % depending on the hydrostatic pressure on the grains. This probably explains the fact that we were not able to obtain a robust value of

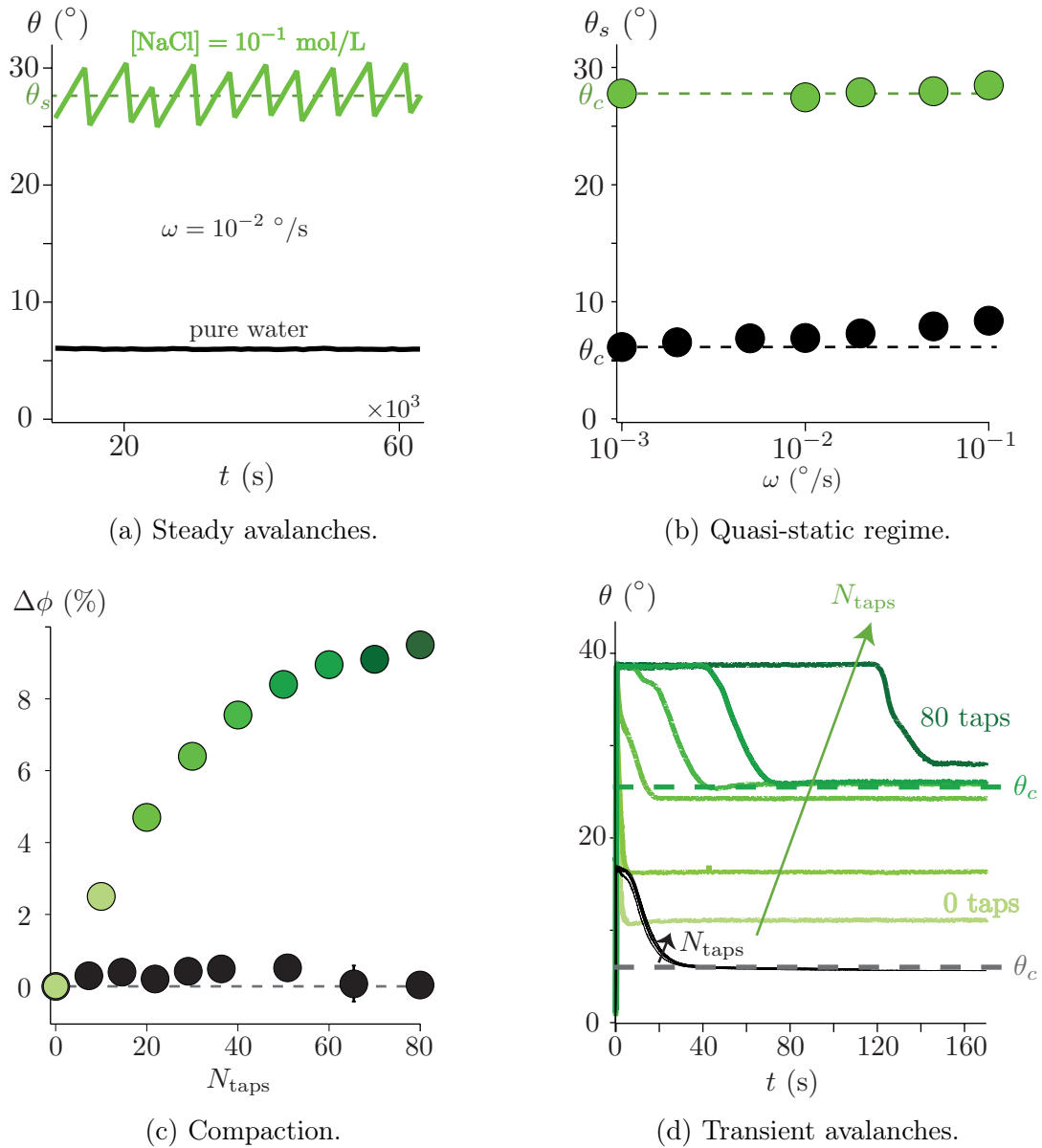
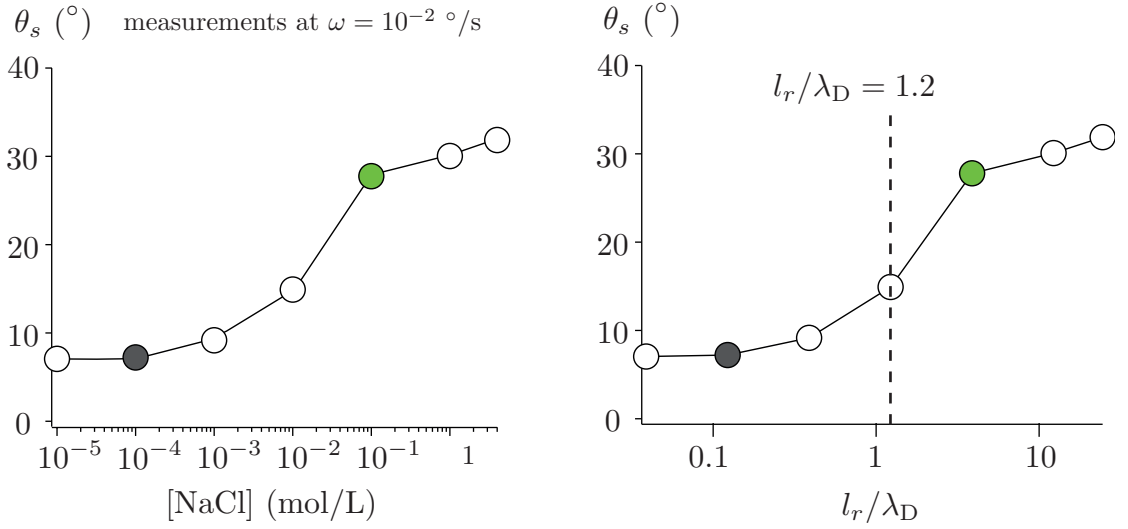


Figure 2.26 – Steady avalanches, compaction, and transient avalanches results for the silica beads, in pure water (black) and in an ionic solution with  $[\text{NaCl}] = 10^{-1} \text{ mol} \cdot \text{L}^{-1}$  (green).

$\phi(0)$  independently of the system's size.

Finally, to understand how the frictionless state in pure water connects to the frictional state at high salt concentrations, we systematically varied the salt concentration  $[\text{NaCl}]$  and measured the steady avalanche angle  $\theta_s$  for a given rotation speed  $\omega = 10^{-2} \text{ } \cdot \text{s}^{-1}$ . Figure 2.27a shows that the suspension's behaviour progressively changes from frictionless:  $\theta_s \simeq 6^\circ$  to frictional:  $\theta_s \simeq 30^\circ$  when the salt concentration  $[\text{NaCl}]$  is increased. We are thus able to evidence a frictional transition with this model suspension.



(a) Frictional transition plotted as a function of the salt concentration [NaCl].

(b) Frictional transition plotted as a function of the ratio between the surface roughness  $l_r$  of the beads and the range  $\lambda_D$  of the electrostatic repulsive force.

Figure 2.27 – Frictional transition in the suspension of silica microbeads ( $d = 23.56 \pm 1.06 \mu\text{m}$ ) in ionic solutions with increasing salt concentrations. The solid black lines are a guide for the eye.

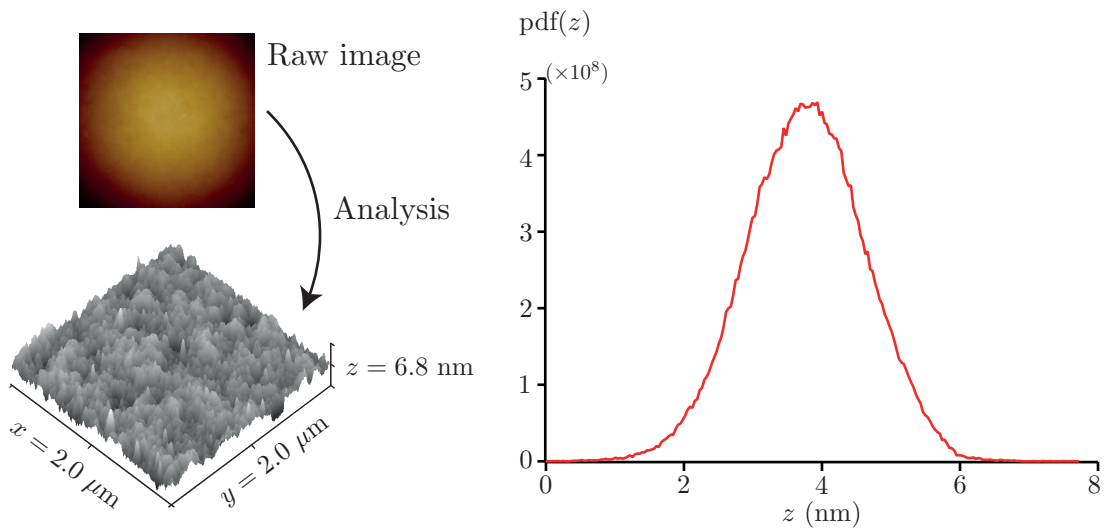
We expect this transition to occur when the confining pressure  $P$  exerted by the weight of the granular layer is enough to overcome the repulsive electrostatic pressure  $P_{\text{rep}}$  and bring the particles into contact:  $P = P_{\text{rep}}$ . To compute this, we model our silica beads as spheres decorated by rough protrusions of typical size  $l_r$ . We also assume that the repulsive pressure can be written as  $P_{\text{rep}}(z) = F_{\text{rep}}(z)/(\pi d^2/4)$ , where  $F_{\text{rep}}(z) = F_0 \exp(-z/\lambda_D)$  is the electrostatic repulsive force (Equation (2.8)) and  $z$  is the distance between the particles' surfaces. Finally, we assume that the confining pressure  $P$  due to the particles' weight is  $P = \phi \Delta \rho N d g \cos(\theta_s)$ , where  $N$  is the number of grains across the flowing depth. The transition then occurs when  $P = P_{\text{rep}}(2l_r)$ , that is:

$$\frac{l_r}{\lambda_D} \sim \frac{1}{2} \ln \left( \frac{F_0}{d} \cdot \frac{4}{\pi \phi \Delta \rho g N d^2 \cos(\theta_s)} \right). \quad (2.10)$$

In this formula, the Debye length  $\lambda_D$  is directly related to the salt concentration [NaCl] (Equation (2.9)). The force  $F_0$  can be estimated from previous measurements using Surface Force Apparatus, giving  $F_0/d \sim 1 \text{ mN} \cdot \text{m}^{-1}$  for silica surfaces in NaCl electrolytes (see [75] and Fig. 2.23a). This yields  $F_0 \sim 20 \text{ nN}$  in our case.

In order to check the validity of this prediction, it is necessary to determine the roughness  $l_r$  of the silica particles and the number  $N$  of particles in the depth of the avalanche. We estimated the particles' roughness using AFM measurements (conducted by Alain Rungis from Centre Interdisciplinaire de Nanosciences de

Marseille), and we analysed the data with the software Gwyddion. Figure 2.28a shows an example of a raw AFM image of a silica bead, and the 3D surface reconstruction obtained after analyzing it. Figure 2.28b is an example of the height distribution obtained with one bead. From this, we computed  $l_r$  as the average height of the peaks present on the beads surface. Using approximately 25 raw images and 9 different beads, we obtained  $l_r = 3.73 \pm 0.80$  nm. To estimate the thickness of the avalanche, we measured the velocity profile for silica beads in pure water at the wall of the rotating drum in the quasi-static regime, and found  $N \simeq 40$  (see Figure 2.29). Using these values for  $F_0$ ,  $l_r$ , and  $N$ , the frictional transition predicted by Equation (2.10) occurs for  $l_r/\lambda_D \simeq 1.2$  (here we took  $\theta_s \simeq 15^\circ$  and  $\phi = 0.6$ ; this ratio depends only very weakly on these values).



(a) Example of an AFM image obtained with one silica bead.

(b) Example of a size distribution of heights at the surface of one silica bead.

Figure 2.28 – AFM measurement of the typical surface roughness of the silica beads.

Figure 2.27b shows the same data as Figure 2.27a, but now the avalanche angle is plotted as a function of the ratio  $l_r/\lambda_D$ . As we can see, the transition indeed occurs for  $l_r/\lambda_D \sim 1$ , in fair agreement with our prediction. This result strongly supports the idea that the frictionless state arises from the interparticle electrostatic repulsive force. When its range is smaller than the particle's roughness, this force becomes ineffective to prevent the grains from touching and the system is frictional. From our model, it is interesting to estimate the repulsive pressure at contact  $P_{\text{rep}}$ , and compare it to the confining pressure  $P \simeq 5$  Pa due to gravity. For the frictionless case, we use  $[\text{NaCl}] = 10^{-4} \text{ mol} \cdot \text{L}^{-1}$  (grey data point in Figures 2.27a and 2.27b). We obtain  $P_{\text{rep}} = 40$  Pa, consistent with the fact that  $P < P_{\text{rep}}$ . For the frictional case, we use  $[\text{NaCl}] = 10^{-1} \text{ mol} \cdot \text{L}^{-1}$  (green data point in Figures 2.27a and 2.27b). We obtain  $P_{\text{rep}} = 2.3 \times 10^{-2} \text{ Pa} < P$ .

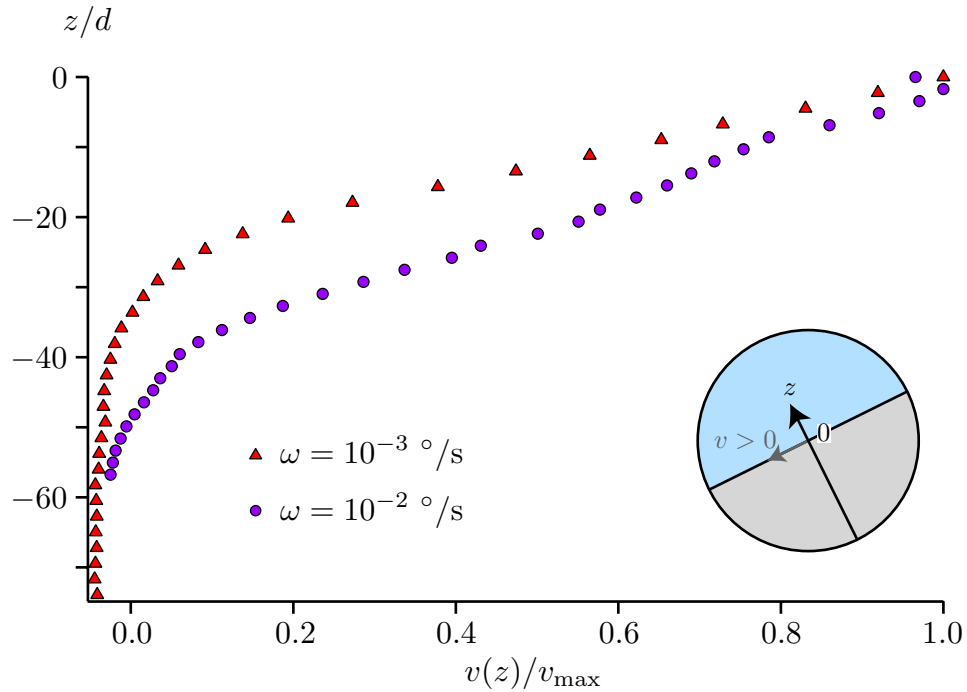


Figure 2.29 – Velocity profiles for silica beads in pure water. Data obtained by Pauline Dame during her internship.

### 2.3.3 Relation to the macroscopic rheology

The previous results show that by decreasing the repulsive force in a model suspension, we are able to shift from a suspension having a frictionless state at low confining pressure to a suspension that is always frictional. We still need to test whether for this model suspension, the existence of a frictionless state under low confining pressure leads to a shear-thickening rheology, and whether the elimination of this state (by screening the repulsive force) restores a Newtonian behaviour.

To this end, we performed rheological measurements on two suspensions of silica particles immersed in water with salt concentrations  $[\text{NaCl}] = 10^{-4} \text{ mol} \cdot \text{L}^{-1}$  and  $[\text{NaCl}] = 10^{-1} \text{ mol} \cdot \text{L}^{-1}$  respectively, that is, before and after the frictional transition observed on Figure 2.27a. It is not possible to match the density of the suspending fluid to that of the particles as we previously did to avoid sedimentation. Indeed, this process requires the addition of ions in the suspending fluid, which in our case would change the nature of the system. To circumvent these difficulties, the measures were thus conducted as follows (see Figure 2.30). In a clean beaker, we first let the particles settle down in their suspending fluid and adjust the liquid level at the sediment's interface. The volume of the sediment  $V_{\text{sed}}$  is measured and its packing fraction is assumed to be equal to a known value  $\phi_{\text{sed}}$ . We then add a given volume  $V_f$  of suspending fluid. We finally suspend the grains in the fluid by rotating a home-made double-helix with tilted blades in the beaker, at 5 rotations per second, during 10 seconds. This way, we create a homogeneous

suspension of packing fraction:

$$\phi = \phi_{\text{sed}} \frac{V_{\text{sed}}}{V_{\text{sed}} + V_f}.$$

After this first preparation step, we impose a rotating speed  $\Omega$  to the helix and measure the time evolution of the torque  $\Gamma$  applied by the suspension on the helix (measurements conducted using an Anton–Paar MCR 501 rheometer). After a short transient regime the torque reaches a plateau value  $\bar{\Gamma}$ . The signal eventually increases, due to sedimentation. In practice, we start the measurements with a low packing fraction, before increasing  $\phi$  by letting the system settle after one measurement and removing a given volume  $\delta V_f$  of suspending fluid (see Figure 2.30).

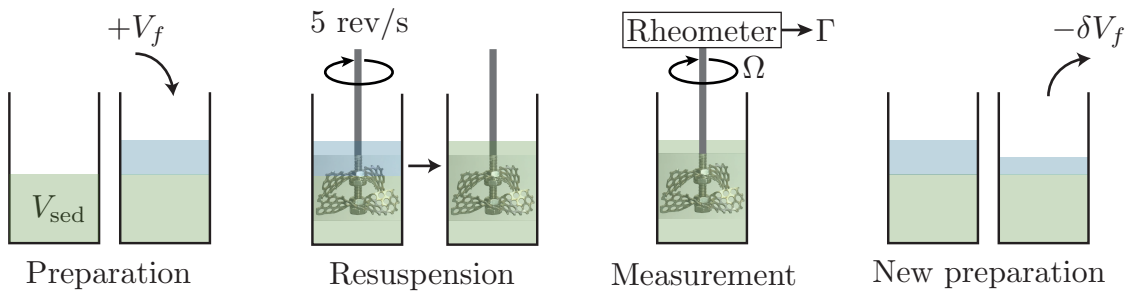


Figure 2.30 – Experimental set-up and protocol for measuring the rheology of silica suspensions in ionic solutions.

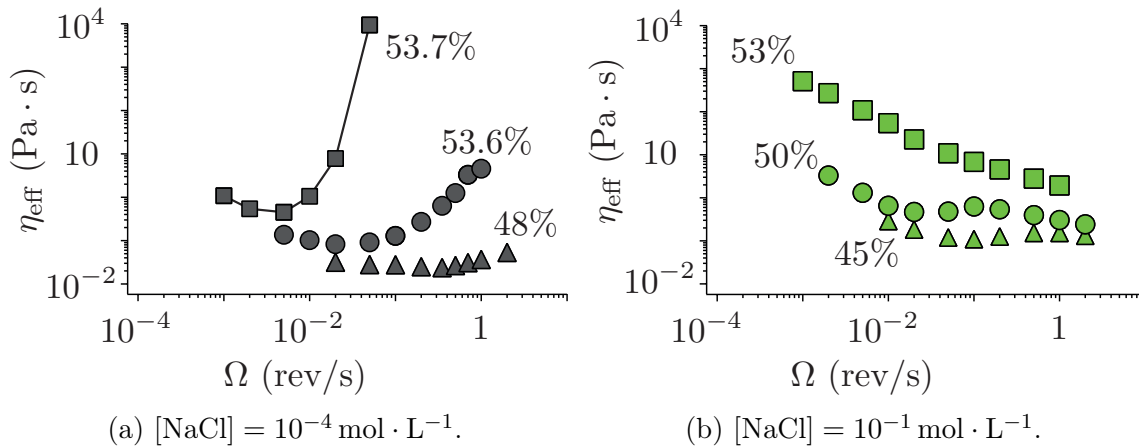


Figure 2.31 – Rheograms of suspensions of silica beads in ionic solutions. The solid black line is simply a guide for the eye.

Figure 2.31 gives the rheograms that we obtained, in the case of silica beads in  $[\text{NaCl}] = 10^{-4} \text{ mol} \cdot \text{L}^{-1}$  (Fig. 2.31a) or  $[\text{NaCl}] = 10^{-1} \text{ mol} \cdot \text{L}^{-1}$  (Fig. 2.31b). The effective viscosity of the suspension is defined by:

$$\eta_{\text{eff}} = \alpha \frac{\bar{\Gamma}}{2\pi\Omega L^3} \quad (2.11)$$

where  $\bar{\Gamma}/L^3$  is an effective stress,  $2\pi\Omega$  is an effective shear rate, and the constant  $\alpha \simeq 0.483$  is set to ensure that the effective viscosity matches the actual viscosity for a Newtonian fluid (we used glycerol for our calibration).

The first result is that the suspension for which  $[\text{NaCl}] = 10^{-4} \text{ mol} \cdot \text{L}^{-1}$ , which has a frictionless state under low granular pressure, displays all the features of a shear-thickening suspension (Fig. 2.31a). It exhibits continuous shear thickening at moderate packing fractions ( $\phi = 48\%$  and  $\phi = 53.6\%$ ), while larger packing fractions lead to a dramatic increase of its viscosity (by about 4 orders of magnitude). By contrast, the same suspension, but now with  $[\text{NaCl}] = 10^{-1} \text{ mol} \cdot \text{L}^{-1}$ , no longer shear thickens (Fig. 2.31b). In this case, we have seen that the repulsive force is screened and no frictionless state exists under low confining pressure. It is important to note that, although our measurement technique does not give access to the absolute values of the suspension's viscosity and packing fraction, the relative evolutions of both quantities at a given  $[\text{NaCl}]$  concentration are quantitative. Our results therefore provide a quantitative link between the existence of a repulsive force, the frictional behaviour of the suspension, and its rheology.

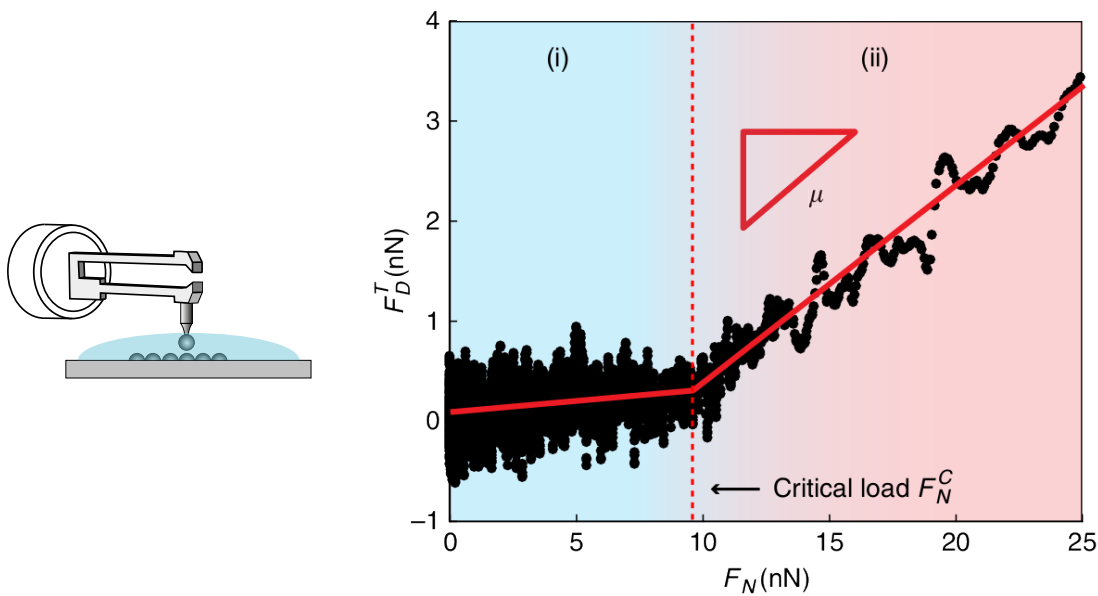
## 2.4 Conclusion of the chapter

In this chapter, we proposed a pressure-imposed approach, inspired from experiments in granular flows, to directly probe the microscopic frictional properties of non-Brownian shear-thickening suspensions. By systematically investigating steady avalanches, compaction, and dilatancy effects in rotating drums experiments, we provide direct proof that shear-thickening suspensions have a frictionless state under low granular pressure. Unlike Newtonian suspensions of frictional particles [28, 63, 67, 78], shear-thickening suspensions under low stress flow with a very small avalanche angle, do not compact and show no dilatancy effect. This phenomenology clearly indicates the absence of friction between particles [57]. Moreover, by using a model suspension of negatively charged silica beads, we find that lowering the range of the repulsive force below the particles' roughness makes the suspension transit from a frictionless to frictional state. The elimination of this frictionless state under low granular pressure also suppresses the shear-thickening behavior of the suspension. These experimental results, by linking microscopic contact physics to the suspension's macroscopic rheology, provide strong evidences that the frictional transition scenario proposed in [1, 3] to explain shear thickening applies in real suspensions. For discontinuous shear thickening to occur, the presence of short range repulsive forces able to prevent inter-particle friction at low stress seems essential.

The experiments we discussed in this chapter use macroscopic signatures of the microscopic friction between the grains. Soon after our publication, Comtet et al. presented another experimental validation of the frictional transition model, by directly measuring the microscopic friction coefficient  $\mu_p$  between the grains of a shear-thickening suspension using a modified AFM technique (see [79]). The authors used a mechanical resonator shaped like a microscopic tuning fork with one particle glued on its tip (see Fig. 2.32a). They probe another particle which is



glued on a solid plate, the whole set-up being immersed in the suspending fluid (see Fig. 2.32a). The resonator is set in motion by an external piezoelectric excitation in both the tangential and normal directions to the bottom plate. The presence of interactions between the particles induces changes in the tuning fork's resonance, which allow the authors to measure the tangential and normal forces between two particles (denoted by  $F_T$  and  $F_N$  respectively), and therefore the microscopic friction coefficient  $\mu_p = F_T/F_N$ . Using this set-up, they showed that the evolution of  $F_T$  with  $F_N$  has two linear regimes (Figure 2.32b): a quasi-frictionless regime with  $\mu_p \simeq 0.02$ , and a frictional regime above a critical normal load  $F_c$ , with  $\mu_p \simeq 0.45$ . The authors also related this critical normal load at the particle scale to the macroscopic critical shear stress  $\tau_c$  at which the suspension shear thickens (see [79]).



(a) Experimental set-up. (b) Tangential force as function of the normal load between two polyvinyl chloride particles in an Hexamoll<sup>®</sup> DINCH solution.

Figure 2.32 – A microscopic evidence of the frictional transition in a shear-thickening suspension. From [79].

By contrast with the microscopic measurements presented above, the rotating drum configuration used in our study provides a simple, yet robust way to characterize inter-particle friction of dense non-buoyant suspensions in the quasi-static steady flow regime and in-situ. Nevertheless, this configuration also has some limitations. When slowly rotating the drum, the thin flowing layer is on top of a pile experiencing solid rotation. Particles thus remain in static contact for a long time. For microparticles coated with polymers, which are often involved in shear thickening, these lasting contacts may age and lead to cohesion between the grains. In this case, the avalanche angle is no longer well-defined, nor is it constant when it exists (see [73, 74] for example). In our experiments performed with silica particles, small adhesive forces may have affected our results, and could for instance

explain the slightly large avalanche angles measured at high salt concentrations (Fig. 2.26a and 2.27a). However, the transition from low to high avalanche angles evidenced here must be dominated by frictional effects. Indeed, the avalanches have a constant slope from the top to the bottom of the avalanche, unlike adhesive powders. Moreover, adhesion alone without friction would not lead to the dilatancy effects observed on Figure 2.26d.

In conclusion, we have been able to evidence the frictional transition predicted by Seto, Mari et al. [1, 2] and Wyart and Cates [3] by lowering the repulsive pressure  $P_{\text{rep}}$  while the granular pressure  $P$  remained fixed (see Fig. 2.27b). Indeed, the rotating drum configuration gives access to the grains' frictional properties only for a fixed (and low) granular pressure, given by the weight of the flowing avalanche at the surface of the sediment. With this configuration, it is not possible to vary the granular pressure exerted on the particles. To fully explore the frictional transition model, this transition should also be addressed by varying  $P$  while keeping  $P_{\text{rep}}$  constant. We have seen in Chapter 1 that promising pressure-imposed rheometers have been recently developed to study the rheology of dense suspensions of macroscopic particles (see [28]). Extending such pressure-imposed approaches to suspensions of shear-thickening and colloidal particles is the goal of Chapter 3.



---

### The Darcytron: a pressure-imposed rheometer for colloidal suspensions

---

THAT WAS A PUNE OR PLAY ON WORDS, ALBERT. I DON'T KNOW IF YOU NOTICED.

DEATH.

In *Hogfather*, by Terry Pratchett.

In the previous chapter, we have shown that the presence of a repulsive force between particles can induce a frictionless behaviour in a suspension when it is subjected to a low granular pressure. Moreover, we also showed that the existence of this frictionless state gives rise to a shear-thickening rheology. These results strongly support the idea that a frictional transition is at the origin of shear thickening. However, the frictional transition we highlighted so far is the one that occurs when the range of the repulsive force between two particles is decreased. To fully explore this transition, we now need to investigate the frictional behaviour of a shear-thickening suspension when the granular pressure is varied. This represents an experimental challenge, since it requires the development of an original rheometer able to perform pressure-imposed measurements on shear-thickening suspensions, which are composed of very small particles. A large part of the work presented in this chapter was dedicated to the development of such a rheometer. The idea is to adjust the granular pressure by imposing a Darcy flow through the suspension, instead of mechanically pushing on the particles as was done for example by Boyer et al. in [28] (see also Chapter 1). First, we present the general concept of this new rheometer, which we named the *Darcytron*. We then validate this concept by investigating the frictional behaviour of a classical suspension. Finally, we present preliminary results obtained with our model shear-thickening suspension of silica particles in pure water.

### 3.1 General concept

As explained in Chapter 1, the appropriate way to probe the frictional behaviour of a suspension is to conduct pressure-imposed experiments. In a pressure-imposed configuration, the suspension's volume (and therefore its packing fraction) is not fixed. The suspension is thus free to expand or compact depending on the values of the applied shear rate and imposed granular pressure. To the best of our knowledge, the only pressure-imposed rheometer built so far is that of Boyer et al. [28], which we briefly presented in Chapter 1 (see Figure 3.1). In this rheometer, a porous grid both rotates to shear the suspension and translates vertically to adjust the volume of the suspension, maintaining a constant level of stress on the particles. This configuration is well-suited to the study of large particles (the authors used particles with a minimum diameter of  $d = 580 \mu\text{m}$ ). However, it is not suited to the study of suspensions of very small particles such as cornstarch grains ( $d \simeq 15 \mu\text{m}$ , see [64]). First, the gap  $l_g$  between the rotating grid and the side wall would inevitably let small particles leak out of the cell. Second, the very small pore size required to retain the particles below the grid would induce very long transients.

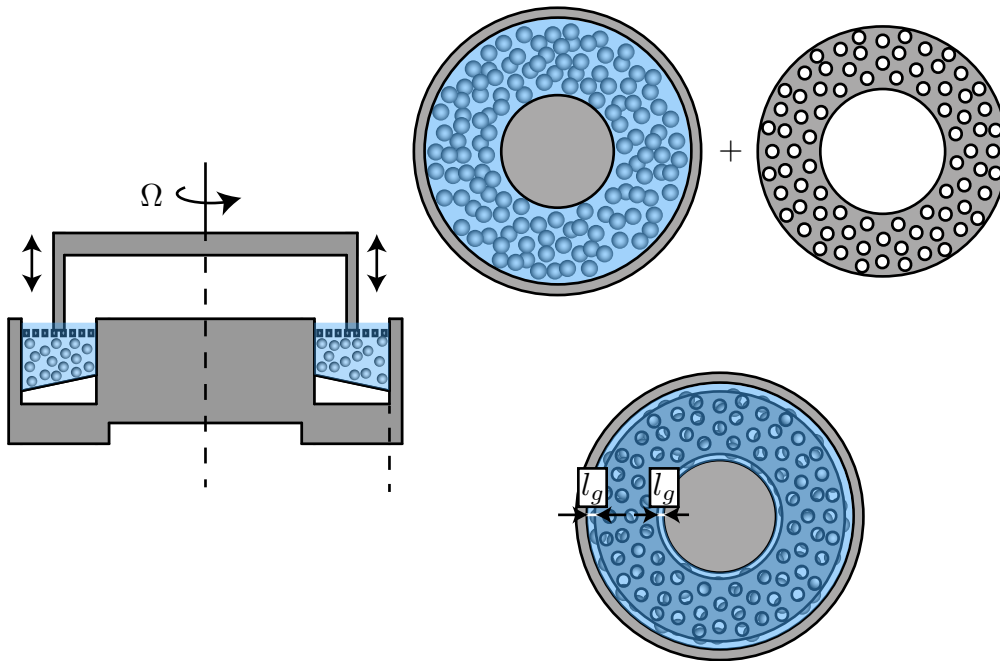


Figure 3.1 – Pressure-imposed experimental set-up used by Boyer et al. in [28]. This set-up is well-suited to the study of suspensions of large particles.

The Darcytron cell that we developed is based on a different concept which circumvents these difficulties. It enables pressure-imposed measurements on non-buoyant colloidal suspensions. A sketch of the Darcytron is presented in Figure 3.2. The configuration is that of an annular shear flow. The particles settle at the bottom of the cell, and the granular pressure is initially imposed by gravity alone. We assume that we can simply write it as  $P(z) = \phi \Delta \rho g z$ , where  $\phi$  is the packing

fraction of the sediment,  $\Delta\rho = \rho_p - \rho_f$  is the density difference between the particles and the suspending fluid,  $g$  is the gravity, and  $z$  is the vertical position in the sediment, measured relatively to its free surface.

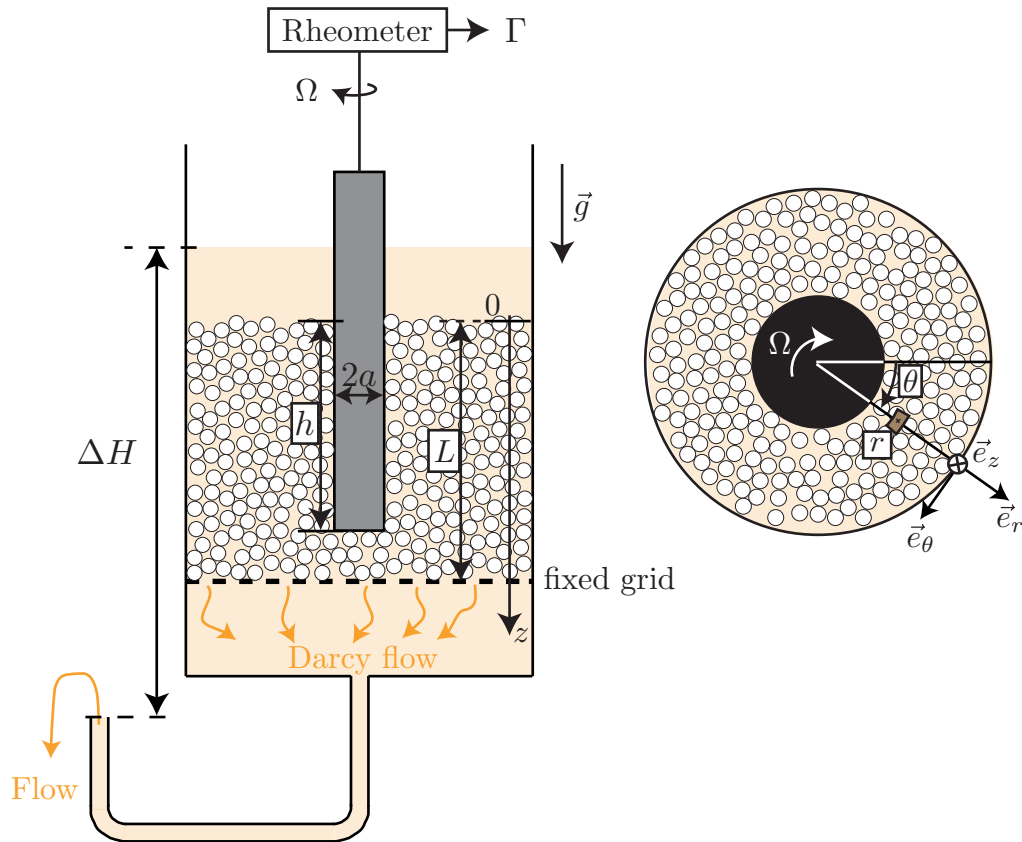


Figure 3.2 – Sketch of the Darcytron cell: a vertical Darcy flow, created by the height difference  $\Delta H$  between the fluid in the cell and the fluid at the end of the bottom tube, is used to impose the granular pressure in an annular shear flow configuration.

The key idea is to impose the granular pressure through a vertical Darcy flow. The wall at the bottom of the sediment is thus made of a fixed grid whose pores are smaller than the particles' size. The flow is driven by the fluid's hydrostatic pressure  $\rho_f g \Delta H$ , where  $\Delta H$  is the height difference between the fluid's free surface and the outlet of a tube connected to the bottom of the cell. Opening the tube and letting the fluid flow through the system gives rise to an additional vertical pressure gradient inside the sediment. The total pressure acting on the particles at depth  $z$  is:

$$P(z) = \phi \Delta \rho g z + C \rho_f g \frac{\Delta H}{L} z, \quad (3.1)$$

where  $L$  is the height of the sediment and  $C$  is a numerical constant accounting for the fact that part of the pressure gradient arising from the Darcy flow is balanced by a pressure loss in the grid. Therefore, everything happens as if the grains were subjected to an effective gravity:

$$g_{\text{eff}} = g \left( 1 + C \frac{\rho_f}{\phi \Delta \rho} \frac{\Delta H}{L} \right), \quad (3.2)$$

and the granular pressure simply writes as:

$$P(z) = \phi \Delta \rho g_{\text{eff}} z. \quad (3.3)$$

By varying the height  $\Delta H$  of the water outlet, we can therefore tune the effective gravity acting on the particles, and thus vary the granular pressure. The main advantage with this set-up is that the grid at the bottom of the cell is fixed, and glued to the side walls. Therefore, there can be no leakage at its edge, nor can there be any transient associated with its motion.

Now that we have described how to vary the granular pressure, let us explain how this configuration allows us to measure the macroscopic friction coefficient  $\mu$  of the suspension. The torque exerted by the grains on the inner cylinder (of radius  $a$ ) is:

$$\Gamma = 2\pi a \cdot \left( \int_0^h \sigma_{r\theta}(z) dz \right) \cdot a, \quad (3.4)$$

where  $h$  is the height of the inner cylinder that is immersed in the sediment and  $\sigma_{r\theta}$  is the tangential stress exerted by the particles in the sediment onto the inner cylinder. In the shear plane, the tangential stress  $\sigma_{r\theta}$  on the inner cylinder is given by  $\sigma_{r\theta} = \mu \sigma_{rr}$ , where  $\sigma_{rr}$  is the orthoradial stress and  $\mu$  is the suspension's macroscopic friction coefficient. We assume that the orthoradial stress in the shear plane is proportional to the vertical normal stress, which is the granular pressure, in the same plane:  $\sigma_{rr} = K P$ , where  $K$  is a constant which accounts for the stress anisotropy.

The torque is then given by:

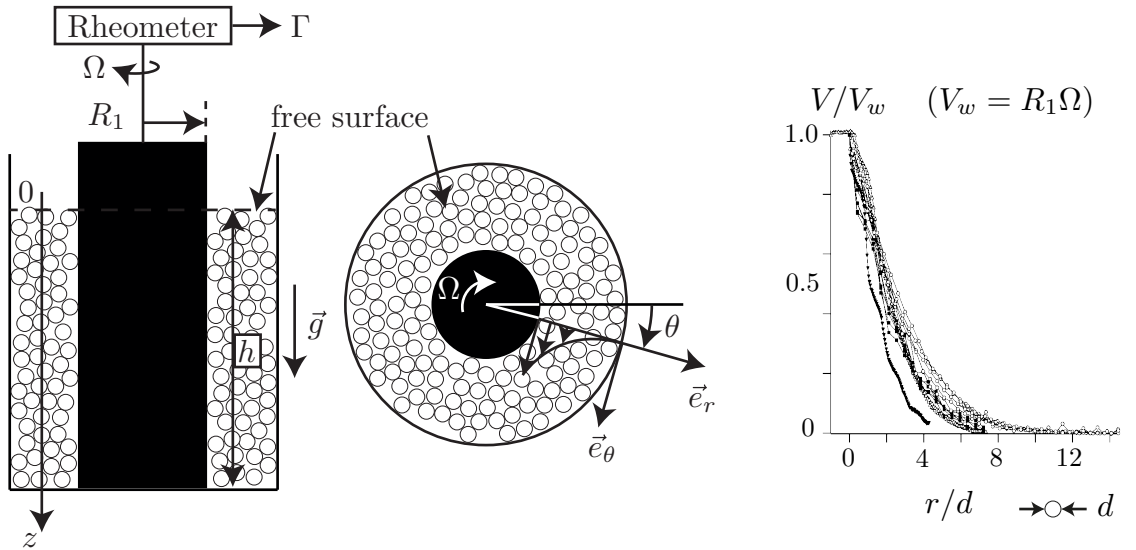
$$\Gamma = \mu \cdot K \pi a^2 \Delta \rho \phi \cdot g_{\text{eff}} \cdot h^2, \quad (3.5)$$

which yields:

$$\mu = \frac{\Gamma}{K \pi a^2 \Delta \rho \phi \cdot g_{\text{eff}} \cdot h^2}. \quad (3.6)$$

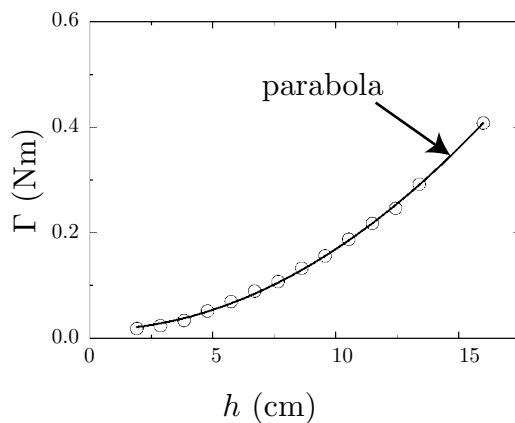
Thus, we have access to the macroscopic friction coefficient of the suspension through the measure  $\Gamma$ . However, in order to compute  $\mu$ , we need to determine the values of two numerical constants:  $C$ , which accounts for pressure drop through the grid, and  $K$ , which accounts for the stress anisotropy. In their work on the rheology of dense suspensions, Dbouk et al. found  $K = 2$  (see [32]). However, they studied suspensions with packing fractions ranging from 20% to 48%. In our experiments, we will focus on the suspension's behaviour in its quasi-static regime (see Section 3.2.2), where  $\phi \rightarrow \phi_c$ . We therefore use  $K = 1$  instead, as reported by Depkens et al. on a granular system (see [80]). The value of  $C$  will be discussed in Section 3.2.3.

Note that similar annular shear flow configurations (without the Darcy flow) have been used as a standard geometry to study dry granular matter (see [60,81]). In such a configuration, the flow in the quasi-static regime is localised near the inner cylinder and spans about 10 particle's diameter, as illustrated in Figure 3.3b. During his PhD, Da Cruz verified that  $\Gamma \propto h^2$  (see [81] and Figure 3.3c), as predicted by Equation (3.5). To vary the granular pressure, he also added a supplementary mass on the grains' free surface, and found that the torque increases

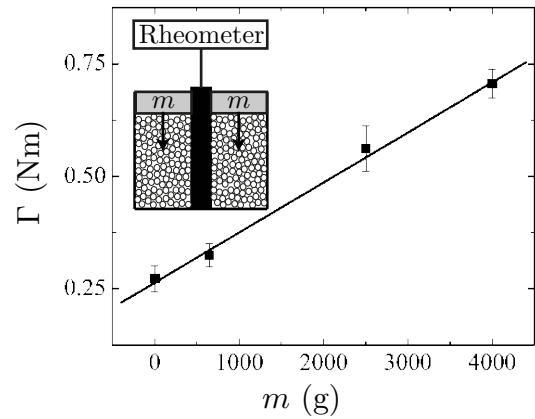


(a) General set-up.

(b) Quasi-static surface velocity profile. From [60].



(c) Evolution of the torque with the height of the granular sediment. From [81].



(d) Evolution of the torque with the applied mass. Adapted from [81].

Figure 3.3 – Annular shear flow configuration to study dry granular media.

linearly with this applied mass (see Figure 3.3d). These results validate our hypothesis that the granular pressure increases linearly with the depth:  $P \propto z$ .

We have described how the Darcytron allows to control the granular pressure and measure the suspension's friction coefficient. Note that this configuration is not an ideal rheometer. Indeed, as in the rotating drum configuration, the stress distribution is inhomogeneous, which can induce migration in the system. However, to access the microscopic frictional properties of a suspension, we only need to probe the quasi-static regime. In this limit, the sediment is homogeneous as  $\phi \rightarrow \phi_c$  and thus there cannot be any migration. In the sequel, we will therefore focus on the quasi-static limit and test the frictional transition model by measur-



ing the quasi-static friction coefficient as a function of the granular pressure. In a classical suspension of frictional beads, the macroscopic friction coefficient should be independent of the imposed granular pressure, because the microscopic friction coefficient  $\mu_p$  is constant. Conversely, for a shear-thickening suspension we expect an increase of the friction coefficient with the applied pressure when the suspension goes from a frictionless state to a frictional one.

## 3.2 Proof of concept with a classical suspension

As for the rotating drum experiments, we started by testing the Darcytron configuration with a classical suspension of frictional grains. In Section 3.2.1, we describe the experimental set-up and protocol we used. Section 3.2.3 is concerned with the first trials we conducted, the experimental difficulties we faced, and the solutions we found. Finally, we present the final results we obtained by conducting systematic experiments in Section 3.2.4.

### 3.2.1 Experimental set-up and protocol

The experimental set-up is sketched in Figure 3.4a. The outer cell of the Darcytron is made of PMMA plates glued and screwed together. It is approximately 12.5 cm high and has an horizontal surface of approximately 10 cm  $\times$  11 cm. The inner cylinder is a roughened metallic cylinder of diameter  $2a = 12.40 \pm 0.01$  mm. It is connected to an Anton–Paar MCR 501 rheometer. The grid used to prevent the grains from flowing into the tube at the bottom of the cell is made of a filter cloth placed between two metallic grids. The cloth has 220  $\mu$ m pores, and the metallic grids have 3 mm holes. These elements are maintained both together and in the cell by being screwed onto four PMMA pieces themselves glued to the cell (represented in grey in Figure 3.4a). The outer edge of the grid is sealed with silicone paste. The tube at the bottom of the cell, which allows us to control the height  $\Delta H$  of the water outlet, was chosen with a large diameter of 9.53 mm to minimise the pressure drop within it. Its end is equipped with a valve (not sketched) which allows to turn the Darcy flow on and off. In order to keep  $\Delta H$ , and therefore the granular pressure, constant during an experiment, it is necessary to refill the cell with the suspending fluid. This operation is done by hand with a beaker, as sketched in Figure 3.4a. Four differential pressure sensors are mounted on one of the side walls to measure the fluid’s pressure within the cell. This is done following the same technique as that used by Dbouk et al. in [32]. Four holes are drilled in the side wall. They are aligned vertically and evenly spaced, each one being set about 2 cm below the next (see Figure 3.4a). They are covered with a piece of filter cloth (with 220  $\mu$ m pores) in order to block the particles. The pressure sensors connected to these holes thus measure the difference  $P_i^{\text{mes}}$  between the fluid’s pressure  $P_i^{\text{fluid}}$  at depth  $h_i$  and the atmospheric pressure  $P^{\text{atm}}$  of the ambient air:  $P_i^{\text{mes}} = P_i^{\text{fluid}} - P^{\text{atm}}$ , which is directly the additional pressure induced in the fluid by the Darcy flow. The signals from these differential pressure sensors are recorded by a computer via a LabVIEW program developed by William Le Coz from IUSTI.

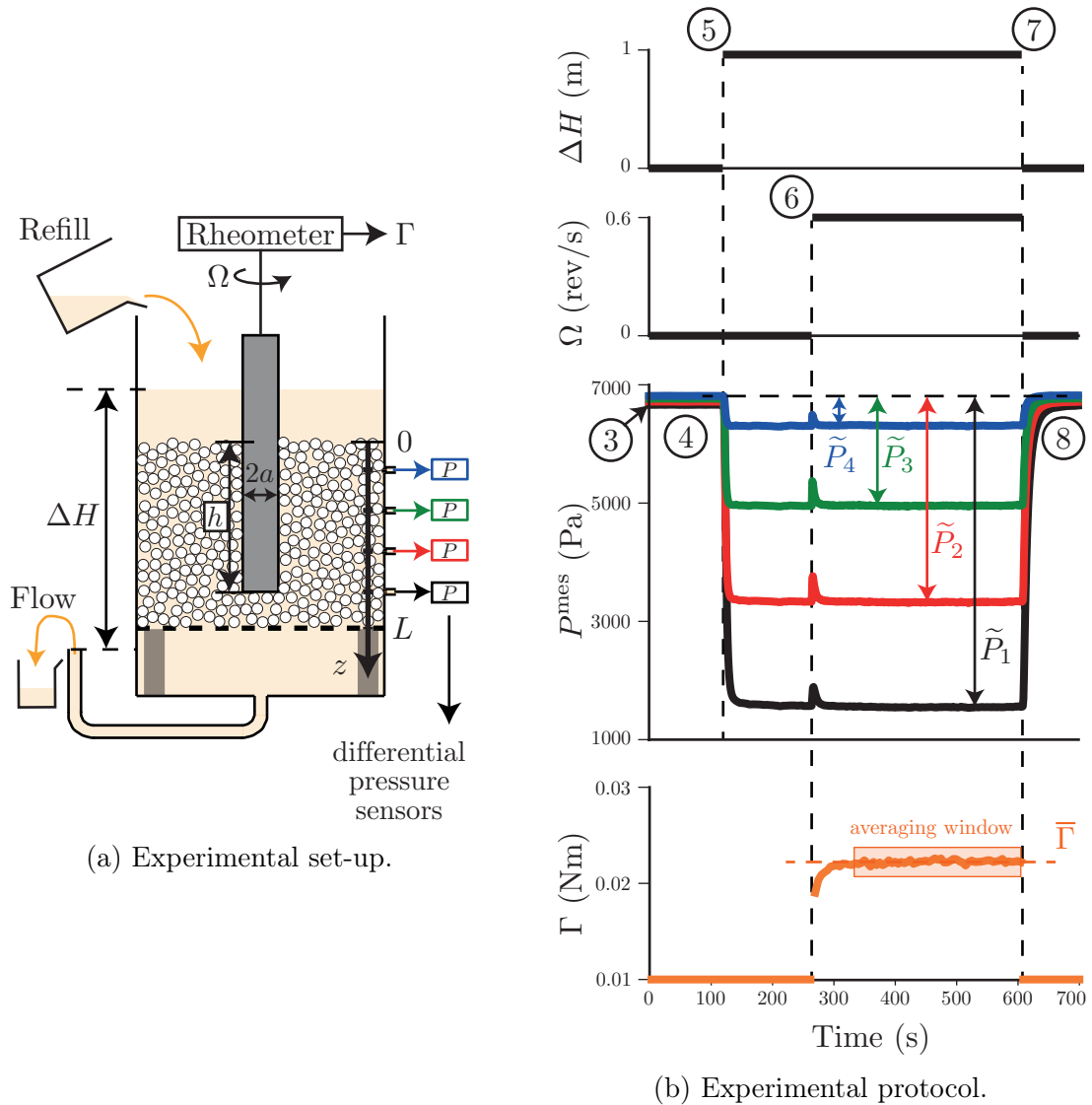


Figure 3.4 – The Darcytron: experimental set-up and protocol.

Figure 3.5 is a screenshot of the program's interface.

We used the same large glass beads as in Chapter 2 (diameter  $d = 487 \pm 72 \mu\text{m}$ ), in Ucon<sup>TM</sup> and water mixes. Once the suspending fluid was prepared, the Darcytron cell was slowly filled with it through the bottom tube. This way, we limited the apparition of air bubbles under the grid. For these experiments, we needed a large amount of clean beads, which was obtained using the following protocol.

1. First we immersed them in pure water, stirred the resulting mix with a clean metallic spoon, subjected it to ultrasound for 15 min, and threw away the supernatant fluid. We repeated this step a second time.
2. Then we put the beads in a 220  $\mu\text{m}$  sieve and thoroughly cleaned them with tap water and soap. At the end of this step we rinsed the beads with tap water until there was no more soap and put the beads in a clean beaker.

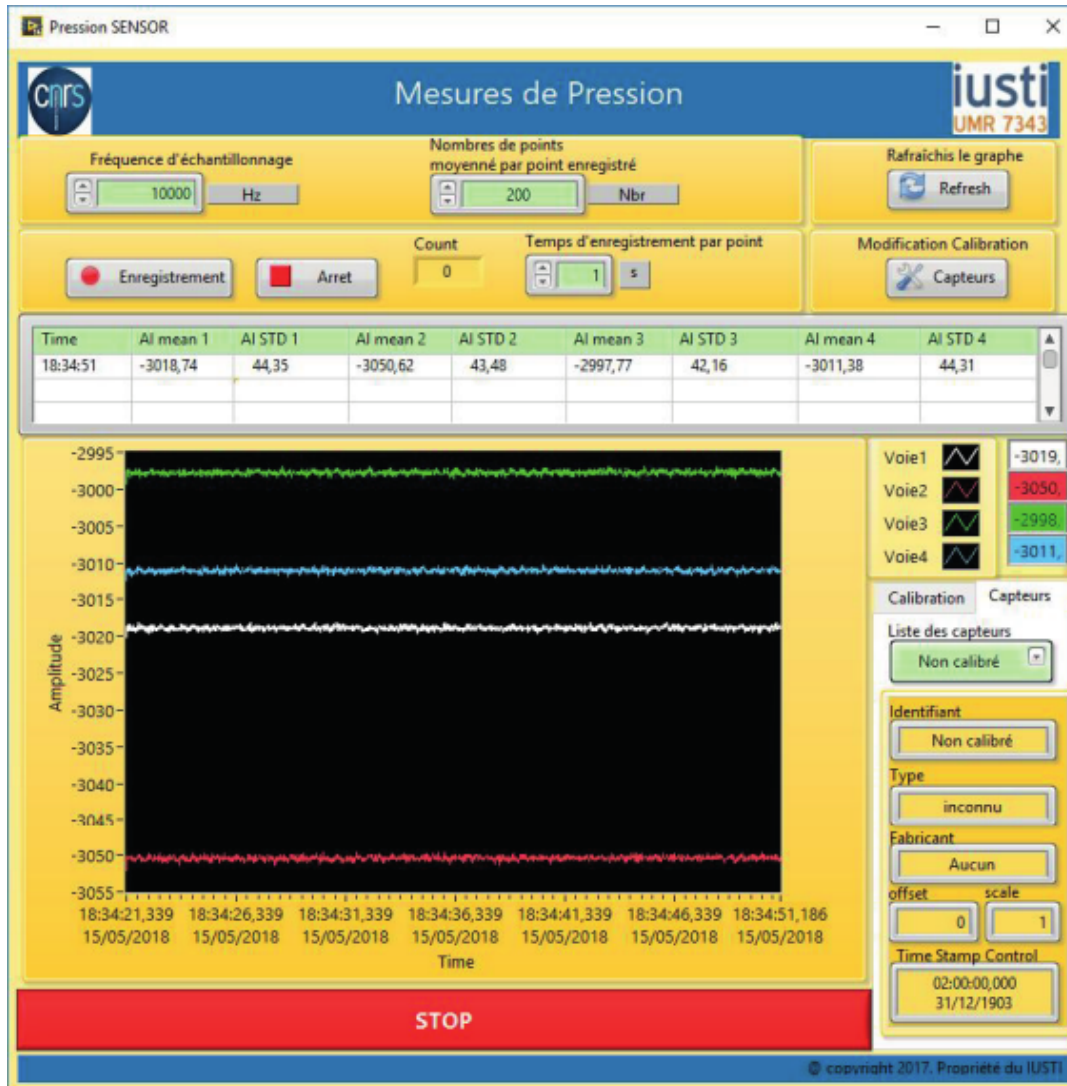


Figure 3.5 – Interface of the LabVIEW program used to record the fluid’s pressure in the Darcytron.

3. We then repeated the first step twice.
4. Finally we put the beads in the 220  $\mu\text{m}$  sieve and left them to dry in the laboratory oven at approximately 50  $^{\circ}\text{C}$ .

Once the beads were dry, we sieved them through a 800  $\mu\text{m}$  screen in order to eliminate beads aggregates that might have sintered in the oven. We then filled the cell with the beads by slowly sprinkling them on the fluid’s free surface and letting them settle, to avoid the formation of air bubbles. At the end of this operation, the sediment’s height was  $L = 8.4$  cm.

The experimental protocol is detailed below and in Figure 3.4b.

1. With the tube’s valve closed, position the tube’s end to the desired value of  $\Delta H$  (1 m in Figure 3.4b).

2. Stir the sediment with a clean metallic spoon, taking care not to incorporate air in the fluid.
3. Once the  $P^{\text{mes}}$  signals reach a steady state, start recording them (this corresponds to the initial time in Figure 3.4b).
4. Wait until the  $P^{\text{mes}}$  plateaus are sufficiently long to compute averaged values.
5. Open the valve to impose the Darcy flow.
6. When the  $P^{\text{mes}}$  signals have relaxed, start the rotation with the desired rotating speed  $\Omega$  and start recording the torque  $\Gamma$ .
7. Once  $\Gamma$  has reached a well-established plateau (of time average value  $\bar{\Gamma}$ ), close the valve, and stop the rotation and the recording of  $\Gamma$ .
8. When the  $P^{\text{mes}}$  signals seem to have relaxed back to their initial value, stop recording them.

Figure 3.4b shows that when the Darcy flow starts, a pressure gradient does develop in the fluid. As explained above, this pressure gradient is what we use to impose a granular pressure on the particles.

### 3.2.2 Definition of the average parameters

Since the shear rate  $\dot{\gamma}$  and the granular pressure  $P$  are not homogeneous in the system, we define spatially averaged macroscopic rheological quantities.

The average shear rate  $\bar{\dot{\gamma}}$  is:

$$\bar{\dot{\gamma}} = 2\pi\Omega \frac{a}{10d}. \quad (3.7)$$

since flowing layer in such an annular shear flow configuration is approximately 10 particles thick in the quasi-static regime (see [60] and Figure 3.3b).

The average granular pressure  $\bar{P}$  is:

$$\bar{P} = \frac{1}{h} \int_0^h P(z) dz. \quad (3.8)$$

The corresponding effective viscous number  $J_{\text{eff}}$  is:

$$J_{\text{eff}} = \frac{\eta_f \bar{\dot{\gamma}}}{\bar{P}}. \quad (3.9)$$

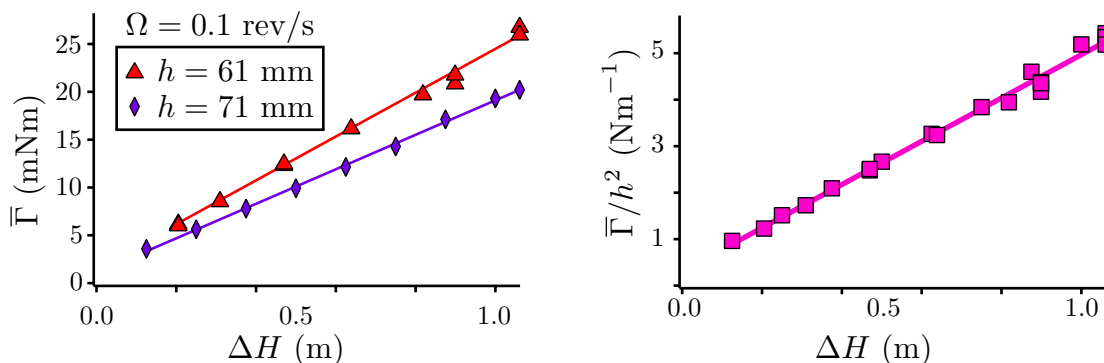
### 3.2.3 Preliminary experiments

The suspending fluid used in the preliminary experiments was prepared by mixing 961.12 g of pure water with 641.08 g of Ucon<sup>TM</sup>. After complete mixing, the resulting fluid was degassed using a vacuum pump. Its initial viscosity was  $\eta_f^0 = 385 \pm 5 \text{ mPa} \cdot \text{s}$ .

For the preliminary experiments, unless otherwise stated we didn't record  $P^{\text{mes}}$ . The experimental protocol was composed of step 1 followed by steps 4 through 6. Data was analysed by determining by eye, for each torque signal, the time at which the plateau started and the time at which it ended, and computing the mean value  $\bar{\Gamma}$  of this plateau.

### Evolution of the torque and validity of our hypotheses

Figure 3.6a presents the evolution of the torque for experiments conducted with different values of  $\Delta H$ , that is, for various intensities of the Darcy flow, and at two different immersion height  $h$  of the inner cylinder. We find that  $\bar{\Gamma} \propto \Delta H$ , as expected. These results are very promising since they indicate that the granular pressure can indeed be controlled by a Darcy flow. This validates the general concept of the Darcytron. Moreover, for the two immersion heights investigated, when the torque is normalised by  $h^2$  the data collapses on the same curve (see Figure 3.6b), suggesting that  $\bar{\Gamma} \propto h^2$  as expected.



(a) Evolution of the torque with  $\Delta H$ , for two values of  $h$ .

(b) Rescaling the torque by  $h^2$  (same data as in Figure 3.6a).

Figure 3.6 – Proof of concept of the Darcytron: the granular pressure can be controlled by imposing a vertical Darcy flow throughout the sediment. The solid lines are least square fits.

### Pressure loss in the grid

Following Equation (3.6), measuring the torque  $\bar{\Gamma}$  gives access to the macroscopic friction coefficient  $\mu$  of the suspension. As explained in Section 3.1, in order to compute  $\mu$  we need to determine the value of the constant  $C$  which accounts for the pressure loss in the grid. To do so, let us recall the expression of the pressure field in the sediment (Eq. (3.1)):

$$P(z) = \phi \Delta \rho g z + C \rho_f g \frac{\Delta H}{L} z.$$

The term  $C \rho_f g \frac{\Delta H}{L} z$  is the pressure gradient imposed by the vertical Darcy flow on the particles. One way to determine this pressure gradient, and thus the value

of  $C$ , is to measure directly the real pressure gradient inside the sediment using the differential pressure sensors. From the recorded signals of  $P^{\text{mes}}$ , we extract the relative fluid pressure  $\tilde{P}$  which we define as:

$$\tilde{P}(z) = P_{\Delta H, \Omega}^{\text{mes}}(z) - P_{\Delta H=0, \Omega=0}^{\text{mes}}(z),$$

as illustrated in Figure 3.4b. By subtracting the pressure when  $\Delta H = 0$  and  $\Omega = 0$ , we correct the measured pressure for its atmospheric and its hydrostatic parts;  $\tilde{P}(h_i)$  thus corresponds to the pressure at height  $h_i$  which arises in the fluid when the Darcy flow is turned on. Figure 3.7 shows an example of the evolution of  $\tilde{P}$  with  $z$ , for a given experiment conducted with  $\Delta H = 1$  m. We see that  $\tilde{P}$  decreases linearly with  $z$ , and can be well fitted by a line of slope  $p < 0$ . This fluid flow resulting from opening the valve presses the grains downward, thus generating an additional pressure of opposite side on the sediment. This additional pressure is therefore given by  $C\rho_f g\Delta H/L = -p$ . This yields:

$$C = \frac{-pL}{\rho_f g\Delta H}. \quad (3.10)$$

Varying  $\Delta H$  with  $\Omega = 0$ , we measured the slope  $p$  as in Figure 3.7 and obtained  $C \simeq 0.7$  using Eq.(3.10). This means that about 30 % of the pressure  $\rho_f g\Delta H$  imposed by the Darcy flow is balanced by the presence of the grid, while 70 % of this pressure is actually acting on the particles.

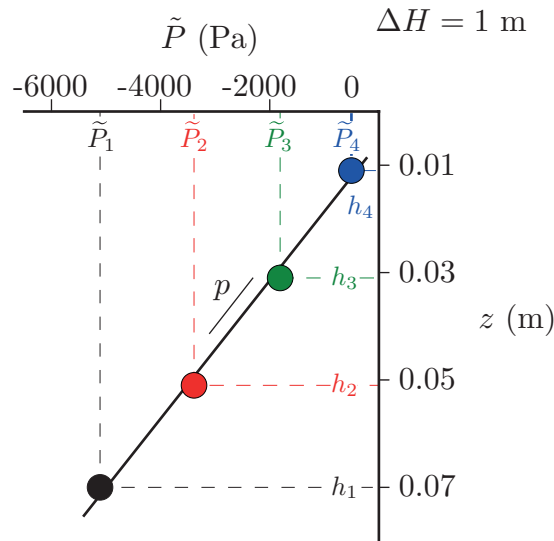


Figure 3.7 – Fluid’s pressure induced by the Darcy flow, directly measured with the differential pressure sensors, for  $\Delta H = 1$  m.

To strengthen our confidence in this measurement, we propose a complementary way to evaluate the value of the constant  $C$ . Darcy’s law combined with the conservation of the fluid’s volumic flow rate across the sediment and the grid yield:

$$\frac{k_s}{\eta_f} \frac{\Delta \tilde{P}_{\text{sed}}}{L} = \frac{k_g}{\eta_f} \frac{\Delta \tilde{P}_{\text{grid}}}{e} \quad (3.11)$$

where  $k_s$  and  $k_g$  are respectively the sediment's and the grid's permeability,  $L$  is the sediment's height,  $e$  is the grid's thickness, and  $\Delta\tilde{P}_{\text{sed}}$  and  $\Delta\tilde{P}_{\text{grid}}$  are respectively the pressure differences in the sediment and in the grid. We neglect the pressure drop in both the fluid layer above the sediment and the tube at the bottom of the cell. The continuity of the pressure field in the fluid then gives:

$$\Delta\tilde{P}_{\text{sed}} + \Delta\tilde{P}_{\text{grid}} = \rho_f g \Delta H. \quad (3.12)$$

Combining Equations (3.11) and (3.12) leads to:

$$\Delta\tilde{P}_{\text{sed}} = \rho_f g \Delta H \frac{1}{1 + \frac{e}{k_g} \frac{k_s}{L}},$$

which yields:

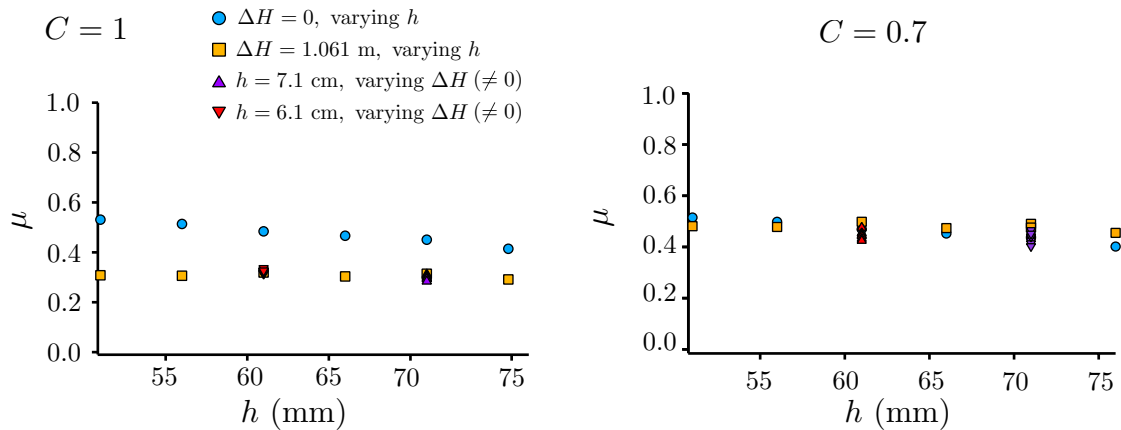
$$\tilde{P}(z) = \rho_f g \frac{\Delta H}{L} \frac{1}{1 + \frac{e}{k_g} \frac{k_s}{L}} \cdot z. \quad (3.13)$$

By identification with the second term in Equation (3.1), this gives:

$$C = \frac{1}{1 + \frac{e}{k_g} \frac{k_s}{L}}. \quad (3.14)$$

The sediment's permeability, which depends on its packing fraction  $\phi$ , can be estimated using Carman–Kozeny's formula (see [55]):

$$k_s(\phi) = \frac{(1 - \phi)^3 d^2}{A\phi^2},$$



(a) Computing  $\mu$  with  $C = 1$ , that is, without correcting for the grid.

(b) Computing  $\mu$  with  $C = 0.7$  as measured.

Figure 3.8 – Effect of the pressure loss in the grid on the computation of the suspension's macroscopic friction coefficient. Measurements conducted with  $\Omega = 0.1 \text{ rev} \cdot \text{s}^{-1}$ .

with  $A$  between 150 and 180, depending on the model. Assuming that  $\phi = 58\%$  and using  $A = 165$ , we get  $k_s \simeq 3 \times 10^{-10} \text{ m}^2$ . To obtain the grid's permeability, we conducted a separate experiment, measuring the flow rate through the grid without particles in the cell. We obtained  $k_g/e \simeq 5.4 \times 10^{-9} \text{ m}$ . Using these values in Equation (3.14), we obtain  $C \simeq 0.6$  (with  $L = 8.4 \text{ cm}$ ). This estimate is in good agreement with the previous direct measurement.

The validity of this correction for the pressure loss in the grid can also be appreciated directly through its effect on the computed values of  $\mu$ . As can be seen in Figure 3.8a, using  $C = 1$  in Equation (3.6) for the computation of  $\mu$  leads to a clear differentiation between any data point at  $\Delta H \neq 0$  and the data points at  $\Delta H = 0$ . Conversely, when using  $C = 0.7$  as measured, thus correcting for the pressure loss in the grid, the values of  $\mu$  obtained for different  $\Delta H$  all collapse.

It is interesting at this point to estimate the orders of magnitude of the two different contributions to the granular pressure involved in our system. The mean hydrostatic pressure arising from the weight of the grains in the sediment is  $\phi \Delta \rho g h / 2$ , which is approximately 300 Pa. The mean pressure imposed by the Darcy flow is  $C \rho_f g h \Delta H / (2L) \sim 2900 \text{ Pa}$  (with  $\Delta H = 1 \text{ m}$ ), about ten times larger than the granular hydrostatic pressure. In practice, this means that for measurements conducted with  $\Delta H$  larger than 0.1 m, the granular pressure is dominated by the effect of the Darcy flow.

### Identification of the quasi-static regime

As explained in Section 3.2.2, we want to measure  $\mu$  as a function of  $\bar{P}$  in the quasi-static regime, that is as  $J_{\text{eff}} \rightarrow 0$ . To identify this regime, we conducted a large number of experiments, varying the height  $\Delta H$  of the water outlet, the immersed length of the inner cylinder  $h$ , and its rotating speed  $\Omega$ . The results are presented in Figure 3.9b. We recover the general form of  $\mu(J)$  as measured in other configurations (see for instance [28]). As the effective viscous number decreases, so does the suspension's macroscopic friction coefficient. Below  $J_{\text{eff}} = 10^{-3}$ , it eventually reaches a plateau corresponding to its quasi-static value. In the inset of Figure 3.9b, we zoomed in on the data to show that for  $J_{\text{eff}} < 10^{-4}$ , the measurements become less reproducible. We find that in general, measurements are more robust when conducted at large  $\Delta H$ , that is at large granular pressure. For a given value of  $J_{\text{eff}}$ , this corresponds to experiments conducted at large rotating speed. It thus seems that experiments conducted at very low rotating speeds, and therefore over a long time, result in less reproducible data. For the systematic results presented in Section 3.2.4, we thus imposed  $J_{\text{eff}} \in [0.5 \times 10^{-3}, 1.2 \times 10^{-3}]$ , in order to be in the quasi-static regime and obtain reproducible results.

### Evaporation

Note that as already stated, the suspending fluid used is a mixture of Ucon<sup>TM</sup> oil and water. It is therefore sensitive to evaporation, which can, in the long run, considerably affect its viscosity. To avoid this, in the following systematic experiments the fluid was regularly renewed, and we also covered the set-up with a lid equipped with a water trap.



- |  |   |
|--|---|
| ◆ $\Delta H = 0$ , $h = 7.6$ cm, varying $\Omega$        | ■ $\Delta H = 1.061$ m, $\Omega = 0.1$ rev/s, varying $h$ |
| ● $\Delta H = 0$ , $h = 7.6$ cm, varying $\Omega$        | ● $\Delta H = 0$ , varying $h$ and $\Omega$               |
| ● $\Delta H = 0$ , $h = 6.6$ cm, varying $\Omega$        | ◆ $\Delta H = 0$ , $h = 7.1$ cm, varying $\Omega$         |
| ● $\Delta H = 0$ , $h = 5.6$ cm, varying $\Omega$        | ● $\Delta H = 0$ , $h = 7.1$ cm, varying $\Omega$         |
| ● $\Delta H = 0$ , $\Omega = 0.1$ rev/s, varying $h$     | ● $\Delta H = 1.061$ m, $h = 7.1$ cm, varying $\Omega$    |
| ▲ $\Omega = 0.1$ rev/s, $h = 7.1$ cm, varying $\Delta H$ | ● $\Delta H = 0.5$ m, $h = 7.1$ cm, varying $\Omega$      |
| ▲ $\Omega = 0.1$ rev/s, $h = 6.1$ cm, varying $\Delta H$ | ● $\Delta H = 0.25$ m, $h = 7.1$ cm, varying $\Omega$     |

(a) Plot key for Figure 3.9b.

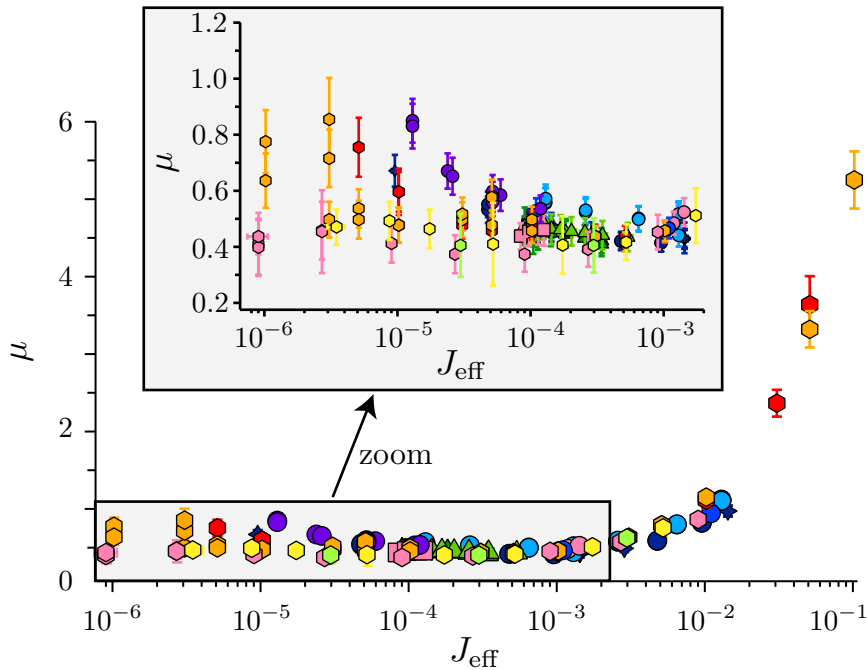

 (b) Macroscopic friction coefficient  $\mu$  as a function of the effective viscous number  $J_{\text{eff}}$ , for all preliminary experiments.

Figure 3.9 – Identification of the quasi-static regime.

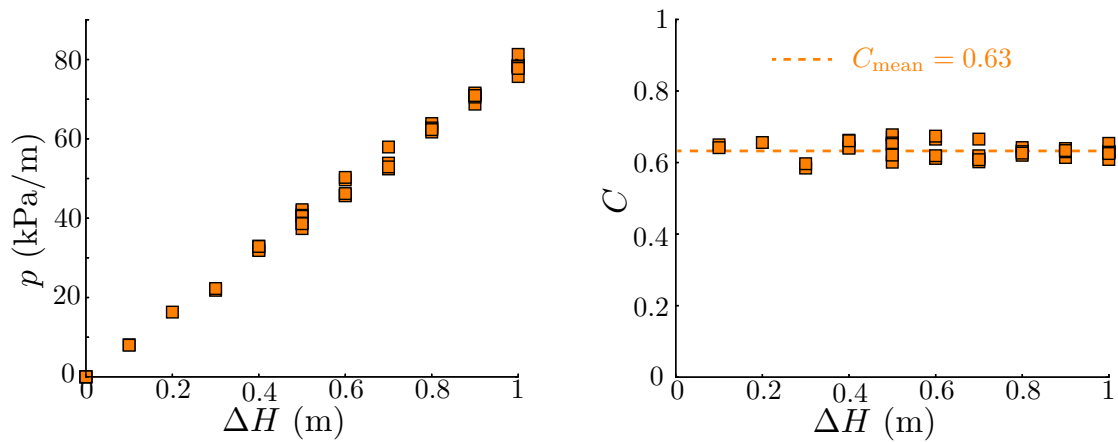
### 3.2.4 Systematic results

We have shown how to correct our measurements to account for the pressure loss induced by the grid, identified the quasi-static regime and solved the problem of evaporation. We thus have a working prototype that we can use to perform a systematic characterisation of the frictional behaviour of our classical frictional suspension of large glass beads. Between the end of the preliminary experiments and the experiments we present in this section, we emptied the Darcytron cell, cleaned it thoroughly, and cleaned the beads again. On average, the suspending fluid's viscosity throughout the experiments was  $\eta_f = 450 \pm 110$  mPa · s. Experiments were conducted at  $h = 71$  mm, for various values of  $\Delta H$ , that is, various intensities of the Darcy flow. For each value of  $\Delta H$ , we set the rotating speed so

that  $J_{\text{eff}} \in [0.5 \times 10^{-3}, 1.2 \times 10^{-3}]$ .

Unless otherwise specified, data analysis was completely automated. We wrote Python programs that read the different data files, recovered the relevant data, and computed all the relevant physical quantities. In particular, these programs estimate the slope  $p$  of the fluid's pressure  $\tilde{P}$  measured with the differential pressure sensors for each experiment, which in turn gives the value of  $C$  using Equation (3.10).

Figure 3.10 shows the evolutions of  $p$  and  $C$  with varying  $\Delta H$ . As expected, we find that the slope  $p$  of the imposed pressure gradient increases linearly with  $\Delta H$ . The value of  $C$  slightly varies from experiment to experiment, which could be explained by the presence of more or less air bubbles in the system. Indeed, this would change the relative permeabilities of the sediment and the grid.



(a) Pressure gradient as a function of  $\Delta H$ . (b) Corresponding values of  $C$  computed using Eq. (3.10)

Figure 3.10 – Evolution of the slope  $p$  of the pressure gradient induced by the Darcy flow and of the corresponding constant  $C$  as a function of  $\Delta H$ .

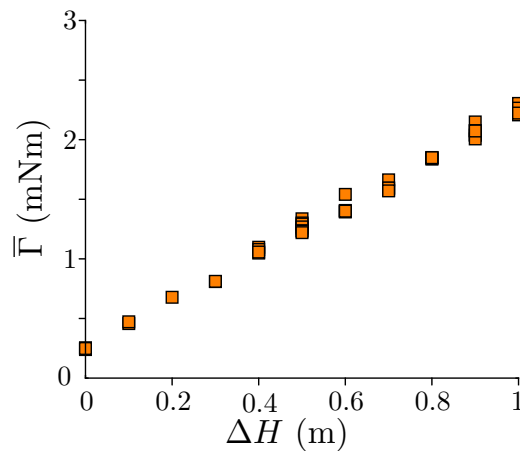
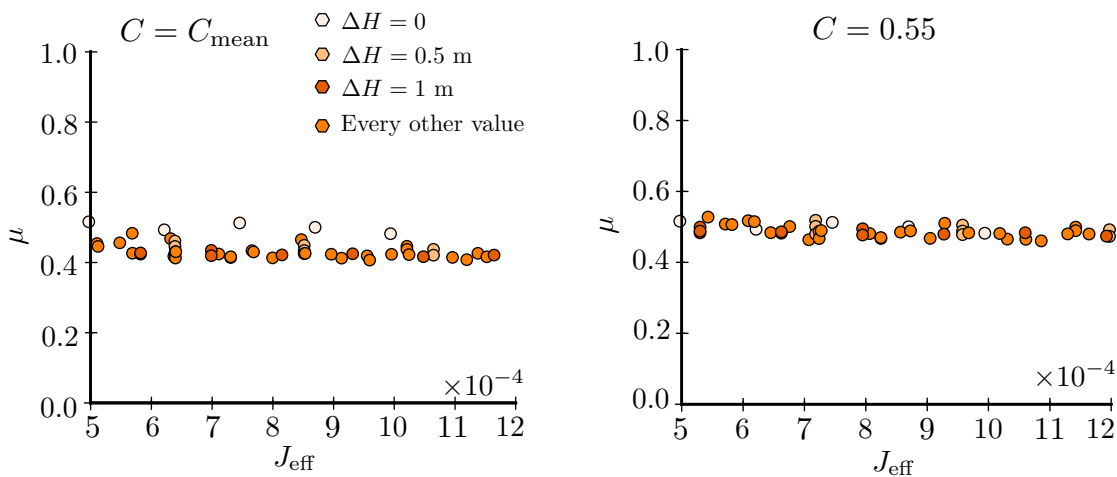


Figure 3.11 – Measured torque  $\bar{\Gamma}$  as a function of the height  $\Delta H$  of the water outlet.

Figure 3.11 shows the evolution of the measured torque  $\bar{\Gamma}$  when varying the height  $\Delta H$  of the water outlet. Again, as predicted by Equation (3.5), we find that  $\bar{\Gamma} \propto \Delta H$ .

From the measurements of  $C$  and  $\bar{\Gamma}$ , we can compute the suspension's macroscopic friction coefficient  $\mu$ . Figure 3.12a shows its evolution as a function of the effective viscous number  $J_{\text{eff}}$ , using  $C = C_{\text{mean}}$  to correct for the pressure loss in the grid. As expected for this range of  $J_{\text{eff}}$ , the system is in the quasi-static regime and  $\mu$  is constant. The experiments conducted with  $\Delta H = 0$  slightly stand out from the other data points. We obtain a better collapse using  $C = 0.55$  instead of  $C_{\text{mean}}$ , as illustrated in Figure 3.12b. It seems that the pressure gradient computed from the differential pressure sensors slightly overestimates the one truly acting on the particles. Indeed, we assumed that the pressure field induced by the Darcy flow is uniform in the radial direction (see Section 3.1). A slight deviation from this could explain why the pressure gradient felt by the particles at the center of the cell is different from the one measured at the wall, where the sensors are located. In the sequel, we will thus use  $C = 0.55$ , which gives a better collapse of our data.



(a) Evolution of  $\mu$  with  $J_{\text{eff}}$ , using  $C = C_{\text{mean}} = 0.63$ .

(b) Same data using  $C = 0.55$ .

Figure 3.12 – Quasi-static macroscopic friction coefficient of a classical frictional suspension of large glass beads (diameter  $d = 487 \pm 72 \mu\text{m}$ ) in a viscous Newtonian fluid (viscosity  $\eta_f = 450 \pm 110 \text{ mPa} \cdot \text{s}$ ).

We can finally present the evolution of the quasi-static macroscopic friction coefficient  $\mu$  when the granular pressure  $\bar{P}$  is varied. As expected for this system of macroscopic frictional particles,  $\mu$  is independent of the applied granular pressure (see Figure 3.13). The measured value of  $\mu$  is  $\mu = 0.49$ , in reasonable agreement with the value obtained with the rotating drum experiments ( $\mu = 0.47$ ).

Overall, these results validate the concept of the Darcytron: by imposing a Darcy flow of adjustable intensity, we are able to impose and control the pressure acting on the particles, while measuring the friction coefficient of the suspension.

The results on the classical frictional suspension, for which the friction coefficient is constant, will also continue a benchmark for our study of shear-thickening suspensions, where we expect a frictional transition to occur. Before presenting this study, we discuss below a discrepancy we observed in the vertical granular pressure profile compared to the hydrostatic prediction.

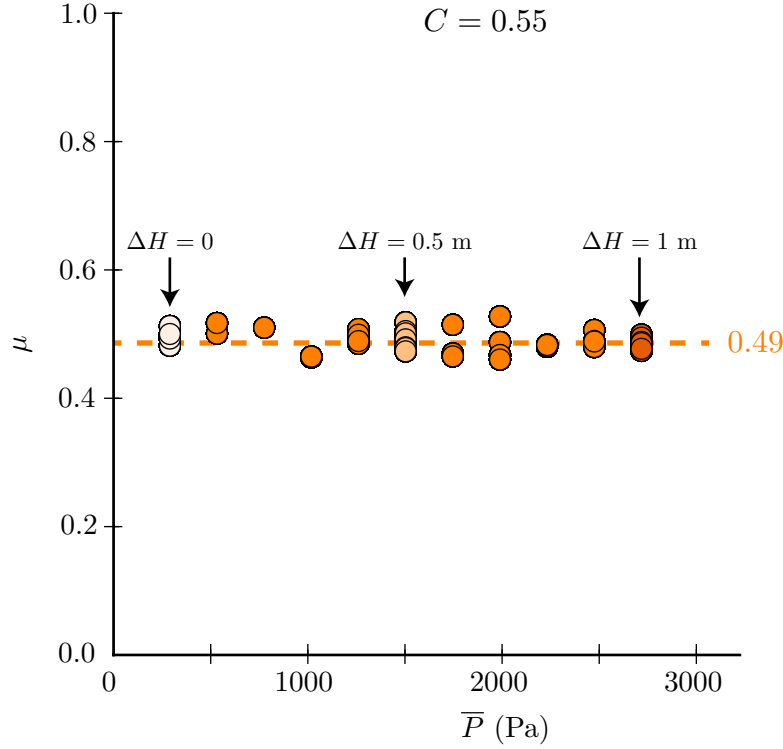


Figure 3.13 – Evolution of the macroscopic coefficient  $\mu$  of a classical suspension of large frictional glass beads (diameter  $d = 487 \pm 72 \mu\text{m}$ ) in a viscous Newtonian fluid (viscosity  $\eta_f = 450 \pm 110 \text{ mPa} \cdot \text{s}$ ) with the average granular pressure  $\bar{P}$ .

### 3.2.5 Discussion

In Section 3.2.3, using data measured at two different values of the immersed length  $h$  of the inner cylinder, we stated that apparently  $\bar{\Gamma} \propto h^2$  as predicted by Equation (3.5) (see Figure 3.6). We conducted additional experiments in order to determine the exact relation between  $\bar{\Gamma}$  and  $h$ , and check the validity of the hypothesis leading to this scaling (which is that  $P \propto z$ ). Imposing  $\Delta H = 0$  (no Darcy flow) and  $\Omega = 0.05 \text{ rev} \cdot \text{s}^{-1}$ , we measured  $\bar{\Gamma}$  as we decreased then increased  $h$ . These experiments were analysed manually. Figure 3.14 shows our data in both linear and logarithmic scales. As we can see in Figure 3.14b, the relation is well-fitted by a power law  $\bar{\Gamma} \propto h^{1.53}$ , which differs from the expected hydrostatic behaviour  $\bar{\Gamma} \propto h^2$  (as reported for example by Da Cruz in [81], see Figure 3.3c).

In order to explain this discrepancy between the measured behaviour of  $\bar{\Gamma}$  and the predictions of the hydrostatic model, we assumed that there were recirculation

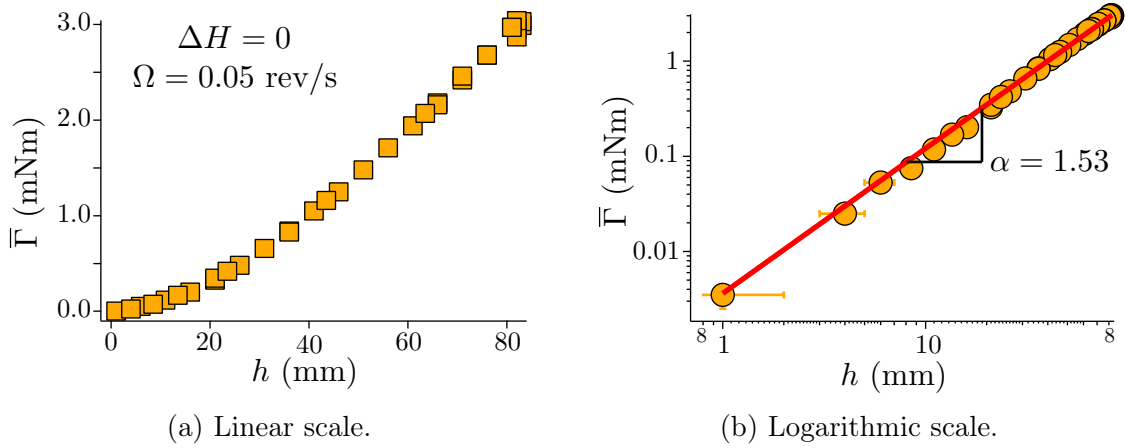


Figure 3.14 – Evolution of the torque  $\bar{\Gamma}$  with the immersed length  $h$  of the inner cylinder, for  $\Delta H = 0$  (no Darcy flow). Solid line in Fig. 3.14b: least squares fit.

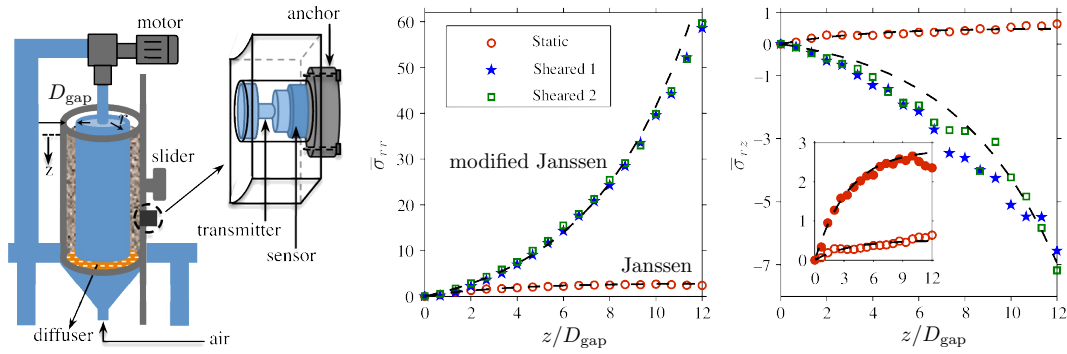


Figure 3.15 – Evolution of the radial and orthoradial stresses with the rescaled depth, for a suspension in a Couette cell. From [82].

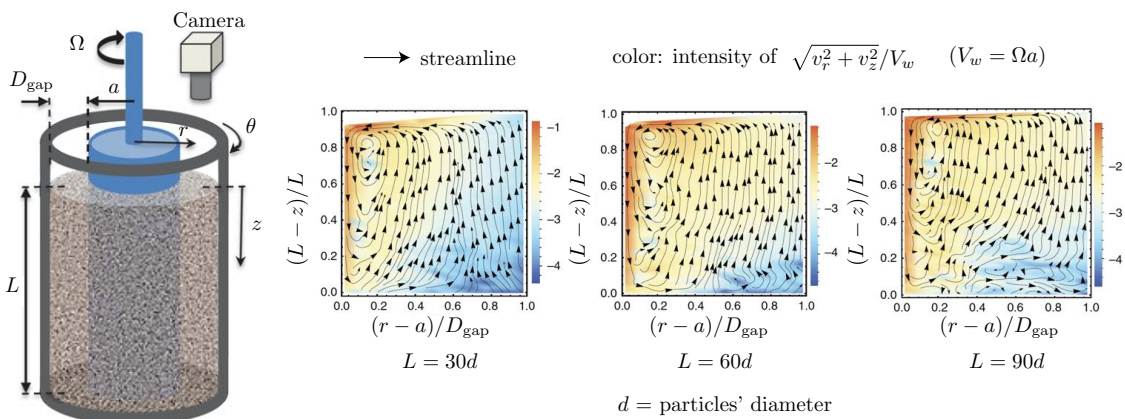


Figure 3.16 – Recirculation rolls in a suspension sheared in a Couette cell. From [83].

rolls in the cell as a result of the shear. This was in part inspired by the work of Mehandia et al. [82] and Krishnaraj and Nott [83]. In [82], the authors show

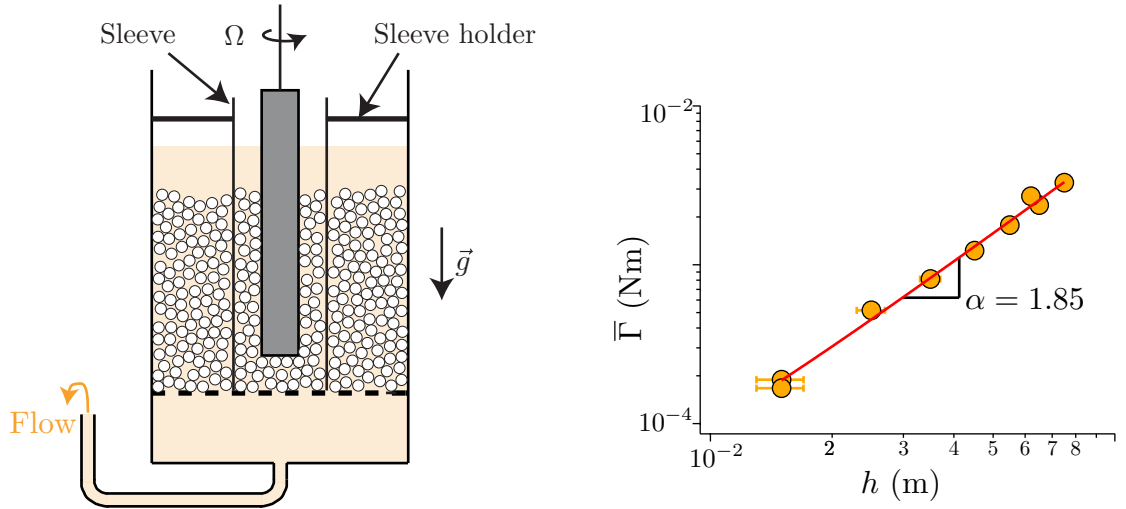
that the stress distributions for a suspension in a Couette cell are not the same as that obtained for a fluid, neither do they follow isotropic plasticity predictions. They argue that this comes from the existence of an anisotropic microstructure ‘which evolves slowly when gravity is perpendicular to the shear plane’. This is illustrated in Figure 3.15, where the authors plot the evolution of the mean radial and orthoradial stresses with the rescaled vertical position. In [83], the authors use a similar Couette cell to evidence the development of a steady state secondary flow consisting in recirculation rolls, as illustrated in Figure 3.16.

The measured scaling, which is close to  $\bar{\Gamma} \propto h^{3/2}$ , suggests that instead of increasing linearly with the depth, the granular pressure  $P$  is in fact proportional to its square root:  $P \propto \sqrt{z}$ . Dimensionally, this requires the introduction of the square root of another length in order to construct a pressureA relevant characteristic length to introduce in our model is the size  $D_{\text{gap}}$  of the gap between the inner and the outer cylinder. Putting these elements together, we get a new expression for the granular pressure:

$$P = \phi \Delta \rho g \sqrt{D_{\text{gap}}} \cdot \sqrt{z}, \quad (3.15)$$

which yields:

$$\bar{\Gamma} = \mu \cdot \frac{4}{3} \pi a^2 \phi \Delta \rho g \sqrt{D_{\text{gap}}} \cdot h^{3/2}. \quad (3.16)$$



(a) The Darcytron cell with its  $2.5 \text{ cm} \times 2.5 \text{ cm}$  sleeve.

(b) Evolution of the torque  $\bar{\Gamma}$  with the immersed length  $h$  of the inner cylinder, for  $\Delta H = 0$  (no Darcy flow), with the sleeve. Solid line: least squares fit.

Figure 3.17 – Effect of the Darcytron cell’s aspect ratio.

We conducted experiments in order to test the role of  $D_{\text{gap}}$  and the potential influence of secondary rolls on the vertical pressure gradient. The radius of the cell was reduced with a PMMA sleeve of horizontal surface  $2.5 \text{ cm} \times 2.5 \text{ cm}$ , centered on the inner cylinder, and held in place by a PMMA sleeve holder, as sketched

in Figure 3.17a. We then measured the evolution of  $\bar{\Gamma}$  with  $h$  in this new configuration. The results from these experiments are shown in Figure 3.17. The data seems to follow a power law, which this time can be well fitted by  $\bar{\Gamma} \propto h^{1.85}$ . When reducing the gap between the inner and the outer cylinders, the exponent thus seems to approach that expected for a linear hydrostatic pressure situation, which would yield  $\bar{\Gamma} \propto h^2$ . Unfortunately, we lacked the time to further investigate this dependency. Our preliminary data suggests that the cell's aspect ratio affects the vertical stress distribution within the sheared granular layer

Note that this dependency of the relation between  $\bar{\Gamma}$  and  $h$  on the aspect ratio of the cell does not undermine our approach. Indeed, our systematic experiments were performed for a fixed value of  $h$ . Moreover, for  $\Delta H > 0.1$  m, the effect of the hydrostatic pressure arising from the weight of the particles is negligible relative to that imposed by the Darcy flow (see Section 3.2.3). Though the exact dependency of  $\bar{\Gamma}$  on  $h$  remains to be determined, assuming  $\bar{\Gamma} \propto h^2$  has only a minor effect on our measurements.

### 3.3 First results with silica suspensions

The results presented in the sequel are preliminary results obtained with a suspension of silica particles in pure water. We had little time to study this system, which furthermore happened to behave in an unexpected way. Nonetheless, we were able to gather these results in order to outline the expected frictional transition. We also present some experiments whose results we do not fully understand, but whose interesting behaviour will be the object of future studies.

#### 3.3.1 Experimental set-up and protocol

We use the same silica particles as in Chapter 2, with  $d = 23.56 \pm 1.06$   $\mu\text{m}$ . They were immersed in pure water to maximise the range of the repulsive force. The Darcytron cell has exactly the same design as that used for the large glass beads, but its dimensions were scaled down to 25 mm  $\times$  25 mm for its horizontal surface and 60 mm for its height. We use the same inner cylinder. The gap between the inner and outer cylinders is thus  $D_{\text{gap}} = 6.3$  mm, which corresponds to approximately  $265d$ . The tube at the bottom of the cell has an inner diameter of 3.22 mm. The grid is made of a filter cloth with 10  $\mu\text{m}$  pores placed between two metallic grids with 3 mm holes. The same differential pressure sensors are placed at different heights to measure the fluid's pressure at the wall. In order to impose a constant value of  $\Delta H$ , we used a burette dripping directly into the cell.

We first measured the grid's permeability  $k_g/e = 1.05 \times 10^{-9}$  m. Using the Carman–Kozeni formula with  $A = 165$  and  $\phi = 60\%$ , we estimated the sediment's permeability to be  $k_s = 6 \times 10^{-13}$  m<sup>2</sup>. These values, together with a sediment's height of  $L = 26$  mm, yield  $C = 0.98$ . After cleaning the beads by subjecting them to ultrasound three times, throwing the supernatant fluid and replacing it by fresh pure water every time, we incorporated the beads into the cell until they formed a sediment of height  $L = 26$  mm. Through the measure of the flow rate for

$\Delta H = 9.8$  cm, we obtained  $C = 0.99$ , in good agreement with the previous estimate. This value of  $C$  very close to 1 means that in this new set-up, the pressure loss in the grid is negligible. In the sequel, we will use  $C = 1$ .

The experimental protocol, described below, is essentially the same as for the experiments with the large glass beads.

1. With the tube's valve closed, position its end at the desired value of  $\Delta H$ .
2. Stir the sediment using a plexiglass rod.
3. Start recording  $P^{\text{mes}}$ .
4. Wait at least 15 min to ensure that sedimentation is over.
5. Open the valve to impose the Darcy flow.
6. When the  $P^{\text{mes}}$  signals have relaxed, start the rotation with the desired rotating speed  $\Omega$  and start recording the torque  $\Gamma$ .
7. Once  $\Gamma$  has reached a well-established plateau, close the valve, and stop the rotation and the recording of  $\Gamma$ .
8. When the  $P^{\text{mes}}$  signals seem to have relaxed back to their initial value, stop recording them.

As explained in Chapter 2, silica particles immersed in pure water acquire a negative surface charge, which gives rise to an electrostatic repulsive force between them. This force should prevent them from coming into solid contacts. In this case, the particles should behave as if they were frictionless. Conversely, under large granular pressure, the repulsive force should be overcome and the particles should therefore recover a frictional behaviour.

In our setting, the granular pressure increases with the depth  $z$  within the sediment as:

$$P(z) = \phi \Delta \rho g z + \rho_f g \frac{\Delta H}{L} z. \quad (3.17)$$

There is therefore a critical depth  $z_c$  at which the granular pressure is equal to the repulsive pressure  $P_{\text{rep}}$ . The latter can be evaluated from Equation (2.8) in Chapter 2 as:

$$P_{\text{rep}} = \frac{4 F_0}{\pi d} \exp\left(-\frac{2l_r}{\lambda_D}\right). \quad (3.18)$$

Using  $F_0/d \simeq 1$  mN · m,  $l_r = 3.73$  nm, and  $\lambda_D \simeq 1$  μm in pure water, yields  $P_{\text{rep}} = 53$  Pa. The system should behave as a sediment of frictionless grains above the critical depth  $z_c$ , and recover a frictional behaviour below it. When no Darcy flow is imposed, that is, when  $P(z) = \phi \Delta \rho g z$ , we obtain  $z_c \simeq 10$  mm using  $\phi = 60\%$ . This means that in order to probe the frictionless state, the immersion height  $h$  of the inner cylinder into the sediment should be less than 10 mm. Note that for  $h \sim 10$  mm, we can no longer neglect the contribution of friction on the bottom-end of the inner cylinder as we implicitly did when working with the large glass beads. Indeed, the aspect ratio of the immersed part of the cylinder is now  $h/2a \sim 1$ . Therefore,



we corrected the expression of the torque to account for this contribution. This leads to:

$$\Gamma = \mu \cdot 2\pi a^2 \phi \Delta \rho g \frac{h^2}{2} \left( 1 + \frac{2a}{3h} \right). \quad (3.19)$$

In the sequel, the macroscopic friction coefficient will be computed using this expression.

### 3.3.2 First experiments: the frictional transition

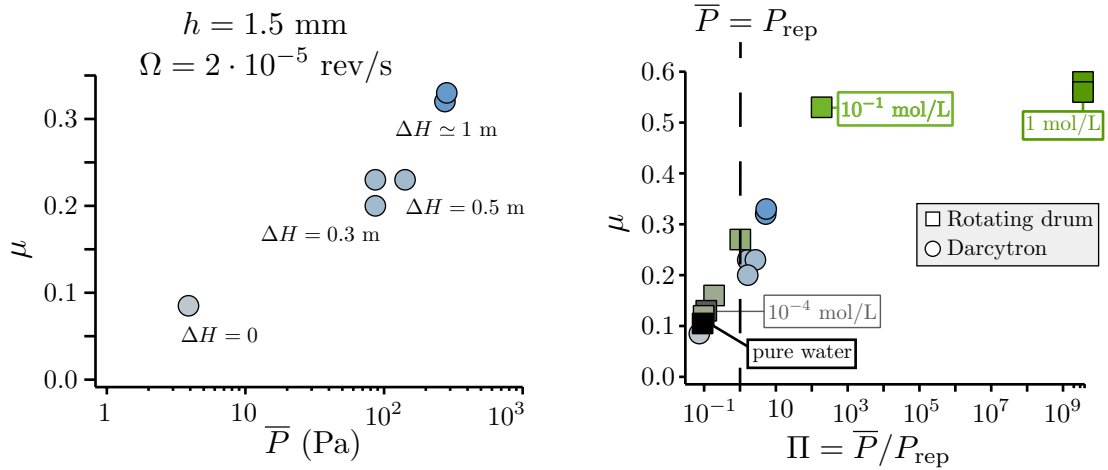
We first present the most relevant results we obtained regarding the frictional transition. They correspond to experiments conducted at a rotating speed  $\Omega = 2 \times 10^{-5} \text{ rev} \cdot \text{s}^{-1}$  and a small immersion height  $h = 1.5 \text{ mm}$ , with different values of  $\Delta H$  in order to change the granular pressure. As shown in Figure 3.18a, when  $\Delta H = 0$ , which corresponds to the lowest achievable granular pressure in our Darcytron set-up, the suspension's macroscopic friction coefficient is  $\mu \simeq 0.1$ . This value is very small, and corresponds to the expected macroscopic friction coefficient of a suspension of frictionless particles. Remarkably, we find that upon increasing the granular pressure by increasing  $\Delta H$ ,  $\mu$  also progressively increases. This is precisely the behaviour predicted by the frictional transition model for such a suspension where particles interact through both a short-range repulsive force and frictional contacts. The friction coefficient reaches  $\mu \simeq 0.32$  for  $\Delta H \simeq 1 \text{ m}$ . Note that the mean pressure is varied between 4 and 350 Pa, thus spanning values both below and above  $P_{\text{rep}} = 53 \text{ Pa}$ . Unfortunately, we only conducted experiments at 4 different values of the granular pressure. We are thus unable to say much about the shape of the transition, or whether the macroscopic friction coefficient saturates or not.

To support these results, obtained by varying the granular pressure  $\bar{P}$ , we compared them to those obtained in the rotating drum configuration, where we varied the repulsive pressure  $P_{\text{rep}}$  instead. To do so, the macroscopic friction coefficient must be plotted as a function of  $\Pi = \bar{P}/P_{\text{rep}}$ . We have:

- $4 \text{ Pa} \leq \bar{P} \leq 350 \text{ Pa}$  and  $P_{\text{rep}} = 53 \text{ Pa}$  in the Darcytron,
- $\bar{P} \simeq 5 \text{ Pa}$  and  $10^{-9} \text{ Pa} \leq P_{\text{rep}} \leq 53 \text{ Pa}$  in the rotating drum.

As we can see in Figure 3.18b, the data collapses reasonably well, especially given the fact that the Darcytron results are quite preliminary. Note that for the rotating drum data, when  $[\text{NaCl}] = 1 \text{ mol} \cdot \text{L}^{-1}$ , the expression used to compute  $P_{\text{rep}}$  ( $P_{\text{rep}} = 4F_0/(\pi d^2) \exp(-2l_r/\lambda_D)$ , recall Chapter 2) is no longer adapted since it only holds for low salt concentrations. This data point was nonetheless left on the plot to show the saturation of the friction coefficient.

The results presented above are encouraging. However, we still need to conduct systematic experiments to investigate the shape of the transition and observe the saturation of  $\mu$  at large  $\Pi$ . Additionally, several experiments exhibited an unexpected oscillatory behaviour (described in Section 3.3.3), which needs to be characterised.



(a) Evolution of  $\mu$  with  $\bar{P}$  for silica beads in pure water. Data obtained with the Darcytron.

(b) Evolution of  $\mu$  with  $\Pi$  for silica beads in ionic solutions. Comparison between the Darcytron and the rotating drums from Chapter 2.

Figure 3.18 – Macroscopic friction coefficient  $\mu$  of a suspension of silica beads (diameter  $d = 23.56 \pm 1.06 \mu\text{m}$ ) in aqueous ionic solutions (viscosity  $\eta_f \simeq 1 \text{ mPa} \cdot \text{s}$ ).

### 3.3.3 Unexpected oscillations

Our main issue when conducting experiments on the silica suspension in pure water with the Darcytron was that we were only able to access the frictionless state by setting the immersed height of the inner cylinder to a very low value:  $h = 1.5 \text{ mm}$ . This value is much smaller than the critical depth  $z_c$  at which the suspension is expected to transit to a frictional state under its own weight. Experiments conducted at larger  $h$  resulted in an unexpected phenomenon: as illustrated in Figure 3.19, the torque spontaneously oscillates.

These oscillations are so regular that at first, we thought it might be a feedback issue coming from the rheometer's PID controller. However, since the rotating speed of the inner cylinder remains constant (within 5%), it is a priori not the case. These intriguing oscillations emerge as an instability and several features suggest that it arises from some physical phenomenon. Below is a list of the major trends supporting this claim.

1. The oscillation period  $T_{\text{osc}}$  of the torque is of the order of 10 s, much smaller than the rotation period of the inner cylinder which is typically between 500 and 5000 s. This excludes any misalignment effect of the cylinder.
2. The fluid's pressure also oscillates, with the same period as the torque (see Figure 3.19). The magnitude of the pressure oscillations, which is  $\Delta\tilde{P} \sim 10 \text{ Pa}$  in Figure 3.19, is of the same order of magnitude as the average hydrostatic pressure:  $\phi\Delta\rho gh/2 \simeq 12 \text{ Pa}$  for  $h \simeq 5 \text{ mm}$  as in Figure 3.19. This suggests that periodic resuspension of the grains within the sheared layer might occur. The amplitude of the expected torque oscillations arising

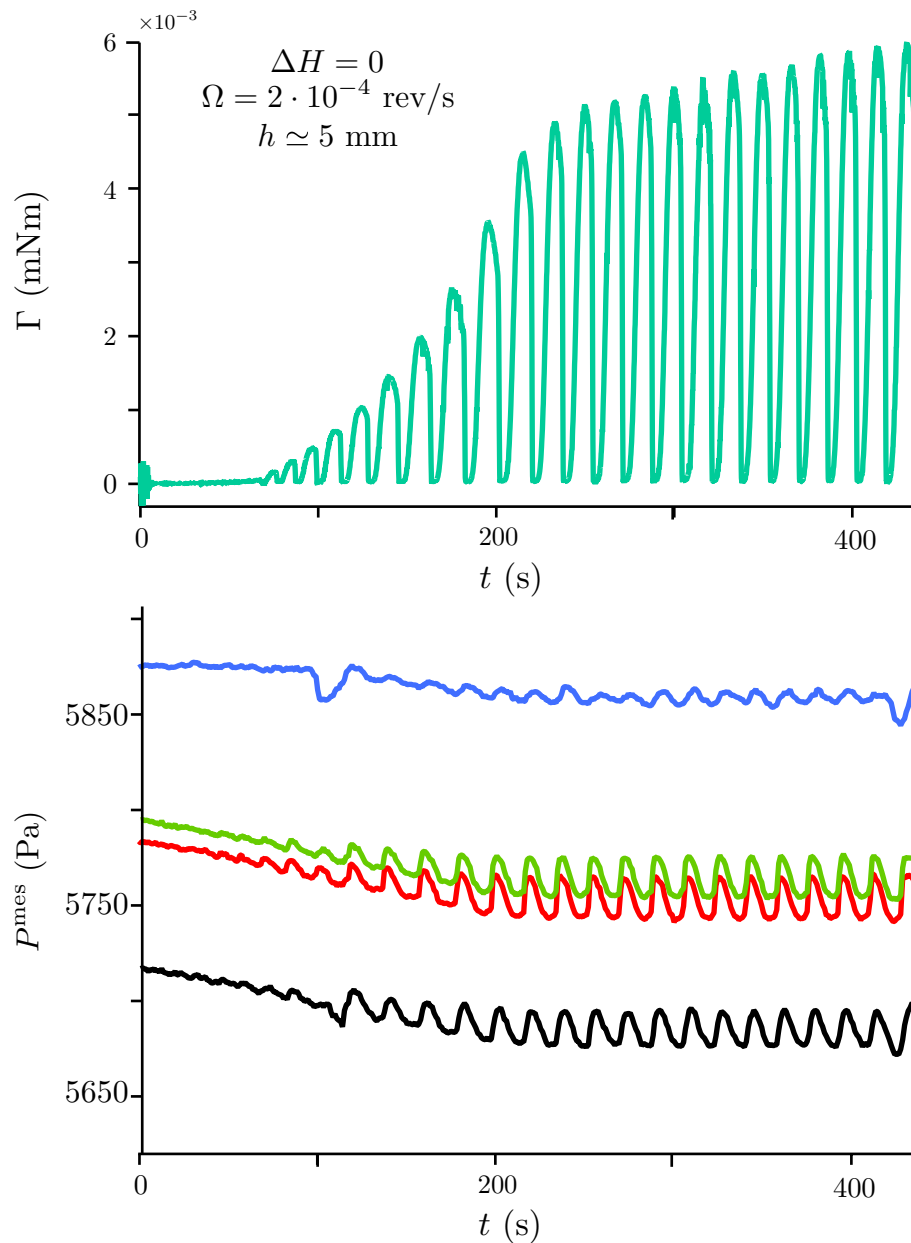


Figure 3.19 – Evolution of the torque  $\Gamma$  (top) and of the fluid’s pressure measured with the differential pressure sensors (bottom) for an immersion height  $h = 5 \text{ mm}$  and for  $\Delta H = 0$ .

from these pressure oscillations can be written as  $\Delta\Gamma = \mu \cdot 2\pi a^2 h \Delta\tilde{P}$ . Using  $\mu = 0.3$ , this gives  $\Delta\Gamma \sim 4 \mu\text{N} \cdot \text{m}$ , which is also of the same order of magnitude as that of the measured torque oscillations:  $\Delta\Gamma \sim 6 \mu\text{N} \cdot \text{m}$  in Figure 3.19. These oscillations may thus arise from a beating effect involving the fluid’s pressure and the resuspension of the granular layer.

3. We also observe that the oscillation’s period  $T_{\text{osc}}$  does not scale linearly with  $\Omega$  (see Figure 3.20b). This seems to indicate that another time scale

$h = 10$ mm	■	$\Omega = 2 \cdot 10^{-4}$ rev/s	Pure water
$h = 20$ mm	◆		
$h = 10$ mm	●	$\Omega = 2 \cdot 10^{-4}$ rev/s	[NaCl] = $10^{-4}$ mol/L
$h = 20$ mm	●		

(a) Plot key for Figures 3.20b, 3.20c, and 3.20d.

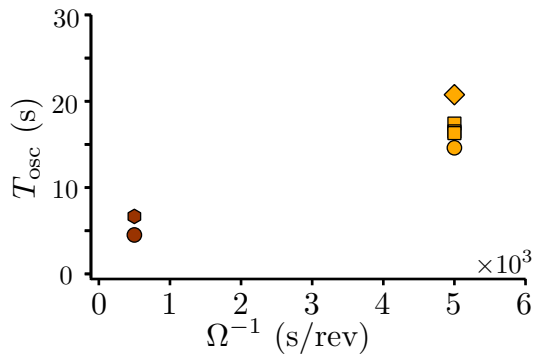
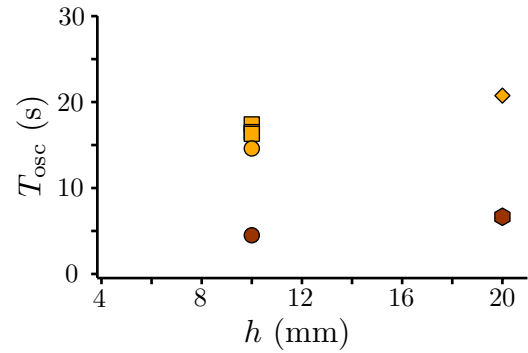
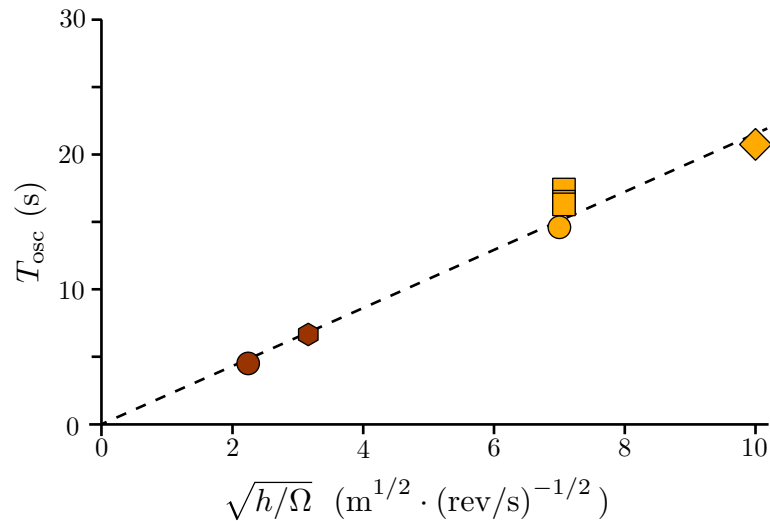

 (b)  $T_{\text{osc}}$  versus  $\Omega$ .

 (c)  $T_{\text{osc}}$  versus  $h$ .

 (d)  $T_{\text{osc}}$  versus  $\sqrt{h/\Omega}$ .

 Figure 3.20 – Evolution of the oscillation period  $T_{\text{osc}}$  of the torque with the rotating speed  $\Omega$  and the immersed height  $h$  of the inner cylinder.

is also involved, which would be consistent with a beating effect. Indeed, we observe that  $T_{\text{osc}}$  depends on the immersion height  $h$  (see Figure 3.20c). To obtain a time scale depending on  $h$ , we assume that the rotation of the cylinder dilates the sheared layer from 64 % to 58 %, and that there is a sed-

imentation time scale associated with its re-compaction. This time scale can be estimated as:

$$T_{\text{sed}} = \frac{h}{V_S f(\phi)} \frac{\Delta\phi}{\phi},$$

where  $\Delta\phi = 6\%$ ,  $V_S = (2/9)\Delta\rho g a^2/\eta_f$  is the Stokes velocity for the silica particles in water, and  $f(\phi) = (1 - \phi)^5$  is the hindrance function of Richardson–Zaki (see [7]). We find  $T_{\text{sed}} \sim 150$  s. The time scale associated with  $\Omega$  is the one associated with the shear rate within the sheared granular layer:

$$T_{\text{shear}} = \frac{1}{\dot{\gamma}} = \frac{10d}{2\pi a\Omega},$$

which yields  $T_{\text{shear}} \sim 40$  s. The oscillations could result from a combination of these two time scales:

$$T_{\text{osc}} = \sqrt{T_{\text{sed}} \cdot T_{\text{shear}}} \propto \sqrt{h/\Omega},$$

in agreement with the rescaling proposed in Figure 3.20d.

4. The amplitude of the oscillations vanishes as the immersion height  $h$  is decreased. This is why we conducted the experiments at  $h = 1.5$  mm, where the torque reaches a constant value in the steady state.

For now, it is still unclear how to explain the mechanism at the origin of these oscillations. They seem to be related to a beating effect involving a periodic resuspension of the sheared granular layer. However, we need to further investigate this intriguing instability. In particular, we intend to systematically probe the influence of  $\Delta H$ ,  $\Omega$ , and  $h$  on the amplitude and the period of both the torque's and the pressure's oscillations.

### 3.4 Conclusion and discussion

In this chapter, we presented the development of an original pressure-imposed rheometer, which we called the Darcytron. This rheometer was designed to test the hypotheses of the frictional transition model. It was therefore required to allow access to the quasi-static macroscopic friction coefficient of colloidal suspensions. We used a classical annular shear flow configuration, whose originality is that the granular pressure in the cell can be imposed through a vertical Darcy flow of adjustable intensity. Moreover, since the sediment is held in place by a fixed porous grid which is sealed to the side wall of the cell, this rheometer is suited to the study of suspensions of particles as small as desired.

To validate the general concept of the Darcytron, we first built a large version of the set-up to investigate the behaviour of a suspension of large frictional glass beads in a Newtonian viscous fluid. We showed that the Darcy flow provides an accurate way to control the granular pressure. We also checked that, as expected for such a suspension, the quasi-static macroscopic friction coefficient of the suspension is independent of the granular pressure.

By measuring the torque for various immersion heights of the inner cylinder, we also explored the vertical granular stress distribution caused by the particles' weight. We found that it deviates from the expected linear hydrostatic trend. Instead, the granular pressure seems to increase as a power law of the depth, with an exponent varying with the aspect ratio of the cell. This trend, which might arise from recirculation rolls, needs to be studied more extensively. However, this can only affect the absolute value of the measured macroscopic friction coefficient of the suspension, and not its relative variations when the granular pressure is varied through the Darcy flow.

In order to use the Darcytron configuration to investigate the frictional behaviour of a shear-thickening suspension of silica particles in pure water, we needed to build a similar but scaled down cell. Using this small cell, we proved that the quasi-static macroscopic friction coefficient  $\mu$  of a suspension of silica beads in pure water increases when increasing the granular pressure, as predicted by the frictional transition model. At the lowest granular pressure achievable, we measured  $\mu \simeq 0.1$ , which corresponds to the expected macroscopic friction coefficient for frictionless spheres. For the largest granular pressure that we could reach, it increases to  $\mu \simeq 0.32$ . We were also able to superimpose the data obtained from both the Darcytron (varying the granular pressure  $\bar{P}$ ) and the rotating drum (varying the repulsive pressure  $P_{\text{rep}}$ ) by plotting  $\mu$  as a function of  $\Pi = \bar{P}/P_{\text{rep}}$ . This is a strong experimental result in favour of the frictional transition model, which anticipated that  $\Pi$  should be the relevant dimensionless parameter controlling this transition.

We must however emphasise that it is too early for now to draw any definitive conclusion from the results obtained with the small Darcytron cell. We still need to conduct more systematic experiments. Additionally, some questions still remain open. In particular, we do not understand why the frictionless state can only be observed for such a small immersion height of the inner cylinder. Moreover, at larger immersion heights we observed unexpected periodic oscillations, which spontaneously appear both on the torque and on the fluid's pressure. At the moment, we have no clear idea how to explain this instability.



---

## Conclusion and future works

---

She wasn't certain what the future held, but coffee would be involved if she had any say in the matter.

---

Terry Pratchett, *Moving Pictures*.

### 4.1 Conclusion

The objective of this PhD was to investigate experimentally the frictional behaviour of shear-thickening suspensions, in order to test the ideas put forward in the frictional transition scenario recently proposed by Seto, Mari et al. [1, 2] and Wyart and Cates [3]. Along with providing a consistent explanation for shear thickening, this model also questions the longstanding vision according to which sheared suspensions are dominated by hydrodynamic forces. Instead, it suggests that the key to understanding the macroscopic rheology of a dense suspension is to take into account the combined effects of friction between particles and short-range interaction forces. Testing this model is therefore important to understand not only the microscopic origins of shear thickening, but also the role of contacts in dense suspension.

The frictional transition model is difficult to investigate experimentally. Indeed, experiments with shear-thickening suspensions require to have a good control over the suspension's physical and chemical properties (pH, ionic concentration, sample preparation, . . .). Moreover, as we have seen (Chapter 1), standard rheological techniques do not give access to the macroscopic friction coefficient  $\mu$  of the suspension, which is the quantity one needs to measure in order to test this model. These techniques are also not suited to the study of very dense suspensions, since their viscosity diverges close to jamming. Recently, a new rheological technique at imposed pressure inspired by granular media physics was developed at IUSTI



by Boyer et al. [28]. It allows access to  $\mu$ , and more generally it allows to explore the rheology of dense suspensions close to their critical packing fraction. However, this technique was developed for suspension of macroscopic particles. It is not adapted to the study of shear-thickening suspensions, whose particles are too small (see Chapter 3). The goal of this work was therefore to develop new techniques for the measure of  $\mu$  in shear-thickening suspensions.

We first used a classical rotating drum configuration, in which the granular pressure is imposed by gravity, and therefore is not a control parameter (see Chapter 2). In order to be able to vary the granular pressure, we developed an entirely new rheometer, which we called the Darcytron, adapted to the study of the frictional behaviour of colloidal suspensions (see Chapter 3).

### 4.1.1 Rotating drum experiments

We investigated three different suspensions: large glass beads in a viscous, Newtonian fluid, which we used as a benchmark for suspensions of frictional particles; potato starch in water, which is a typical shear-thickening suspension; and finally suspensions of silica beads in aqueous ionic solutions, as an ideal experimental system to test the frictional transition model. Our results are summarised in Figure 4.1.

	frictional transition → [NaCl]			
	Large glass beads + Ucon™ + water	Potato starch + water	Silica beads + 10 <sup>-4</sup> mol/L [NaCl]	Silica beads + 10 <sup>-1</sup> mol/L [NaCl]
Quasi-static steady avalanche angle	25°	8.5°	6°	27.5°
Compaction	Yes	No	No	Yes
Dilatancy	Yes	No	No	Yes
Frictional behaviour under low granular pressure	<b>Frictional</b>	<b>Frictionless</b>	<b>Frictionless</b>	<b>Frictional</b>
Rheology	<b>Newtonian</b>	<b>Shear-thickening</b>	<b>Shear-thickening</b>	<b>Newtonian (shear-thinning)</b>

Figure 4.1 – Summary of the results obtained with rotating drums

The rotating drum configuration is a simple yet robust way to access the frictional properties of a suspension through macroscopic signatures of microscopic friction: the quasi-static steady avalanche angle, and compaction and dilatancy

effects. These clearly indicate whether the suspension's behaviour is frictional or frictionless. To complete our study, we also characterised the rheological behaviour of our suspensions, in order to link the macroscopic rheology with the frictional properties.

Our rotating drum experiments are characterised by two main features. First, the measurements were conducted in the quasi-static regime. Therefore, we only probed the quasi-static frictional properties of the suspensions. Second, the granular pressure in a rotating drum is fixed by gravity. In our experiments, it was approximately 1 Pa. Therefore, we probed the frictional properties of the suspension under very low stress.

The main conclusions of our work are the following.

1. A large quasi-static steady avalanche angle, the presence of compaction under vibration, and dilatancy effects on transient avalanches, all indicate that the particles in the suspension form frictional contacts. As expected we observed these three characteristics for our benchmark suspension of large glass beads. We also observed them in suspensions of silica beads in aqueous ionic solutions, when the salt concentration of the suspending fluid was large enough.
2. Conversely, a low quasi-static steady avalanche angle, the absence of compaction under vibration, and the absence of dilatancy effects, all indicate that the particles in the suspension behave as frictionless ones. We observed these characteristics for the suspension of potato starch in pure water, which is a typical example of shear-thickening suspensions. We also observed them in suspensions of silica beads in aqueous ionic solutions, when the salt concentration of the suspending fluid was small enough. To the best of our knowledge, these results constitute the first experimental realisation of granular materials flowing without interparticle friction. Our measurements of low avalanche angle ( $6^\circ$ ) and lack of Reynolds' dilatancy are fully consistent with previous predictions of numerical simulations of frictionless hard spheres, conducted with or without fluid. This frictionless behaviour is also consistent with the behaviour of other frictionless soft systems like dense emulsions or foam (see [84]).
3. A suspension which has a frictionless state under low granular pressure, such as potato starch in water and silica beads in ionic solutions of low salt concentration, is shear-thickening. Conversely, frictional suspensions without repulsion do not shear thicken. These behaviours were predicted by the frictional transition model.
4. Short-range repulsive forces between the particles can induce a frictionless state in a suspension under low stress, as evidenced with the suspensions of silica particles. As already mentioned, this relates to a shear-thickening rheology. When the range of this repulsive force is lowered below the particles' roughness, this frictionless state disappears, and so does the shear-thickening behaviour.

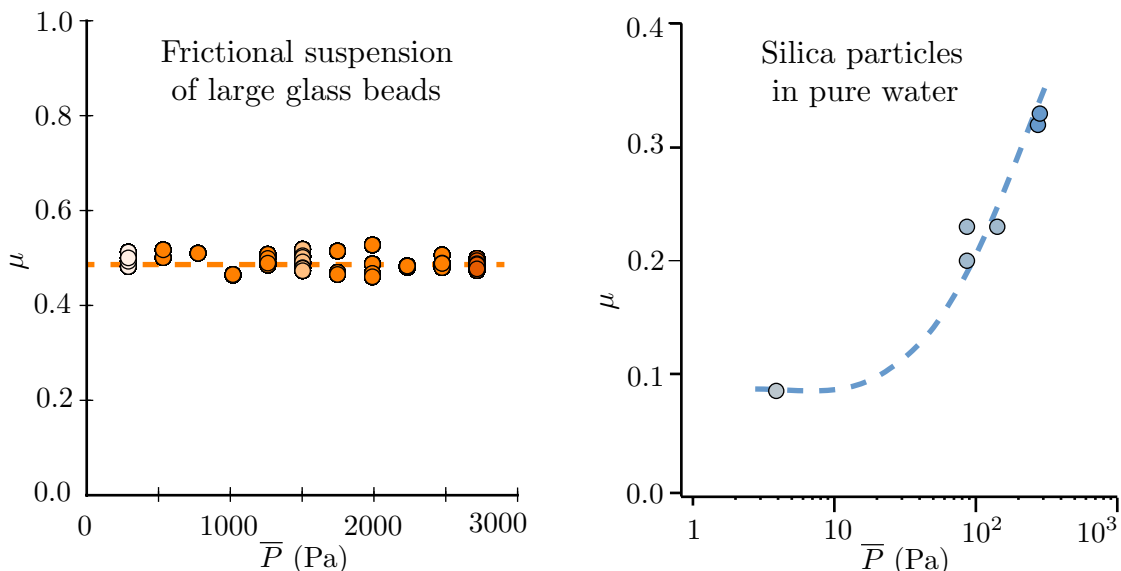
These experimental results revealed the relation between shear thickening and the presence of short-range repulsive forces able to prevent inter-particle friction at low stress. This provided strong experimental evidence that the frictional transition scenario applies in real suspensions.

However, as already stated, in a rotating drum the granular pressure is fixed. This configuration thus cannot be used to fully explore the frictional transition. This led us to develop a new pressure-imposed rheometer: the Darcytron.

### 4.1.2 Experiments with the Darcytron

This original rheometer is adapted to study the frictional properties of non-buoyant shear-thickening suspensions, whose particles are small. The idea of the Darcytron is to impose the granular pressure through the creation of a Darcy flow within the sediment formed by the particles.

We validated the general concept on which the Darcytron is built using the suspension of large glass beads in a Newtonian fluid mentioned in the previous section as a benchmark. As expected, its friction coefficient does not depend on the imposed granular pressure (see Figure 4.2a). Our main result with this experimental set-up is that, for a suspension of silica beads in pure water, the friction coefficient instead increases with the granular pressure (see Figure 4.2b). This behaviour stems from the presence of a repulsive force between the grains, which prevents the formation of frictional contacts, as predicted by the frictional transition model.



(a) Large frictional glass beads in a Newtonian fluid. The dotted line represents the average value of  $\mu$ .

(b) Silica particles in pure water. The dotted line is a guide for the eye.

This new, pressure-imposed rheometer we developed allows to investigate the rheology of very dense suspensions, where conventional rheometers fail to do so

because of to the divergence of the viscosity with the packing fraction. Additionally, the Darcytron gives access to the suspension's friction coefficient, a quantity which is not accessible through conventional rheology. The technique used to impose the granular pressure on the particles opens the way to pressure-imposed rheology on colloidal and even Brownian suspensions. The potential applications of the Darcytron thus extend beyond the scope of this PhD, in both fundamental physics and industrial research.

Due to lack of time, we were not able to finalise our study of shear-thickening suspensions with the Darcytron. In particular:

- more systematic experiments are needed to investigate the shape of the transition,
- we also need to change the repulsive force by varying the ionic concentration,
- it would be very interesting to change the particles' roughness, as it also affects  $P_{\text{rep}}$ ,
- finally, we have evidenced an unexpected instability in the system. Investigating and modeling this instability constitutes an exciting challenge.

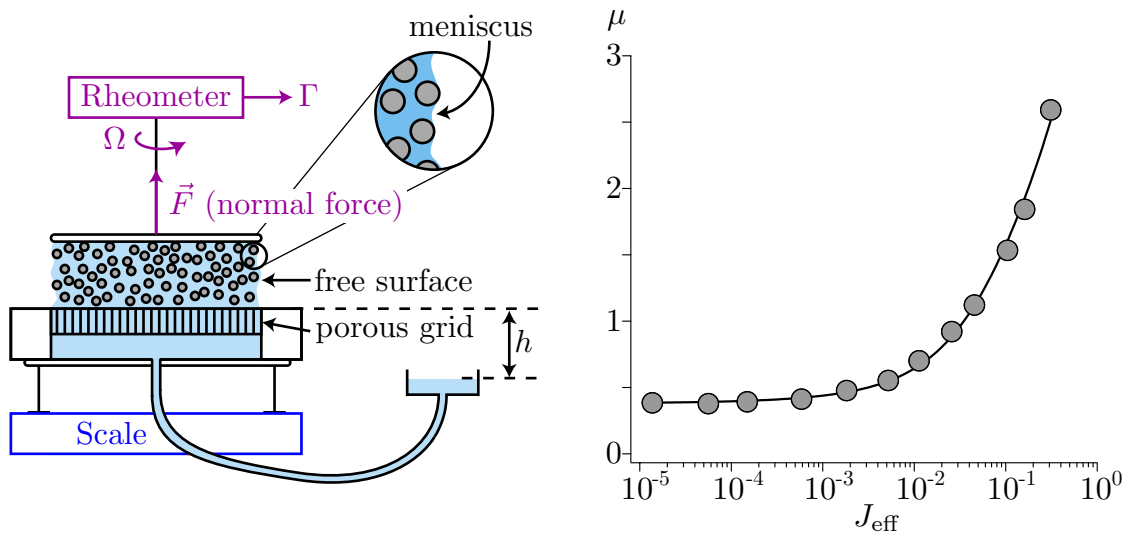
As discussed above, our work with the Darcytron has opened interesting possibilities for future research. In the sequel, we present two other major prospects that have emerged from my PhD work.

## 4.2 Future works

### 4.2.1 The Capillarytron

The rotating drum configuration and the Darcytron allowed us to study the frictional behaviour of shear-thickening suspensions by varying either the repulsive pressure  $P_{\text{rep}}$  between the grains or the granular pressure  $P$ . However, both set-ups were limited to the study of non-buoyant suspensions, and more importantly they were restricted to measurements in the quasi-static regime. It was therefore natural to try to develop another technique which would enable the measurement of the suspension's macroscopic friction coefficient  $\mu$  as a function of both the dimensionless pressure  $\Pi = P/P_{\text{rep}}$  and the viscous number  $J$ , thus completely exploring the constitutive laws of shear-thickening as proposed by the frictional transition model.

Along with the development of the Darcytron, we thus worked on another concept to measure the macroscopic friction coefficient of a suspension as a function of the applied granular pressure. This experimental set-up, sketched in Figure 4.3a, was inspired in part by Dbouk et al. [32] (see Chapter 1). It relies on capillary effects to impose the pressure, hence its name: the *Capillarytron*. Contrarily to the Darcytron, the Capillarytron is only adapted to suspensions of particles in a density-matched fluid. The idea is to shear the suspension in a classical plane-plane configuration with a porous bottom plate. Under this porous plate, there is



(a) Experimental set-up.

(b) Preliminary results obtained with a classical suspension of large glass beads. The solid line is a guide for the eye.

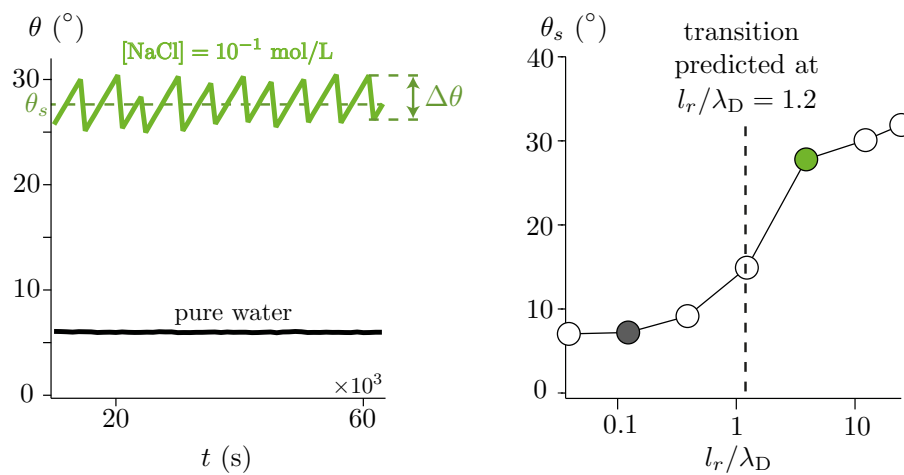
Figure 4.3 – The Capillarytron: experimental-set-up and preliminary results.

a water reservoir connected to a smaller reservoir whose height  $h$  we can control. At equilibrium, the fluid's negative pressure arising from this height difference  $h$  must be balanced by capillary forces induced by the deformation of the menisci at the air/suspension interface. The top-plate is free to translate, and we control the normal force  $\vec{F}$  with the rheometer. This way, the suspension is free to adjust its packing fraction given the imposed granular pressure. Finally, the set-up is sitting on a scale which measures the force arising from both the granular pressure  $P$  and the fluid's pressure  $P^f$  acting on the bottom plate. By measuring the torque applied on the top plate by the suspension, we can compute the macroscopic friction coefficient  $\mu$ .

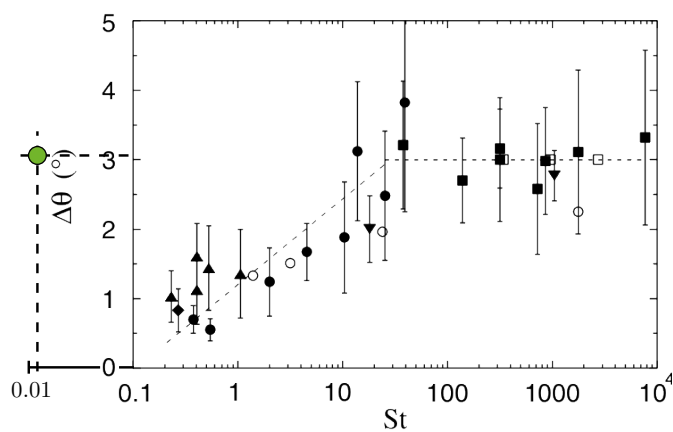
During Alla Fahs' internship, we validated the general concept behind the Capillarytron by measuring the evolution of the macroscopic friction coefficient  $\mu$  of a Newtonian suspension of large frictional glass beads. As shown in Figure 4.3b, using the Capillarytron we recover the standard form of  $J \mapsto \mu(J)$  (see [24]). We now intend to use this rheometer to investigate the behaviour of shear-thickening suspensions.

## 4.2.2 Hysteresis

In Chapter 2, we used a rotating drum to measure the steady avalanche angle of suspensions of silica beads in aqueous ionic solutions, as a function of the suspending fluid's salinity. These results are recalled in Figure 4.4a. The time evolution of the avalanche angle (on the left) shows an intriguing feature which we have not discussed so far. We see that when the particles are frictional, that is, at large ionic concentrations, the avalanche angle is not constant in time but instead presents



(a) Reminder of our results from Chapter 2.



(b) Comparison of our data with that of Courrech du Pont et al. from [61].

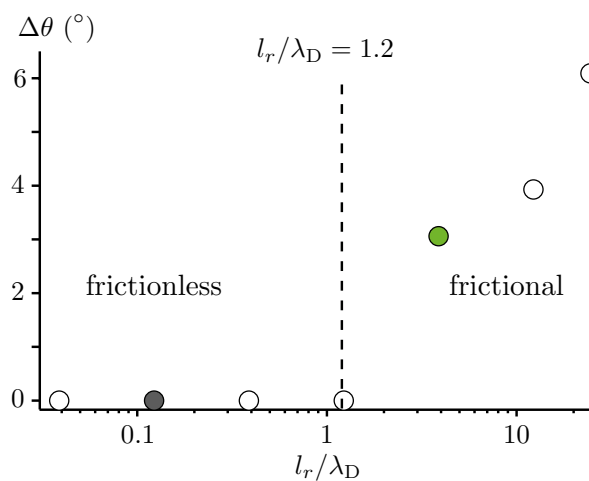
(c) Evolution of the stick-slip amplitude with the ratio  $l_r/\lambda_D$ .

Figure 4.4 – Preliminary study of the stick-slip amplitude in our suspensions of silica beads in ionic solutions.

a hysteretic behaviour. Hysteresis is a classical property of granular media (see Chapter 2), but it is generally believed to result from inertial effects. In [61], Courrech du Pont et al. showed that the amplitude of this *stick-slip* vanishes as the Stokes number  $St$  vanishes, see Figure 4.4b. What is surprising in our results is that a large hysteresis persists even though the Stokes number is very low. For instance, with  $[\text{NaCl}] = 10^{-1} \text{ mol} \cdot \text{L}^{-1}$  (in green in Figure 4.4), we obtain  $\Delta\theta \simeq 3^\circ$  for  $St = 1.2 \times 10^{-2}$ . This is at odds with the results reported by Courrech du Pont et al., see Figure 4.4b.

Moreover, as we can see in Figure 4.4c, we find a strong correlation between the frictional properties of the grains and the presence of hysteresis. Our data suggests that hysteresis disappears when the particles become frictionless. This seems to indicate that the Stokes number is not the only parameter controlling the existence of a hysteretic behaviour in granular avalanches. Understanding what mechanism is at play in the hysteresis observed at low Stokes number is now one of the objectives of the post-doctoral research of Hugo Perrin, who is continuing my work of those aspects.

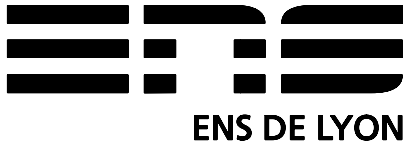
## ANNEXE A

---

Rhéologie d'un milieu granulaire répulsif 2D : une expérience  
modèle pour comprendre le rhéoépaississement

---





MASTER SCIENCE DE LA MATIÈRE  
École Normale Supérieure de Lyon  
Université Claude Bernard Lyon I

Stage 2014–2015  
Cécile Clavaud  
M2 Physique

---

# Rhéologie d'un milieu granulaire répulsif 2D :

## une expérience modèle pour comprendre le rhéo-épaississement

---

**Résumé :** Le rhéo-épaississement est un phénomène se produisant dans certaines suspensions. Il consiste en une augmentation brutale de la viscosité lorsque le taux de cisaillement imposé dépasse une certaine valeur critique. Un tel comportement possède un large champ d'applications, par exemple en médecine avec la création de prothèses souples. Très étudié, le rhéo-épaississement reste assez mal compris. Récemment, des modèles microscopiques ont ouvert de nouvelles pistes de recherche. Le but du stage était de tester expérimentalement le scénario proposé par ces modèles théoriques. Pour cela, nous avons conçu une expérience permettant d'étudier la rhéologie d'un milieu granulaire modèle à deux dimensions. Ce rapport présente et discute nos résultats expérimentaux.

**Mots clés :** *milieux granulaires, fluides complexes, suspensions, jamming (blocage), rhéologie.*

Stage encadré par :

Yoël Forterre  
yoel.forterre@univ-amu.fr

Bloen Metzger  
bloen.metzger@univ-amu.fr

Institut Universitaire des Systèmes Thermiques Industriels (IUSTI)  
Technopôle de Château-Gombert,  
5 rue Enrico Fermi,  
13453 Marseille cedex 13,  
France.  
<http://iusti.univ-provence.fr>



# Remerciements

Je remercie Bloen et Yoël de m'avoir offert cette opportunité de travailler sur un sujet passionnant, et également d'avoir accepté de continuer l'aventure avec moi en thèse. Merci pour votre patience et l'aide que vous m'avez apportée. Merci aussi pour votre enthousiasme et votre bonne humeur.

Je remercie également les membres du laboratoire pour leur accueil et l'ambiance chaleureuse qui règne à l'IUSTI. Merci à Mathieu d'avoir répondu à mes questions tant de physique qu'à propos du fonctionnement du labo. Thanks Saif for giving me the opportunity to practice my English. Thank you and Yxian for letting me join the band. Je voudrais aussi remercier Pascal Champion et Arianne Bunel pour leur aide administrative, et Laurence pour son aide, ses conseils et sa bonne humeur.

# Table des matières

<b>1</b>	<b>Rhéologie-épaississement des suspensions : état de l'art</b>	<b>1</b>
<b>2</b>	<b>Expérience modèle : un milieu granulaire répulsif 2D</b>	<b>4</b>
2.1	Dispositif expérimental . . . . .	4
2.2	Mise en place et difficultés . . . . .	6
<b>3</b>	<b>Expériences à "volume" imposé</b>	<b>7</b>
3.1	Rappels de rhéologie des milieux granulaires à volume imposé . . . . .	7
3.2	Méthodologie . . . . .	8
3.3	Résultats . . . . .	8
<b>4</b>	<b>Expériences à "pression" imposée</b>	<b>11</b>
4.1	Rappels de rhéologie des milieux granulaires à pression imposée . . . . .	11
4.2	Méthodologie . . . . .	12
4.3	Résultats . . . . .	13
4.4	Discussion . . . . .	16
<b>5</b>	<b>Perspectives</b>	<b>17</b>
5.1	Expérience modèle . . . . .	17
5.2	Suspensions réelles . . . . .	18
<b>A</b>	<b>Code Matlab (couplemètre)</b>	<b>22</b>
<b>B</b>	<b>Code Matlab (traitement des images)</b>	<b>22</b>
<b>C</b>	<b>Macro ImageJ</b>	<b>23</b>

## Introduction

Le rhéo-épaississement est un phénomène physique spectaculaire qui apparaît dans certaines suspensions de particules. Il consiste en une augmentation brutale de la viscosité lorsque le taux de cisaillement imposé dépasse une certaine valeur critique. Un des exemples les plus connus de fluides complexes présentant ce comportement est le mélange d'amidon de maïs (par exemple de la Maïzena) avec de l'eau. Prenez un récipient et mélangez environ 50 % d'amidon de maïs à 50 % d'eau (en volume). Si vous déplacez un objet très lentement dans la suspension ainsi obtenue, celle-ci se comporte comme un fluide visqueux et coule autour de l'objet. Si maintenant vous essayez de déplacer cet objet plus rapidement, le mélange résiste et présente un comportement "solide". C'est ce qui permet aux enfants sur la figure 1 de "courir sur l'eau". Plusieurs applications moins ludiques de ce phénomène ont été envisagées, comme la conception de prothèses souples en médecine, d'armures souples pour remplacer les gilets pare-balles, ou d'amortisseurs plus performants. Cependant, le phénomène de rhéo-épaississement est pour l'instant mal compris d'un point de vue fondamental. Cela limite le développement de suspensions rhéo-épaississantes artificielles et de leurs applications.

Cette situation pourrait avoir changé récemment à la suite de travaux théoriques [22] et numériques [20, 17], qui proposent un nouveau mécanisme pour expliquer le rhéo-épaississement. Les auteurs de ces travaux suggèrent que ce phénomène pourrait provenir d'une transition frictionnelle induite par la présence de forces répulsives à courte portée entre les grains. Ce scénario est prometteur car il fournit un cadre simple et cohérent pour décrire le rhéo-épaississement mais il n'a pas encore été validé expérimentalement. Lors de mon stage, j'ai participé à la conception d'un dispositif expérimental permettant de le tester et réalisé plusieurs expériences en ce sens.

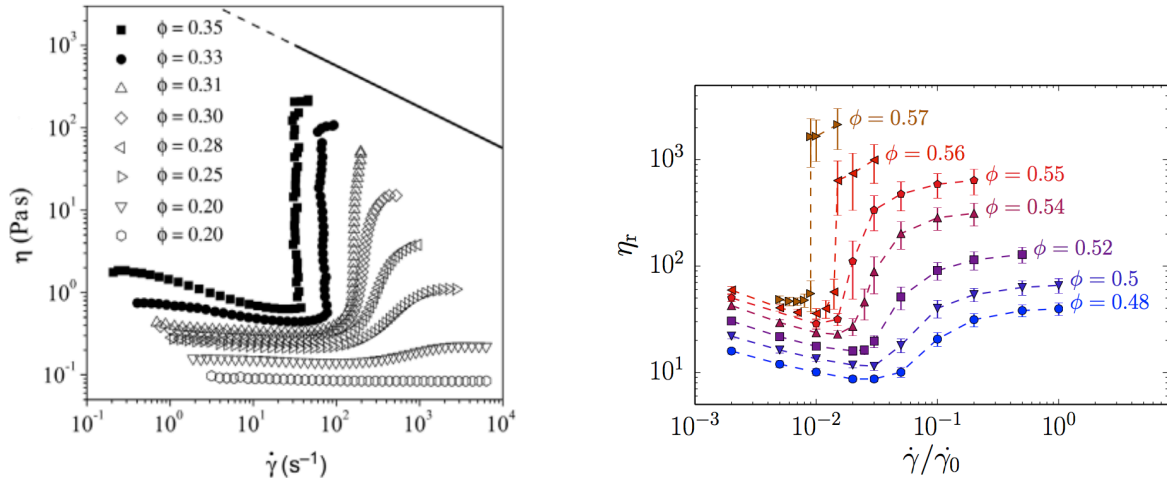
Ce rapport s'organise comme suit. La section 1 présente l'état des connaissances sur le rhéo-épaississement et l'idée principale des modèles de Seto, Mari et al. [20, 17] et Wyart et Cates [22]. La section 2 décrit le dispositif expérimental que nous avons conçu, ainsi que sa mise en place. Les sections 3 et 4 présentent les expériences réalisées, ainsi que les résultats et leurs interprétations. Enfin, la section 5 présente des perspectives qui seront à la base de mon travail de thèse.



FIGURE 1 – Enfants courant sur une piscine remplie d'un mélange d'eau et d'amidon de maïs. Source : <http://www.tuxboard.com/seriez-vous-capable-de-marcher-sur-leau/>, dernière consultation le 3 août 2015.

## 1 Rhéo-épaississement des suspensions : état de l'art

La première mention du phénomène de rhéo-épaississement date d'un article de 1938 par Freundlich et Röder [15]. Les auteurs y évoquent la *dilatance* de suspensions d'amidon de maïs, de riz ou de pomme de terre dans de l'eau. Depuis, le phénomène a été étudié par de nombreux chercheurs, tant expérimentalement que théoriquement. La figure 2 présente l'évolution de la viscosité d'une suspension rhéo-épaississante en fonction du taux de cisaillement  $\dot{\gamma}$ , à différentes fractions volumiques  $\phi$ . La figure 2a (adaptée de [19]) correspond à des mesures expérimentales et la figure 2b (adaptée de [17]) à une simulation numérique. Dans les deux cas on constate une augmentation de la viscosité avec le taux de cisaillement, contrairement à ce qui se produit dans les suspensions classiques de sphères dures macroscopiques (Boyer et al. [4]). À forte fraction volumique,



(a) Courbes expérimentales donnant l'évolution de la viscosité en fonction du taux de cisaillement dans une suspension rhéo-épaississante, pour différentes fractions volumiques (adaptée de [19]).

(b) Simulations numériques donnant l'évolution de la viscosité en fonction du taux de cisaillement dans une suspension rhéo-épaississante, pour différentes fractions volumiques (adaptée de [17]).

FIGURE 2 – Mesures expérimentales et simulations numériques donnant l'évolution de la viscosité en fonction du taux de cisaillement dans une suspension rhéo-épaississante, pour différentes fractions volumiques (adaptées de [19, 17]). On observe le même comportement qualitatif.

la viscosité devient discontinue et présente un saut à un taux de cisaillement critique  $\dot{\gamma}_c$ .

Les observations expérimentales suggèrent que le rhéo-épaississement est susceptible d'apparaître dans de nombreuses suspensions. Le plus souvent, il est observé dans des suspensions composées de grains dont le diamètre n'excède pas  $40 \mu\text{m}$ . La littérature est assez riche en ce qui concerne l'étude des suspensions browniennes, c'est-à-dire dans lesquelles les grains sont sub-micrométriques, et donc sensibles à l'agitation thermique [2, 16]. Cependant, le rhéo-épaississement a aussi été observé dans des suspensions non browniennes, composées de grains plus gros [11, 7, 15]. Cela suggère que l'agitation thermique n'est pas nécessaire à l'apparition de ce phénomène. Il est également important de noter que la rhéologie des suspensions, et en particulier l'apparition du rhéo-épaississement, semble très sensible à la physico-chimie à la fois des grains et du fluide. Par exemple, dans l'industrie du ciment, certains polymères dits superplastifiants semblent capables d'influencer fortement la rhéologie des suspensions utilisées [12, 13].

Plusieurs explications et modèles théoriques ont été développés afin d'expliquer le rhéo-épaississement. Une première interprétation est la formation d'*hydro-clusters* [5, 6, 21], c'est-à-dire de régions où la densité de grains est localement très forte. Celle-ci s'appuie sur des résultats de simulations numériques basées sur la dynamique stokésienne, qui est une méthode numérique utilisée pour décrire les suspensions. Dans ce cadre, une suspension est constituée de grains rigides immergés dans un fluide newtonien. Les forces en présence sont les interactions hydrodynamiques et l'agitation thermique. Ces travaux expliquent l'apparition du rhéo-épaississement à fort taux de cisaillement par la formation d'hydro-clusters, qui sont fortement dissipatifs à cause des forces de lubrification. Cependant, ces résultats numériques ne prédisent qu'un rhéo-épaississement continu et assez faible [6, 3, 18], alors que certaines suspensions, comme le mélange d'amidon de maïs et d'eau, présentent un rhéo-épaississement discontinu et de forte amplitude. De plus, le rhéo-épaississement que les auteurs observent est probablement dû à l'introduction de l'agitation thermique, car la rhéologie d'une suspension non brownienne idéale est nécessairement newtonienne [22]. Ces simulations n'expliquent donc pas le rhéo-épaississement observé dans les systèmes non browniens.

Une seconde approche suggère que le rhéo-épaississement résulte d'une transition entre un comportement visqueux de la suspension et un comportement inertiel. La loi d'échelle de Bagnold [1] prédit que, dans le régime inertiel, la viscosité  $\eta$  d'une suspension non brownienne n'est plus constante mais augmente linéairement avec le taux de cisaillement  $\dot{\gamma}$ . Cependant, encore une fois ce modèle n'explique pas les augmentations très violentes de viscosité observées expérimentalement. De plus, il ne décrit que le rhéo-épaississement apparaissant dans des suspensions atteignant un comportement inertiel. Or, Fall et al. [11] ont observé du rhéo-épaississement dans des suspensions à faible nombre de Stokes. Ceci semble indiquer que la présence d'effets inertiels n'est pas une condition nécessaire à l'apparition de ce phénomène.

Enfin, certains chercheurs en viennent à remettre en cause l'existence même du rhéo-épaississement comme loi rhéologique intrinsèque. Leurs arguments reposent principalement sur la difficulté des mesures rhéologiques et la quantité d'artefacts expérimentaux qui en découlent. Effectivement, le phénomène de migration des grains ou les effets de confinement dus aux parois à fortes concentrations peuvent conduire à un rhéo-épaississement apparent au niveau des mesures [7, 8, 10]. Cependant, il nous semble que, si ces articles nous alertent avec justesse sur la nécessité de prendre des précautions lors de mesures de rhéologie, les artefacts expérimentaux ne permettent pas d'expliquer le mécanisme à l'oeuvre lors de la traversée de la piscine (figure 1).

## Un nouveau modèle

Récemment, Seto, Mari et al. [20, 17] et Wyart et Cates [22] ont proposé un mécanisme microscopique qui échappe aux problèmes évoqués précédemment et fournit un cadre cohérent pour décrire le rhéo-épaississement. L'idée principale est d'introduire une force répulsive à courte portée entre les grains. Cela introduit une échelle de force supplémentaire qui permet d'avoir une rhéologie dépendant du taux de cisaillement.

À faible taux de cisaillement, la répulsion empêche les grains d'entrer en contact. Le milieu se comporte alors comme une suspension visqueuse de grains non frottants. Lorsque le taux de cisaillement dépasse une certaine valeur critique, la force répulsive est vaincue et les grains entrent en contact. Le frottement entre grains rend alors le milieu très dissipatif. Dans ce scénario, on s'attend à ce que le taux de cisaillement critique  $\dot{\gamma}_c$  corresponde à l'équilibre entre la force répulsive à courte portée, notée  $F_r$ , et la force hydrodynamique :

$$F_r = 3\pi\eta\dot{\gamma}_c d^2,$$

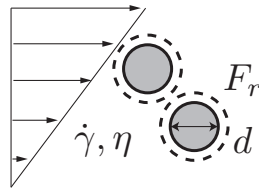
où  $\eta$  est la viscosité du fluide et  $d$  le diamètre des grains (voir figure 3a). Le point clé du modèle est la transition entre un contact frottant et un contact non frottant.

Pour comprendre l'importance de cette transition, appuyons-nous sur la rhéologie des suspensions de sphères dures. Dans ces suspensions, la viscosité augmente avec la fraction volumique  $\phi$  jusqu'à une fraction volumique critique  $\phi_c$  où elle diverge, et au delà de laquelle le système est bloqué et ne peut plus couler. La fraction volumique critique dépend du coefficient de frottement  $\mu$  entre les grains. Dans le cas frottant on a  $\phi_c^{\mu \neq 0} \simeq 58\%$ , et dans le cas non frottant  $\phi_c^{\mu=0} \simeq 64\%$  (voir figure 3b). Dans un modèle de suspension avec force répulsive à courte portée, on a deux rhéologies possibles. À faible taux de cisaillement, la suspension se comporte comme une suspension de grains non frottants et évolue sur la branche bleue de la figure 3b (faible viscosité). À fort taux de cisaillement, des contacts frottants entre grains apparaissent et la suspension évolue alors sur la branche rouge (forte viscosité). Il y a donc un saut de viscosité lorsqu'on passe du cas non frottant (branche bleue) au cas frottant (branche rouge). Pour des fractions volumiques comprises entre  $\phi_c^{\mu \neq 0}$  et  $\phi_c^{\mu=0}$ , le système peut couler à faible taux de cisaillement mais se bloque à fort taux de cisaillement. En effet, il n'y a plus de branche visqueuse frottante pour  $\phi > \phi_c^{\mu \neq 0}$ . Le diagramme de phase ( $\phi, \dot{\gamma}$ ) de la figure 3c résume les différents régimes observés dans le cadre de ce modèle.

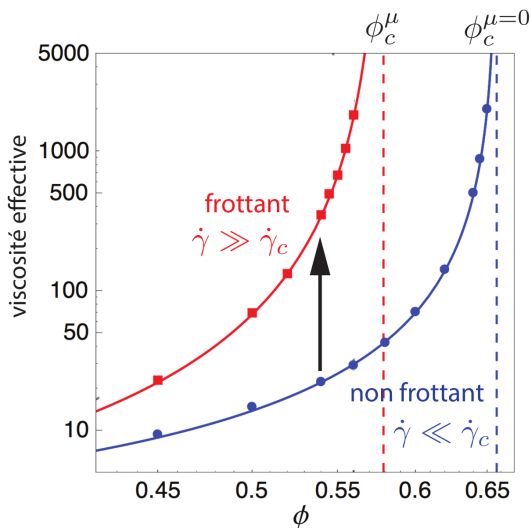
Ce nouveau scénario offre donc un cadre simple et cohérent pour expliquer le rhéo-épaississement des suspensions non browniennes. Cependant, il est difficile de le tester expérimentalement sur des suspensions réelles. En effet, les interactions entre grains à courte portée (répulsion, friction, lubrification) sont difficiles à contrôler et fortement couplées à la physico-chimie des grains et du fluide utilisé. De plus, les suspensions rhéo-épaississantes sont composées de grains de taille micrométrique, ce qui rend difficile la visualisation directe du mouvement des grains.

## Objectifs du stage

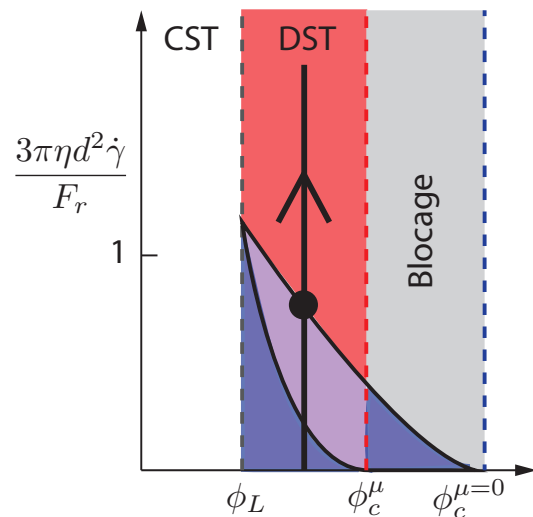
L'objectif de mon stage était de mettre en place une expérience macroscopique modèle permettant d'étudier le scénario décrit ci-dessus. L'idée était de se retrancher aux éléments essentiels : présence de frottement et présence d'une force répulsive. L'hydrodynamique ne semblant pas jouer un rôle, nous avons développé une expérience sans fluide. Pour cela, nous avons choisi d'étudier un milieu granulaire à deux dimensions, constitué de grains répulsifs, grâce à l'introduction d'une force magnétique entre eux-ci. L'objectif était d'étudier la rhéologie de ce système modèle. Comment se comporte un tel milieu lorsqu'on le cisaille en y déplaçant un objet en rotation ? Peut-on observer une transition de rhéo-épaississement dans ce système minimal, en l'absence de tout fluide ?



(a) Introduction des notations du problème.



(b) Rhéologie d'un milieu frottant et d'un milieu non frottant (adapté de [17]).



(c) Espace des phases accessible à une suspension rhéo-épaississante (adapté de [17]).

FIGURE 3 – Transition de rhéo-épaississement d'une suspension de sphères dures frottantes et répulsives, prédite par les simulation numériques de Seto et al. [20, 17]. Figure 3b : Viscosité effective en fonction de la fraction volumique, dans les cas frottant (en rouge) et non frottant (en bleu). Adapté de [17]. Figure 3c : espace des phases accessible à une suspension rhéo-épaississante visqueuse comportant une force de répulsion au contact (portée nulle) entre les grains. Adapté de [17]. On observe différents régimes d'écoulement possibles. CST signifie *continuous shear-thickening* (rhéo-épaississement continu). DST signifie *discontinuous shear-thickening* (rhéo-épaississement discontinu). La zone rouge correspond à un écoulement frottant, la zone bleue à un écoulement non frottant, et la zone de recouvrement bleu-rouge correspond à une zone d'hystérésis du milieu. Lorsque le milieu suit la flèche tracée dans l'espace des phases figure 3c, il passe d'un état frottant à un état non frottant. La transition entre ces deux types d'écoulement se produit au niveau du point, qui correspond à la flèche tracée entre les deux courbes de rhéologie sur la figure 3b.

## 2 Expérience modèle : un milieu granulaire répulsif 2D

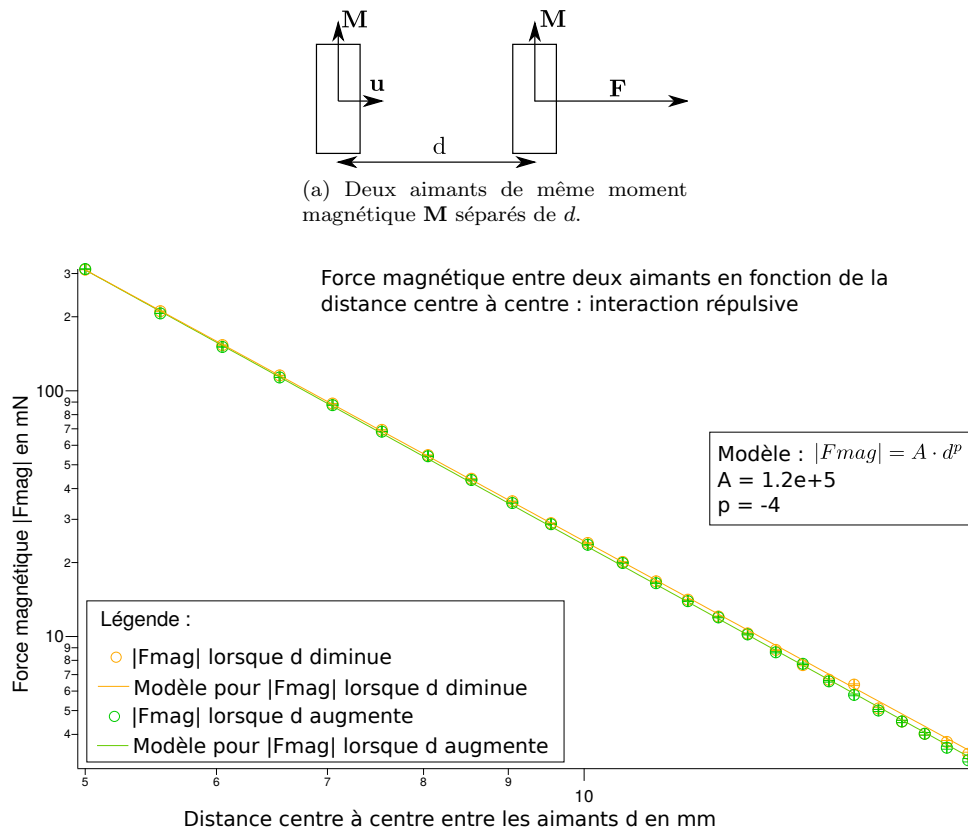
### 2.1 Dispositif expérimental

Le dispositif a été conçu pour contenir les ingrédients-clés du précédent modèle : des grains frottants interagissant via des forces répulsives. Pour cela, nous avons conçu une expérience à deux dimensions contenant un milieu formé de grains rugueux se repoussant entre eux, dans lequel on peut imposer un taux de cisaillement. En réponse à ce taux de cisaillement, le milieu exerce un couple que nous voulons mesurer. Nous avons utilisé des grains cylindriques, contenant des aimants pour introduire une force de répulsion. Ces grains sont en lévitation sur une table à coussin d'air, afin que l'expérience soit à deux dimensions. Dans le milieu, un objet relié à une table de rotation par une tige permet d'imposer un cisaillement. Sur cette tige, nous avons disposé un couplemètre nous permettant de mesurer le couple exercé par le milieu sur l'objet en réponse au cisaillement.

## Grains et force répulsive

Les grains sont des cylindres creux en laiton dont la surface latérale est texturée pour les rendre rugueux. Il est possible de jouer sur le frottement entre grains en utilisant des grains plus ou moins texturés. Le creux permet d'ajouter les aimants dans les grains. Nous avons utilisé des grains de deux tailles différentes : des petits grains de diamètre  $d_{pg} = 1.0$  cm, et des gros grains de diamètre  $d_{gg} = 1.2$  cm. C'est une méthode classique en rhéologie des milieux granulaires pour éviter la cristallisation du milieu.

La force répulsive entre les grains est obtenue, comme indiqué précédemment, en introduisant des aimants cylindriques dans les grains. Considérons les aimants comme deux dipôles magnétiques ayant le même moment magnétique  $\mathbf{M}$  (voir le schéma 4a). On peut calculer la force magnétique répulsive entre ces aimants. Elle s'écrit  $\mathbf{F}_{\text{mag}} = \nabla(\mathbf{M} \cdot \mathbf{B})$ , où  $\mathbf{B}$  est le champ magnétique généré par l'aimant de gauche et  $\mathbf{F}_{\text{mag}}$  la force subie par l'aimant de droite. Comme les aimants sont parallèles, on obtient  $\mathbf{F}_{\text{mag}} = \frac{3\mu_0\mathbf{M}^2}{4\pi d^4}\mathbf{u}$ , où  $\mu_0$  est la perméabilité magnétique du vide,  $d$  la distance entre les aimants et  $\mathbf{u}$  le vecteur unitaire pointant de l'aimant de gauche vers l'aimant de droite. La figure 4b présente la force magnétique entre deux aimants en fonction de la distance  $d$  entre leurs centres (pour les aimants utilisés dans l'expérience). Comme attendu  $\mathbf{F}_{\text{mag}}$  est proportionnelle à  $d^{-4}$ . L'ordre de grandeur de la force de répulsion magnétique entre deux grains au contact est  $F_M \simeq 20$  mN, ce qui correspond à une "pression" magnétique (linéique) de répulsion  $P_M \sim \frac{F_M}{d}$ , c'est-à-dire  $P_M \simeq 20$  mN.cm<sup>-1</sup>.



(b) Force magnétique entre deux aimants en fonction de la distance centre à centre. Points obtenus en orientant les pôles des aimants de façon à ce que la force soit répulsive. Deux séries de points : en orange, points obtenus en éloignant les aimants l'un de l'autre, en vert, points obtenus en rapprochant les aimants.

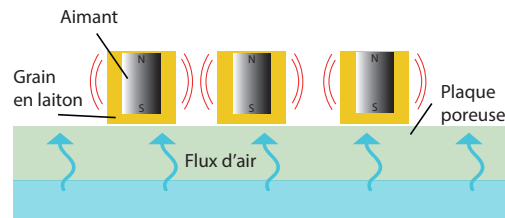
FIGURE 4 – Schéma indiquant les notations du problème, et mesure de la force magnétique entre deux aimants tels que ceux utilisés durant ce stage.

Afin que l'expérience reste à deux dimensions, il faut s'affranchir des frottements entre les grains et leur support. Pour cela, nous avons utilisé une plaque d'oxyde d'alumine, qui est un matériau poreux (taille des pores :  $10 \mu\text{m}$ , plaque carrée de 29 cm de côté), au travers de laquelle nous avons imposé un flux d'air sous une pression de 0.6 bar. Cela crée un coussin d'air suffisant pour faire léviter les grains. La figure 5a résume la mise en place du milieu granulaire. Celui-ci se compose d'environ 200 petits grains et 300 gros grains, ces valeurs ayant été modifiées au cours des expériences afin de modifier la fraction volumique de grains.

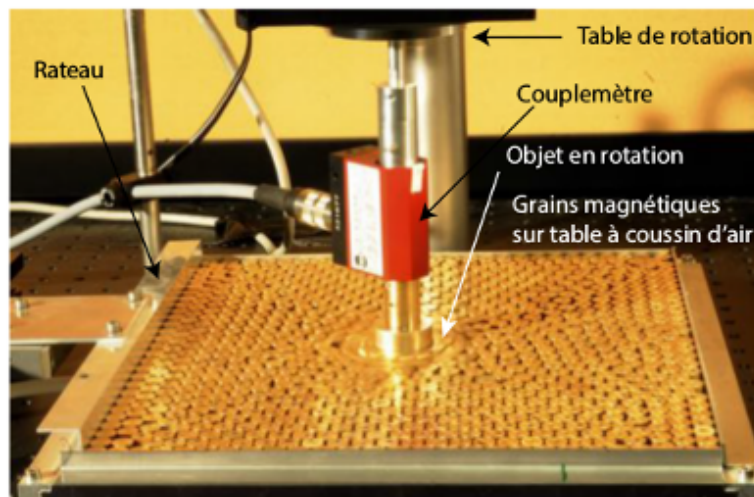


## Rhéomètre

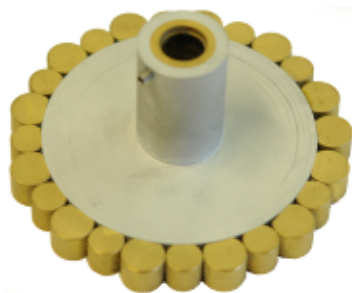
Pour étudier la rhéologie de ce milieu, il faut imposer un cisaillement au système et mesurer la contrainte associée. Pour cela nous faisons tourner un objet dans le milieu grâce à une table de rotation (PI MS62 PD, vitesse de rotation maximale 90 degrés par seconde). Afin de mesurer le couple, un couplemètre (TEI, couple maximum 0.5 Nm, couple minimum  $5.10^{-4}$  Nm) est monté sur la tige reliant la table de rotation à l'objet tournant dans le milieu. L'acquisition du signal émis par le couplemètre se fait via le logiciel SignalExpress. La figure 5b présente le dispositif expérimental.



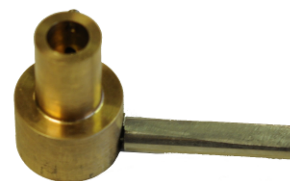
(a) Schéma du dispositif expérimental.



(b) Photographie du dispositif expérimental.



(c) Premier objet utilisé pour cisailier le milieu.



(d) Objet utilisé pour cisailier le milieu dans les mesures présentées dans ce rapport.

FIGURE 5 – Schéma et photographie du dispositif expérimental, mise en place.

## 2.2 Mise en place et difficultés

La mise en place de ce dispositif expérimental a posé quelques difficultés qui nous ont amenées à l'améliorer. Nous allons ici décrire ce processus de mise en place, qui a constitué une partie significative du stage.

Le premier problème rencontré a été celui de la stabilité des petits grains. Ceux-ci étant légers, ils ont tendance à se retourner sur eux mêmes ou à sauter en s'expulsant du milieu sous l'effet des forces magnétiques.



Afin de les en empêcher, nous avons recouvert le milieu d'une plaque de plexiglass (absente de la figure 5b). Celle-ci ne touche pas les grains, pour ne pas introduire de frottement et conserver une expérience à deux dimensions. Elle empêche cependant les petits grains de se retourner.

Le deuxième problème est celui du choix de l'objet tournant permettant d'imposer un taux de cisaillement. Nous avons commencé par utiliser un cylindre (de diamètre 8 cm) sur lequel nous avons collé des grains, comme on peut le voir sur la figure 5c. Cette géométrie correspondait à un rhéomètre de Couette cylindrique à deux dimensions. Cependant, une telle géométrie induit de la migration dans le milieu. La zone proche du cylindre cisailant le milieu est alors déplétée et le couple exercé par le milieu est trop faible pour être exploitable avec notre capteur. Afin de nous affranchir de ce problème, nous avons utilisé un cylindre beaucoup plus petit (diamètre 3 cm) sur lequel nous avons fixé une barre de métal cylindrique (longueur 5 cm, diamètre 1 cm), comme on peut le voir sur la figure 5d. Cette géométrie est moins idéale car le cisaillement généré est fortement inhomogène et non unidirectionnel, mais la tige permet de bien brasser le milieu et de générer un couple mesurable avec notre dispositif. De plus, les mesures deviennent beaucoup moins sensibles aux effets de migration.

### 3 Expériences à “volume” imposé

Dans un premier temps, nous avons effectué des expériences à volume (aire à deux dimensions) imposé. Avant de détailler les expériences réalisées et les résultats obtenus, nous allons commencer par quelques rappels de rhéologie à volume imposé dans le cas de milieux granulaires classiques (non répulsifs).

#### 3.1 Rappels de rhéologie des milieux granulaires à volume imposé

Considérons un milieu granulaire sec confiné entre deux plaques distantes de  $H$ , auquel on impose un taux de cisaillement  $\dot{\gamma}$  (figure 6). Les grains sont des sphères infiniment rigides, de diamètre  $d$  et de densité  $\rho_g$ . On a une certaine fraction volumique  $\phi$  de grains, où  $\phi = \frac{\text{Volume occupé par les grains}}{\text{Volume total}}$ . On se place dans le cas où  $H \gg d$ , c'est-à-dire qu'on néglige les effets de bords. Les paramètres de contrôle dont on dispose sont  $\phi$ ,  $\dot{\gamma}$ ,  $d$  et  $\rho_g$ , soit quatre paramètres en tout. Par analyse dimensionnelle, on voit que le système est décrit par un nombre sans dimension, puisqu'on a trois dimensions pour quatre paramètres. Or, on dispose déjà d'un nombre sans dimension : la fraction volumique  $\phi$ .

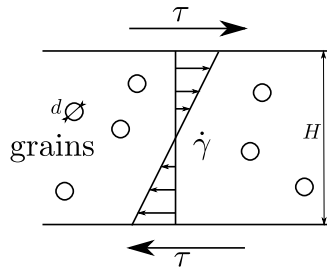


FIGURE 6 – Schéma introduisant les notations du problème.

On cherche à présent à exprimer la contrainte de cisaillement  $\tau$  et la contrainte normale, c'est-à-dire la pression  $P$ , en fonction des paramètres de contrôle. Dimensionnellement, on a  $\tau = \rho_g d^2 f_1(\phi) \dot{\gamma}^2$ , où  $f_1$  est une fonction de  $\phi$  qu'on ne connaît pas a priori. De la même façon, on trouve que  $P = \rho_g d^2 f_2(\phi) \dot{\gamma}^2$ , où  $f_2$  est une autre fonction de  $\phi$ . En réalité, on peut ajouter d'autres paramètres pour décrire le système, comme  $\mu$  le coefficient de frottement entre grains, ou  $e$  le coefficient de restitution élastique. Comme ce sont déjà des nombres sans dimensions, on obtient simplement une dépendance de plus dans  $f_1$  et  $f_2$ . Dans ce rapport, on ne s'intéressera jamais à  $e$ , mais  $\mu$  pourra avoir une influence. Au final, on obtient les lois de Bagnold 3.1 et 3.2 [1] :

$$(3.1) \quad \tau = \rho_g d^2 f_1(\phi, \mu) \dot{\gamma}^2,$$

$$(3.2) \quad P = \rho_g d^2 f_2(\phi, \mu) \dot{\gamma}^2.$$

La différence avec le cas des suspensions visqueuses est que ces quantités sont proportionnelles à  $\dot{\gamma}^2$  et non à  $\dot{\gamma}$ . En revanche, comme pour les suspensions, les fonctions  $f_1$  et  $f_2$  divergent pour une certaine valeur  $\phi_c$  de la fraction volumique, qui dépend du coefficient de frottement entre grains  $\mu$ . En présence de forces répulsives,

on s'attend donc, comme dans les suspensions, à observer une transition (saut de contrainte) entre une branche non frottante  $f_1(\phi, \mu = 0)$  et une branche frottante  $f_1(\phi, \mu \neq 0)$  (voir figure 3).

### 3.2 Méthodologie

Nous allons à présent nous pencher sur les expériences qui ont été réalisées, dans le cas où on contraint le milieu à rester dans un certain volume. Tout d'abord, rappelons qu'il s'agit d'une expérience à deux dimensions. Par abus de langage, nous parlerons de mesures à volume imposé, mais c'est en réalité la surface que nous imposons. Afin de contrôler celle-ci, un des côtés de la table à coussin d'air constituée par la plaque poreuse a été équipé d'un rateau, monté sur une table de translation munie d'un vernier. Grâce à ce rateau, la dimension  $L$  de la table peut être modifiée (voir figure 7). Cela permet d'imposer  $\phi$ , qui est ici défini par  $\phi = \frac{\text{Surface occupée par les grains}}{\text{Surface totale}}$ . Nous appellerons  $\phi$  la fraction volumique par abus de langage, étant entendu qu'il s'agit ici en réalité d'une fraction surfacique. Il convient de noter que  $\phi$  n'est pas homogène, et que la fraction volumique qu'on impose est donc une fraction volumique moyenne.

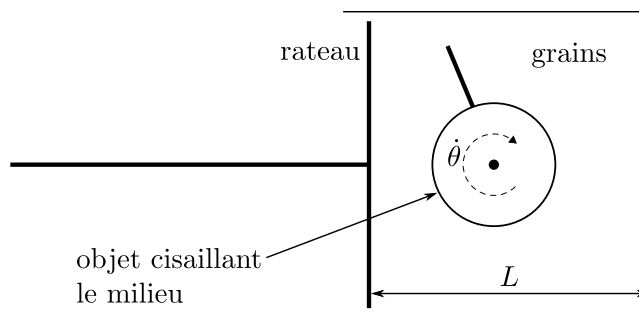


FIGURE 7 – Schéma du dispositif expérimental à volume imposé.

Les paramètres que nous contrôlons ici sont  $\phi$ , via le contrôle de  $L$ , et  $\dot{\theta}$  la vitesse de rotation de l'objet, via la table de rotation. Nous mesurons le couple  $\Gamma$  qu'exerce le milieu sur l'objet grâce au couplemètre. À cause de la géométrie compliquée de notre objet, nous n'avons pas accès dans l'expérience à la contrainte de cisaillement  $\tau$  et au taux de cisaillement  $\dot{\gamma}$ , qui sont fortement inhomogènes dans le milieu. Nous travaillons donc avec des grandeurs macroscopiques (le couple  $\Gamma$  et la vitesse de rotation  $\dot{\theta}$ ).

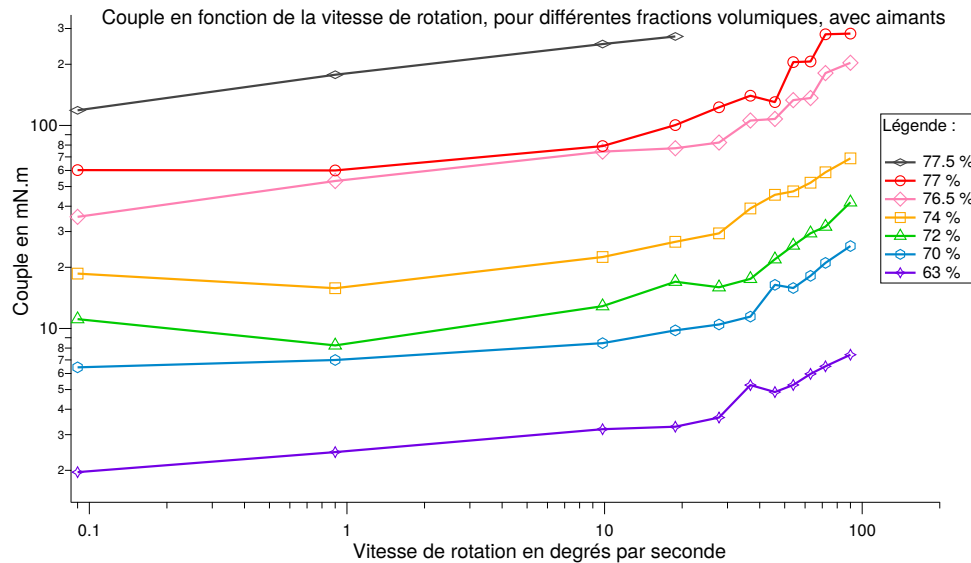
Chaque mesure a été réalisée en faisant une acquisition du signal émis par le couplemètre pendant cinq tours. On moyenne ensuite sur les trois tours centraux, afin de s'affranchir d'un éventuel régime transitoire. Pour chaque mesure, la fréquence d'échantillonnage de l'acquisition a été réglée de façon à ce qu'il y ait 1000 points par tour, quelle que soit la vitesse de rotation de l'objet. Le signal venant du couplemètre présente un offset dû à la carte d'acquisition, qui est systématiquement soustrait au signal. Le logiciel Matlab a été utilisé pour traiter les données et extraire le couple moyenné sur trois tours. Le code utilisé pour traiter les données constitue l'annexe A.

Nous avons utilisé un protocole légèrement différent pour les mesures faites à une vitesse de rotation imposée de 0.09 degrés par secondes. Comme chaque point à cette vitesse aurait demandé une acquisition de plus de cinq heures pour cinq tours, nous n'avons acquis le signal que sur un tour, et avons moyenné le signal entier, soit 1000 points.

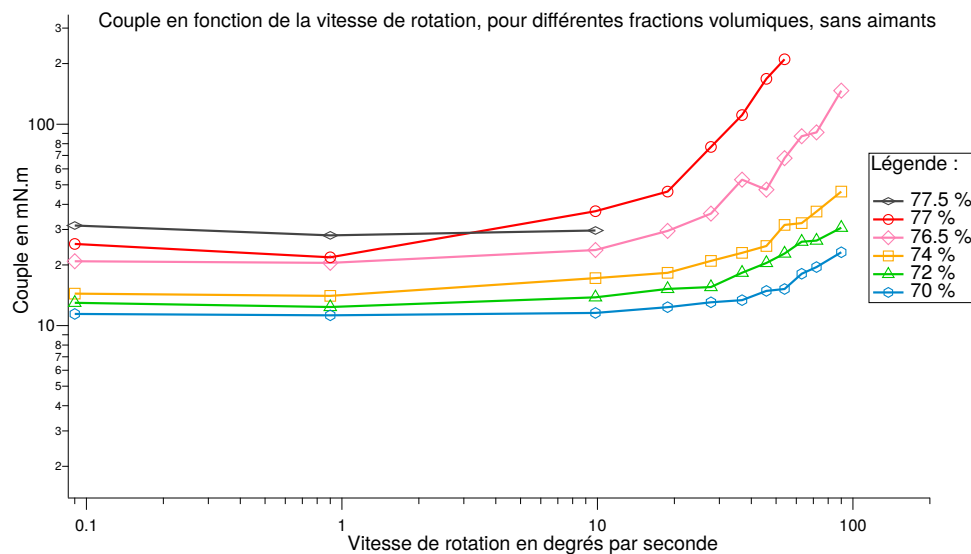
### 3.3 Résultats

La figure 8a présente la variation du couple moyen qui s'exerce sur l'objet en fonction de sa vitesse de rotation pour différentes fractions volumiques, dans le cas avec aimants. Les courbes présentent toutes la même allure. À très basse vitesse de rotation, il existe un couple seuil dans le milieu, dont la valeur dépend fortement de la fraction volumique. Quand la vitesse de rotation augmente, on observe tout d'abord un plateau de couple, puis une augmentation du couple à forte vitesse. Tant le couple seuil que le couple à vitesse maximale (90 degrés par seconde) semblent diverger à une fraction volumique  $\phi \simeq 78\%$ , comme le montre la figure 9a. On remarque, sur la figure 8, que certains points acquis à forte vitesse pour les fortes fractions volumiques  $\phi$  n'apparaissent pas. Ceci est dû au phénomène de *jammimg*, ou blocage : le milieu se fige et ne peut plus couler, ce qui nous empêche d'effectuer la mesure. C'est un des problèmes des expériences menées à volume imposé, qui est dû à la divergence des fonctions  $f_1$  et  $f_2$  apparaissant dans 3.1 et 3.2. Ces effets de blocages sont bien visible sur la figure 10, qui

présente une acquisition dans le temps du signal du couplemètre pour une fraction volumique proche de  $\phi_c$ . On constate que celui-ci présente de fortes fluctuations, qui sont de l'ordre de la moyenne temporelle du signal. Celles-ci sont la signature de blocages transitoires de l'écoulement, qui sont dus à la petite taille de notre système.



(a) Couple en fonction de la vitesse de rotation, cas répulsif.



(b) Couple en fonction de la vitesse de rotation, cas non répulsif.

FIGURE 8 – Tracé du couple en fonction de la vitesse de rotation pour différentes fractions volumiques, avec aimants (cas répulsif) et sans aimants (cas non répulsif).

Le constat le plus important sur la figure 8a est qu'on n'observe pas de transition de rhéo-épaississement lorsqu'on augmente la vitesse de rotation, même aux plus hautes fractions volumiques que nous avons pu étudier. Malgré la présence d'une force répulsive entre les grains, ce système ne se comporte pas, à volume imposé, comme prédit par le modèle de transition frictionnelle dont nous avons parlé dans la section 1. Pour mieux comprendre le rôle de la force répulsive, nous avons effectué les mêmes expériences en enlevant les aimants. Dans ce cas, on devrait retrouver un milieu granulaire classique à deux dimensions, pour lequel la rhéologie est bien connue et donnée par les lois de Bagnold 3.1 et 3.2.

La figure 8b présente la variation du couple qui s'exerce sur l'objet en fonction de sa vitesse de rotation, pour différentes fractions volumiques, dans le cas sans aimants. De façon surprenante l'allure des courbes est très similaire à celle obtenue avec les aimants. Il existe une contrainte seuil, puis une augmentation du couple

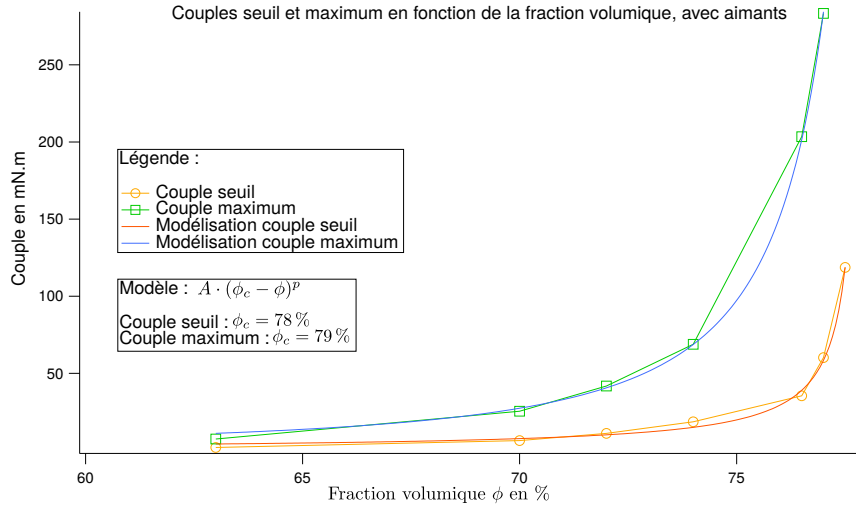
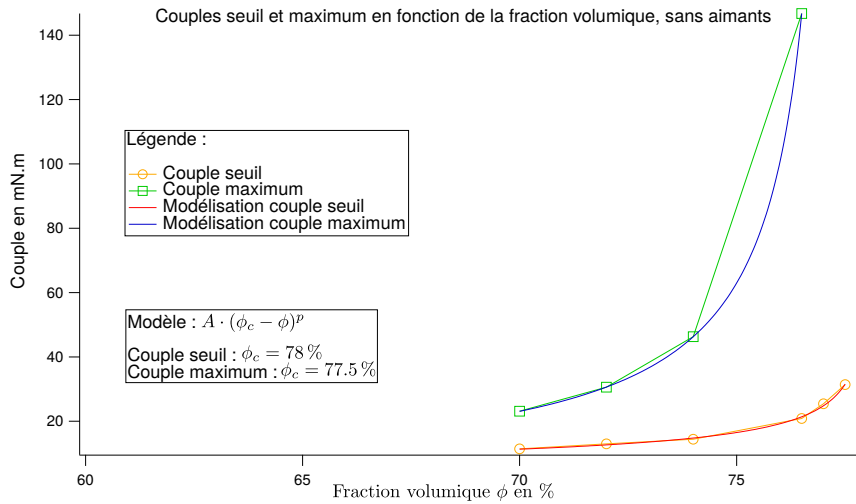
(a) Couple seuil et couple maximum en fonction de  $\phi$ , cas répulsif.(b) Couple seuil et couple maximum en fonction de  $\phi$ , cas non répulsif.

FIGURE 9 – Tracé du couple seuil et du couple maximum en fonction de la fraction volumique pour différentes vitesses de rotation, avec aimants (cas répulsif) et sans aimants (cas non répulsif).

avec la vitesse de rotation. Nous n’observons donc pas du tout le comportement prédit par Bagnold, pour lequel il n’existe pas de contrainte seuil et les contraintes varient proportionnellement à  $\dot{\gamma}^2$ . La rhéologie qualitative du milieu semble être la même dans le cas répulsif et dans le cas non répulsif, mis à part que les courbes sont moins dispersées avec  $\phi$  dans le cas non répulsif. Ce comportement provient sans doute d’effets de taille finie, car la taille de notre système n’est pas très grande par rapport à la taille des grains. Ces effets induisent un seuil parasite dans l’expérience à volume imposé, même sans force de répulsion entre les grains.

On constate enfin (figure 9) que les divergences du couple seuil et du couple à la vitesse maximale ont lieu à la même fraction volumique  $\phi \sim 78\%$ . Là encore, ceci est très différent du comportement prédit par le modèle avec force répulsive à courte portée. En effet, nous nous attendions à ce que le système avec aimants présente deux divergences, selon la vitesse de rotation. À faible vitesse de rotation, la force répulsive empêche le contact entre grains et les contraintes divergent pour  $\phi_c^{\mu=0}$ . À forte vitesse de rotation, la répulsion est vaincue, le système devient frottant, et se bloque donc à  $\phi_c^{\mu \neq 0} < \phi_c^{\mu=0}$ . Ce n’est pas ce que l’on observe dans notre expérience avec aimants, qui ne présente qu’une seule divergence.

Il est difficile d’aller plus loin dans l’interprétation de ces expériences à volume imposé car la taille finie de notre système nous empêche d’étudier proprement la rhéologie lorsqu’on s’approche du blocage. Ce problème est bien connu dans l’étude des milieux granulaires. Un moyen de s’en affranchir est de travailler à pression

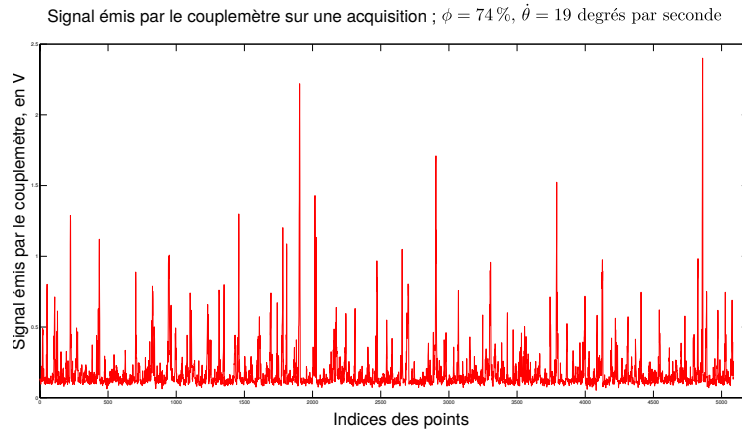


FIGURE 10 – Signal émis par le couplemètre en fonction du temps. Acquisition de cinq tours (5000 points), fraction volumique  $\phi = 74\%$ , vitesse de rotation  $\dot{\theta} = 19$  degrés par seconde.

imposée plutôt qu'à volume imposé. Nous avons donc conçu un nouveau dispositif en ce sens.

## 4 Expériences à “pression” imposée

Nous avons vu qu'à volume imposé, l'approche du blocage est difficile. Lorsqu'on impose la pression au lieu du volume, on laisse au milieu la possibilité de se dilater, ce qui lui permet de ne pas se bloquer sur les bords à cause de l'apparition d'une microstructure locale ne présentant pas de possibilité d'écoulement. Dans cette section, nous allons présenter les expériences que nous avons réalisées à pression imposée. Afin de mieux comprendre le comportement de notre système, nous commençons cette section par quelques rappels de rhéologie à pression imposée dans le cas de milieux granulaires classiques (non répulsifs).

### 4.1 Rappels de rhéologie des milieux granulaires à pression imposée

Considérons un milieu granulaire sec confiné entre deux plaques distantes de  $H$ , sur lesquelles on impose une pression  $P$ , et dans lequel on impose un taux de cisaillement  $\dot{\gamma}$  (voir figure 11). Les grains sont de nouveau des sphères infiniment rigides, de diamètre  $d \ll H$  et de densité  $\rho_g$ . Les paramètres de contrôle sont cette fois  $P$ ,  $\dot{\gamma}$ ,  $d$  et  $\rho_g$ , soit de nouveau quatre paramètres. Ici  $\phi$  n'est pas un paramètre de contrôle, puisque le volume total n'est pas fixé. La fraction volumique n'est donc pas imposée par l'expérimentateur, la distance entre les plaques s'ajuste et  $\phi$  varie avec  $H$ . L'analyse dimensionnelle nous dit qu'il existe de nouveau un nombre sans dimension décrivant le système, mais ce n'est pas  $\phi$ . On construit une grandeur adimensionnée  $I = \dot{\gamma} d \sqrt{\frac{\rho_g}{P}}$  appelée *nombre inertiel*. On cherche à exprimer  $\tau$  et  $\phi$  en fonction des paramètres de contrôle.

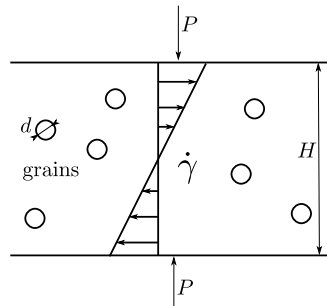


FIGURE 11 – Schéma introduisant les notations du problème.

Dimensionnellement, on obtient  $\tau = f(I)P$ , et  $\phi = \phi(I)$  directement puisque  $\phi$  est sans dimension. La fonction  $f$  est a priori inconnue. Par analogie avec les lois d'Amontons-Coulomb, on l'interprète comme un

coefficient de frottement macroscopique et on le note  $\tilde{\mu}$ . Comme précédemment, on peut ajouter  $\mu$ , le coefficient de frottement entre grains, dans le problème. Attention,  $\mu$  est un coefficient de frottement *microscopique*, a priori différent de  $\tilde{\mu}$ . On obtient au final les lois :

$$(4.1) \quad \tau = \tilde{\mu}(I, \mu)P,$$

$$(4.2) \quad \phi = \phi(I, \mu).$$

Il convient de préciser que la rhéologie intrinsèque du milieu ne change pas selon qu'on travaille à volume ou à pression imposée. Seule la méthode expérimentale utilisée pour sonder la rhéologie change. Il existe une correspondance entre les équations 3.1 et 3.2 et les équations 4.1 et 4.2 (voir [14]).

L'intérêt de travailler à pression imposée est que, contrairement au cas à volume imposé, les fonction  $\tilde{\mu}$  et  $\phi$  ne divergent pas quand on s'approche de la transition de blocage, c'est à dire quand  $I$  tend vers zéro. La figure 12, adaptée de [14], présente l'allure de  $\tilde{\mu}(I)$  et de  $\phi(I)$ . On a

$$\tilde{\mu} \xrightarrow{I \rightarrow 0} \tilde{\mu}_{\text{seuil}} \quad \text{et} \quad \phi \xrightarrow{I \rightarrow 0} \phi_c.$$

On a déjà vu que  $\phi_c$  dépendait du coefficient de frottement microscopique  $\mu$ , c'est également le cas pour  $\tilde{\mu}_{\text{seuil}}$ . Ainsi, quand on cisaille de façon quasi-statique un milieu granulaire à pression imposée, on accède directement à la fraction volumique critique et au coefficient de frottement macroscopique du milieu, qui sont reliés au frottement entre grains.

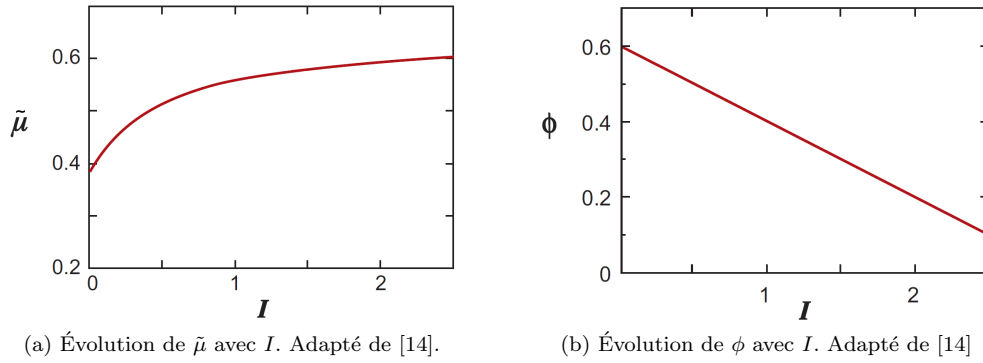


FIGURE 12 – Évolution des fonctions  $\tilde{\mu}$  et  $\phi$  avec le nombre inertiel  $I$ . Adapté de [14].

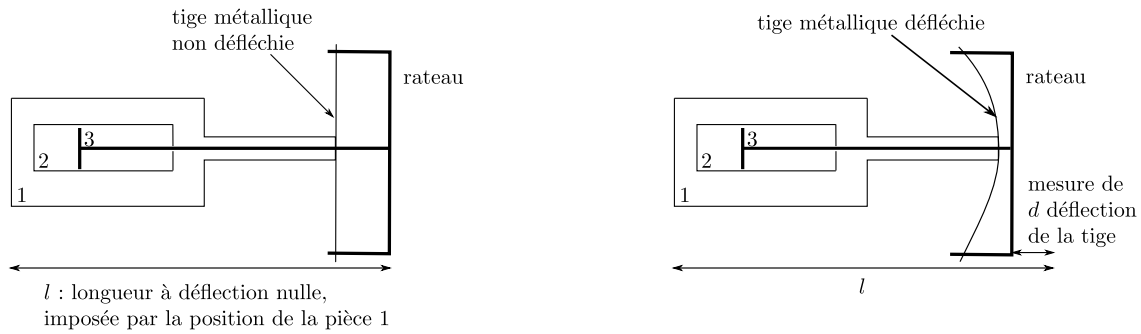
## 4.2 Méthodologie

Penchons-nous à présent sur les expériences réalisées. Nous allons commencer par décrire la méthodologie utilisée. Afin d'imposer la pression, nous avons conçu une *arbalette*, qui a remplacé le rateau utilisé pour imposer le volume (voir section 3). Son principe est résumé sur les figures 13a et 13b.

Un nouveau rateau (pièce 3) se déplace horizontalement dans une glissière (pièce 2) pour accommoder les fluctuations de volume du milieu. La taille de la pièce 2 limite l'amplitude de ce déplacement. La pièce 2 est fixée sur une table de translation, dont la partie mobile est la pièce 1. Celle-ci est munie d'un vernier, afin qu'on puisse modifier la position moyenne du rateau. Enfin, une tige en métal joue le rôle de ressort en s'opposant plus ou moins aux mouvements du rateau par rapport à la glissière. En jouant sur la raideur de ce ressort, nous pouvons donc contrôler la pression exercée par le rateau sur le milieu. Remarquons qu'il s'agit ici d'une pression linéique, puisque l'expérience est à deux dimensions. On a  $P_{\text{imp}} = \frac{F_{\text{imp}}}{L_{\text{rateau}}}$ , où  $P_{\text{imp}}$  est la pression imposée par l'arbalette au milieu,  $F_{\text{imp}}$  est la force imposée par l'arbalette via le ressort, et  $L_{\text{rateau}}$  est la longueur du rateau. Nous avons muni le rateau d'un curseur (non représenté sur le schéma) qui se déplace au dessus d'une règle. Il est ainsi possible de mesurer la déflexion de la tige.

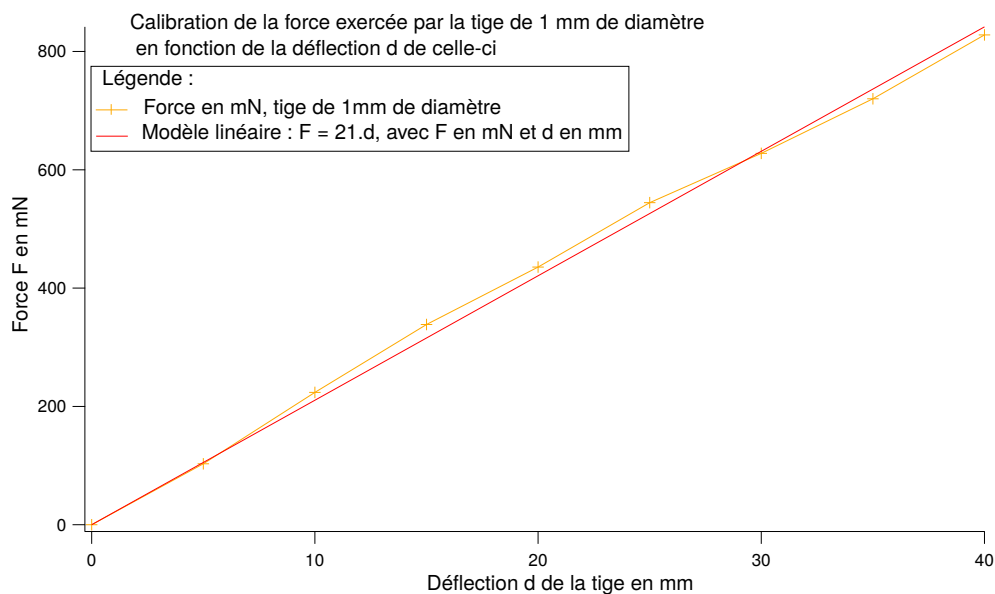
Afin de connaître la pression imposée dans le milieu grâce à ce dispositif, nous avons dû l'étalonner pour chacune des tiges métalliques utilisées. Un exemple d'un tel étalonnage est donné sur la figure 13c. Cette figure montre que la force exercée par la tige qui fait office de ressort dépend linéairement de sa déflexion.

Les paramètres que nous contrôlons dans ces expériences sont  $P_{\text{imp}}$ , via l'arbalette, et  $\dot{\theta}$  via la table de rotation. Nous mesurons toujours le couple  $\Gamma$  qu'exerce le milieu grâce au couplemètre. Nous mesurons également la position du curseur en prenant, en parallèle de l'acquisition du couple, une photo par seconde au niveau du rateau de l'arbalette. Cette mesure est essentielle puisque c'est elle qui nous permet, a posteriori, de calculer la



(a) Arbalette avec la tige non défléchie : pas de contrainte imposée au milieu.

(b) Arbalette avec la tige défléchie : on impose une contrainte sur le milieu.



(c) Exemple d'une courbe de calibration de l'arbalette avec une tige de 1 mm de diamètre.

FIGURE 13 – Fonctionnement de l'arbalette et exemple de calibration.

pression que nous avons exercée sur le milieu. La mesure de la position du curseur nous permet également de calculer la fraction volumique au cours du temps.

Les mesures ont été réalisées à vitesse faible pour être dans le régime quasi-statique que nous avons décrit précédemment ( $I \rightarrow 0$ ). Pour le vérifier, nous avons effectué certaines expériences en changeant la vitesse de rotation de l'objet (9 degrés par seconde et 19 degrés par seconde). Nous n'avons pas observé de changement du couple ou de la fraction volumique avec la vitesse, suggérant que nous sommes bien dans le régime quasi-statique. Les acquisitions ont été faites sur cinq tours. Le couple a été moyenné sur les trois tours centraux. Les photos ont été mises en forme avec le logiciel ImageJ, puis traitées avec Matlab. On trouvera les codes ImageJ et Matlab pour le traitement d'images en annexe (C et B). La déflexion a été calculée en faisant la moyenne sur toute l'acquisition, soit cinq tours. Des problèmes techniques nous ont empêchés, pour certains points, de régler la fréquence d'échantillonnage à la bonne valeur afin d'avoir de nouveau 1000 points par tours. Pour ces points, la fréquence d'échantillonnage est de 10 Hz. Nous n'avons pas observé de différence significative de comportement entre ces points de mesure et ceux comportant bien 1000 points par tour.

### 4.3 Résultats

Nous avons commencé par étudier notre dispositif en utilisant les grains non aimantés, pour vérifier que nous retrouvions le comportement classique d'un milieu granulaire cisailé à pression imposée. Les symboles pleins

verts des figures 14 et 15 présentent l'évolution du rapport entre le couple mesuré et la pression imposée :  $\frac{\Gamma}{P_{imp}}$  d'une part, et la fraction volumique critique  $\phi_c$  d'autre part, en fonction de la pression imposée au système. Le rapport  $\frac{\Gamma}{P_{imp}}$  peut s'interpréter comme un analogue du coefficient de frottement macroscopique du milieu  $\tilde{\mu} = \frac{\tau}{P_{imp}}$ , et nous utiliserons ce vocabulaire par la suite.

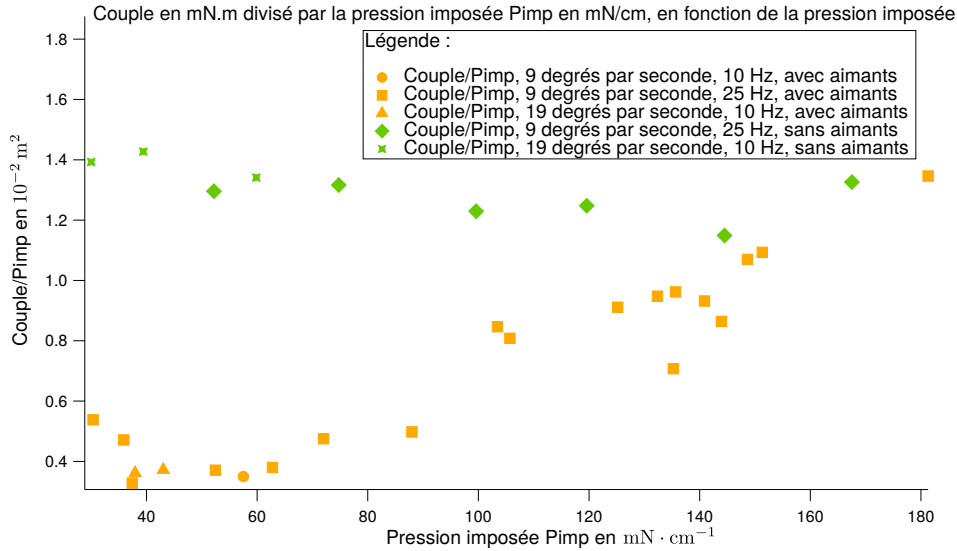


FIGURE 14 – Couple divisé par la pression imposée (analogue du coefficient de frottement macroscopique) en fonction de la pression, avec aimants (cas répulsif) et sans aimants (cas non répulsif).

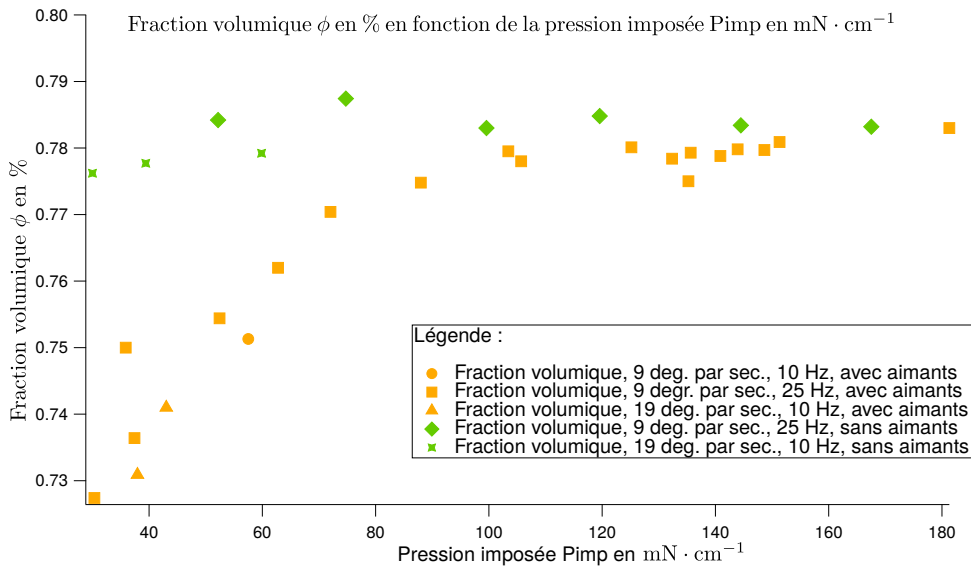


FIGURE 15 – Fraction volumique en fonction de la pression, avec aimants (cas répulsif) et sans aimants (cas non répulsif).

Nous constatons que le coefficient de frottement du milieu et la fraction volumique sont constants, indépendants de la pression imposée. Ce comportement est normal dans le cas d'un milieu granulaire classique en régime quasi-statique. Dans ce cas, nous avons vu que le coefficient de frottement  $\tilde{\mu}$  tend vers le coefficient de frottement seuil  $\tilde{\mu}_{seuil}$  et que la fraction volumique tend vers la fraction volumique critique  $\phi_c$ , qui sont des constantes du milieu. La fraction volumique critique mesurée dans notre expérience est  $\phi_c \simeq 78\%$ , similaire à celle estimée lors de nos mesures à volume imposé. Elle est aussi en accord avec les fractions volumiques critiques obtenues dans les simulations 2D de milieux granulaires frottants de da Cruz et al. [9]. Pour calculer un coefficient de



frottement effectif dans notre cas, on peut construire une contrainte linéique  $\tau$  à partir du couple mesuré en utilisant la taille  $l$  de l'objet qui brasse le milieu :  $\tau \sim \frac{\Gamma}{2\pi l^2}$ . En prenant  $l = 6.5$  cm, on trouve  $\tilde{\mu}_{\text{seuil}} \sim \frac{\tau}{P_{\text{imp}}} \sim 0.5$ , ce qui est un ordre de grandeur raisonnable dans le cas de grains très rugueux comme dans notre expérience.

Nous avons ensuite étudié la rhéologie à pression imposée du système avec grains aimantés (symboles pleins oranges sur les figures 14 et 15). On constate cette fois une différence claire entre le cas non répulsif et le cas répulsif. En présence de force répulsive, le coefficient de frottement macroscopique du milieu n'est plus constant, mais dépend fortement de la pression imposée. À faible pression de confinement, on trouve  $\frac{\Gamma}{P_{\text{imp}}} \sim 0.4$ , ce qui correspond à un coefficient de frottement macroscopique très faible  $\tilde{\mu}_{\text{seuil}} \sim 0.15$ . Le frottement macroscopique du milieu augmente ensuite à peu près linéairement avec la pression de confinement pour retrouver ensuite la valeur du milieu sans aimants à fortes pressions de confinement. On observe également que la fraction volumique dépend de la pression. En présence d'une force magnétique, elle n'est plus constante. La fraction volumique critique du milieu part d'une valeur assez basse à faible pression ( $\phi_c \sim 72\%$ ) puis augmente continûment avec la pression jusqu'à saturer à la même valeur que dans le cas non répulsif.

L'observation d'une augmentation du coefficient de frottement macroscopique avec la pression dans notre système répulsif est la signature d'une transition frictionnelle dans le milieu. En effet, ce coefficient dépend directement du coefficient de frottement microscopique entre les grains. Tant que la pression de confinement est faible par rapport aux forces de répulsion magnétique, les grains ne sont pas en contact et le milieu se comporte comme un milieu granulaire sans frottement. Quand la pression de confinement dépasse les forces de répulsions, les grains entrent en contact et le frottement entre grains est mobilisé. Cela correspond à une augmentation forte du coefficient de frottement macroscopique du milieu, comme attendu dans le scénario de rhéo-épaississement décrit section 1.

L'évolution de la fraction volumique critique avec la pression est en revanche très différente de celle prédite par le modèle théorique. En effet, lorsque les grains sont non frottants, c'est-à-dire aux faibles pressions, ce scénario prédit que la fraction volumique critique  $\phi_c^{\mu=0}$  est *plus élevée* que celle pour des grains frottants  $\phi_c^{\mu \neq 0}$ , que l'on obtient à forte pression. Dans notre expérience, c'est l'inverse : la fraction volumique du milieu non frottant est *plus faible* que celle du milieu frottant. Cette différence essentielle vient certainement du fait que notre force répulsive magnétique est à longue portée. Avec les aimants que nous avons utilisés, son intensité reste importante sur une distance de l'ordre du diamètre d'un grain. Ainsi, pour une faible pression de confinement, il existe une fraction volumique d'équilibre plus faible que  $\phi_c^{\mu \neq 0}$  correspondant à l'équilibre entre la pression extérieure et la force magnétique. Dans ce régime, les grains ne se touchent pas et le milieu est compressible (ou élastique). Cette élasticité à longue portée ne permet pas de rapprocher les grains jusqu'au contact à force nulle, comme dans les modèles de Seto et al et Wyatt et Cates. Nous verrons dans la discussion que cela a des conséquences importantes sur la possibilité d'observer du rhéo-épaississement dans notre système.

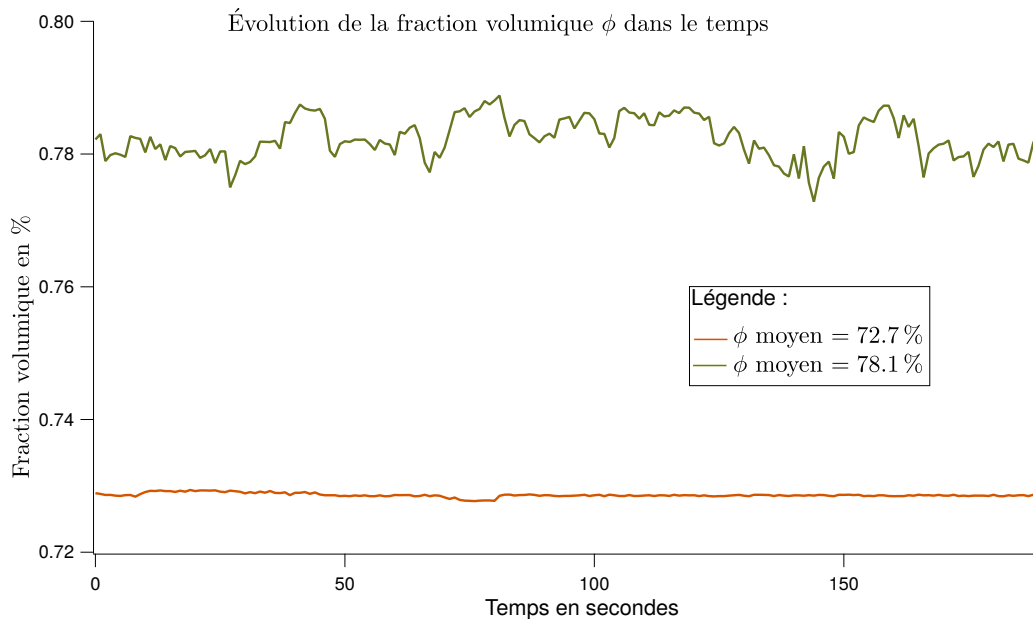


FIGURE 16 – Variations temporelles de la fraction volumique, pour deux valeurs de  $\phi_{\text{moyen}}$  différentes.

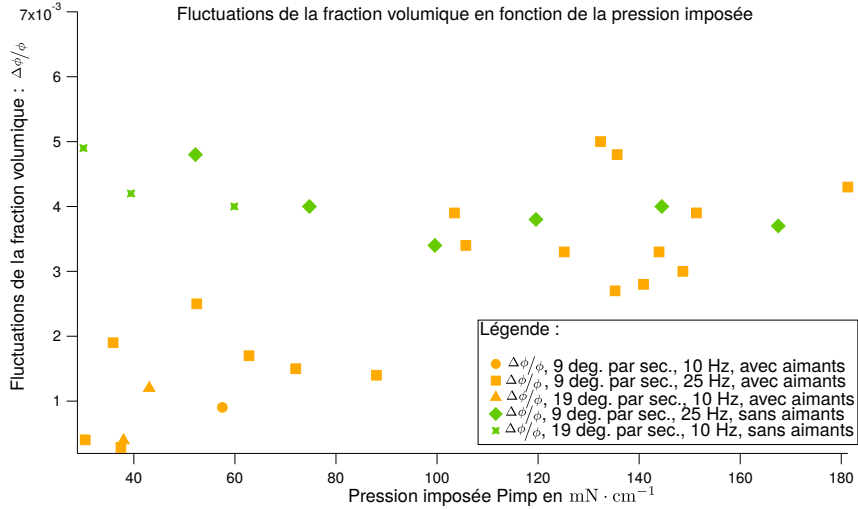


FIGURE 17 – Fluctuations relatives de la fraction volumique en fonction de la pression, avec (cas répulsif) et sans (cas non répulsif) aimants.

La transition entre un régime “mou” sans frottement et un régime granulaire frottant que nous mettons en évidence est également visible quand on s’intéresse aux fluctuations de densité du milieu à pression imposée. La figure 16 présente les fluctuations temporelles de la fraction volumique du milieu dans le cas répulsif. Nous avons superposé le cas d’une pression de confinement faible (en orange, régime “mou” non-frottant) et d’une pression de confinement forte (en vert, régime granulaire frottant). On constate qu’à faible pression, les fluctuations sont faibles, tandis qu’à forte pression elles sont élevées. Cette tendance est confirmée sur la figure 17, qui compare les fluctuations de fraction volumique du système avec ou sans aimants, en fonction de la pression imposée. Cette différence suggère une différence qualitative entre l’écoulement quasi-statique d’un milieu confiné mou et l’écoulement d’un milieu granulaire rigide confiné. Dans le cas du milieu mou, il semble que les réarrangement du milieu restent localisés dans l’espace. Dans le cas d’un milieu rigide au contraire, des chaînes de force se créent dans le milieu et s’ancrent sur les parois. Pour que l’écoulement se poursuive, il est nécessaire de les casser. Les réarrangements sollicitent alors l’ensemble de la taille du système.

#### 4.4 Discussion

Les expériences à pression imposée nous ont permis de clarifier le comportement rhéologique de notre système. Nous mettons bien en évidence une transition frictionnelle entre un milieu “non frottant” à faible pression de confinement et un milieu frottant à forte pression de confinement, comme dans les modèles récents de rhéo-épaississement en présence de forces répulsives. En revanche, la portée relativement élevée de la force magnétique entre deux grains dans notre expériences introduit une différence majeure avec ces modèles : il existe une pression non nulle d’origine magnétique avant même que les grains n’entrent en contact. Cette “élasticité” du milieu explique sans doute que nous n’ayons pas pu observer de rhéo-épaississement dans nos expériences à volume imposé. Pour le comprendre, nous pouvons reprendre le diagramme de phase présenté dans l’état de l’art section 1 pour des suspensions visqueuses avec une force de répulsion  $F_r$  de portée nulle (figure 18). Dans ce diagramme, le paramètre sans dimension qui contrôle la transition de rhéo-épaississement est le rapport entre la force de cisaillement,  $\eta\dot{\gamma}d^2$  et la force de répulsion  $F_r$ . Dans notre expérience, il y a deux différences avec cette situation. Premièrement, nous ne sommes pas dans une suspension visqueuse puisqu’il n’y a pas de fluide entre les grains. La force de cisaillement varie donc comme  $\rho\dot{\gamma}^2d^3$ , où  $\rho$  est la densité surfacique de nos grains (puisque l’on est à 2D). Deuxièmement, les forces magnétiques entre grains sont à longue portée. La barrière de force à franchir pour mettre les grains au contact n’est donc pas  $F_M = P_M d$ , où  $P_M$  est la pression magnétique lorsque tous les grains se touchent, mais  $(P_M - P_0(\phi))d$ , où  $P_0(\phi)$  est la pression magnétique à taux de cisaillement nul pour  $\phi < \phi_c^{\mu \neq 0}$ . La fonction  $P_0(\phi)$  est précisément la réciproque de la fonction  $\phi_c(P)$  que l’on a mesurée dans l’expérience à pression imposée avec les aimants, dans le régime quasi-statique ( $I \rightarrow 0$ ). Par conséquent, la transition frictionnelle doit avoir lieu, dans notre expérience, lorsque  $\rho\dot{\gamma}^2d^3 \sim (P_M - P_0(\phi))d$ , soit quand le paramètre sans dimension  $\rho d^2 \dot{\gamma}^2 + P_0(\phi)/P_M \sim 1$ . La figure 18 présente le diagramme de phase modifié que l’on

imagine dans le cas de notre système inertiel avec des forces répulsives à longue portée. On constate que même à taux de cisaillement nul, le paramètre sans dimension qui décrit la transition frictionnelle n'est pas nul, mais vaut  $P_0(\phi)/P_M$  (courbe verte sur la figure 18). On ne peut pas explorer l'espace des phases en dessous de cette courbe et la zone verte de la figure 18 nous est donc interdite. La présence d'une force à longue portée nous masque donc une partie importante de l'espace des phases, celle qui correspond à la transition discontinue de rhéo-épaississement et au blocage dans le cas de force à très courte portée. Cela explique sans doute que nous n'ayons pas vu de transition brutale de rhéo-épaississement dans les expériences à volume imposée (indépendamment des problèmes de tailles finie). De plus, la présence d'une pression  $P_0(\phi)$  non nulle pour  $\phi < \phi_c^{\mu \neq 0}$  introduit une contrainte seuil dans le milieu, qui masque sans doute la zone de rhéo-épaississement continue a priori accessible dans notre système.

Nous ne pouvons pas superposer de façon quantitative la fonction  $P_0(\phi)/P_M$  obtenue dans nos expériences sur l'espace des phases, car celui ci correspond à un système différent (force très courte portée). Nous constatons de plus que dans nos expériences, la transition a lieu à une pression critique  $P_c$ , qui devrait correspondre à la pression magnétique  $P_M$  qui règne dans le milieu lorsque tous les grains sont au contact. Cependant, avec nos données  $P_c \sim 100 \text{ mN} \cdot \text{cm}^{-1}$ , alors qu'en calculant l'ordre de grandeur de  $P_M$  on trouve  $P_M \sim 20 \text{ mN} \cdot \text{cm}^{-1}$ . Pour l'instant, nous ne savons pas à quoi cette différence est due. Pour établir proprement l'espace des phases dans notre système et conclure quand à la possibilité ou non d'observer une transition de rhéo-épaississement, il faudrait poursuivre l'étude à pression imposée en variant également  $I$ .

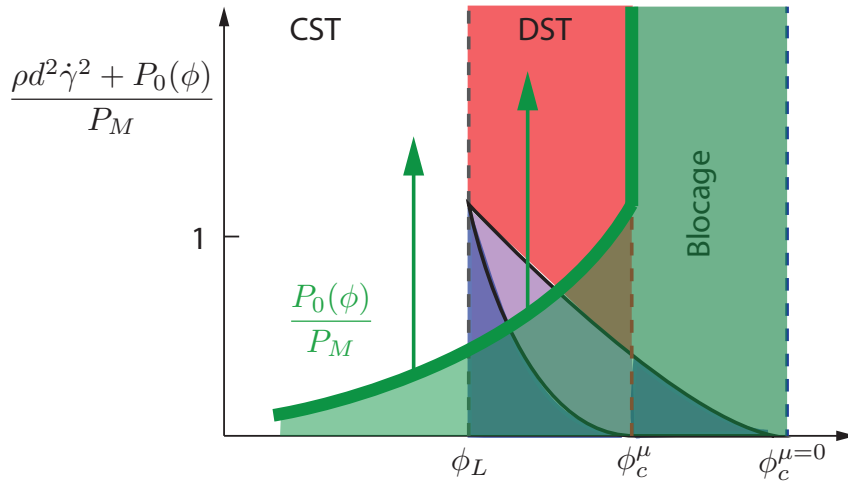


FIGURE 18 – Allure de l'espace des phases auquel nous nous attendons pour notre milieu répulsif. On a toujours CST = rhéo-épaississement continu et DST = rhéo-épaississement discontinu (cf figure 3c).

## 5 Perspectives

Ce stage a constitué un premier pas vers une thèse étudiant l'origine microscopique du phénomène de rhéo-épaississement dans le but de concevoir, à terme, des suspensions rhéo-épaississantes artificielles à la rhéologie contrôlées. Nous proposons donc ici plusieurs pistes à explorer durant cette thèse.

### 5.1 Expérience modèle

Nous voudrions tout d'abord minimiser autant que possible les effets de bords. Pour cela, nous envisageons un dispositif de plus grande taille dans lequel l'écoulement sera induit dans le milieu par une courroie montée sur deux poulies (voir figure 19). L'avantage de cette configuration est qu'elle produit un écoulement homogène (taux de cisaillement constant). Nous contrôlerons ainsi mieux les expériences. Ce dispositif sera également équipé d'un système permettant d'imposer la pression. Notre but est de pouvoir explorer des écoulements pour différentes valeurs de  $I$  et pas seulement pour  $I \rightarrow 0$ .

De plus, comme nous l'avons vu, notre milieu granulaire répulsif ne peut pas atteindre des fractions volumique très fortes lorsque la pression imposée est faible. Cela est dû à la portée de l'interaction dipolaire magnétique qui

constitue notre force répulsive. La zone de l'espace des phases  $\left(\frac{\rho d^2 \gamma^2 + P_0(\phi)}{P_M}, \phi\right)$ , figure 18 dans laquelle se situe la transition frictionnelle est donc largement inaccessible à notre système. Pour l'atteindre, il faut impérativement que la force répulsive entre grains soit de courte portée. Nous sommes donc en train de chercher une alternative aux aimants utilisés ici afin de réduire la portée de la répulsion.

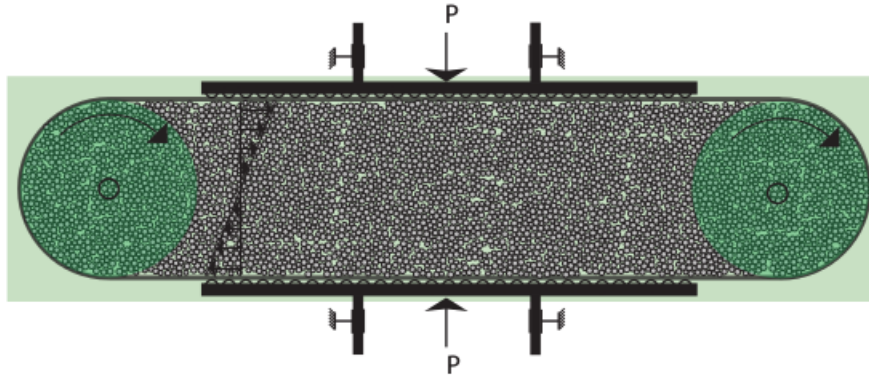


FIGURE 19 – Schéma de la future expérience modèle à 2D permettant d'imposer un taux de cisaillement homogène.

## 5.2 Suspensions réelles

L'idée du projet de thèse est de comprendre le phénomène de rhéo-épaississement dans le but de développer des suspensions rhéo-épaississantes artificielles dont on pourrait contrôler la rhéologie. Pour ce faire, nous voulions, en premier lieu, tester la validité expérimentale du modèle de transition frictionnelle. Avec l'expérience modèle décrite dans le rapport, nous cherchons à confirmer que la présence de frottements et de répulsion suffit à induire du rhéo-épaississement dans un milieu. Cependant, il est nécessaire de vérifier ensuite si ce mécanisme simple est bien celui à l'oeuvre dans les suspensions rhéo-épaississantes courantes. Il est donc nécessaire d'étudier leur rhéologie.

L'exemple typique des suspensions rhéo-épaississantes est le mélange d'amidon de maïs et d'eau. Ce système est difficile à étudier expérimentalement car il vieillit rapidement : dans l'eau, les grains d'amidons se détériorent (à cause de la réaction d'hydrolyse) et pourrissent (sous l'action de divers microorganismes). Nous avons tenté de mélanger l'amidon à d'autres solvants afin de ralentir le vieillissement, mais cela a parfois pour effet de tuer le rhéo-épaississement, qui est sensible à la physico-chimie. Une alternative nous a été proposée par la société Chryso, avec qui nous avons commencé un partenariat. Cette société produit des adjuvants chimiques pour la fabrication des bétons modernes. Dans ces bétons, il est souvent introduit une faible quantité de polymères dit superplastifiants qui ont pour effet de fortement diminuer la viscosité du mélange. Cette diminution de la viscosité pourrait avoir un lien avec la transition de rhéo-épaississement : les polymères, en se greffant à la surface des grains constituant le ciment, pourraient faire apparaître une force répulsive entre grains. Ceux-ci, initialement frottants, deviendraient ainsi répulsifs, donc presque non frottants. Ce système devrait alors pouvoir couler beaucoup plus facilement à faible taux de cisaillement, si on s'appuie sur le modèle de transition frictionnelle présenté à la section 1. Nous avons conduit des expériences préliminaires avec des suspensions de grains de calcite additionnées de polymères superplastifiants venant des entreprises Chryso et Sika. La rhéologie de ces systèmes, qui est comparée à celle d'un mélange d'amidon de maïs (ici de la marque Maïzena) et d'eau dans la figure 20, montre qu'ils sont fortement rhéo-épaississant. Le grand avantage de la calcite par rapport à l'amidon de maïs est qu'elle est stable dans l'eau. Nous envisageons par la suite d'utiliser des suspensions de calcite additionnées polymères pour étudier le rhéo-épaississement dans les suspensions réelles.

Dans la suite, nous avons pour projet de développer un rhéomètre original à pression imposée permettant de sonder la transition frictionnelle dans des suspensions réelles. Le principe de fonctionnement est le suivant (voir figure 21) : la hauteur d'eau  $H$  impose un gradient de pression dans le milieu. Ce gradient de pression induit un écoulement de Darcy (figuré par les flèches bleues sur le schéma figure 21). À une profondeur  $z$  donnée, la pression *entre les grains* vaut  $P_g = (\rho_g - \rho_f)\phi gz + \frac{\rho_f g H}{L}$ , où :  $\rho_f$  est la densité du fluide,  $\rho_g$  est la densité des grains,  $\phi$  est la fraction volumique de grains dans la suspension et  $g$  est l'accélération de la pesanteur. Ainsi, on peut imposer la pression en choisissant de travailler à une certaine profondeur. On impose également la contrainte

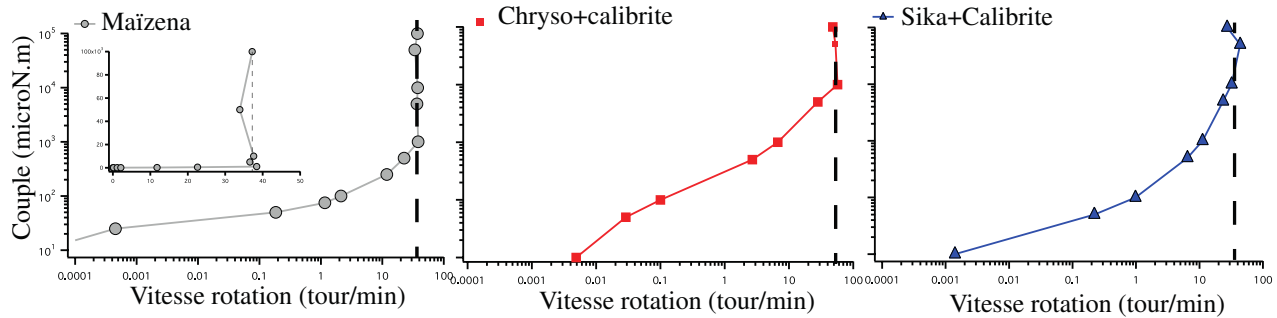


FIGURE 20 – Rhéologie de trois suspensions rhéo-épaississantes différentes, échelle logarithmique. À gauche, insertion : échelle linéaire.

de cisaillement  $\tau$  grâce à la tête de rhéomètre qui tourne dans la suspension. Ainsi, on connaît à la fois  $\tau$ , qu'on mesure, et  $P_g$ , qu'on impose. Il est donc possible de remonter au coefficient de frottement macroscopique  $\tilde{\mu} = \frac{\tau}{P_g}$ , et de connaître son évolution en fonction de  $P_g$ . Une fois le rhéomètre conçu, il nous faudra tester son fonctionnement sur des milieux granulaires simples dont la rhéologie est connue. Une fois le fonctionnement calibré, nous pourrons l'utiliser pour tester l'hypothèse de transition frictionnelle dans les suspensions d'amidon de maïs, ainsi que dans des suspensions de calcite additionnées de polymères superplastifiants. Nous espérons ensuite comprendre suffisamment bien les mécanismes mis en oeuvre dans ces suspensions pour contrôler la rhéologie en jouant sur la nature des polymères.

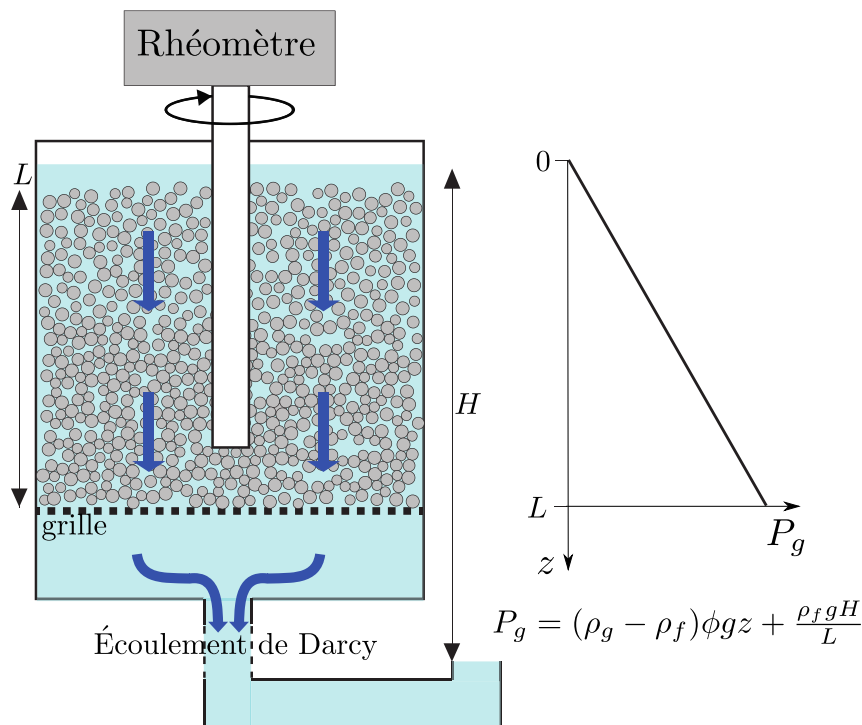


FIGURE 21 – Schéma illustrant le principe de fonctionnement du rhéomètre original à pression imposée que nous développerons dans la suite du projet.

## Conclusion

L'objectif de ce stage était de tester un modèle microscopique récent (Seto, Mari et al. [20, 17], Wyart et Cates [22]) proposant d'expliquer le rhéo-épaississement par une transition frictionnelle. Pour cela, nous avons

conçu une expérience modèle simple contenant les éléments clés de cette nouvelle théorie : des grains frottants se repoussant entre eux. Avec cette expérience, nous voulions comprendre le comportement d'un tel système sous cisaillement, et cherchions à observer une transition de rhéo-épaississement.

Nous avons tout d'abord étudié la rhéologie de notre milieu dans des expériences à volume imposé. Dans cette configuration, les données ne nous permettent pas de conclure. On sait qu'il est difficile de s'approcher du blocage d'un milieu granulaire lorsqu'on impose le volume. De plus, dans notre système, nous sommes dominés par les effets de bords. Nous nous sommes donc tournés vers des expériences à pression imposée.

Dans ce cas, les résultats sont beaucoup plus satisfaisants. En effet, nous observons bien une transition du coefficient de frottement macroscopique  $\tilde{\mu}$  autour d'une valeur critique  $P_c$  de la pression. Il convient toutefois de nuancer ce succès par plusieurs observations. Tout d'abord,  $P_c$  ne semble pas correspondre à la pression magnétique exercée dans le milieu, qui est pourtant notre échelle de pression a priori. De plus, si le comportement de  $\tilde{\mu}$  est bien celui attendu, celui de  $\phi$  nous montre que la transition que nous voulions observer est masquée par les forces longue portée. Celles-ci introduisent une élasticité dans le milieu, et nous observons en réalité une transition allant d'un milieu mou vers un milieu rigide.

Pendant, les résultats obtenus dans les expériences à pression imposée nous encouragent à poursuivre dans cette voie. L'expérience modèle sera améliorée en tenant compte des difficultés rencontrées. Nous nous tournerons également vers les suspensions rhéo-épaississantes réelles, et étudierons leur rhéologie afin, à terme, d'être capable de la contrôler.

## Références

- [1] R. A. Bagnold, *Experiments on a gravity-free dispersion of large solid spheres in a Newtonian fluid under shear*, Proc. R. Soc. Lond. **225** (1954), no. 1160, 49–63.
- [2] J. W. Bender and N. J. Wagner, *Optical measurement of the contributions of colloidal forces to the rheology of concentrated suspensions*, J. Colloid Interface Sci. **172** (1995), no. 1, 171–184.
- [3] G. Bossis and J. F. Brady, *The rheology of Brownian suspensions*, J. Chem. Phys. **91** (1989), no. 3, 1866–1874.
- [4] F. Boyer, E. Guazzelli, and O. Pouliquen, *Unifying suspension and granular rheology*, Phys. Rev. Lett. **107** (2011), 188301.
- [5] J. F. Brady and G. Bossis, *The rheology of concentrated suspensions of spheres in simple shear flow by numerical simulation*, J. Fluid Mech. **155** (1985), 105–129.
- [6] ———, *Stokesian dynamics*, Ann. Rev. Fluid Mech. **20** (1988), no. 1, 111–157.
- [7] E. Brown and H. M. Jaeger, *The role of dilation and confining stresses in shear-thickening of dense suspensions*, J. Rheol. **56** (2012), no. 4, 875–923.
- [8] ———, *Shear-thickening in concentrated suspensions : phenomenology, mechanisms and relations to jamming*, Rep. Prog. Phys. **77** (2014), no. 4, 046602.
- [9] F. da Cruz, S. Emam, M. Prochnow, J.-N. Roux, and F. Chevoir, *Rheophysics of dense granular materials : discrete simulation of plane shear flows*, Phys. Rev. E **72** (2005), 021309.
- [10] A. Fall, F. Bertrand, D. Hautemayou, C. Mezière, P. Moucheront, A. Lemaître, and G. Ovarlez, *Macroscopic discontinuous shear-thickening versus local shear jamming in cornstarch*, Phys. Rev. Lett. **114** (2015), 098301.
- [11] A. Fall, A. Lemaître, F. Bertrand, D. Bonn, and G. Ovarlez, *Shear-thickening and migration in granular suspensions*, Phys. Rev. Lett. **105** (2010), 268303.
- [12] N. Fernandez, *From tribology to rheology impact of interparticle friction in the shear-thickening of non-Brownian suspensions*, Ph.D. thesis, ETH Zurich, 2014.
- [13] N. Fernandez, R. Mani, D. Rinaldi, D. Kadau, M. Mosquet, H. Lombois-Burger, J. Cayer-Barrioz, H. J. Herrmann, N. D. Spencer, and L. Isa, *Microscopic mechanism for shear-thickening of non-Brownian suspensions*, Phys. Rev. Lett. **111** (2013), 108301.
- [14] Y. Forterre and O. Pouliquen, *Flows of dense granular media*, Ann. Rev. Fluid Mech. **40** (2008), no. 1, 1–24.
- [15] H. Freundlich and H. L. Roder, *Dilatancy and its relation to thixotropy*, Trans. Faraday Soc. **34** (1938), 308–316.

- [16] B. J. Maranzano and N. J. Wagner, *The effects of particle size on reversible shear-thickening of concentrated colloidal dispersions*, J. Chem. Phys. **114** (2001), no. 23, 10514–10527.
- [17] R. Mari, R. Seto, J. F. Morris, and M. M. Denn, *Shear thickening, frictionless and frictional rheologies in non-Brownian suspensions*, J. Rheol. **58** (2014), no. 6, 1693–1724.
- [18] J. R. Melrose and R. C. Ball, *“contact networks” in continuously shear-thickening colloids*, J. Rheol. **48** (2004), no. 5, 961–978.
- [19] J. Mewis and N. J. Wagner, *Colloidal suspension rheology*, 1 ed., Cambridge series in chemical engineering, Cambridge University Press, Cambridge, 2012.
- [20] R. Seto, R. Mari, J. F. Morris, and M. M. Denn, *Discontinuous shear-thickening of frictional hard-sphere suspensions*, Phys. Rev. Lett. **111** (2013), 218301.
- [21] N. J. Wagner and J F Brady, *Shear-thickening in colloidal dispersions*, Phys. Today **62** (2009), no. 10, 27–32.
- [22] M. Wyart and M. E. Cates, *Discontinuous shear-thickening without inertia in dense non-Brownian suspensions*, Phys. Rev. Lett. **112** (2014), 098302.

## A Code Matlab (couplemètre)

```

%%%%%%%%%%%%%%%%%%%%%%%%%%%%%%%%%%%%%%%%%%%%%%%%%%%%%%%%%%%%%%%%%%%%%%%%
%   Traitement des données du couplemètre   %
%%%%%%%%%%%%%%%%%%%%%%%%%%%%%%%%%%%%%%%%%%%%%%%%%%%%%%%%%%%%%%%%%%%%%%%%

%%%%%%%%%%%%%%%%%%%%%%%%%%%%%%%%%%%%%%%%%%%%%%%%%%%%%%%%%%%%%%%%%%%%%%%%
clear all;
close all;
clc;

% Offset du a la carte d'acquisition, a soustraire au signal
Coffset=0.2100;

% Recuperation du fichier de donnees
NomDossier='Nom du dossier';
NomFichier=strcat('Nom du fichier','.txt');
Fichier=strcat(NomDossier,NomFichier);

% Creation des variables couple et t (temps)
[x, couple]=textread(Fichier,'%f %f');
t=x-x(1);

% Trace des donnees
plot(couple-Coffset,'r');
hold on;

% Calcul de la moyenne du signal sur les trois tours du milieu
Cmean = mean(couple(1000:4000)-Coffset,1);
%%%%%%%%%%%%%%%%%%%%%%%%%%%%%%%%%%%%%%%%%%%%%%%%%%%%%%%%%%%%%%%%%%%%%%%%

```

## B Code Matlab (traitement des images)

```

%%%%%%%%%%%%%%%%%%%%%%%%%%%%%%%%%%%%%%%%%%%%%%%%%%%%%%%%%%%%%%%%%%%%%%%%
%   Analyse des images traitees avec ImageJ   %
%%%%%%%%%%%%%%%%%%%%%%%%%%%%%%%%%%%%%%%%%%%%%%%%%%%%%%%%%%%%%%%%%%%%%%%%

%%%%%%%%%%%%%%%%%%%%%%%%%%%%%%%%%%%%%%%%%%%%%%%%%%%%%%%%%%%%%%%%%%%%%%%%
clear all;
close all;
clc;

% Echelle pour conversion pixel -> mm (40 mm = 1469 pixels)
Echelle = 40/1462;

% Position du vernier, en mm
PositionVernier=30;

% Epaisseur du curseur (calibration faite en lisant la position du bord
% droit, programme : acquiert la position du bord gauche)
EpaisseurCurseur=80*Echelle; % taille en pixel * echelle = epaisseur en mm

% Recuperation du fichier de donnees
NomDossier='Nom du dossier';
NomFichier=strcat('Analyse','.tif');
NomImage = strcat(NomDossier,NomFichier);

```



```

% Boucle sur les images contenues dans le stack fait par ImageJ
for l=1:190

%%%%%%%%%%%%%%%%%%%%%%%%%%%%%%%%%%%%%%%%%%%%%%%%%%%%%%%%%%%%%%%%%%%%%%%%
%   Traitement de l'image l   %
%%%%%%%%%%%%%%%%%%%%%%%%%%%%%%%%%%%%%%%%%%%%%%%%%%%%%%%%%%%%%%%%%%%%%%%%

%%%%%%%%%%%%%%%%%%%%%%%%%%%%%%%%%%%%%%%%%%%%%%%%%%%%%%%%%%%%%%%%%%%%%%%%

% Chargement de l'image
Image = double(imread(NomImage,'tiff',l));

% Compteur pour creer le vecteur position
c=1;

% Boucle sur toutes les lignes de l'image
for i=1:size(Image,1)

    % On cherche le premier pixel non blanc (bord gauche du
    % curseur) et on stocke sa position dans un vecteur
    u=find(Image(i,:)>0);
    Position(c)=u(1);

    % Incrementation du compteur
    c=c+1;
end

% Position moyenne du curseur pour l'image l (moyenne sur les lignes)
PositionCurseurImageL(l)=mean(Position,2);

%%%%%%%%%%%%%%%%%%%%%%%%%%%%%%%%%%%%%%%%%%%%%%%%%%%%%%%%%%%%%%%%%%%%%%%%
end

%%%%%%%%%%%%%%%%%%%%%%%%%%%%%%%%%%%%%%%%%%%%%%%%%%%%%%%%%%%%%%%%%%%%%%%%
%   Calcul de la pression imposee   %
%%%%%%%%%%%%%%%%%%%%%%%%%%%%%%%%%%%%%%%%%%%%%%%%%%%%%%%%%%%%%%%%%%%%%%%%

%%%%%%%%%%%%%%%%%%%%%%%%%%%%%%%%%%%%%%%%%%%%%%%%%%%%%%%%%%%%%%%%%%%%%%%%
PositionCurseur=mean(PositionCurseurImageL,2)*Echelle+EpaisseurCurseur;
% moyenne sur les colonnes ; position en mm
Deflection = (60-PositionVernier)+(47-PositionCurseur);
Pmesuree = (132/29)*Deflection
% calcul a partir de la calibration, attention la calibration depend du diametre de la tige
Phydro = 5.4-0.057*PositionCurseur;
% calcul a partir de la calibration
Pimposee = Pmesuree-Phydro;

%%%%%%%%%%%%%%%%%%%%%%%%%%%%%%%%%%%%%%%%%%%%%%%%%%%%%%%%%%%%%%%%%%%%%%%%

%%%%%%%%%%%%%%%%%%%%%%%%%%%%%%%%%%%%%%%%%%%%%%%%%%%%%%%%%%%%%%%%%%%%%%%%

```

## C Macro ImageJ

```

run("Image Sequence...", "open=[chemin+nom du fichier] sort");
//setTool("rectangle");

```

```
makeRectangle(coordonnées des 4 sommets du rectangle);
run("Duplicate...", "title=titre duplicate range=1-taille du stack");
saveAs("Tiff", "Chemin\\Regle.tif");
//setTool("rectangle");

makeRectangle(coordonnées des 4 sommets du rectangle);
run("Duplicate...", "title=Regle-1.tif duplicate range=1-taille du stack");
```



## APPENDIX B

---

### Revealing the frictional transition in shear-thickening suspensions

---

For compatibility reasons, it is not possible for me to include this article in the online version of the manuscript. You can find it at <https://doi.org/10.1073/pnas.1703926114>.



## ANNEXE C

---

### Suspensions rhéoépaississantes : principes et applications

---

For compatibility reasons, it is not possible for me to include this article in the online version of the manuscript. You can ask me for it at [cecileclavaud@free.fr](mailto:cecileclavaud@free.fr).



---

## Bibliography

---

- [1] R. Seto, R. Mari, J. F. Morris, and M. M. Denn, “Discontinuous shear-thickening of frictional hard-sphere suspensions,” *Physical Review Letters*, vol. 111, 2013.
- [2] R. Mari, R. Seto, J. F. Morris, and M. M. Denn, “Shear thickening, frictionless and frictional rheologies in non-Brownian suspensions,” *Journal of Rheology*, vol. 58, no. 6, pp. 1693–1724, 2014.
- [3] M. Wyart and M. E. Cates, “Discontinuous shear-thickening without inertia in dense non-Brownian suspensions,” *Physical Review Letters*, vol. 112, 2014.
- [4] C. Clavaud, A. Bérut, B. Metzger, and Y. Forterre, “Revealing the frictional transition in shear-thickening suspensions,” *Proceedings of the National Academy of Sciences*, vol. 114, no. 20, pp. 5147–5152, 2017.
- [5] C. Clavaud, A. Bérut, B. Metzger, and Y. Forterre, “Suspensions rhéo-épaississantes Principes et applications,” *Techniques de l’Ingénieur*, 2018.
- [6] É. Guyon, J.-P. Hulin, and L. Petit, *Hydrodynamique physique*. CNRS Édition, 3 ed., 2012.
- [7] É. Guazzelli, J. F. Morris, and S. Pic, *A physical introduction to suspension dynamics*. Cambridge Texts in Applied Mathematics, Cambridge University Press, 2011.
- [8] E. Brown and H. M. Jaeger, “The role of dilation and confining stresses in shear-thickening of dense suspensions,” *Journal of Rheology*, vol. 56, no. 4, pp. 875–923, 2012.
- [9] J. Mewis and N. J. Wagner, *Colloidal suspension rheology*. Cambridge series in chemical engineering, Cambridge: Cambridge University Press, 2012.
- [10] A. Fall, F. Bertrand, D. Hautemayou, C. Mezière, P. Moucheront, A. Lemaître, and G. Ovarlez, “Macroscopic discontinuous shear-thickening versus local shear jamming in cornstarch,” *Physical Review Letters*, vol. 114, 2015.



- [11] Y. Madraki, S. Hormozi, G. Ovarlez, E. Guazzelli, and O. Pouliquen, “Enhancing shear thickening,” *Physical Review Fluids*, vol. 2, p. 033301, Mar 2017.
- [12] R. V. Williamson and W. W. Heckert, “Some properties of dispersions of the quicksand type,” *Industrial and Engineering Chemistry*, 1931.
- [13] H. Freundlich and H. L. Röder, “Dilatancy and its relation to thixotropy,” *Transactions of the Faraday Society*, vol. 34, pp. 308–316, 1938.
- [14] W. H. Boersma, J. Laven, and H. N. Stein, “Shear thickening (dilatancy) in concentrated dispersions,” *AIChE Journal*, vol. 36, no. 3, pp. 321–332, 1990.
- [15] E. Brown and H. M. Jaeger, “Shear-thickening in concentrated suspensions: phenomenology, mechanisms and relations to jamming,” *Reports on Progress in Physics*, vol. 77, no. 4, 2014.
- [16] H. A. Barnes, “Shear-thickening (“dilatancy”) in suspensions of nonaggregating solid particles dispersed in Newtonian liquids,” *Journal of Rheology*, vol. 33, no. 2, pp. 329–366, 1989.
- [17] E. Brown, N. A. Forman, C. S. Orellana, H. Zhang, B. W. Maynor, D. E. Betts, J. M. DeSimone, and H. M. Jaeger, “Generality of shear thickening in dense suspensions,” *Nature Materials*, vol. 9, 2010.
- [18] A. A. Tracton, *Coatings technology handbook*. CRC press, 2005.
- [19] M. B. Stauffer, “Chocolate behavior-What influences your selection?,” *Manufacturing Confectioner*, vol. 78, pp. 75–80, 1998.
- [20] N. Fernandez, *From tribology to rheology: impact of interparticle friction in the shear-thickening of non-Brownian suspensions*. PhD thesis, ETH Zurich, 2014.
- [21] S. R. Waitukaitis and H. M. Jaeger, “Impact-activated solidification of dense suspensions via dynamic jamming fronts,” *Nature*, vol. 487, no. 7406, pp. 205–209, 2012.
- [22] N. J. Wagner and J. F. Brady, “Shear thickening in colloidal dispersions,” *Physics Today*, 2009.
- [23] A. Einstein, “On the movement of small particles suspended in liquids at rest required by the molecular-kinetic theory of heat,” *Annalen der Physik*, vol. 17, 01 1905.
- [24] É. Guazzelli and O. Pouliquen, “Rheology of dense granular suspensions,” *In preparation*, 2018.
- [25] G. I. Barenblatt, *Scaling, self-similarity, and intermediate asymptotics: dimensional analysis and intermediate asymptotics*, vol. 14. Cambridge University Press, 1996.
- [26] Y. Forterre and O. Pouliquen, “Flows of dense granular media,” *Annual Review of Fluid Mechanics*, vol. 40, no. 1, pp. 1–24, 2008.

- [27] C. Cassar, M. Nicolas, and O. Pouliquen, “Submarine granular flows down inclined planes,” *Physics of Fluids*, vol. 17, no. 10, 2005.
- [28] F. Boyer, É. Guazzelli, and O. Pouliquen, “Unifying suspension and granular rheology,” *Physical Review Letters*, vol. 107, 2011.
- [29] S. Chialvo, J. Sun, and S. Sundaresan, “Bridging the rheology of granular flows in three regimes,” *Physical Review E*, vol. 85, Feb 2012.
- [30] M. Trulsson, E. DeGiuli, and M. Wyart, “Effect of friction on dense suspension flows of hard particles,” *Physical Review E*, vol. 95, Jan 2017.
- [31] A. Deboeuf, G. Gauthier, J. Martin, Y. Yurkovetsky, and J. F. Morris, “Particle pressure in a sheared suspension: a bridge from osmosis to granular dilatancy,” *Physical Review Letters*, vol. 102, Mar 2009.
- [32] T. Dbouk, L. Lobry, and E. Lemaire, “Normal stresses in concentrated non-Brownian suspensions,” *Journal of Fluid Mechanics*, vol. 715, pp. 239–272, 2013.
- [33] O. Reynolds, “LVII. On the dilatancy of media composed of rigid particles in contact. With experimental illustrations,” *The London, Edinburgh, and Dublin Philosophical Magazine and Journal of Science*, vol. 20, no. 127, pp. 469–481, 1885.
- [34] J. N. Israelachvili, *Intermolecular and surface forces*. Academic press, 2011.
- [35] R. J. Morgan, “A study of the phenomenon of rheological dilatancy in an aqueous pigment suspension,” *Transactions of the Society of Rheology*, vol. 12, no. 4, pp. 511–533, 1968.
- [36] D. I. Lee and A. S. Reder, “The rheological properties of clay suspensions, latex and clay-latex systems,” *Papers Presented at the 23rd Annual TAPPI Coating Conference, San Francisco, May 1972*, vol. 27, pp. 190–195, 01 1973.
- [37] J. F. Brady and G. Bossis, “The rheology of concentrated suspensions of spheres in simple shear flow by numerical simulation,” *Journal of Fluid Mechanics*, vol. 155, pp. 105–129, 1985.
- [38] J. F. Brady and G. Bossis, “Stokesian dynamics,” *Annual Review of Fluid Mechanics*, vol. 20, no. 1, pp. 111–157, 1988.
- [39] G. Bossis and J. F. Brady, “The rheology of Brownian suspensions,” *Journal of Chemical Physics*, vol. 91, no. 3, pp. 1866–1874, 1989.
- [40] X. Cheng, J. H. McCoy, J. N. Israelachvili, and I. Cohen, “Imaging the microscopic structure of shear thinning and thickening colloidal suspensions,” *Science*, vol. 333, no. 6047, pp. 1276–1279, 2011.
- [41] A. Fall, A. Lemaître, F. Bertrand, D. Bonn, and G. Ovarlez, “Shear-thickening and migration in granular suspensions,” *Physical Review Letters*, vol. 105, 2010.

- [42] N. Fernandez, R. Mani, D. Rinaldi, D. Kadau, M. Mosquet, H. Lombois-Burger, J. Cayer-Barrioz, H. J. Herrmann, N. D. Spencer, and L. Isa, “Microscopic mechanism for shear-thickening of non-Brownian suspensions,” *Physical Review Letters*, vol. 111, 2013.
- [43] R. A. Bagnold, “Experiments on a gravity-free dispersion of large solid spheres in a Newtonian fluid under shear,” *Proceedings of the Royal Society of London*, vol. 225, no. 1160, pp. 49–63, 1954.
- [44] A. Lemaître, J.-N. Roux, and F. Chevoir, “What do dry granular flows tell us about dense non-Brownian suspension rheology?,” *Rheologica Acta*, vol. 48, pp. 925–942, Oct 2009.
- [45] M. Trulsson, B. Andreotti, and P. Claudin, “Transition from the viscous to inertial regime in dense suspensions,” *Physical Review Letters*, vol. 109, 2012.
- [46] A. Fall, N. Huang, F. Bertrand, G. Ovarlez, and D. Bonn, “Shear thickening of cornstarch suspensions as a reentrant jamming transition,” *Physical Review Letters*, vol. 100, 2008.
- [47] E. DeGiuli, G. Düring, E. Lerner, and M. Wyart, “Unified theory of inertial granular flows and non-Brownian suspensions,” *Physical Review E*, vol. 91, Jun 2015.
- [48] D. Lootens, H. Van Damme, and P. Hébraud, “Giant stress fluctuations at the jamming transition,” *Physical Review Letters*, vol. 90, Apr 2003.
- [49] S. Lee and N. D. Spencer, “Sweet, Hairy, Soft, and Slippery,” *Science*, vol. 319, no. 5863, pp. 575–576, 2008.
- [50] R. Mari, R. Seto, J. F. Morris, and M. M. Denn, “Discontinuous shear thickening in Brownian suspensions by dynamic simulation,” *Proceedings of the National Academy of Sciences*, vol. 112, no. 50, pp. 15326–15330, 2015.
- [51] B. M. Guy, M. Hermes, and W. C. K. Poon, “Towards a unified description of the rheology of hard-particle suspensions,” *Physical Review Letters*, vol. 115, Aug 2015.
- [52] N. Y. C. Lin, B. M. Guy, M. Hermes, C. Ness, J. Sun, W. C. K. Poon, and I. Cohen, “Hydrodynamic and contact contributions to continuous shear thickening in colloidal suspensions,” *Physical Review Letters*, vol. 115, Nov 2015.
- [53] J. R. Royer, D. L. Blair, and S. D. Hudson, “Rheological signature of frictional interactions in shear thickening suspensions,” *Physical Review Letters*, vol. 116, May 2016.
- [54] F. Blanc, F. Peters, and E. Lemaire, “Local transient rheological behavior of concentrated suspensions,” *Journal of Rheology*, vol. 55, no. 4, pp. 835–854, 2011.

- 
- [55] B. Andreotti, Y. Forterre, and O. Pouliquen, *Granular media: between fluid and solid*. Cambridge University Press, 2013.
- [56] M. A. Carrigy, “Experiments on the angles of repose of granular materials,” *Sedimentology*, vol. 14, no. 3–4, pp. 147–158, 1970.
- [57] P.-E. Peyneau and J.-N. Roux, “Frictionless bead packs have macroscopic friction, but no dilatancy,” *Physical Review E*, vol. 78, Jul 2008.
- [58] C.-Y. Hung, C. P. Stark, and H. Capart, “Granular flow regimes in rotating drums from depth-integrated theory,” *Physical Review E*, vol. 93, Mar 2016.
- [59] H.-T. Chou and C.-F. Lee, “Cross-sectional and axial flow characteristics of dry granular material in rotating drums,” *Granular Matter*, vol. 11, no. 1, pp. 13–32, 2009.
- [60] GDRMiDi, “On dense granular flows,” *The European Physical Journal E*, vol. 14, no. 4, pp. 341–365, 2004.
- [61] S. Courrech du Pont, P. Gondret, B. Perrin, and M. Rabaud, “Granular avalanches in fluids,” *Physical review letters*, vol. 90, no. 4, 2003.
- [62] S. Courrech du Pont, P. Gondret, B. Perrin, and M. Rabaud, “Wall effects on granular heap stability,” *Europhysics Letters*, vol. 61, no. 4, p. 492, 2003.
- [63] S. Courrech du Pont, *Avalanches granulaires en milieu fluide*. PhD thesis, Université Paris XI, 2003.
- [64] B. Boursier, “Amidons natifs et amidons modifiés alimentaires,” *Techniques de l’Ingénieur*, 2005.
- [65] P. Richard, M. Nicodemi, R. Delannay, P. Ribière, and D. Bideau, “Slow relaxation and compaction of granular systems,” *Nature Materials*, vol. 4, pp. 121–128, 2005.
- [66] C. P. Wroth, “Soil behaviour during shear-existence of critical voids ratios,” *Engineering*, vol. 186, pp. 409–413, 1958.
- [67] M. Pailha, M. Nicolas, and O. Pouliquen, “Initiation of underwater granular avalanches: influence of the initial volume fraction,” *Physics of Fluids*, vol. 20, no. 11, 2008.
- [68] N. N. Hellman, T. F. Boesch, and E. H. Melvin, “Starch granule swelling in water vapor sorption,” *Journal of the American Chemical Society*, vol. 74, no. 2, pp. 348–350, 1952.
- [69] D. R. Lineback, “Current concepts of starch structure and its impact on properties,” *Journal of the Japanese Society of Starch Science*, vol. 33, pp. 80–88, 1986.

- [70] J. Huang, N. Wei, H. Li, S. Liu, and D. Yang, “Outer shell, inner blocklets, and granule architecture of potato starch,” *Carbohydrate Polymers*, vol. 103, pp. 355–358, 2014.
- [71] L. Oyarte Gálvez, S. de Beer, D. van der Meer, and A. Pons, “Dramatic effect of fluid chemistry on cornstarch suspensions: linking particle interactions to macroscopic rheology,” *Physical Review E*, vol. 95, Mar 2017.
- [72] H. Park, S. Xu, and K. Seetharaman, “A novel in situ atomic force microscopy imaging technique to probe surface morphological features of starch granules,” *Carbohydrate Research*, vol. 346, no. 6, pp. 847–853, 2011.
- [73] A. W. Alexander, B. Chaudhuri, A. Faqih, F. J. Muzzio, C. Davies, and M. S. Tomassone, “Avalanching flow of cohesive powders,” *Powder Technology*, vol. 164, no. 1, pp. 13–21, 2006.
- [74] P. Y. Liu, R. Y. Yang, and A. B. Yu, “Dynamics of wet particles in rotating drums: effect of liquid surface tension,” *Physics of fluids*, vol. 23, no. 1, 2011.
- [75] G. Vigil, Z. Xu, S. Steinberg, and J. Israelachvili, “Interactions of silica surfaces,” *Journal of Colloid and interface science*, vol. 165, no. 2, pp. 367–385, 1994.
- [76] V. Valmacco, M. Elzbieciak-Wodka, C. Besnard, P. Maroni, G. Trefalt, and M. Borkovec, “Dispersion forces acting between silica particles across water: influence of nanoscale roughness,” *Nanoscale Horizons*, vol. 1, no. 4, pp. 325–330, 2016.
- [77] S. H. Behrens and D. G. Grier, “The charge of glass and silica surfaces,” *The Journal of Chemical Physics*, vol. 115, no. 14, pp. 6716–6721, 2001.
- [78] J. J. S. Jerome, N. Vandenberghe, and Y. Forterre, “Unifying impacts in granular matter from quicksand to cornstarch,” *Physical Review Letters*, vol. 117, no. 9, 2016.
- [79] J. Comtet, G. Chatté, A. Niguès, L. Bocquet, A. Siria, and A. Colin, “Pairwise frictional profile between particles determines discontinuous shear thickening transition in non-colloidal suspensions,” *Nature communications*, vol. 8, 2017.
- [80] M. Depken, J. B. Lechman, M. van Hecke, W. van Saarloos, and G. S. Grest, “Stresses in smooth flows of dense granular media,” *Europhysics Letters*, vol. 78, no. 5, p. 58001, 2007.
- [81] F. Da Cruz, *Ecoulement de grains secs : frottement et blocage*. PhD thesis, École Nationale des Ponts et Chaussées, 2004.
- [82] V. Mehandia, K. J. Gutam, and P. R. Nott, “Anomalous stress profile in a sheared granular column,” *Physical Review Letters*, vol. 109, Sep 2012.

- [83] K. P. Krishnaraj and P. R. Nott, "A dilation-driven vortex flow in sheared granular materials explains a rheometric anomaly," *Nature Communications*, 2016.
- [84] R. Lespiat, S. Cohen-Addad, and R. Höhler, "Jamming and flow of random-close-packed spherical bubbles: an analogy with granular materials," *Physical Review Letters*, vol. 106, p. 148302, Apr 2011.

